



# Nanostructures

*Edited by*

**Alessandra L. Da Róz**  
Federal Institute of Education,  
Science and Technology of São Paulo Itapetininga,  
São Paulo, Brazil

**Marystela Ferreira**  
Federal University of São Carlos,  
Center for Sciences and Technology for Sustainability,  
Sorocaba, São Paulo, Brazil

**Fábio de Lima Leite**  
Federal University of São Carlos,  
Center for Sciences and Technology for Sustainability,  
Sorocaba, São Paulo, Brazil

**Osvaldo N. Oliveira Jr**  
São Carlos Institute of Physics  
University of São Paulo (USP)  
São Carlos, São Paulo, Brazil



AMSTERDAM • BOSTON • HEIDELBERG • LONDON • NEW YORK • OXFORD  
PARIS • SAN DIEGO • SAN FRANCISCO • SINGAPORE • SYDNEY • TOKYO

William Andrew is an imprint of Elsevier

William Andrew is an imprint of Elsevier  
The Boulevard, Langford Lane, Kidlington, Oxford, OX5 1GB, United Kingdom  
50 Hampshire Street, 5th Floor, Cambridge, MA 02139, United States

Copyright © 2017 Elsevier Inc. All rights reserved.

This English edition of Nanostructures by Osvaldo Novais de Oliveira, Jr, Marystela Ferreira, Alessandra Luzia Da Róz, Fabio Leite is published by arrangement with Elsevier Editora Ltda.

Originally published in the Portuguese language as Nanoestruturas 1st edition (ISBN 978-85-352-8089-0)  
© Copyright 2015 Elsevier Editora Ltda.

No part of this publication may be reproduced or transmitted in any form or by any means, electronic or mechanical, including photocopying, recording, or any information storage and retrieval system, without permission in writing from the publisher. Details on how to seek permission, further information about the Publisher's permissions policies and our arrangements with organizations such as the Copyright Clearance Center and the Copyright Licensing Agency, can be found at our website: [www.elsevier.com/permissions](http://www.elsevier.com/permissions).

This book and the individual contributions contained in it are protected under copyright by the Publisher (other than as may be noted herein).

#### Notices

Knowledge and best practice in this field are constantly changing. As new research and experience broaden our understanding, changes in research methods, professional practices, or medical treatment may become necessary.

Practitioners and researchers must always rely on their own experience and knowledge in evaluating and using any information, methods, compounds, or experiments described herein. In using such information or methods they should be mindful of their own safety and the safety of others, including parties for whom they have a professional responsibility.

To the fullest extent of the law, neither the Publisher nor the authors, contributors, or editors, assume any liability for any injury and/or damage to persons or property as a matter of products liability, negligence or otherwise, or from any use or operation of any methods, products, instructions, or ideas contained in the material herein.

#### Library of Congress Cataloging-in-Publication Data

A catalog record for this book is available from the Library of Congress

#### British Library Cataloguing-in-Publication Data

A catalogue record for this book is available from the British Library

ISBN: 978-0-323-49782-4

For information on all William Andrew publications  
visit our website at <https://www.elsevier.com/>



Working together  
to grow libraries in  
developing countries

[www.elsevier.com](http://www.elsevier.com) • [www.bookaid.org](http://www.bookaid.org)

*Publisher:* Matthew Deans

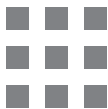
*Acquisition Editor:* Simon Holt

*Editorial Project Manager:* Sabrina Webber

*Production Project Manager:* Jason Mitchell

*Designer:* Greg Harris

Typeset by Thomson Digital



# List of Contributors

## **L. Caseli**

Institute of Environmental, Chemical and Pharmaceutical Sciences, Federal University of São Paulo,  
São Paulo, São Paulo, Brazil

## **A.L. Da Róz**

Federal Institute of Education, Science and Technology of São Paulo Itapetininga, São Paulo, Brazil

## **A. de Barros**

State University of Campinas, Institute of Chemistry, Campinas, São Paulo, Brazil

## **M.L. de Moraes**

Institute of Science and Technology, Federal University of São Paulo, São Paulo, São Paulo, Brazil

## **R.F. de Oliveira**

Brazilian Center for Research in Energy and Materials, Brazilian Nanotechnology National Laboratory,  
Campinas, São Paulo, Brazil

## **M. Ferreira**

Federal University of São Carlos, Center for Sciences and Technology for Sustainability, Sorocaba,  
São Paulo, Brazil

## **F. de Lima Leite**

Federal University of São Carlos, Center for Sciences and Technology for Sustainability, Sorocaba,  
São Paulo, Brazil

## **R. Marchiori**

Interdisciplinary Department of Science and Technology, Federal University of Rondônia, Ariquemes,  
Rondônia, Brazil

## **C.M. Miyazaki**

Federal University of São Carlos, Center of Sciences and Technology for Sustainability, Sorocaba,  
São Paulo, Brazil

## **Osvaldo N. Oliveira Jr**

São Carlos Institute of Physics, University of São Paulo (USP), São Carlos, São Paulo, Brazil

**F.R. Passador**

Institute of Science and Technology, Federal University of São Paulo, São Paulo, São Paulo, Brazil

**L.G. Paterno**

Institute of Chemistry, University of Brasilia, University Campus Darcy Ribeiro, Brasilia, Brazil

**L.A. Pessan**

Department of Materials Engineering, Federal University of São Carlos, São Carlos, São Paulo, Brazil

**A. Riul Jr**

"Gleb Wataghin" Institute of Physics, State University of Campinas, Campinas, São Paulo, Brazil

**A. Ruvolo-Filho**

Department of Materials Engineering, Federal University of São Carlos, São Carlos, São Paulo, Brazil

**F.R. Simões**

Institute of Marine Sciences, Federal University of São Paulo, Santos, SP, Brazil

**J.R. Siqueira Jr**

Institute of Exact Sciences, Natural and Education, Federal University of Triângulo Mineiro (UFTM), Uberaba, Minas Gerais, Brazil

**J.S. Santos**

Federal University of São Carlos, Center for Sciences and Technology for Sustainability, Sorocaba, São Paulo, Brazil

**M.A.G. Soler**

Institute of Physics, University of Brasília, University Campus Darcy Ribeiro, Brasilia, Brazil

**M. Souza Sikora**

Federal Technological University of Paraná, Pato Branco, Paraná, Brazil

**H.H. Takeda**

Department of Interdisciplinary Sciences and Technology, Federal University of Rondônia, Ariquemes, Rondônia, Brazil

**F. Trivinho-Strixino**

Federal University of São Carlos, Center for Sciences and Technology for Sustainability, Sorocaba, São Paulo, Brazil

# Basic Concepts and Principles

F.R. Simões\*, H.H. Takeda\*\*

\*INSTITUTE OF MARINE SCIENCES, FEDERAL UNIVERSITY OF SÃO PAULO,  
SANTOS, SP, BRAZIL; \*\*DEPARTMENT OF INTERDISCIPLINARY SCIENCES AND  
TECHNOLOGY, FEDERAL UNIVERSITY OF RONDÔNIA, ARIQUEMES, RONDÔNIA, BRAZIL

## CHAPTER OUTLINE

1.1	Introduction .....	1
1.1.1	Understanding the Nanoscale and Nanotechnology .....	1
1.1.2	Nanoscience: History, Concepts, and Principles .....	3
1.1.3	Investments, Strategies, Actions, and Research in Nanotechnology .....	14
1.1.4	Commercial Products Involving Nanotechnology .....	17
1.2	Final Considerations .....	26
	List of Symbols .....	27
	References .....	27

## 1.1 Introduction

### 1.1.1 Understanding the Nanoscale and Nanotechnology

To understand nanoscience and nanotechnology, it is necessary to know the origin of the prefix *nano*, which is Greek and means “dwarf.” One nanometer (nm) is simply 1 billionth of 1 m ( $1 \text{ nm} = 1 \times 10^{-9} \text{ m}$ ). For comparison, the ratio between the size of a soccer ball and the Earth is approximately the same as that between a soccer ball and a sphere of 60 carbon atoms known as a C-60 fullerene (Fig. 1.1). The Earth is approximately 100 million times larger than a soccer ball, and in turn, the ball is approximately 100 million times larger than the fullerene [1].

Several other common examples can be used to understand the “nano” scale. Fig. 1.2 compares different nanoscale materials. A human hair is approximately 100,000 nm wide, whereas a red blood cell is approximately 7,000 nm in diameter. Even smaller are typical viruses, which are between 45 and 200 nm in size. On the atomic scale, the length of a typical bond between carbon atoms and the spaces between atoms in a molecule are on the order of 0.12–0.15 nm [1–4].

Thus, structures of nanoscale materials (called nanostructures) are intermediate between the smallest structure that can be produced by man and the largest molecules of living systems. Humans’ abilities to control and manipulate nanostructures, therefore,

## 2 NANOSTRUCTURES

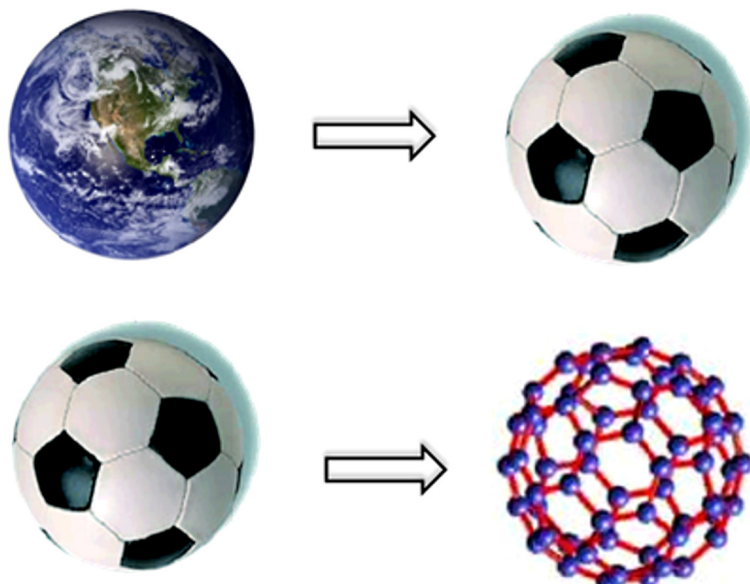


FIGURE 1.1 Illustration of the diameter ratios between the Earth and a ball, and between a ball and a C-60 fullerene.

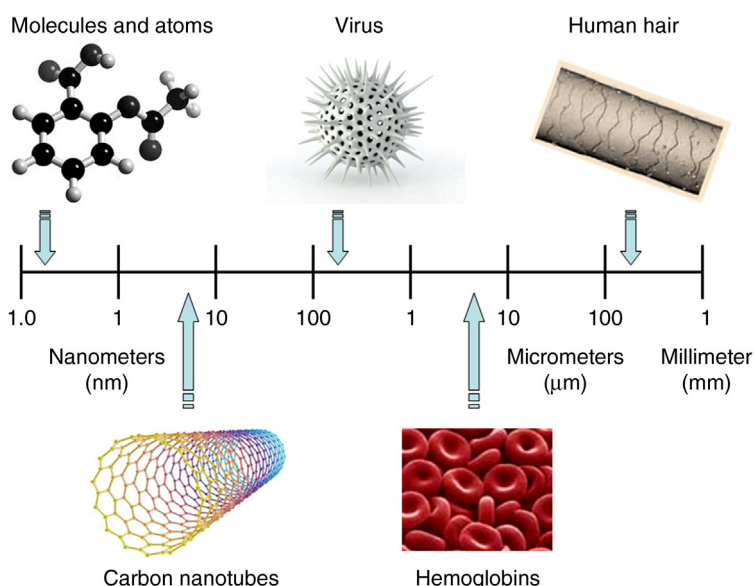


FIGURE 1.2 Illustrations of various materials ranging from millimeter (mm) to nanometer (nm) scales.

facilitate exploring novel physical, biological, and chemical properties of systems that are of intermediate size between atoms and molecules, such as, nanoscale materials.

Two standard definitions exist for the term nanotechnology: one given by the International Organization for Standardization–Technical Committee (ISO–TC) and the other given by the National Nanotechnology Initiative of the US (NNI). According to the ISO–TC, “(i) Understanding and control of matter and processes at the nanoscale, typically, but not exclusively, below 100 nanometres in one or more dimensions where the onset of size-dependent phenomena usually enables novel applications; and (ii) Utilizing the properties of nanoscale materials that differ from the properties of individual atoms, molecules, and bulk matter, to create improved materials, devices, and systems that exploit these new properties.” Therefore, for a device to be considered “nanotechnological,” in addition to nanometric dimensions, it must also have unique properties associated with the nanoscale [2–5]. In contrast, as defined by the NNI, nanotechnology must fall between 1 and 100 nm in size [2]. The lower limit is defined by the size of atoms, as this branch of science must construct devices from atoms and molecules. For example, one hydrogen atom has a diameter of approximately one quarter of a nanometer ( $d = 0.25 \text{ nm}$ ). The upper limit was established based on our ability to modulate properties on scales up to 100 nm and observe the resulting phenomena in larger structures that can be used to generate specific devices [2]. These phenomena differentiate truly nanoscale devices from those that are simply miniaturized versions of an equivalent macroscopic device. Thus, such larger-scale devices should be considered as microtechnologies [3].

Thus, nanotechnology is used to describe molecular-scale engineering systems. More specifically, this term refers to the ability to design, construct or manipulate devices, materials and functional systems on the nanometric scale [4,5].

### 1.1.2 Nanoscience: History, Concepts, and Principles

Between the discovery of fire by man and the present day, tremendous advancements have occurred in science and technology, accompanied by remarkable development in the research and manufacture of new products, including new materials, pharmaceuticals, and foods. For example, very light materials with mechanical resistances exceeding that of steel have been produced as a result of advances in nanoscience, which can be defined as *the science that governs the study of nanotechnology for the development or improvement of materials based on the possibility of manipulating atoms and/or molecules with observed effects that are closely linked to the nanoscale and that have attractive physical, chemical and/or biological properties* [6].

Although a large number and variety of technologies and articles have recently been published on the topic of nanotechnology, this science has been applied and studied for a long time, albeit without knowledge of the relationship among the scale, the product and the resulting properties. In other words, man has manipulated materials at the nanometer level for a long time without understanding that the effects obtained were related to their nanoscale natures. One example is medieval glass-blowers who, using mixtures of

## 4 NANOSTRUCTURES

gold nanoparticles of various sizes, produced differently colored stains for the fabrication of stained glass windows. A study by a research team at the University of Queensland [7] found that, in addition to the staining produced by gold nanoparticles, these nanoparticles also functioned as photocatalytic air purifiers: for example, when sunlight shone on the stained glass, air purification occurred. Another example is the experiment conducted by Michael Faraday (late 19th century), who synthesized gold nanoparticles [8] but did not understand their properties.

Regarding the manipulation of particles at the atomic level, scientists have investigated the nanometric world to find explanations and rationales for their theories, such as the atomic theory first proposed by Democritus in 400 BC, which was refined in 1913 by Ernest Rutherford and Niels Bohr [9]. Additionally, in 1867, James Clerk Maxwell performed an experiment known as Maxwell's demon, confirming that the second law of thermodynamics has only one statistical certainty. Briefly, in this experiment, Maxwell used a chamber containing a gas at equilibrium that was divided into two parts by a wall containing a door. When the door was opened, only the particles with higher and lower velocities could change sides, resulting in the heating of one side of the chamber and the cooling of the other [10]. Thomson (1906) and Lewis (1916) [9] developed the theory of chemical bonds (ionic and covalent bonding) to describe the formation of molecules. From 1934 to 1938, Lise Maitner, Otto Frisch, Otto Hahn, and Fritz Strassman studied the radioactive isotopes produced by bombarding uranium with neutrons (the experiment was conducted by Enrico Fermi). Based on their results, they discovered the phenomenon of nuclear fission, which releases 200 MeV of energy. This discovery led to the development of atomic bombs and nuclear power plants [11]. Another example is the nuclear fusion that occur in the Sun,  $n$  (Fig. 1.3), in which four hydrogen atoms fuse to form a helium atom, generating all the energy we observe and feel on Earth [12].

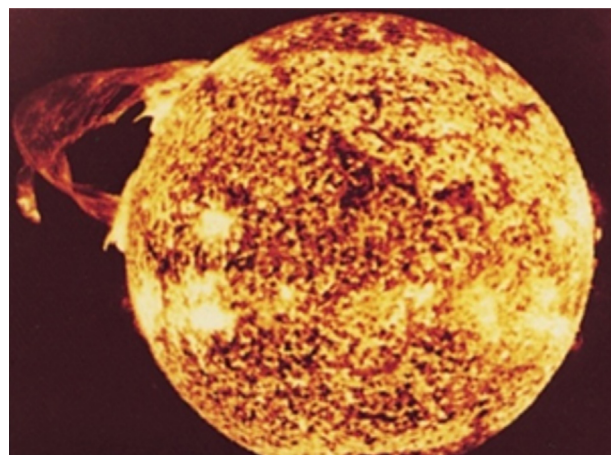


FIGURE 1.3 The Sun, a star undergoing constant nuclear fusion [12].

Many scientists have confirmed their theories or answered chemical and/or physical questions by simply observing the phenomena resulting from the atomic or molecular behaviors of materials, and thus, it can be concluded that a scientific field and its foundation develop via studies and the formulations of theories, concepts and principles based on experimental observations. Thus, defining the basic concepts and principles of nanoscience and nanotechnology would be much more difficult without the theoretical knowledge of other branches of sciences. Indeed, most of the laws, concepts and principles that govern nanoscience are essentially the same ones that govern physics and chemistry. To illustrate this, we simply review the portion of the definition of nanotechnology that states that *nanotechnology is a novel branch of science responsible for the study and development of materials at the atomic and molecular levels that have unique characteristics associated with the nanoscale*. This concept confirms that the manipulation of atoms or molecules first requires theoretical knowledge of atomic theory and chemical bonds, as indicated previously.

Nanoscience is not only related to chemical and physical knowledge. There is also a great demand for biological knowledge. Biology and biochemistry also have much to gain from nanoscientific advances because DNA, viruses, and organelles are considered nano-structures [13]. For example, the National Aeronautics and Space Administration (NASA) has studied the development of nanoparticles containing DNA repair enzymes and ligands for the recognition of damaged cells [14].

In 1959, the American physicist Richard Feynman (Fig. 1.4), in his lecture “There’s plenty of room at the bottom” [15], introduced the first nanoscientific approach. Feynman explained that the entire area on the head of a pin (1/16 in.), if amplified 25,000 times, would have an area capable of housing all the pages of the Encyclopedia Britannica. He explained that the resolving power of the human eye (approximately 1,120 points per inch) corresponds to approximately the diameter of one of the tiny dots in the high-quality half-tone reproductions in the Encyclopedia. If this dot could be demagnified by over 25,000 times, it would have a diameter of 80 Å, which is sufficient space for 32 atoms of a common metal.



FIGURE 1.4 Richard Feynman [16].

## 6 NANOSTRUCTURES

In other words, Feynman explained that one such dot (1,120 of which can be seen by the human eye in 1 in. is large enough to contain approximately 1,000 atoms, and therefore, the size of each dot can be easily adjusted, as required by photoengraving. As a result, the entire contents of the Encyclopedia could fit on the head of a pin.

The term “*Nanotechnology*” was coined in 1974 by Norio Taniguchi of Tokyo University and used to describe the ability to create nanoscale materials. Until the term was formally defined, nanotechnology had not undergone major developments because it is a field that manipulates atoms and molecules, but no methods to observe and, thus, manipulate material in a controlled manner existed. However, since the invention of the first microscope, scientists have sought to amplify their ability to observe matter. Using a typical microscope with optical lenses, objects invisible to the naked eye and smaller than the wavelength of light can be observed. In contrast, with an electron microscope, it is possible to observe smaller particles with better definition, although individual atoms cannot be clearly distinguished. Then, in 1981, in the International Business Machines (IBM) laboratories in Zurich, Switzerland, Gerd Binning and Heinrich Rohrer developed a microscope known as the scanning tunneling microscope (STM), which won the Nobel Prize in Physics in 1986 and opened the door to nanotechnology and nanoscience. [Fig. 1.5](#) shows the first commercially offered STM.

Briefly, this microscope is equipped with a very fine probe that very closely scans the sample, removing electrons and generating an image of the atomic topography on the sample surface. The Binnig and Rohrer's STM gave rise to an entire family of instruments and techniques that revolutionized our ability to visualize surfaces and materials that

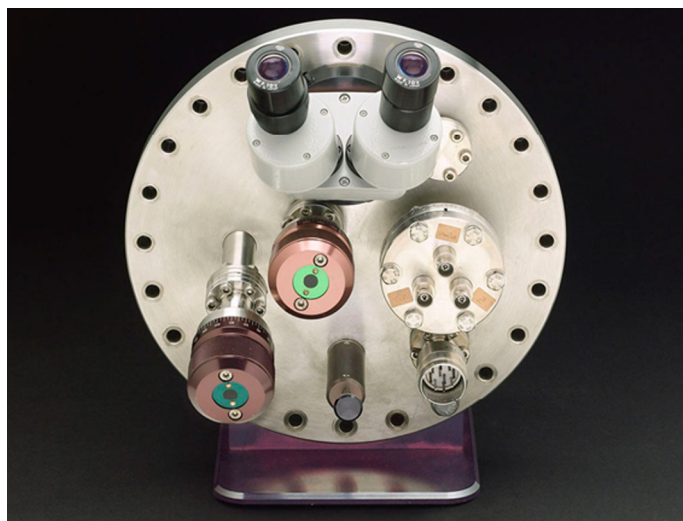


**FIGURE 1.5** First scanning tunneling microscope (STM) produced by “W.A. Technology of Cambridge” in 1986. Free license Image, Creative Commons License, provided by Science Museum London, Flickr. Available from: <https://www.flickr.com/photos/sciencemuseum/9669013645> [17].

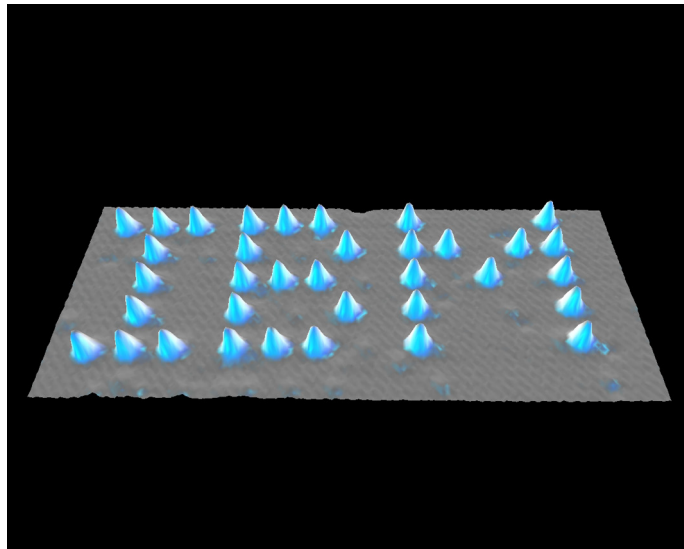


**FIGURE 1.6** An STM image of the International Business Machines (IBM) initials [18].

previously could not be observed. Atomic force microscopy (AFM) is one example of a technique derived from STM that allowed visualizing materials that do not conduct electricity. Indeed, these novel microscopes permitted not only visualization but also manipulation of matter on the nanoscale.

One example of such manipulation is the experiment conducted by Donald M. Eigler and Erhard Schweinzer in 1989 at IBM. In their work, they manipulated 35 xenon atoms on a nickel substrate to spell out the company's initials [18] (Fig. 1.6).

Based on this experiment, many other researchers demonstrated the possibility of manipulating matter on the nanoscale. For example, researchers at the Brazilian Agricultural Research Corporation (EMBRAPA), in the Agricultural Instrumentation division, developed a method for the nanomanipulation of a compact disk's (CD's) polycarbonate surface involving mechanical modification via nanolithography using a phosphorus-doped silicon tip. They used this method to "draw" the EMBRAPA symbol and the Brazilian flag on the polycarbonate substrate in a controlled manner in an area of  $10 \mu\text{m} \times 10 \mu\text{m}$  [19] (Fig. 1.7).

More recently, in 2009, researchers at Stanford University led by Hari Manoharan wrote the initials of Stanford University (SU) in letters smaller than atoms by encoding 35 bits of information per electron [20] (Fig. 1.8).

Given these advances in atomic-scale microscopy, interest in nanoscience and nanotechnology has been steadily growing. According to Whitesides [13], there are six reasons to study nanoscience:

1. Many properties remain mysterious, such as, the operation of the flagellar motor of *E. coli* bacteria and how electrons move through organometallic nanowires.

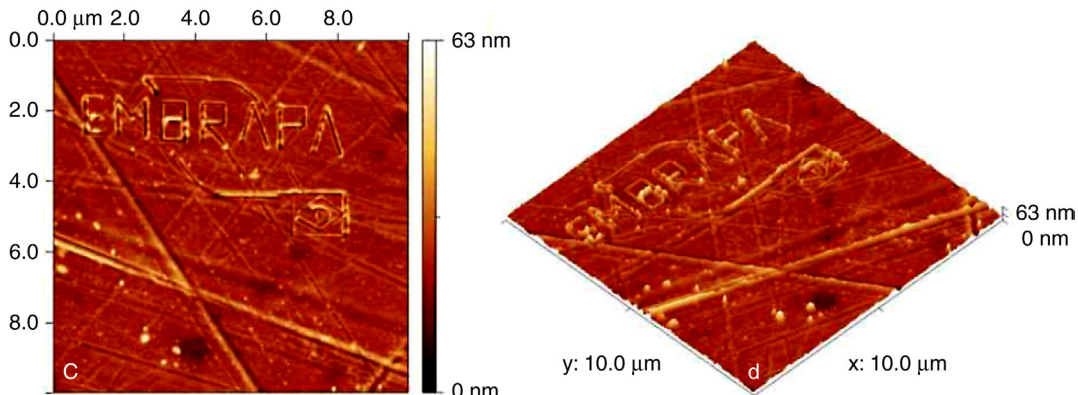


FIGURE 1.7 “EMBRAPA” and an image of the Brazilian national flag scratched onto the surface of a polycarbonate compact disk (CD) with an atomic force microscopy (AFM) tip [19].

2. Nanomaterials are relatively difficult to obtain. Unlike colloids, micelles and crystal nuclei, molecules are easily obtained and characterized. The development of chemical syntheses of colloids that are as accurate as those of molecules remains highly challenging.
3. Many nanostructures are still inaccessible, and their study may lead to the observation of new phenomena.
4. Nanostructures have many sizes in which quantum phenomena (especially quantum entanglement and other reflections of the material’s wave character) are expected to occur. Observing such quantum phenomena will contribute to explaining the behaviors and properties of atoms and molecules, but they are typically masked by the classical behaviors of matter and macroscopic structures. For example, quantum dots and nanowires have been produced and found to exhibit unique electronic properties.
5. The nanometric and functional structures responsible for the primary functions of a cell represent the frontier of biology. For example, ribosomes, histones, chromatin, the Golgi apparatus, the interior structure of the mitochondria, the flagellar micromotor, the centers of photosynthetic reactions, and ATPases of cells are nanostructures that must be characterized and understood.
6. Nanoscience is the basis for the development of nanoelectronics and photonics.

The word nanotechnology is relatively new, but this field is not. It is estimated that nature has evolved on Earth for approximately 3.8 billion years, and nature includes many materials, objects and processes that function on the macroscale to the nanoscale [4]. Thus, understanding the behaviors and properties of these materials and processes may facilitate the production of nanomaterials and nanodevices. *Biomimicry*, a term derived from the Greek word *biomimesis*, was defined by Otto Schmitt in 1957 and denotes the development of biologically inspired designs that are derived or adapted from nature [4]. The term

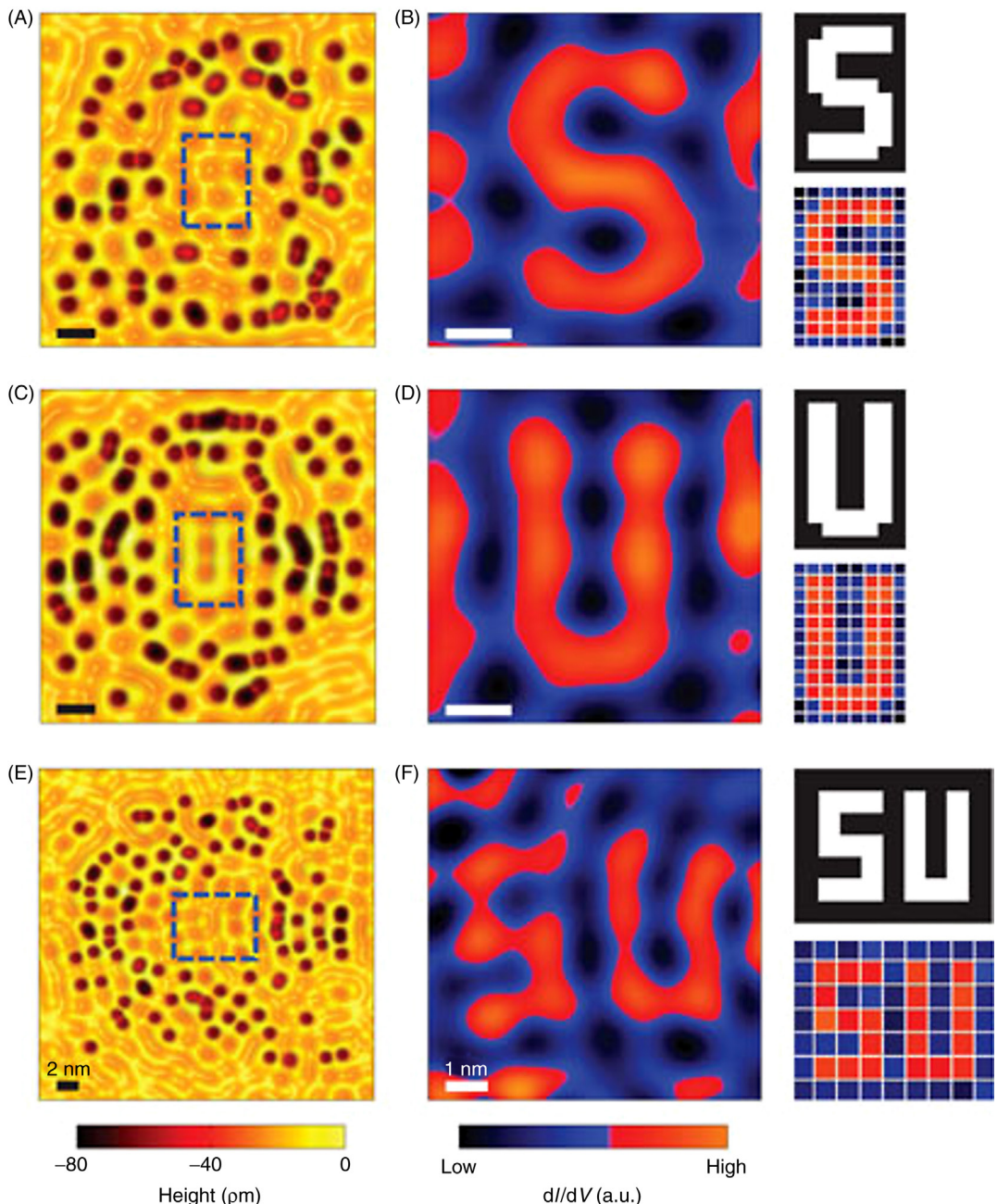


FIGURE 1.8 Stanford University's initials (SU) written using electron waves in a piece of copper and used to design a tiny hologram [20].

biomimicry is relatively new, but our ancestors have looked to nature for the inspiration and know-how to develop various devices for many centuries [21,22]. Indeed, throughout history, many objects and beings, including bacteria, plants, soil, aquatic animals, shells and spider webs, have been found to have commercially interesting properties.

Bacterial flagella rotate at more than 10,000 rpm [23] and constitute an example of a molecular biological machine. The flagella motor is driven by proton flow caused by electrochemical potential differences across the cell membrane. The diameter of the bearings is approximately 20–30 nm, and the gap is approximately  $\approx 1$  nm [4].

Many billions of years ago, molecules began to organize themselves into the complex structures that gave rise to life. Photosynthesis uses solar energy to support plant life. The molecular assemblies present in the leaves of plants (such as chlorophyll) take the energy from sunlight and transform it into chemical energy to power the biochemical processes of plant cells, which have processes ranging from the nanometric to the micrometric scale. This technology has been exploited and developed for solar energy applications [4].

Some natural surfaces, including plant leaves with water repellents, are known to be superhydrophobic and self-cleaning because of their roughness (arising from nanostructures) and the presence of a wax coating [24]. Using roughness to imbue surfaces with superhydrophobicity and self-cleaning properties is of interest for many applications, including windows, windshields, exterior paints, ships, kitchenware, tiles, and textiles. Superhydrophobic surfaces can also be used for energy conversion and storage [25], whereas surfaces with low wettability can reduce the friction of contacting surfaces at machine interfaces [26].

The fixation structures present on the feet of various creatures, including many insects (e.g., beetles and flies), spiders and lizards, can adhere to a variety of surfaces and be used for locomotion. These structures cling to and detach from different types of surfaces [27,28]. The dynamic adhesion capacity is called reversible adherence or smart adhesion. Common adhesives leave residues and are not reversible. Thus, replicating the characteristics of gecko feet would facilitate the development of a super adhesive polymer tape capable of clean, dry, and reversible adhesion [4]. Such a tape would have potential applications in everyday objects and high-tech applications, such as, microelectronics.

Many aquatic animals can move at high speeds through water with low drag energy. For example, most shark species move through water with high efficiency. Shark skin is fundamental for this behavior, reducing friction, and exhibiting a self-cleaning effect that removes ectoparasites from its surface [4]. These characteristics are attributable to very small structures present in shark skin, called dermal denticles, which are ridges with longitudinal grooves that result in very effective mobility through water and minimize the adherence of barnacles and algae [4].

Speedo developed a full-body, shark skin-based swimsuit, called Fastskin, for elite swimming. Furthermore, the builders of boats, ships, and aircraft have also attempted to mimic shark skin to reduce drag and minimize the fixation of organisms on the surfaces of these craft. The mucus on the skin of aquatic animals, including sharks, acts as a barrier against the osmotic salinity of sea water, protects against parasites and infections, and

functions as a friction-reducing agent. Artificial fish-derived mucus products are currently used to propel crude oil through the Alaskan pipeline [4].

Shells are natural nanocomposites with laminated structures and superior mechanical properties. Spider webs are made of silk fiber with high tensile strength. The materials and structures used in these objects have led to the development of various materials and fibers with high mechanical resistance [4]. Moths have eyes with multifaceted surfaces on the nanoscale and are structured to reduce the reflection of light. Their antireflective structure inspired the development of antireflective surfaces [29].

Biological systems' self-healing abilities are highly interesting. For example, the chemical signals originating from the site of a fracture initiate a systemic response that sends agents to repair the injury. Inspired by these activities, various artificial self-structuring materials have been developed [30]. Human skin, for example, is sensitive to impact, which leads to purple discoloration of affected areas. This behavior led to the development of coatings that indicate impact-related damage [21].

Sensor arrays "mimicking" human senses, such as smell [31] and taste [32–35], consist of a set of sensors based on nanostructured materials and have been widely used in various applications, such as gas and liquid sensing, respectively [31,36–40].

Nanostructured materials are typically named according to their shapes and sizes and may take the forms of particles, tubes, wires, films, flakes and reservoirs, provided they have at least one nanoscale dimension [41,42]. One material that has been widely studied in nanotechnology is carbon nanotubes (Fig. 1.9), which are so named because their

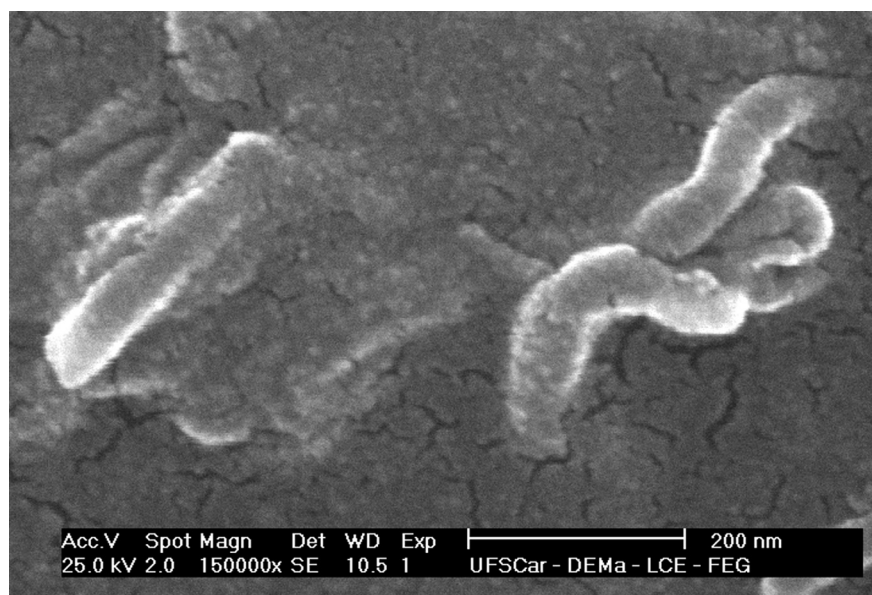


**FIGURE 1.9** Image of carbon nanotubes immobilized onto a film of poly(allylamine) hydrochloride obtained with a high-efficiency electron microscope [a scanning electron microscope coupled with a field emission gun (SEM-FEG)] in the Materials Engineering Department of the Federal University of São Carlos (DEMA-UFSCar) [43].

## 12 NANOSTRUCTURES

diameters are between 1 and 100 nm, although their lengths are typically on the order of hundreds of nanometers.

There are two main modes of developing nanotechnological materials. In the bottom-up approach, materials and devices are built from molecular components that are chemically organized according to the principles of molecular recognition. In contrast, in the top-down approach, nanoscale objects are built from other, larger scale objects, without control at the atomic level [44]. Many methods using these two modes have been reported.

In the bottom-up approach, a DNA molecule may, for example, be used to build other larger and well-defined structures using DNA and other nucleic acids [4]. Another example is the self-assembly technique, which can create self-organized molecular layer films [45,46]. Additionally, as previously discussed, an AFM tip can be used as a nanoscale recording head [19].

Due to top-down approach, many “solid-state” technologies used to create silicon-based microprocessors are now able to use resources on a scale smaller than 100 nm. Other techniques can also be applied to create devices known as Nano Electro Mechanical Systems (NEMS) derived from Micro Electro Mechanical Systems (MEMS) [4,5].

Examples of NEMS include microcantilevers with integrated nanotips for STM and AFM, AFM tips for nanolithography, molecular gears used to attach benzene molecules to the outer walls of carbon nanotubes, magnetic media used in hard disk drives, magnetic tape units [4], and ion beams that can directly remove or deposit materials in the presence of precursor gases. AFM can also be used in the top-down approach for the deposition of resistive films on a substrate that is subsequently subjected to an etching process [3–5,41,42].

Based on the manipulation of materials on the nanoscale, nanoelectronics can also be used to create computer memory using individual molecules or nanotubes capable of storing bits of information, molecular switches, nanotube transistors, flat-panel nanotube displays, integrated circuits, fast-access logic gates, nanoscopic lasers, and nanotubes as electrodes in fuel cells [4].

BioMEMS or BioNEMS are micro- or nanoelectromechanical systems with biological applications and have been increasingly used commercially [5,47–51]. These devices have been applied for chemical and biochemical analyses (biosensors) for medical diagnoses (e.g., DNA, RNA, proteins, cells, blood pressure, and toxin detection and identification) [51,52] and in implantable devices for controlled drug release [53]. Biosensors have also been developed to monitor liquids and gases [54–58]. A wide variety of biosensors are based on the principles of micro-/nanofluids [55,57,58]. Indeed, micro-/nanofluid devices offer the ability to work with smaller reagent volumes and reduced reaction times and facilitate performing various analyses simultaneously [52]. Other types of biosensors include micro-/nanoarrays able to perform one type of analysis millions of times [48–52].

Micro-/nanoarrays are used in biotechnology research to analyze DNA or proteins for disease diagnosis and drug discovery. They are also known as DNA arrays and can simultaneously identify thousands of genes. They consist of microarrays of silicon nanowires with diameters of a few nanometers, which are able to selectively interact with and even

detect a single biological molecule, such as a DNA or a protein, or microarrays of carbon nanotubes capable of electrically detecting glucose. Detection occurs via nanoelectronics that sense small variations in an electric signal generated by the interaction of the analyte (e.g., DNA, protein or glucose) with the micro-/nanoassay [59].

BioMEMS and BioNEMS are also being developed to minimize invasive surgical procedures, including endoscopic surgery, laser angioplasty, and microscopic surgery. Other applications include implantable drug-release devices (micro-/nanoparticles encapsulating drug molecules in functionalized shells for activity at specific locations) or silicon capsules with nanoporous membranes for controlled release [4,48,49].

Nanoscale structures assumed key roles in technological development for a variety of reasons, some of which are listed next [1].

In quantum mechanics, the wave properties of electrons inside matter are influenced by nanoscale variations. Through the nanoscale design of materials, it is possible to vary their micro- and macroscopic properties, such as their charge capacity, magnetization and melting temperature, without altering their chemical composition [1].

The systematic organization of matter on the nanoscale is a key feature of biological systems. Nanoscience and nanotechnology seek to achieve powerful combinations of biology and materials science by adding artificial nanostructured systems to living cells and creating new materials using the self-structuring properties found in nature.

On the nanoscale, the surface areas of various materials are generally much larger than their geometric volumes, which favors their use in various applications, such as, composites for drug delivery and reaction systems and the storage of both chemical energy (such as hydrogen and natural gas) and electrochemical energy (batteries and supercapacitors) [2–5].

Macroscopic systems developed from nanostructures can have much higher densities than those obtained from microstructures. Therefore, when controlling the complexity of interactions on the nanoscale, these systems may be better conductors of electricity and thereby allow the development of novel electronic devices and smaller and faster circuits with more sophisticated functions and significantly reduced power consumption [2–5].

Currently, researchers from universities and companies worldwide are developing nanomaterials to create new products and lead to technological advances in engineering, chemistry, physics, computer science, and biology. Among these numerous technological advances, some easily recognized examples include the development of faster processors, more effective drugs, lighter and more resistant materials, new charge devices (e.g., more efficient batteries) and equipment with lower energy consumption and better image definition [e.g., organic light-emitting diode (OLED) screens] [2–5].

Nanotechnology represents a new world that is finally within our reach, thanks to quantum mechanics and sufficiently advanced simulation and analysis techniques. Currently, nanotechnology has important potential applications in all fields.

Due to technological advances in visualization and the ability to manipulating matter at the atomic and molecular levels, nanotechnology has become a major research theme for the development or improvement of products. Indeed, its popularity is reflected by the

abundant news items reported in the media (television, radio, newspapers, magazines, and the Internet). The term “nanotechnology” has become synonymous with quality. Thus, the nanoscience knowledge domain will be of fundamental importance for the development of new technologies.

### 1.1.3 Investments, Strategies, Actions, and Research in Nanotechnology

Since nanotechnology has benefitted the development or improvement of a wide variety of commercial products, the term nanotechnology has been popularized worldwide. Indeed, its use has not been restricted to the world of scientific research, and as a result, the term “nano” is sometimes improperly used to increase sales volumes or stimulate sales; therefore, “nano” products should be thoroughly reviewed [60]. As explained previously, standard definitions of “nano” exist and must be followed. Furthermore, many products have actually benefitted from nanotechnology research and have significantly influenced the global economy. According to the National Science Foundation (NSF), 1 trillion US dollars were exchanged in the nanotechnology market involved in 2015. Furthermore, Lux Research reported that in 2014, this market was valued at 2.6 trillion US dollars and that in 2012, worldwide, the total investment in this field was approximately 7.9 billion US dollars [61,62]. **Table 1.1** summarizes the invested amounts up to 2015 [63].

Both private and public sectors are strongly interested in this scientific field, as demonstrated by the study conducted by Allianz, which investigated many countries’ nanotechnology-development programs. Such programs are funded by and involve various organizations, ministries, government agencies, and the private sector. Countries that stand out are the United States, China, Japan, Germany, Spain, France, England, Sweden, Italy, the Netherlands, and Finland [63]. Since 2001, more than 60 countries have instituted national programs in nanotechnology [64].

To optimize these investments, long-term plans have also been studied, such as the Horizon 2020 plan (investment plan for 2014–20) launched by the European Union (EU). In this plan, after the closing of the Framework Panel 7 (FP-7) with an investment of €77 billion, an investment of €6.6 billion is destined for the Horizon 2020 program in six areas of nanotechnology: advanced manufacturing of nanotechnology, advanced materials, nanoelectronics, photonics and biotechnology. Additionally, €5 billion in investments from

**Table 1.1** Countries With the Largest Investments in Nanotechnology [63]

Country	Amount Invested	Period
United States	US \$15.6 billion	2001–12
Japan	€2.8 billion	2011
China	€1.8 billion	2011–15
Germany	€500 million	Per year
France	€400 million	Per year
United Kingdom	€250 million	Per year
Other European Union Countries	€100 million	Per year

public and private investors are predicted. Japan has an investment plan lasting until 2020 that provides an investment of US \$1 billion per year [65].

All nanotechnological successes depend on both investments and the relationships between research and development centers (universities and public or private companies). To contextualize the importance of such relationships, we highlight the case study reported by Sá [66], who investigated the actions taken by the University of Albany (the United States) to create the first college of nanotechnology as part of a larger center for research and development with the intent of building a regional cluster for nanoelectronics research: the College of Nanoscale Science and Engineering-Albany Nanotech. For the success of this project, in addition to the invested capital, it was necessary to establish new ways of thinking and administrating. Traditional models of relationships between universities and the corporate world were dispensed with, and a new model was created. Research professors with entrepreneurial interests were highly important for this development. Thus, the University of Albany concentrated on several characteristics, including building a university campus and a technology park and establishing an agent to promote regional and industrial development [66].

This study showed the importance of not only financial investment but also new ideas, the breaking of paradigms, and strategic and specific actions, which can be critical for the success of nanotechnological development.

Another factor, which is somewhat curious and can assist in the development of nanotechnology, has nothing to do with money or commercial interests. Instead, it relates to public commitment, combining civil society, and scientific and technological research. With the emergence of new policies, at least in the United States, Australia, and Europe, public commitment has become important in deciding the path of innovation. In Europe, for example, the Responsible Research Innovation (RRI) program seeks not only to align society with science but also to make research centers accessible to society, especially regarding decision-making about relevant problems. This type of engagement between civil society and the scientific world is a form of upstream public engagement, which is the opposite of downstream public participation, in which society participates only in the final stages of technological development, for example, after important decisions have already been made and the developed product is ready to enter the market. Upstream public engagement is a public commitment allowing civil society to provide input from the beginning regarding the course that scientific and technological research should take to produce new, beneficial products [67].

As mentioned previously, the success of nanotechnology is evident and have attracted high investiment. As a result, there is concern among governments and investors regarding the evaluation and justification of the impact of spending on nanotechnology. For example, in the United States and Japan, there are specialized programs for such evaluations: the Science of Science and Innovation Policy (SciSIP) and the National Institute of Science and Technology Policy (NISTEP), respectively. In addition, there is also great interest on the part of society and especially development agencies and investment sectors in the impact and quality of publications resulting from research and development [68].

Therefore, bibliometric and scientometric studies are used in the identification, quantification, qualification, classification, and frequency of publications in nanoscience and nanotechnology. Such studies have a certain level of complexity, and one way to contextualize this complexity is by discussing how such studies are conducted: searching for articles on relevant sites [for example, the Web of Science (WOS)] using keywords. In the case of nanotechnology, because of the large number of variations involving the term “nano,” “nano” itself can be used as a keyword. However, the articles generated from such a search may or may be relevant to nanoscience and nanotechnology, and thus, the results must be carefully evaluated. Thus, this type of study is as complex as the actual research in nanoscience and nanotechnology, and abundant relevant articles have been published in the area. One example is the study of Porter et al. [69], who evaluated the performance of software used to search for publications on the subject of nanotechnology. In the WOS, 406,000 papers and more than 53,000 micropatents and patents were found between 1990 and mid-2006. Another assessment performed from 1990 to mid-2011 indicated that 820,000 documents could be identified in the WOS [70]. Two other studies were conducted by Shapira and Wang: one study evaluated the quantity and quality of articles published from 2008 to 2009, identifying 91,500 articles published on the subject nanotechnology, among which only 67% were informative articles [64]. The other study evaluated the impact factor and quality of published papers. That study revealed that the quality of the publishing journal and the number of citations were linked to the major sponsors of the study [68]. Stopar and Bartol conducted a very restricted evaluation of the scientific output in nanoscience and nanotechnology in 2012, searching for articles in the ten journals with the most publications containing the term “nano” in the title. Journals were selected by researching the core collection (old citation index) of the WOS. The Scopus database was also evaluated, revealing the same ten journals identified in the core collection of the WOS. These 10 journals were the *Journal of Materials Chemistry*, *Journal of Physical Chemistry C*, *Applied Physics Letters*, *Journal of Nanoscience and Nanotechnology*, *Journal of Applied Physics*, *ACS Nano*, *Nano Letters*, *Nanotechnology*, *Nanoscale*, and *Materials Letters* [71].

Among all the assessments made in this study, the most striking results was that in 2012, a total of 2,700 journals published articles with the term “nano” in the title, but of these 2,700 journals, only 50 published more than 200 articles; furthermore, the ten journals selected in the study had published approximately 9,000 articles on the subject of nanoscience or nanotechnology. Another interesting result was the number of compound terms containing the term nano that were found. In ascending order, the terms most commonly found were as follows: nanoparticle, nanowire, nanotube, nanostructur\*, nanocrystal, nanocompos\*, nanorod, nanoscale, nanofiber, nanopor\*, nanoribbon, nanosheet, nanocluster, nanosphere, nanometer, nanomaterial, nanobelt, nanocube, nanopillar, nanoplate, nanopattern, nanodot, nanoflake, nanosize, nanohybrid, nanoplatelet, nanoantenna, nanoring, nanoimprint, nanosecond, nanopowder, nanomechanic, nanocapsule, nanoshell, nanogap, nanomembrane, nanoindent\* and nanoflower [71].

Finally, this study reported the number of articles in the literature published over a 1-year period and indicated how complex it is to perform this type of study. Clearly,

**Table 1.2** Number of Articles Published Between 2012 and 2015 Containing the Three Most-Cited Nanoterms in 2012

Nanoterms	Number of Articles (2012–15)
Nanoparticle	18,336
Nanowire	7,348
Nanotube	36,547
Total	62,331

Source: [webofknowledge.com](http://webofknowledge.com).

abundant scientific articles are produced, as indicated by the studies cited and by a simple search of the WOS. When we searched for titles included the top three most-cited keywords containing the term “nano,” according to a study by Stopar and Bartol covering 2012–15, we obtained the following results ([Table 1.2](#))

The numbers listed previously were not subjected to scientometric or bibliometric evaluation; indeed, only a search for article titles containing the indicated nano-terms was performed. However, these results provide perspective regarding the vast number of articles in the literature. One thing is certain: all of these numbers are the result of the popularity of research in nanoscience and nanotechnology.

As shown, nanoscience and nanotechnology have provoked important changes in the political, economic, administrative, social, and scientific spheres. Given the data evaluated here, it may be concluded that more than half of the globe benefits from and participates in this new branch of science. Furthermore, financial investments increased during each studied period. Interest in this new science is attracting increasing attention from many sectors ranging from technology to health, and the dissemination of scientific research results, as reflected by the huge quantity of publications, indicates the popularity of this new scientific field.

#### 1.1.4 Commercial Products Involving Nanotechnology

Currently, given the recent technological advances, high-resolution electron microscopes, and the ability to manipulate and manufacture materials and devices with controlled properties at the nanoscale, many companies have invested in quality improvements or producing new products.

The most easily identifiable applications are electronic devices: nanotechnology is critical to the development of various components, such as, microprocessors, digital screens, and batteries.

The production of data-storage chips begins with the wafer, which consists of a disk cut from a single silicon crystal with a diameter of at least 300 mm and is typically between 500 and 800  $\mu\text{m}$  thick. Integrated circuit structures are built layer by layer on the surface of the chip using etching techniques, such as, lithography [[72](#)]. The development of the transistor (the building block of integrated circuits and microchips) was based on complementary metal–oxide semiconductors (CMOSs); transistors have existed for decades

and are part of our everyday lives. The smallest of these structures was as low as 22 nm in 2015 (the “router” transistor) and is near the operating limit, approximately 5 nm, for metal–oxide semiconductor field-effect transistor technology; this limit is based on the high leakage current that should occur inside the chip and will likely be reached within the next 20 years [73]. These developments represent major technological challenges because of the manufacturing process itself and performing heat-management tests in circuits (a modern high-performance chip can dissipate heat at a density of  $100 \text{ W}\cdot\text{cm}^{-2}$ , which exceeds the ability of a domestic kitchen hot plate) [74].

Silicon is envisaged as an important semiconductor material, but to fabricate ever smaller structures, new photoresistors must be developed. Furthermore, thin silicon oxide films become increasingly less efficient as they become thinner, and their leakage currents become very high. Thus,  $\text{SiO}_2$  was replaced by physically thicker layers with higher dielectric constants. New semiconductors must satisfy some conditions, such as, high dielectric constants, thermal and kinetic stabilities, band shifts, good quality Si interfaces, and low defect densities. Hafnium oxides ( $\text{HfO}_2$ ) have emerged as attractive oxides, typically with the incorporation of nitrogen. Ge has also been incorporated into the structure of CMOS transistors to maximize performance [75]. The origin of ferromagnetism is based on both electron charges and spin. Therefore, the miniaturization of magnetic memories has been limited not by the final size of the ferromagnetic domain but by the sensitivity of the magnetic sensors. In other words, the main limitation is not the ability to make very small storage cells but the ability to detect very small magnetic fields [74].

The influence of rotation on the electron conductivity was invoked by Nevill Mott in 1936 but remained virtually unexplored until the discovery of giant magnetoresistance (GMR) in 1988 [74,76]. The main application of spintronics (loosely defined as the field of devices in which electron spin plays a role) is the development of ultrasensitive magnetic sensors for magnetic reading memories. GMR is used for the reading and writing heads of computer hard disk drives [76].

A second type of magnetic sensor is based on the magnetic tunnel junction (MTJ), in which a very thin dielectric layer that is nonconductive under applied voltage separates the ferromagnetic layers (electrode) and the electron tunnel. The sensitivity of the magnetic field exceeds that of GMR devices. MTJ devices also have high impedance, allowing high output signal values. Unlike GMR devices, electrodes are magnetically independent and may have different critical fields to change the orientation of the magnetic moment. The first laboratory samples of MJT devices ( $\text{NiFe-Al}_2\text{O}_3\text{-Co}$ ) were reported in 1995 [74].

As previously described, there are no limits on the demand for devices that are smaller, lighter, and more efficient and have lower power consumption. When merely considering the development of mobile telephone devices (cellular phones), in just 20 years, development in this segment has been remarkable. In 1993, smartphones were fiction, a distant possibility at best. At that time, at least in Brazil, cell phones were not prevalent. Furthermore, although they had existed since the 1980s, even in the 1990s, the predominant devices were expensive, large, and heavy; had antennas; and operated using analog networks.



**FIGURE 1.10** Mobile devices from the early 1980s to the present day. (A) Motorola DynaTAC 8000X (1983), (B) Pager Motorola (1980–90), (C) Motorola MicroTAC 9800X (1989), (D) Motorola StarTAC (1996), (E) Apple iPhone 1 (2007), and (F) iPhone 6 Plus (2015).

Currently, cellular phones are energy-efficient machines, are fast and provide all the functions of notebook computers, and combine multiple devices into one, including a personal computer, digital camera, sound recorder, text and spreadsheet editor, gaming station, and Global Positioning System (GPS). There are also numerous manufacturers and a wide range of models and prices. The evolution of mobile phones went through a period of miniaturization, and now, with the advent of smartphones, these devices are growing again, providing increasing numbers of functions (Fig. 1.10). Recently, smart watches have also been developed that are similar to smartphones.

Another example from everyday life is the evolution of television sets and computer monitors, and the emergence of different displays in portable devices. Briefly, all of this evolution began in the mid-18th century with Charles Du Fay, who studied the electron emission from a heated metal surface, which is known as the thermionic effect [77]. Since then, several studies on this subject were performed until it was concluded that this phenomenon was attributable to cathode rays [78]. These rays were further studied in 1897 by Joseph John Thomson [9], who found that cathode rays were simply electrons and that they behave as particles rather than waves. It should be noted that in parallel to the research of J.J. Thomson, Wilhelm Conrad Roentgen also investigated the behavior of cathode rays and discovered how the X-ray machines used in the medical field worked [79]. Finally, building on these discoveries (thermionic effect and the nature of cathode rays), the kinescope was developed; this device was responsible for image formation in the first televisions and computer monitors [80].

The television sets and computer monitors that used cathode ray tubes for image generation have since been replaced by other devices because of the development of the

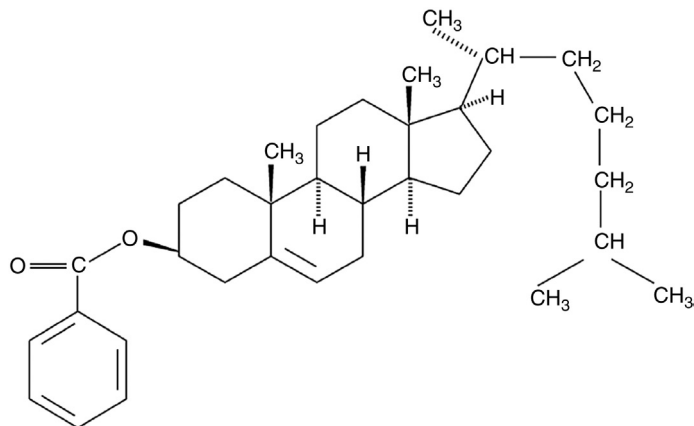


**FIGURE 1.11** Structure of cholesteryl benzoate [84].

liquid crystal displays (LCDs). LCD screens comprise a combination of polymers and glass slides coated with indium tin oxide (ITO) [81]. The discovery of liquid crystals is attributed to the botanist Friederich Reinitzer in 1888 [82], when he observed the double melting point of cholesteryl benzoate (Fig. 1.11). However, the term liquid crystal was coined by Coube Lehmann, who believed that the degree of fluidity was the only difference between liquid crystals and solid crystals. However, liquid crystals are actually characterized by the degree of molecular order between the long-range orientational and positional orders of a solid crystal and the long-range disorder of isotropic liquids and gases [83].

In the Web of Knowledge database, when the title search keyword “liquid crystal displays” is used, the first works that describe this technology can be seen to date back to 1968: *Liquid Crystals—A Step Closer To Low-Voltage Displays* (anonymous author) [85] and *Reflective Liquid Crystal Television Display* [86]. However, 99,644 other works are also found (searched on September 16, 2013) that describe the development and diverse applications of LCDs. Initially, the displays that used liquid crystal materials had very limited image resolutions and were used only in wristwatches and calculators [87]. An account of their development is given by Toshiaki Fujii et al. [87], who developed a LCD with a resolution capable of reproducing not only letters and numbers but also graphics, figure patterns, and even Chinese characters. In summary, this LCD revealed the possibility of replacing cathode ray tube monitors. The results reported in that article were based on a screen tested using a computer, and the authors were believed to have developed the first LCD monitor at the time. Given the constant evolution of this technology, currently, there is competition between LCD screens and OLEDs, which were first described by two researchers from Eastman Kodak in 1987. They developed an electroluminescent device with a thickness of 135 nm that operated at low voltage (below 10V) [88]. Indeed, currently, OLEDs are LCDs’ main rivals (Fig. 1.12).

The basic structure of an OLED consists of one or more emissive (electroluminescent) polymeric layers (organic part) placed between a transparent anode and a metallic



FIGURE 1.12 Organic light-emitting diode (OLED) developed to increase the power of light emission [89].

cathode. Typically, the organic layers are composed of a hole-transporting layer (HTL), an emitting layer (EL) and an electron-injection layer (EIL), and thus, a variety of architectures and desired effects can be achieved [90]. All OLEDs require at least one transparent electrode. Traditionally, ITO has been used, but the Earth's supply of indium is very limited, and at current consumption rates, it may be completely exhausted within 2–3 years. Furthermore, constant advances in integration and miniaturization are causing the effective recycling of indium from discarded components to become increasingly complicated. Thus, there is great interest in the fabrication of transparent polymer additives containing a small proportion of carbon nanotubes for conductivity.

One additional advantage of organic electronic devices is their ability to be deposited on any substrate, including flexible and robust plastic sheets. New organic light-emitting polymers are currently in the research phase and have potential for the development of thinner and flexible displays with high resolution and low power consumption [90,91] (Fig. 1.13).

In addition to the development of electronic devices, nanotechnology is used in all other areas, including health, sports, clothing, automotive, and food.

A natural textile fiber, such as, cotton has an intricate nanostructure. Many of the comfortable properties of traditional textiles result from a favorable combination of chemistry and morphology. These factors are what allow the properties of natural textiles to be equal or superior to those of synthetic materials. Furthermore, nanoadditives can increase some of the properties of natural textile fibers, such as, mechanical strength, durability, heat and flame resistance, self-cleaning capability, color, and antiseptic effect.

Some textiles release useful chemical substances passively or actively. These advanced functional fabrics are often used in special applications, serving as a type of “scaffold” for cells facilitating tissue regeneration and wound sterilization to facilitate healing [74].



**FIGURE 1.13** OLED screens: (A) 2-mm-thick OLED monitor; (B) concept for a future OLED screen, which could be rolled up like a scroll inside of a pen-sized device when not in use [91].

Dr. Robert Burrell of the University of Alberta (Canada) developed dressings with silver nanocrystalline films in 1995 [92]. While working for Westaim Corp's NUCRYST Pharmaceuticals, he invented Acticoat (Fig. 1.14), a silver-based dressing, which had antimicrobial properties and increased the healing rate. This dressing is often used in burn units and is now sold worldwide combined with common adhesive bandages. This work earned awards, including the World Union of Wound Healing Society Lifetime Achievement Award recognizing contributions to wound healing and, in 2009, the ASM Engineering Materials Achievement Award.

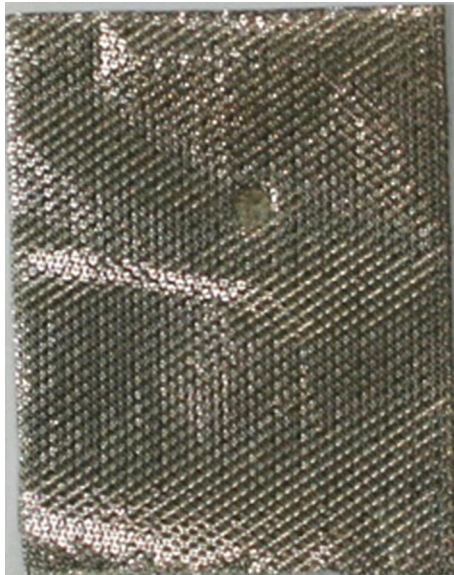


FIGURE 1.14 Acticoat antimicrobial adhesive [93].

Wall papers with antibacterial properties have also been developed, in which zinc oxide ( $ZnO$ ) nanoparticles are incorporated into the cellulose fibers and react with the gram-positive bacteria *Staphylococcus aureus* and gram-negative bacteria *Escherichia coli*, the main causes of nosocomial infections, and the fungus *Aspergillus niger* [94].

Tennis is a good example of the integration of nanotechnology in sports. Wilson, one of the largest tennis sporting goods manufacturers in the world, manufactures balls with less-permeable rubber than traditional balls (nanoclays are mixed with the rubber to achieve this effect) and lighter, more-resistant tennis racquets produced using carbon nanotube fiber structures [95].

Eyeglasses, sunglasses, windows, and even photographic camera lenses may also include nanometric particles that function as conductive polymers and change color based on the absorption of UV light from sunlight. This mechanism is known as “photochromism,” and today, it is widely commercially available.

In the automotive industry, nanotechnology has an increasingly important role in the development of new vehicles. The main overriding goal is to reduce vehicle weight without compromising other attributes, such as, safety. Therefore, researchers are especially interested in replacing the heavy metals used in components with lighter polymers that are reinforced by nanoparticulate materials or nanofiber additives. Other, more specific objectives include formulating lightweight, electrically conductive materials for use in fuel lines to prevent static electricity and abrasion-resistant paints, reducing friction, and developing lights (LED), automotive sensors, multimedia devices, and electronics [74]. Polymeric

nanomaterials, such as, carbon nanotubes, have been used in bumpers with safety and resistance levels similar to those of conventional bumpers while being significantly lighter, directly influencing vehicle fuel consumption. In Brazil, Fiat, for example, developed its FCC II car with clay nanocomposites. The body is composed of fibers containing nanoclay, which is a clay with a nanoparticle-based chemical additive. This composite has characteristics similar to those of fiberglass but is lighter, cheaper, and easier to recycle [96].

Another example is the use of nanoparticles in automotive paints. Mercedes-Benz recently developed a special paint with nanometric paint bubbles that can regenerate small scratches in the paint. When a scratch occurs, these small bubbles break and release paint that covers the exposed area, improving both the protection and aesthetics of the vehicle. Additionally, a special paint has been developed that allowed a car painted yellow to change color with the application of a low current or because of the incidence of sunlight [97].

In the health field, substantial research and development has been invested in products using nanotechnology for controlled drug delivery and use in surgical catheters.

Nanomedicine is defined as the application of nanotechnology in human health. In recent decades in particular, medicine has been characterized by important technological advances, accompanied by an enormous and concomitant expansion of its ability to diagnose and cure diseases.

Molecular biology can be considered an example of conceptual nanotechnology because the structures involved are on the nanoscale. Furthermore, molecular biologists' work increasingly involves nanometrology, such as, the use of microscopic scanning probes. As mentioned earlier, biomimicry is the use of nanotechnology to artificially recreate natural nanoscale materials, devices, and systems. Since Drexler presented biology as a "proof of principle" of nanotechnology [98], a close relationship has developed between biology and nanotechnology. Thus, nanotechnology can influence the health field, and the resulting social changes have greatly impacted human health. In other words, the impact of nanotechnology on human health is not restricted to the development of drug delivery systems or devices and equipment [74].

In the pharmaceutical industry, three major developments are currently predicted: sensing, automated diagnosis, and personalized pharmaceutical products. The development of ever smaller sensors able to penetrate the body using minimally invasive procedures, such as endoscopy, is an example of the direct application of nanotechnology. Researchers are even seeking to develop such sensors as permanently implanted devices. Indeed, these devices may be able to continuously monitor physiologically relevant physicochemical parameters, such as, temperature and the concentrations of selected biomarkers. Presently, one of the greatest challenges is the automatic diagnosis of disease [74]. The third development, which is believed to be the most accessible, is the creation of custom pharmaceuticals using microfluidic mixers and reactors; however, these methods are not based on nanoscale techniques.

Prostheses and biomedical devices must be biocompatible [74]. Implants that play structural roles, such as bone substitutes, should be assimilated by the host. When

assimilation fails, the implant typically becomes coated with a layer of fibrous material, which can move, causing irritation and weakening the implant's structural role. For implants in the bloodstream (arterial stents and, possibly, future sensors), the opposite behavior is required: Blood proteins should not attach to such devices. In this case, adsorption has two deleterious effects: The accumulation of protein layers may clog the blood vessel, and the adsorbed proteins may change and therefore appear foreign to the host organism, triggering inflammatory responses. Thus, to achieve the required assimilation behavior, structures with appropriate surfaces (textures) must be developed [74].

For nonimplanted medical devices, such as scalpels or needles, researchers are focusing on developments to improve their sterilization and decrease their coefficients of friction to minimize the physical force required to penetrate the skin and, thereby, minimize patients' pain [74]. These improvements can be achieved by high-precision machining and rough surface finishing at the nanoscale. Long-term implants should be designed to minimize the chance of bacterial infection. Once bacteria colonize an implant, their phenotype generally changes so that the cells become "invisible" to the immune system and antibiotics, resulting in persistent inflammation without destruction of the bacterial colony [74].

Implants with contact surfaces, such as those used in arthroplasty, typically generate particles as a result of wear, which can be relatively large and cause inflammation [74].

The oldest well-documented example of the use of nanoparticles in medicine is Paracelsus's deliberate synthesis of gold nanoparticles (called "soluble gold") as a pharmaceutical formulation [74]. The use of nanoparticles in medicine has recently become a flourishing field. Applications include magnetic nanoparticles directed by external fields to the site of a tumor and then energized by an external electromagnetic field to kill the particles' neighboring cells, nanoparticles acting as carriers for drugs and nanoparticles that can be used as markers for disease diagnosis [74]. The use of nanoparticles for drug release is being intensively researched and developed, and many products are undergoing clinical trials. A major obstacle for the successful development of new drugs is that many drugs that exhibit good therapeutic interactions with a target molecule (e.g., an enzyme) have very low solubility in water. However, these compounds can be encapsulated in nanoparticles with hydrophilic outer surfaces. Such surfaces also prevent adsorption and the triggering of an adverse immune response, such as, protein denaturation during the passage of the particle through the bloodstream [74]. Thus, this technique facilitates not only controlled drug release but also targeting these nanocapsules (Fig. 1.15) to the desired location and thus avoiding side effects in healthy organs, such as, those caused by the chemotherapeutic agents used to treat cancer [99].

Molecular biology and clinical research constitute an important market for nanoparticle. For example, nanoparticles may be useful as biomarkers: By coating them with chemical products with specific affinities for particular targets (e.g., antibodies), nanoparticles can be used to more easily map the locations of those targets using microscopy. Such particles may simply consist of heavy metals, which are easily visualized under an electron microscope, or fluorescent particles [74].

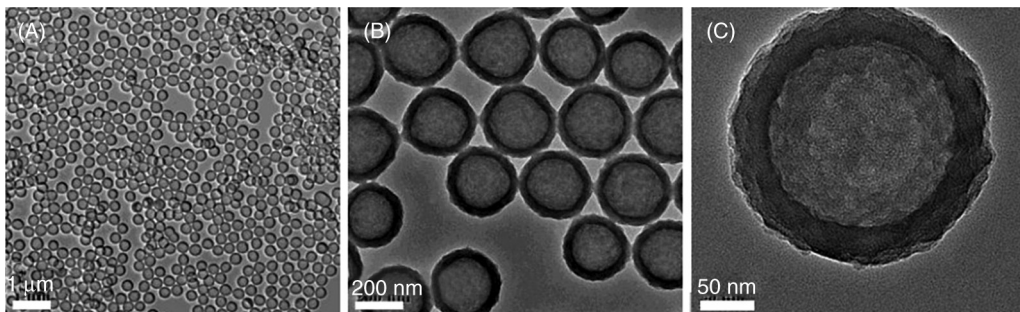


**FIGURE 1.15** Images of silica nanocapsules (A–C) used in experiments investigating the treatment of tumors in rabbits obtained with a transmission electron microscope (TEM). [99].

The use of toxic materials for cosmetic purposes (e.g., applying them to the skin of the face) has a long history, as in the case of antimony salts, which were popular among the Romans. Nanotechnology contributed to creating new sunscreen formulations using smaller nanoscale particles in their emulsions. The advantages of these new formulas mainly include better spreading of the emulsions and, thus, improved skin coverage. Furthermore, upon spreading, the particles become invisible to the naked eye, and the whitish color common in older formulations is avoided. Additionally, advances in our knowledge of toxicity yielded much more benign materials, although the recent use of very fine particles (e.g., zinc oxide nanoparticles in sunscreens) has generated further concern regarding the possibility of their penetration through the outer layers of the skin or into cells and causing unknown effects [74].

Robots (microscopic or nanoscopic) are extensions of existing ingestible devices that move slowly through the gastrointestinal tract and provide information (mainly images [74]). As noted by Hogg [100], the minimum future requirements for such devices are as follows: detection (chemical), communication (receiving information and transmitting information out of the body, communicating with other nanobots), locomotion, computing (highly miniaturized electronics would be very attractive for the construction of the on-board logic circuitry), and power (it is estimated that power on the order of picowatts would be sufficient to propel a nanobot at a speed of approximately  $1 \text{ mm}\cdot\text{s}^{-1}$ ). To be effective, these nanobots will likely need to operate in swarms, making the requirement that they be able to communicate increasingly important.

Nanoscale materials have been used to solve problems in various fields of research and development. From a simple package to a high-tech device, nanoscience is clearly of fundamental scientific importance.

## 1.2 Final Considerations

Nanoscience is the main tool supporting this century's scientific and technological developments. The domain of the atomic world is the main focus of this branch of science. Another key factor for the development of this field is its multidisciplinary character, as demonstrated, for example, by the numerous improvements and development of new

products in technology and medicine. In this context, engineers, biologists, physicists, chemists, doctors, and many other professionals in health and technology may be involved. Additionally, given the variety of problems solved, the development of new products, and the ability to add value to existing nanotechnology products, political and economic sciences are also contributing to the development of nanotechnology worldwide. The investments in Japan, the United States, the EU and other countries are enormous, notwithstanding the substantial investments from the private sector. Thus, the nanotechnology market is expected to achieve a one-trillion-dollar valuation in the coming decades.

In scientific terms, substantial activity is occurring among scientists with regard to technical and scientific publications and mass media, and as a result, ordinary people are engaging with the scientific world. In fact, prior to nanotechnology, society was never so interested in this community. However, despite major advances and numerous problems solved by nanotechnology in health fields, some studies and research groups have expressed concern about the potentially harmful effects of nanotechnology, that is, the ability of these nanoparticles to damage health human [101–111]. Therefore, ethics and thoughtfulness are necessary in this field, particularly with respect to the disposal of nano-materials, including laboratory or industrial waste and commercialized products, especially electronics.

The smallest unit of matter has inspired major events worldwide. Science does not stop.

## List of Symbols

<b>d</b>	Diameter
<b>mm·s<sup>-1</sup></b>	Millimeters per second
<b>nm</b>	Nanometer
<b>rpm</b>	Rotations per minute
<b>V</b>	Volt
<b>W·cm<sup>-2</sup></b>	Watts per square centimeter
<b>μm</b>	Micrometer

## References

- [1] G.A. Mansori, *Principles of Nanotechnology: Molecular-Based Study of Condensed Matter in Small Systems*. [S.I.], World Scientific, Singapore, (2005) p 358.
- [2] F. Allhoff, P. Lin, D. Moore, *What is Nanotechnology and Why Does It Matter?* [S.I.], John Wiley and Sons, New Jersey, NJ, (2010) pp. 3-5.
- [3] S.K. Prasad, *Modern Concepts in Nanotechnology*, [S.I.]: [s.n.], Discovery Publishing House, New Delhi, (2008) pp. 31-32.
- [4] B. Bhushan, *Springer Handbook of Nanotechnology*, Springer-Verlag Berlin Heidelberg, New York, (2010) 1222 p.
- [5] C.P. Poole, F.J. Owens, *Introduction to Nanotechnology*, John Wiley & Sons, Hoboken, (2003).
- [6] A. Merkoçi, *Biosensing using nanomaterials*, in: A. Merkoçi (Ed.), *Nanoscience and Nanotechnology*, Wiley Series, Hoboken, 2009, pp. XV.

- [7] Laboratório de Química do Estado Sólido [Laboratory of Solid State Chemistry]. Available from: <http://lques.iqm.unicamp.br/>; [http://lques.iqm.unicamp.br/canal\\_cientifico/lques\\_news/lques\\_news\\_cit/lques\\_news\\_2008/lques\\_news\\_novidades\\_1208.html](http://lques.iqm.unicamp.br/canal_cientifico/lques_news/lques_news_cit/lques_news_2008/lques_news_novidades_1208.html)
- [8] E. Longo, L.H. Toma, Novos Materiais e Nanotecnologia [New Materials and Nanotechnology], Anais da Reunião Anual da SBPC [Annals of the 56 th Annual Meeting of the Brazilian Society for the Advancement of Science], Cuiabá, MT, 56, (2004), ISBN: 85-86957-07-0. Available from: [http://www.sbpcnet.org.br/livro/56ra/banco\\_conf\\_simp/textos/ElsonLongo.htm](http://www.sbpcnet.org.br/livro/56ra/banco_conf_simp/textos/ElsonLongo.htm), 2004.
- [9] J.B. Russell, Química Geral [General Chemistry], São Paulo, McGraw Hill, (1982) pp. 197–251.
- [10] L. Brillouin, Maxwell's demon cannot operate: information and entropy. I, *J. Appl. Phys.* 22 (3) (1951) 334–337.
- [11] S.S. Mizrahi, Mulheres na Física: Lise Meitner [Women in Physics: Lise Meitner], *Revista Brasileira de Ensino de Física* 27 (2005) 491–493.
- [12] R. Chang, Química Geral-Conceitos Essenciais [General Chemistry-Essential Concepts], seventh ed., McGraw-Hill, São Paulo, (2007) 929 p.
- [13] G.M. Whitesides, Nanoscience, nanotechnology, and chemistry, *Small* 1 (2) (2005) 172–179.
- [14] NASA, National Aeronautics and Space Administration. Available from: <http://science.nasa.gov/science-news/science-at-nasa/2002/15jan.nano/>
- [15] A.D. Romig, et al. An introduction to nanotechnology policy: opportunities and constraints for emerging and established economies, *Technol. Forecast. Soc. Change* 74 (2007) 1634–1642.
- [16] Wikipedia Free Encyclopedia. Available from: [http://en.wikipedia.org/wiki/main\\_page](http://en.wikipedia.org/wiki/main_page); [http://en.wikipedia.org/wiki/File:Feynman\\_at\\_Los\\_Alamos.jpg](http://en.wikipedia.org/wiki/File:Feynman_at_Los_Alamos.jpg)
- [17] Science Museum London, Flickr. Available from: <https://www.flickr.com>; <https://www.flickr.com/photos/sciencemuseum/9669013645>
- [18] Ibm, Ibm. Available from: [http://www-03.ibm.com/ibm/history/exhibits/vintage/vintage\\_4506VV1003.html](http://www-03.ibm.com/ibm/history/exhibits/vintage/vintage_4506VV1003.html), 2013.
- [19] A. Manzoli, et al., Nanomanipulação de superfície polimérica: Nanolitografia [Nanomanipulation of Polymer Surfaces: Nanolithography]. Embrapa Instrumentação Agropecuária, São Carlos—SP, 2007, pp. 4–13 (1678-0434).
- [20] C.R. Moon, et al. Quantum holographic encoding in a two-dimensional electron gas, *Nat. Nano-technol.* 4 (3) (2009) 167–172.
- [21] Y. Bar-Cohen, Biomimetics—Biologically Inspired Technologies, [S.l.]: [s.n.], CRC Press, Florida, (2005).
- [22] B. Bhushan, Biomimetics: lessons from nature—an overview, *Philos. Trans. R. Soc. A-Math. Phys. Eng. Sci.* 32 (2009) 1445–1486.
- [23] C.J. Jones, S. Aizawa, The bacterial flagellum and flagellar motor: structure, assembly, and functions, *Adv. Microb. Physiol.* 32 (1991) 109–172.
- [24] B. Bhushan, Y.C. Jung, Wetting, adhesion and friction of superhydrophobic and hydrophilic leaves and fabricated micro-/nanopatterned surfaces, *J. Phys. D* 20 (2008).
- [25] M. Nosonovsky, B. Bhushan, Multiscale effects and capillary interactions in functional biomimetic surfaces for energy conversion and green engineering, *Philos. Trans. R. Soc. A-Math. Phys. Eng. Sci.* 367 (2009) 1511–1539.
- [26] B. Bhushan, Principles and Applications of Tribology, John Wiley & Sons, New York, (1999).
- [27] K. Autumn, Adhesive force of a single gecko foot-hair, *Nature* 405 (2000) 681–685.
- [28] B. Bhushan, Adhesion of multi-level hierarchical attachment systems in gecko feet, *J. Adhes. Sci. Technol.* 21 (2007) 1213–1258.
- [29] C.G. Bernhard, W.H. Miller, A.R. Moller, The insect corneal nipple array: a biological, broad-band impedance transformer that acts as a antireflection coating, *Acta Physiol. Scand.* 21 (2007) 1213–1258.

- [30] J.P. Youngbloob, N.R. Sottos, Bioinspired materials for self-cleaning and self-healing, *Mater. Res. Soc. Bull.* 18 (2008) 732–738.
- [31] J.W. Gardner, P.N. Bartlett, A brief-history of electronic noses, *Sensor. Actuat. B: Chem.* 18 (1994) 211–220.
- [32] A. Riul, An artificial taste sensor based on conducting polymers, *Biosens. Bioelectron.* 18 (2003) 1365–1369.
- [33] A. Riul Jr., et al. An electronic tongue using polypyrrole and polyaniline, *Syn. Met.* 132 (2) (2003) 109–116.
- [34] Y. Vlasov, A. Legin, A. Rudnitskaya, Electronic tongues and their analytical application, *Analytical and bioanalytical chemistry* 373 (2002) 136–146.
- [35] K. Toko, A taste sensor, *Measurement science & technology* 9 (1998) 1919–1936.
- [36] T. Zhang, A gas nanosensor unaffected by humidity, *Nanotechnology* 20 (2009).
- [37] R. Bogue, Nanosensors: a review of recent research, *Sensor Rev.* 29 (2009) 310–315.
- [38] S.N. Shtykov, T.Y. Rusanova, Nanomaterials and nanotechnologies in chemical and biochemical sensors: capabilities and applications, *Russ. J. Gen. Chem.* 78 (2008) 2521–2531.
- [39] R. Bogue, Nanosensors: a review of recent progress, *Sensor Rev.* 28 (2008) 12–17.
- [40] A. Ramanavicius, A. Ramanaviciene, A. Malinauskas, Electrochemical sensors based on conducting polymer—polypyrrole, *Electrochim. Acta.* 51 (2006) 6025–6037.
- [41] J. Kahn, Nanotechnology, *Nat. Geo.* (2006) 98–119.
- [42] I. Amato, White House. Available from: <http://www.whitehouse.gov/>; <http://www.ostp.gov/nstc/html/iwgn/iwgn.public.brochure/welcome.htm>
- [43] H.H. Takeda, et al. Differential pulse voltammetric determination of ciprofibrate in pharmaceutical formulations using a glassy carbon electrode modified with functionalized carbon nanotubes within a poly(allylamine hydrochloride) film, *Sensor Actuat. B: Chem.* 161 (2012) 755–760.
- [44] Y. Gogotsi (Ed.), *Nanomaterials Handbook*, Taylor & Francis-CRC Press, Philadelphia, 2006.
- [45] N.I. Kovtyukhova, Layer-by-layer self-assembly strategy for template synthesis of nanoscale devices, *Mater. Sci. Eng. C-Bio.* S.V 19 (2002) 255–262.
- [46] L.G. Paterno, L.H.C. Mattoso, O.N. De Oliveira, Ultrathin polymer films produced by the self-assembly technique: Preparation, properties and applications, *Química Nova* 24 (2001) 228–235.
- [47] E.A. Rietman, *Molecular Engineering of Nanosystems*, Berlin: [s.n.], 2001.
- [48] M. Okandan, P. Galambos, S.S. Mani, J.F. Jakubczak, Development of surface micromachining technologies for microfluidics and bioMEMS. Proceedings of The International Society for Optics and Photonics (SPIE), vol. 4560, Microfluidics and BioMEMS, San Francisco, CA, USA, (2001), p. 133.
- [49] M.J. Heller, A. Guttman, *Integrated Microfabricated Biodevices*, Marcel Dekker, New York, (2001).
- [50] H. Becker, L.E. Locascio, Polymer microfluidic devices, *Talanta* 56 (2002) 267–287.
- [51] A. Van Der Berg, *Lab-on-a-Chip: Chemistry in Miniaturized Synthesis and Analysis Systems*, Elsevier, Amsterdam, (2003).
- [52] P. Gravesen, J. Branebjerg, O.S. Jensen, Microfluidics—a review, *J. Micromech. Microeng.* 3 (1993) 168–182.
- [53] K. Park, *Controlled Drug Delivery: Challenges and Strategies*, American Chemical Society, Washington DC, (1997).
- [54] D. Grieshaber, Electrochemical biosensors—sensor principles and architectures, *Sensors* 8 (2008) 1400–1458.
- [55] P. Pandey, M. Datta, B.D. Malhotra, Prospects of nanomaterials in biosensors, *Anal. Lett.* 41 (2008) 159–209.

## 30 NANOSTRUCTURES

- [56] U. Yugeswaran, S.M. Chen, A review on the electrochemical sensors and biosensors composed of nanowires as sensing material, *Sensors* 8 (2008) 290–313.
- [57] L.G. Carrascosa, Nanomechanical biosensors: a new sensing tool, *Trac-Trend. Anal. Chem.* 25 (2006) 196–206.
- [58] M.N. Helmus, Nanotechnology-enabled chemical sensors and biosensors, *Am. Lab.* 38 (2006) 34.
- [59] C. Lai Poh San, E.P.H. Yap, *Frontiers in Human Genetics*, World Scientific, Singapore, (2001).
- [60] A.D. Roming Jr., et al. An introduction to nanotechnology policy: opportunities and constraints for emerging and established economies, *Technol. Forecast. Soc. Change* 74 (2007) 1634–1642.
- [61] X. Liu, et al. Nanotechnology knowledge diffusion: measuring the impact of the research networking and a strategy for improvement, *J. Nanopart. Res.* 16 (9) (2014) 2613.
- [62] F. Karaca, M.A. Öner, Scenarios of nanotechnology development and usage in Turkey, *Technol. Forecast. Soc. Change* 91 (2015) 327–340.
- [63] I.C. Ezema, P.O. Ogbobe, A.D. Omah, Initiatives and strategies for development of nanotechnology in nations: a lesson for Africa and other least developed countries, *Nanoscale Res. Lett.* 9 (133) (2014) 1–8.
- [64] J. Wang, P. Shapira, Funding acknowledgement analysis: an enhanced tool to investigate research sponsorship impacts: the case of nanotechnology, *Scientometrics* 87 (2011) 563–586.
- [65] B. Bhushan, Governance, policy, and legislation of nanotechnology: a perspective, *Microsyst. Technol.* 21 (2015) 1137–1155.
- [66] C.M. Sá, Redefining university roles in regional economies: a case study of university–industry relations and academic organization in nanotechnology, *High Educ.* 61 (2011) 193–208.
- [67] L. Krabbenborg, H.A.J. Mulder, Upstream public engagement in nanotechnology: constraints and opportunities, *Sci. Commun.* 37 (4) (2015) 452–484.
- [68] J. Wang, P. Shapira, Is there a relationship between research sponsorship and publication impact? An analysis of funding acknowledgments in nanotechnology papers, *PLoS One* 10 (2) (2015) 1–19.
- [69] A.L. Porter, et al. Refining search terms for nanotechnology, *J. Nanotechnol. Res.* 10 (2008) 715–728.
- [70] S.K. Arora, et al. Capturing new developments in an emerging technology: an updated search strategy for identifying nanotechnology research outputs, *Scientometrics* 95 (2013) 351–370.
- [71] T. Bartol, K. Stopar, Nano language and distribution of article title terms according to power laws, *Scientometrics* 103 (2015) 435–451.
- [72] A.G. Mamalis, A. Markopoulos, D.E. Manolakos, Micro and nanoprocessing techniques and applications, *Nanotechnol. Percept.* 1 (2005) 63–67.
- [73] H. Iwai, Roadmap for 22 nm and beyond, *Microelectron. Eng.* 86 (7–9) (2009) 1520–1528.
- [74] J.R. Ramsden, *Applied Nanotechnology*. [S.I.], Elsevier, Oxford, (2009).
- [75] J. Robertson, R.M. Wallace, High-K materials and metal gate for CMOS applications, *Mater. Sci. Eng. R* 88 (2015) 1–41.
- [76] M.N. Baibach, Giant magnetoresistance of (001)Fe/(001)Cr magnetic superlattices, *Phys. Rev. Lett.* 61 (1988) 2472–2475.
- [77] E.F. De Lima, M. Foschini, M. Magini, O efeito termoionico: Uma nova proposta experimental [The thermoionic effect: A new experimental proposal], *Revista Brasileira de Ensino de Física* 23 (2001) 4.
- [78] J.M.F. Bassalo, A crônica da física do estado sólido: Do tudo de Geissler às válvulas a vácuo [The chronicle of solid state physics: From the Geissler tube to vacuum tubes], *Revista Brasileira de Ensino de Física* 15 (1993) 1–4.
- [79] R. Da Silva Lima, J.C. Afonso, L.C.F. Pimentel, Raios-X: Fascinação, medo e ciência [X-rays: fascination, fear and science], *Química Nova* 32 (1) (2009) 263–270.

- [80] M. Tolentino, R.C. Rocha-Filho, O átomo e a tecnologia [The atom and technology], Química Nova na Escola 3 (1996) 4–7.
- [81] P.C. Wang, A.G. Macdiarmid, Integration of polymer-dispersed liquid crystal composites with conducting polymer thin films toward the fabrication of flexible display devices, Displays 28 (3) (2007) 101–104.
- [82] A. Trokhymchuk, On Julius Planer's 1861 paper "Notiz über das Cholestearin" in Annalen der Chemie und Pharmacie, Condens. Matter Phys. 13 (3) (2010) 1–4.
- [83] I.H. Bechtold, Cristal líquido: Um sistema complexo de simples aplicação [Liquid crystals: a complex system of simple application], Revista Brasileira de Ensino de Fca 27 (2005) 333–342.
- [84] B. Çaliskan, et al. EPR of gamma irradiated single crystals of cholesteryl benzoate, Radiation Eff. Defect. S. 159 (2004) 1–5.
- [85] Anônimo, Liquid crystals—a step closer to low-voltage displays, Electron. Eng. 27 (1968) 17.
- [86] J.A.V. Raalte, Reflective liquid crystal television display, Proc. IEEE 56 (1968) 2146–2149.
- [87] T. Fujii, et al. Dot matrix LCD module for graphic display (64 × 320 dots). IEEE transactions on consumer electronics, AGOSTO CE-28 (3) (1982) 196–201.
- [88] C.W. Tang, S.A. Van Slyke, Organic electroluminescent diodes, Appl. Phys. Lett. 51 (12) (1987) 913–915.
- [89] C.H. Lu, et al. Output power enhancement of InGaN/GaN based green light-emitting diodes with high-density ultra-small in-rich quantum dots, J. Alloys Compd. 555 (2013) 250–254.
- [90] A. Pereira, et al. Investigation of the energy transfer mechanism in OLEDs based on a new terbium β-diketonate complex, Org. Electron. 13 (1) (2012) 90–97.
- [91] S.R. Forrest, The path to ubiquitous and low-cost organic electronic appliances on plastic, Nature 6986 (2004) 911–918.
- [92] H.Q. Yin, R. Langford, R.E. Burrel, Comparative evaluation of the antimicrobial activity of ACTIOCOAT antimicrobial barrier dressing, J. Burn Care Rehab. 3 (1999) 195–200.
- [93] B. Boonkaew, et al. Antimicrobial efficacy of a novel silver hydrogel dressing compared to two common silver burn wound dressings: Acticoat™ and PolyMem Silver®, Burns 40 (1) (2014) 89–96.
- [94] M. Jaisai, S. Baruah, J. Dutta, Paper modified with ZnO nanorods—antimicrobial studies, Beislein J. Nanotechnol. 3 (2012) 684–691.
- [95] Introduction to nanotechnology. Applications of nanotechnology. Available from: <http://nanogloss.com/nanotechnology/applications-of-nanotechnology/#axzz2g1HmcoTE>
- [96] E. Hiroshi, Fiat FCC 2. Car and Drive-Brasil. Available from: <http://caranddriverbrasil.uol.com.br/carro-moto-testes/13/artigo123553-1.asp>
- [97] K. Craveiro, UOL. Uol Carros. Available from: <http://carros.uol.com.br/ultnot/2008/10/04/ult634u3225.jhtm>
- [98] K.E. Drexeler, Molecular engineering: an approach to the development of general capabilities for molecular manipulation, Proc. Natl. Acad. Sci. 78 (1981) 5275–5278.
- [99] X. Wang, et al. Au-nanoparticle coated mesoporous silica nanocapsule-based multifunctional platform for ultrasound mediated imaging, cytolysis and tumor ablation, Biomaterials 34 (2013) 2057–2068.
- [100] T. Hogg, Evaluating microscopic robots for medical diagnosis and treatment, Nanotechnol. Percept. 3 (2007) 63–73.
- [101] C.E. Handford, et al. Awareness and attitudes towards the emerging use of nanotechnology in the agri-food sector, Food Control 57 (2015) 24–34.

## 32 NANOSTRUCTURES

- [102] L.Y.Y.L. Lu, et al. Ethics in nanotechnology: what's being done? What's missing?, *J. Bus. Ethics* 109 (2012) 583–598.
- [103] K.H. Keller, Nanotechnology and society, *J. Nanopart. Res.* 9 (2007) 5–10.
- [104] P.A. Schulte, et al. Occupational safety and health criteria for responsible development of nanotechnology, *J. Nanopart. Res.* 16 (2153) (2014) 1–17.
- [105] D. Parr, Will nanotechnology make the world a better place? *Trends in biotechnology*, 23, n. 8. 395–398.
- [106] J.J. Bang, L.E. Murr, Atmospheric nanoparticles: preliminary studies and potential respiratory health risks for emerging nanotechnologies, *J. Mater. Sci. Lett.* 21 (2002) 361–366.
- [107] K.A.D. Guzmán, M.R. Taylor, J.F. Banfield, Environmental risks of nanotechnology: national, nanotechnology initiative funding, 2000–2004, *Environ. Sci. Technol.* 40 (2006) 1401–1407.
- [108] R. Justo-Hanani, T. Dayan, European risk governance of nanotechnology: explaining the emerging regulatory policy, *Res. Policy* 44 (2015) 1527–1536.
- [109] V. Türk, C. Kaiser, S. Schaller, Invisible but tangible? Societal opportunities and risks of nanotechnologies, *J. Clean. Prod.* 16 (2008) 1006–1009.
- [110] A. Capon, et al. Perceptions of risk from nanotechnologies and trust in stakeholders: a cross sectional study of public, academic, government and business attitudes, *BMC Public Health* 15 (424) (2015) 1–13.
- [111] Z.A. Collier, et al. Tiered guidance for risk-informed environmental health and safety testing of nanotechnologies, *J. Nanopart. Res.* 17 (155) (2015) 1–21.

# Supramolecular Systems

M.L. de Moraes\*, L. Caseli\*\*

\*INSTITUTE OF SCIENCE AND TECHNOLOGY, FEDERAL UNIVERSITY OF SÃO PAULO,  
SÃO PAULO, SÃO PAULO, BRAZIL; \*\*INSTITUTE OF ENVIRONMENTAL, CHEMICAL AND  
PHARMACEUTICAL SCIENCES, FEDERAL UNIVERSITY OF SÃO PAULO, SÃO PAULO, SÃO  
PAULO, BRAZIL

## CHAPTER OUTLINE

<b>2.1 General Concepts of Supramolecular Systems.....</b>	<b>33</b>
<b>2.2 Molecular Recognition.....</b>	<b>34</b>
<b>2.3 Self-Organized Systems.....</b>	<b>35</b>
2.3.1 Surfactants and Detergents.....	35
2.3.2 Micelles: Formation and Critical Micelle Concentration.....	37
2.3.3 Lipid Bilayers and Vesicular Systems .....	39
2.3.4 Preparation Method of Liposomes and Multilayer Systems.....	41
2.3.5 Biomedical Applications of Liposomes .....	43
2.3.6 Cell Membranes: Chemical Composition and Physicochemical Properties .....	45
<b>2.4 Multicyclic Supramolecular Systems.....</b>	<b>49</b>
<b>References .....</b>	<b>51</b>

## 2.1 General Concepts of Supramolecular Systems

A supramolecular system is an assembly of molecular subunits that are organized via intermolecular interactions that can be ionic or covalent. These interactions include hydrogen bonds, metallic coordination, hydrophobic interactions, Van der Waals forces and ionic interactions [1].

Supramolecular systems can be classified into two types:

1. macrocycle compounds that are formed via cyclic chemical structures and are linked by covalent bonds (e.g., compounds derived from porphyrin and phthalocyanine); and
2. systems with molecular self-aggregation, such as, micelles and lipid vesicles.

There are some interesting technological and scientific applications of supramolecular systems, such as, molecular recognition, catalysis, biomimetic systems, and transport of substances [2–4].

Many macrocycles, as well as self-aggregated disperse systems, have the capability to recognize and “capture” substances and, in many cases, to carry them to strategic locations. In general, molecular recognition is not an exclusive property of supramolecular systems. Molecular recognition was first described for biomacromolecules, such as enzymes, and later for nucleic acids. Hermann Emil Fischer [5], was one of the pioneers to identify the systems capable of recognizing molecules in 1902. He described the interactions between an enzyme and its substrate using the “key and lock” model. However, his comprehension of structure was very superficial. At the beginning of the 20th century, Van der Waals forces (noncovalent molecular interactions) improved the understanding of protein structure and of several biological processes.

In this context, an important advance for elucidating molecular recognition processes was the assumption that noncovalent bonds were fundamental for maintaining many of the aforementioned structures. The possibility of synthesizing structures capable of recognizing molecules or, at least, of “capturing” them using noncovalent interactions came when Charles J. Pedersen described the synthesis of crown ethers in the 1980s [6], which improved the understanding of self-organized structures in solutions, such as, micelles and liposomes.

The 1987 Nobel Prize in Chemistry was awarded to Donald J. Cram, Jean-Marie Lehn, and Charles J. Pedersen for their work in developing high selectivity molecules of the “host-guest” type. This can be considered as an acknowledgement of the importance of supramolecular chemistry. Later, other researchers started to develop molecular machinery with self-organized structures and complex sensors using construction blocks, such as, fullerenes and dendrimers.

The self-assembly concept must be highlighted for self-aggregation systems. Self-assembly involves the construction of systems in which the molecules are driven to assemble structures via noncovalent interactions. Thus, self-assembly can be subdivided into intermolecular and intramolecular. Intramolecular assembly involves macromolecules, such as, DNA and proteins. Intermolecular assembly involves the interaction of a certain number of smaller molecules for building larger structures, such as, micelles, vesicles, membranes, and liquid crystals.

## 2.2 Molecular Recognition

Molecular recognition is a specific interaction between a host molecule and a complementary guest molecule, which results in a host-guest complex. The designation of which substance is a “host” and which one is a “guest” is typically arbitrary. Molecules are capable of recognizing each other via noncovalent interactions. The main applications of this field are the construction of molecular sensors and catalysis.

In the case of template-driven synthesis, self-assembly can be used with reactive species to organize a system for a chemical reaction. Intermolecular interactions may facilitate the desired chemical interaction by minimizing the effect of side reactions. The molecule used as a template can be removed after the reaction.

The systems that are formed via molecular printing follow this principle. In these systems, the host is built from small molecules using a species of interest as a template. Therefore, the molecule (typically a polymer) is synthesized around the template molecule. The model is removed after the construction. This leaves only the host with a region in its chain (i.e., a cavity) with a molecular geometry that is equal or similar to the geometry of the molecule that was removed. The construction model of the cavity can subtly differ from the guest-molecule, which is a molecule of interest that is to be molecularly recognized later.

Some supramolecular recognition systems are considered “bioinspired” or “biomimetic” because they try to copy some functions of biological systems. This includes the production of biosensors or high-efficiency catalytic systems.

## 2.3 Self-Organized Systems

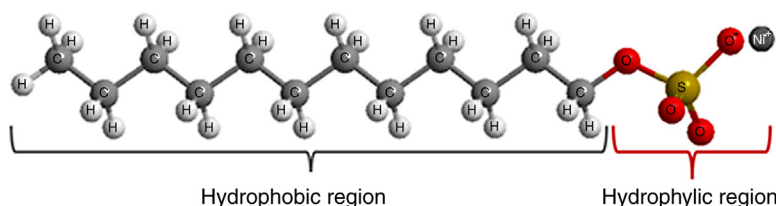
### 2.3.1 Surfactants and Detergents

Surfactants are amphiphilic substances. These molecules have one hydrophobic end and one hydrophilic end (Fig. 2.1) and are capable of changing the surface and interface tensions of a liquid. This effect occurs because of the strong adsorption of surfactant molecules at the air-water interface that reduces its surface energy, which is a consequence of the Gibbs theory [7].

Amphiphilic molecules have different properties that depend on the composition of their hydrophilic parts, which can range from hydroxyl to more complex groups, and their hydrophobic parts that may have saturated, unsaturated, or ramified chains. Surfactants are classified according to their hydrophilic part. Specifically, surfactants are classified as cationic, anionic, nonionic, and amphoteric or zwitterionic. The latter type has both positive and negative charges at different locations. Table 2.1 shows some surfactants with different charge types.

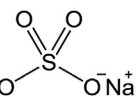
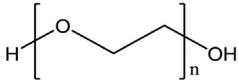
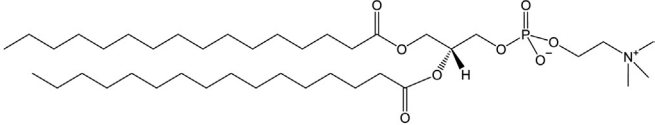
Additionally, surfactants are classified according to their function or application (i.e., detergents, foaming agents, conditioning agents, bactericides, moisturizers, emollients, dispersants, and solubilizing agents).

Detergents are surfactants that remove oily or greasy materials from surfaces, such as fabric fibers or human skin, and disperse these dirty materials in an aqueous medium. In



**FIGURE 2.1 Amphiphilic molecule—sodium dodecyl sulfate (SDS).** Hydrophobic and hydrophilic regions are composed of a hydrocarbon chain and a sulfate group, respectively.

**Table 2.1** Some Example of Surfactants

Surfactant	Application
<b>Anionic</b>	
SDS	
	Solubilize proteins Protein electrophoresis cosmetics cleanliness
<b>Cationic</b>	
CTAB	
	Protein electrophoresis Synthesis of nanoparticles DNA extraction
<b>Nonionic</b>	
PEG	
	Pharmaceutical products Controlled drug delivery Eye lubricant
<b>Zwitterionic</b>	
DPPC	
	Controlled drug delivery Mimic cell membranes

CTAB, Cetyltrimethylammonium bromide; DPPC, dipalmitoylphosphatidylcholine; PEG, polyethylene glycol; SDS, sodium dodecyl sulfate.

biochemistry, detergents also solubilize a large range of species, such as, membrane proteins for biophysical analysis.

Oily materials are removed via detergent adsorption on the oily or greasy surface, which increases its contact angle. Thus, the grease and oil droplets are easily removed using mechanical action, and the surfactant, which is adsorbed around the droplet surface, stabilizes the oily material in an aqueous solution (Fig. 2.2) [8].

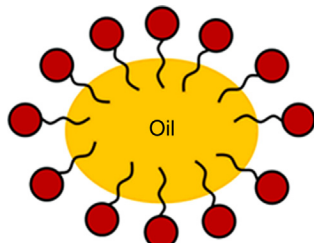
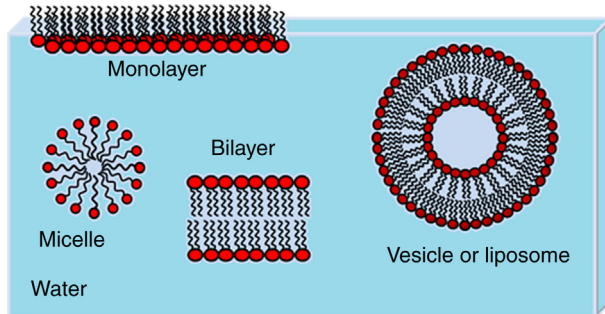


FIGURE 2.2 Adsorbed detergent around the surface of an oil droplet.



**FIGURE 2.3** Lipid aggregates in aqueous medium.

#### 2.3.1.1 Lipid Aggregates

Amphiphatic lipids upon contact with water form lipid aggregates. Thus, the hydrophilic region of the molecules remains in contact with water, and the hydrophobic part aggregates itself via hydrophobic interactions. This molecular ordering results in a higher thermodynamic stability. [9] Different types of aggregates can be formed (e.g., monolayers at the air–water interface, bilayers, micelles, vesicles, or liposomes) depending on the composition and shape of the lipid in aqueous medium (Fig. 2.3).

The lipid aggregate structure can be predicted by the critical packing parameter (*PP*), which considers the volume, length of the hydrocarbon tail (hydrophobic region), and the polar head area (hydrophilic region). Thus, the critical *PP* can be calculated using Eq. (2.1):

$$PP = \frac{V}{al_c} \quad (2.1)$$

where, *V* is the hydrophobic volume, *a* is the surface area occupied by the polar region of the amphiphilic molecule at the water–air interface, and *l<sub>c</sub>* is the hydrophobic region length.

The *PP* can be used as a guide of the surfactant architecture. The typical values and their corresponding structures are shown in Table 2.2.

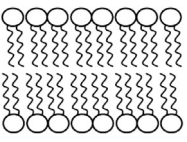
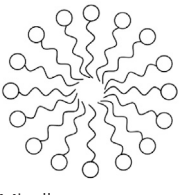
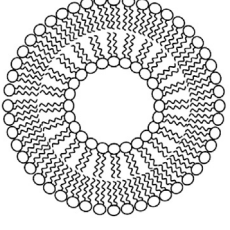
The *PP* is useful for predicting the structure of a lipid aggregate. However, the structure can be changed through the addition of an electrolyte, such as ionic cosurfactant, as well as by temperature change or by the insertion of ramified or unsaturated chains.

The control of architecture of these structures has a broad potential in many biochemistry areas, such as, controlled drug delivery, catalysis, and solubilization of membrane proteins of low-solubility species. Some of these applications will be discussed in Section 2.3.6.

#### 2.3.2 Micelles: Formation and Critical Micelle Concentration

Micelle aggregate formation occurs due to the shape and size of a surfactant and due to its concentration. The micelle structure forms only if the surfactant or monomer concentration is equal or higher than the critical micelle concentration (CMC) (Fig. 2.4). If the surfactant concentration is below the CMC, micelle formation does not occur, and the solution will only contain the surfactant monomers. [10]

**Table 2.2** Use of the Critical Packing Parameter for Predicting the Lipid Aggregate Structure.

$PP = V/aI_c$	Shape	Structure
$PP \sim 1$ Example: phosphatidylethanolamine		 Bilayers
$PP < 1$ Example: single phospholipids		 Micelles
$PP > 1$ Example: phosphatidylcholine		 Vesicles or liposomes

PP, Packing parameter.

Source: Adapted from R.M. Pashley, M.E. Karaman, Applied Colloid and Surface Chemistry, J. Wiley, Chichester, West Sussex, England; Hoboken, N.J., 2004 [7].

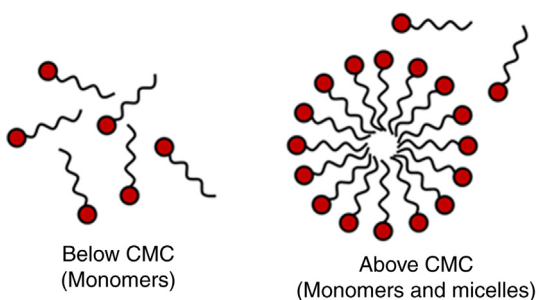


**FIGURE 2.4** Dependence of micelle formation on the surfactant concentration.

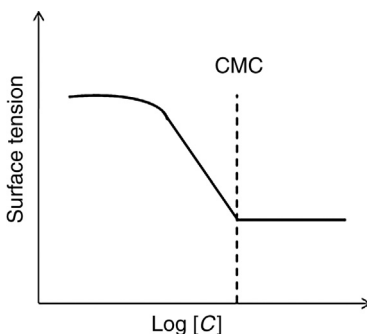


**FIGURE 2.5** Typical graph of surface tension versus surfactant concentration for obtaining the critical micelle concentration (CMC).

The main method for determining surfactant CMC is through surface tension measurement. However, other methods, such as electrical conductivity, spectroscopy, electrochemistry, light scattering and viscosity [11–13], are also available.

It is possible to determine the CMC from the curve of surface tension versus surfactant concentration. Additionally, this curve defines a surface excess ( $\Gamma$ ) parameter, which is associated with the surfactant excess at the surface at any cross-section inside the solution. [8,14,15] This parameter is determined through the Gibbs adsorption equation (Eq. 2.2):

$$\Gamma = -\frac{1}{2RT} \left( \frac{\partial \gamma}{\partial \ln C} \right)_T \quad (2.2)$$

where  $\gamma$  is the surface tension,  $C$  is the surfactant concentration,  $R$  is the gas constant and  $T$  is the absolute temperature.

Fig. 2.5 shows the behavior of the curve of surface tension versus the logarithm of the surfactant concentration ( $\log C$ ). When  $C$  is well below the CMC, the increase of the surfactant volume does not result in a significant increase of surface tension or adsorption density. When the surfactant concentration is close to the CMC, the surface tension decreases abruptly, and there are changes in conductivity and turbidity. When the surfactant concentration reaches the CMC,  $d\gamma/d\ln C = 0$ , micelle aggregates are formed, the surface becomes completely charged, and no additional alteration of surface tension is observed.

Additionally, micelle aggregates may occur in nonpolar solvents. In this case, inverted or reverse micelles are formed. Reverse micelles have the hydrophilic region of the surfactant inside the aggregate and the hydrophobic region toward the nonpolar medium (Fig. 2.6)

### 2.3.3 Lipid Bilayers and Vesicular Systems

A lipid bilayer is another type of lipid aggregate that can be formed in an aqueous medium, in which two single layers form a bidimensional sheet. The hydrophobic tails of each single layer interact with each other and exclude water, while the hydrophilic heads interact with

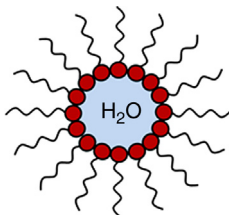


FIGURE 2.6 Typical reverse micelle structure.

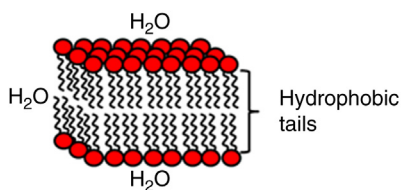


FIGURE 2.7 Lipid bilayer structure.

water in each bilayer surface (Fig. 2.7). Since the hydrophobic region at the ends of a bilayer is in contact with water, the bilayer sheet is relatively unstable, and it spontaneously turns into other lipid aggregates that are spherical structures called vesicles or liposomes.

Liposomes or vesicles were first described by Alec D. Bangham in 1964 [15], and since then, they have raised the interest of many researchers. Because their structure mimics a cell membrane, liposomes have been used as membrane models for physical and chemical studies, as drug carriers to target cells, to solubilize and incorporate biomolecules and as barriers to viral and bacterial invasions.

In general, vesicles are formed because of the tension applied at the hydrophobic–hydrophilic interface. This causes molecules to group to minimize contact of the hydrocarbon elements with the aqueous phase. The equilibrium is reached via steric repulsion among the hydrophilic groups and the entropic repulsion among acyl chains of single layers. The formed spheres capture water and create an aqueous compartment inside lipid bilayers, which is separated from the medium via a hydrophobic barrier (Fig. 2.8). The

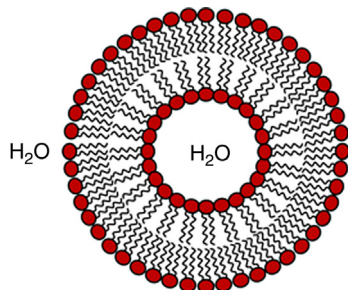
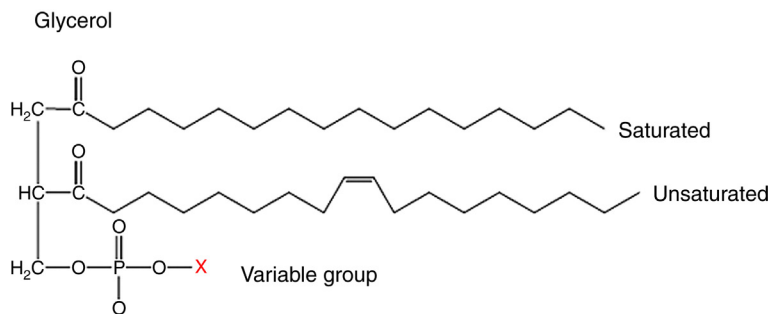


FIGURE 2.8 Structure of a vesicle or liposome.



**FIGURE 2.9 General phospholipid structure.**

lipid bilayer mimics biological or cell membranes that consist of an approximately 3-nm-thick lipid bilayer that contains proteins. Proteins that are inserted in the cell membrane bilayer help with molecular diffusion between the medium and the inside of the bilayer. In the case of vesicles or liposomes produced in laboratories, a bilayer made of pure lipids is essentially nonpermeable to polar solutes. A lipid bilayer has a flexible structure with the ability to change its shape without losing its integrity. This property is a consequence of noncovalent interactions among the lipids in a bilayer.

The lipids that constitute a bilayer (i.e., phospholipids) may vary both in the size of the hydrocarbon part and of the hydrophilic group, as shown in [Table 2.3](#). The hydrophobic group consists of a fatty acid chain [i.e., a carboxylic group ( $-\text{COOH}$ )] linked to an alkyl chain of 4–28 carbon atoms that can generally be saturated or unsaturated] and a polar head group with a positive, negative or zwitterionic charge ([Fig. 2.9](#)).

Another property of phospholipids is the phase transition temperature or critical temperature ( $T_c$ ) at which, depending on the phospholipid composition, the membrane passes from a crystalline to a fluid phase [[16](#)]. At conditions close to physiologic temperatures (20–40°C), when the lipids have 12–14 carbon atoms in the hydrophilic tail and are not unsaturated, the membrane will most likely be in a crystalline phase (i.e., the gel phase). If the hydrophobic tail is unsaturated, it is probable that the bilayer structure will be in a fluid phase, which favors the rotation of molecules in the bilayer ([Table 2.3](#)). Thus, the membranes that are more fluid tend to allow the solute to flow through the bilayer of the aqueous compartment to the external medium and vice versa.

### 2.3.4 Preparation Method of Liposomes and Multilayer Systems

When lipid bilayers are hydrated, they separate during agitation and self-organize into spherical structures to form multilamellar vesicles (MLVs). Once MLVs are formed, it is possible to reduce the size and quantity of lamellas by introducing either sonic (sonication) or mechanical (extrusion) energy to the system. In general, liposomes are prepared using the following stages: [[4,17,18](#)]

**Table 2.3** Properties of Phospholipids

Name (abbreviation)	Fatty Acid Chain	Transition Temperature $T_c$ (°C)	Charge in pH 7.4
DLPC	12:0	-1	0
DMPC	14:0	23	0
DPPC	16:0	41	0
DSPC	18:0	55	0
DOPC	18:1	-20	0
DMPE	14:0	50	0
DPPE	16:0	63	0
DOPE	18:1	-16	0
DMPA	14:0	50	-1.3
DPPA	16:0	67	-1.3
DOPA	18:1	-8	-1.3
DMPG	14:0	23	-1
DPPG	16:0	41	-1
DOPG	18:1	-18	-1
DMPSD	14:0	35	-1
DPPSD	16:0	54	-1
DOPSD	18:1	-11	-1

DL, Dilauryl; DM, dimyristoyl; DO, dioleyl; DP, dipalmitoyl; PA, phosphatidic acid; PC, phosphatidylcholine; PE, phosphatidylethanolamine; PG, phosphatidylglycerol; PSD, phosphatidylserine.

#### *Stage 1: Dissolution of lipids*

Phospholipids are dissolved in an organic solution, typically chloroform or a chloroform–methanol mixture, to obtain a homogeneous solution. The choice of solvent depends on the phospholipid composition.

#### *Stage 2: Lipid film formation*

Organic solvent is removed to form a film on the flask wall. The solvent can be evaporated using the compressed air or nitrogen flow.

#### *Stage 3: Formation of MLVs*

The dry lipid film is hydrated via the addition of an aqueous medium followed by agitation. The hydration temperature must be above the phase transition temperature during the entire hydration process. Hydration time depends on the composition and phospholipid structure. In general, 1 h of agitation is enough for most phospholipids. The hydration product is an MLV. Its structure resembles an onion, with bilayers or lamellas separated by a water layer.

#### *Stage 4: Formation of unilamellar vesicles (SUVs)*

SUVs can be obtained via sonication or extrusion of the MLV suspension.

##### 2.3.4.1 Sonication

The breakage of MLVs with sonic energy (i.e., sonication) produces SUVs with diameters between 15 and 150 nm. The diameter depends on the composition, lipid concentration, temperature, and sonication time. Sonication conditions influence the breakage

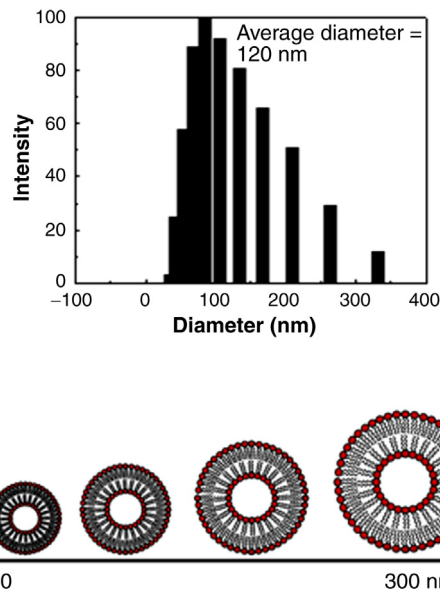


**FIGURE 2.10** Size distribution measured via light scattering of DPPG liposomes prepared using a titanium tip sonicator. Adapted from M.L. Moares, M.S. Baptista, R. Itri, V. Zucolotto, O.N. Oliveira, Immobilization of liposomes in nanostructured layer-by-layer films containing dendrimers. *Mater. Sci. Eng. C*, 28 (4) (2008) 467–471 [19].

reproducibility. Therefore, the average diameter of SUVs that are obtained via sonication may vary between the preparations. In addition, SUVs with a small diameter, between 15 and 50 nm, have a high degree of curvature that makes them unstable. Due to high degree of curvature, fusion among SUVs occurs spontaneously to form larger vesicles. This occurs when the solution is stored below the phase transition temperature.

The following equipment is commonly used for sonication: ultrasound baths and sonicators with titanium tips. Fig. 2.10 shows the size distribution measured via light scattering of liposomes that were prepared using a titanium tip sonicator.

#### 2.3.4.2 Extrusion

In the extrusion technique, MLVs are forced through a filter (i.e., a polycarbonate membrane with a defined pore size) to obtain particles with diameters close to pore diameters. In addition, extrusion must be performed above the phase transition temperature of the lipid. This technique results in a more defined size distribution. For example, a membrane with a 100-nm pore size has an average size distribution of 120–140 nm.

#### 2.3.5 Biomedical Applications of Liposomes

Phospholipid vesicles or liposomes have been widely explored since the 1970s [20]. Liposomes have been used as model membrane systems, especially to mimic the processes of adsorption and incorporation of biomolecules as well as drug carriers to target cells [21–23]. The use of liposomes to treat diseases is favored because of the biocompatibility and

capability to stabilize proteins and soluble and nonsoluble drugs, in addition to the versatility of lipid composition, which may help to guide the drug to a specific organ.

As a result, different formulations have been investigated. Thus, this technique became potentially useful to treat certain diseases. Many formulations are already commercially available. Liposome systems for treating cancer and antibacterial and antifungal diseases have attracted significant attention regarding controlled drug delivery because of the potential for minimizing side effects. Doxil, a doxorubicin, is an example of a liposome system for systemic administration of chemotherapy against cancer.

In addition, immobilized liposomes in solid substrates have been explored for the controlled release of drugs in patches [24,25] and to build biosensors [26]. Drug release from patches is a promising application because the transdermal delivery system occurs using diffusion across skin layers, which allows continuous drug administration. In this case, the use of liposome systems is more viable because of its higher skin diffusivity compared to the majority of pure drugs. [27]

Geraldo and coworkers described the production of layer-by-layer (LbL) films made with liposomes that incorporate ibuprofen, which is an antiinflammatory drug. The dipalmitoylphosphatidylcholine (DPPC), dipalmitoylphosphatidylglycerol (DPPG), and palmitoyl-2-oleoyl-sn-glycero-3-phosphoglycerol (POPG) liposomes containing ibuprofen were assembled using the alternate adsorption of generation 4 polyamidoamine dendrimer (PAMAM). The release of ibuprofen incorporated in liposomes was slower than that of the free drug.

Additionally, LbL films with liposomes were explored by Xavier et al. [25] to release aloin, a component of *Aloe vera* with scar healing properties. The authors investigated aloin encapsulated in liposomes and immobilized in LbL films with a polyelectrolyte. The aloin release was followed from the solutions and LbL films with liposomes of different phospholipid compositions using fluorescence spectroscopy. After comparing different phospholipid compositions of the systems, the authors concluded that the main factors that control the release are the electrostatic interactions that involve charged phospholipids and the drug. Thus, these interactions can be estimated in self-assembled films that break the ground for new systems for the controlled delivery of drugs. Fig. 2.11 represents the release of aloin that is incorporated in liposomes and is immobilized in self-assembled films with the insertion of a polyelectrolyte.

Liposomes that were wrapped in LbL films in suspension were explored for the development of vaccines [28] and as drug release vehicles [29,30].

Liposomes that were wrapped in LbL films (*layersomes*) were studied by Harde et al. [28] to develop a bivalent vaccine. Layersomes were prepared using phospholipid hydration in the presence of toxoids, followed by the LbL assembly of polyacrylic acid (PAA) and polyallylamine hydrochloride (PAH) polyelectrolytes. The formulation was stable in biomimetic medium and kept its structural integrity and preserved the biological activity and conformational stability of toxoids.

Chen et al. [29] encapsulated paclitaxel, which is used in cancer treatment, in liposomes wrapped in multilayers of PAA and chitosan to improve the stability of the drug

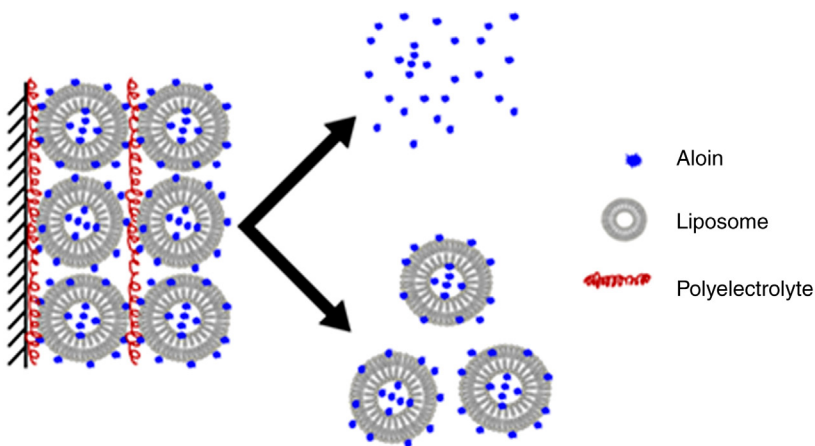


**FIGURE 2.11** Schematic of aloin release after its incorporation in liposomes and immobilization in self-assembled films.

release system. The formulation had good stability in gastrointestinal fluids and was stable after 6 months of storage both at 4°C and at ambient temperature. The release of paclitaxel in vitro in the chitosan-PAA-liposome-paclitaxel formulation had a retention time of approximately 3 h, which is shorter than that of liposome-paclitaxel. Furthermore, compared to the formulation without chitosan, the formulation that contained chitosan showed an increase of cytotoxicity induced by paclitaxel in a culture medium of human cervical cancer cells.

Additionally, liposomes have been used in the construction of immunosensors [26]. In this case, the bioreceptor [i.e., the specific biomolecule (an enzyme, an antibody or a peptide)] is incorporated in the phospholipid vesicle and is immobilized in solid substrates. The stability of the bioreceptor is maximized when it is encapsulated in liposomes before its immobilization, compared to a bioreceptor that is immobilized directly on the substrate. This occurs because the encapsulated bioreceptor has its secondary structure induced, in addition to being immobilized by noncovalent bonds and kept free in a microspace, which reduces denaturation and/or structural changes during immobilization. The schematic of biorecognition and structural organization of the bioreceptor encapsulated in liposomes and immobilized in thin films is shown in Fig. 2.12. The response of the electrochemical immunosensor shows that there is a change in the current when the antibody interacts with the bioreceptor.

### 2.3.6 Cell Membranes: Chemical Composition and Physicochemical Properties

Many self-organized systems are used as models of biological membranes. Therefore, it is important to know basic aspects of the composition, structure, and properties of a cell membrane.

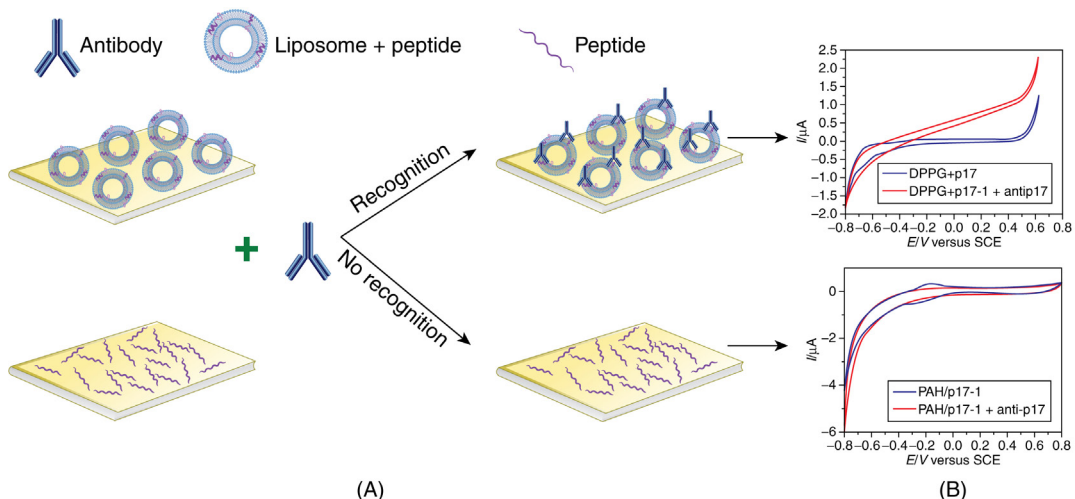


**FIGURE 2.12** (A) Schematic of an immunosensor with a bioreceptor immobilized directly on the substrate, and when a bioreceptor is incorporated in liposomes. (B) Antigen/antibody biorecognition response of the electrochemical immunosensor. Adapted from Petri et al., *Toward preserving the structure of the antigenic peptide p17-1 from the HIV-1 p17 protein in nanostructured films*, *J. Nanosci. Nanotechnol.* 11 (8) (2011) 6705–670 [26].

A cell membrane is a bilayer that separates the inside of all cells from the external environment [31,32]. It is selectively permeable to substances that enter or leave through it, controls their flow to the inside and the outside of the cell and protects the cell against external forces. Chemically speaking, it is formed by lipids that constitute the functional skeleton of a membrane (Fig. 2.13) and may or may not have proteins incorporated to it. Cell membranes are involved in a series of cellular process (e.g., cellular adhesion, ionic conductivity, and cellular signaling) and serve as a surface for attaching different extracellular structures such as the cell wall and intracellular cytoskeleton. [12] Cell membranes can be artificially assembled using different techniques, including lipid vesicles.

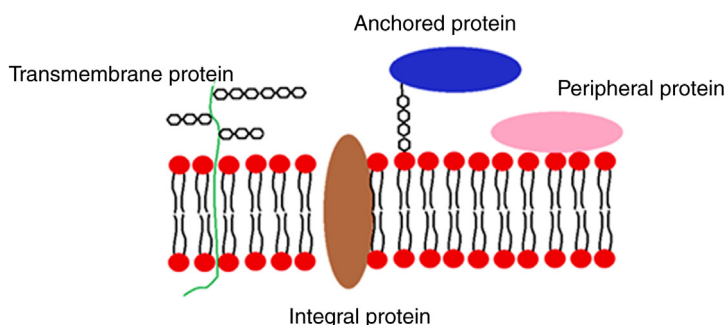


**FIGURE 2.13** Schematic of a cell membrane lipid bilayer showing integral, transmembrane, peripheral, and anchored proteins.

The most fundamental model for explaining the structure of a cell membrane is the “Fluid mosaic model,” which was developed by Singer and Nicolson (1972) [33] and replaced a previous model by Davson and Danielli (1935) [34]. In this model, the cell membrane can be considered as a bidimensional liquid in which lipid and protein molecules are spread laterally. Although lipid bilayers are capable of forming bidimensional liquids without the presence of other substances, the plasmatic membrane also has a large number of proteins that influence the physical and structural properties of the membrane. Some specific agglomerates of proteins and lipids make the cell membrane laterally heterogeneous. An example of this is the existence of lipid rafts, which are relatively condensed surface dominions in the membrane that are surrounded by a relatively fluid matrix. The composition of these rafts is specific and is formed specifically by cholesterol, sphingolipids and specific proteins, such as, immunoglobulins and alkaline phosphatases. In addition, the inner and outer layers of the membrane are chemically different [35].

Lipid bilayers can be formed via physical self-assembly (without covalent interactions). Lipids can be classified as amphipathic or amphiphilic molecules because they have a polar region with an affinity for water (a hydrophilic head) and a nonpolar region with a low affinity for water (a hydrophobic tail). These terms are used because the nonpolar region—a long alkyl chain (approximately 10–20 carbon atoms)—resembles a “tail,” while the relatively smaller hydrophilic region resembles a “head.”

A cell membrane primarily consists of a thin layer of lipids that spontaneously combine in a way that the hydrophobic tails are isolated from the surrounding polar fluid. Similarly, the hydrophilic heads tend to associate with the intracellular (cytosolic) and extracellular faces of the resulting bilayer. This forms a continuum that originates a relatively spherical lipid bilayer. Van der Waals and electrostatic forces, hydrogen bonds, and noncovalent interactions contribute to lipid bilayer formation.

In general, hydrophobic interactions are the driving force for forming lipid bilayers. Additionally, entropy ( $S$ ) increases because of the higher mobility of hydrophobic tails that are protected from aqueous environments and thermodynamically contributes to the bilayer formation process, as per the Gibbs equation at constant pressure and temperature:

$$\Delta G = \Delta H - T\Delta S \quad (2.3)$$

where  $G$  is the Gibbs free energy,  $H$  is the enthalpy,  $T$  is the absolute temperature, and  $S$  is the entropy. From this equation, it can be seen that an increase in the entropy of the system favors the spontaneity of lipid bilayer formation and reduces  $G$ . Lipid bilayers are generally impermeable to ions and polar molecules. The arrangement of hydrophilic heads and hydrophobic tails of the lipid bilayer may impede the diffusion of polar solutes (e.g., amino acids, nucleic acids, carbohydrates, proteins, and ions) through the membrane but usually allows passive diffusion of hydrophobic molecules. This provides the cell with a capability to control the movement of these substances using transmembrane protein complexes, such as, pores and channels. A certain material can be incorporated into the membrane through the fusion of intracellular vesicles with the membrane (exocytose). However, if a membrane is continuous with a tubular structure that is made of the membrane material,

the tube material can be continuously dragged into the membrane. In addition, there are molecular exchanges between the lipid and aqueous phases.

Additionally, there are variety of lipids inside the cell, such as, main membrane phospholipids and glycolipids (i.e., phosphatidylcholine, phosphatidylethanolamine, phosphatidylinositol and phosphatidylserine). A cell membrane consists of three classes of amphipathic lipids: phospholipids, glycolipids, and sterols. The amount of each depends on the cell type. However, in most cases, phospholipids are the most abundant class. The chains that originate from fatty acids in phospholipids and glycolipids typically have an even number of carbon atoms that can be saturated or unsaturated. The length and degree of unsaturation of the fatty acid chains influence membrane fluidity. Thus, unsaturated lipids, due to the angular torsion of hydrophobic chains, impede the regular packing of the chains, reduce the melting temperature and increase membrane fluidity. Another consequence of fluidity diminution is the increase in lateral membrane compressibility. In other words, the membrane withstands a high compression or decompression rate without a significant increase in its lateral pressure. This indicates a low lateral elasticity. In addition, surface viscosity can be increased by the presence of chains with torsion or ramifications.

Therefore, membrane composition determines its fluidity, surface elasticity, and viscosity properties. It is important to highlight that a membrane is heterogeneous in two aspects: (1) if we compare the internal and external layers, and (2) if we compare different regions of the same layer (e.g., aggregates of the “lipid raft” type that contain the characteristic lipid and protein composition). Lipid rafts and caveolae are examples of cholesterol-rich microdomains in the cell membrane. This molecule adapts well to irregular spaces between the hydrophobic tails of the membrane lipids, which provides a condensation and reinforcement effect to the cell membrane structure.

Thus, cell membranes can be studied as models. In addition to liposomes, Langmuir films (1917) [36] are also useful models. They are made of thin films oriented as monolayers at the liquid–air interface, as shown in Fig. 2.14. These films are formed when organic solutions of amphiphilic materials are spread at the air–water interface. If the material is insoluble in water and the solvent is volatile, a film of monomolecular thickness can be formed at the interface. Usually, the substance must spread uniformly at the interface to form a stable film. Thus, the film can be characterized in different ways, using tensiometric,

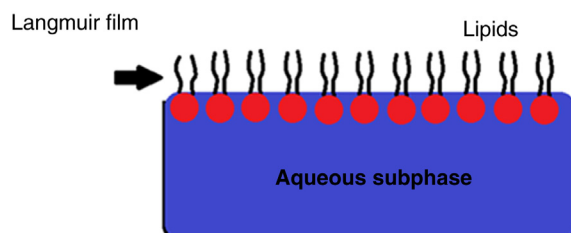


**FIGURE 2.14** Schematic of a Langmuir film that is mounted on an aqueous subphase.

volumetric, microscopic, and spectroscopic measurements. The most classical characterization approach is via surface pressure measurement ( $\pi$ ), defined as:

$$\pi = \gamma_0 - \gamma \quad (2.3)$$

where  $\gamma_0$  is the surface tension of pure water and  $\gamma$  is the surface tension in the presence of the Langmuir film.

Langmuir films have been used in the interaction of membrane enzymes [37,38] as well as in molecular recognition processes [39] or in the interaction of drugs with cell membranes [40,41].

## 2.4 Multicyclic Supramolecular Systems

Ions or molecules that are close to the central atom are called binders. Binders are generally linked to the central atom via a coordinated covalent bond. Specifically, a pair of non-bonded electrons in an empty metallic orbital is donated, which is said to be coordinated with the atom.

The coordination number and the number of ligands bonded to the metal define the ligand structure, which is determined by the interactions between the p and s orbitals of the ligands and the d orbitals of the metallic ions. Specifically, lanthanides and actinides, in addition to transition metals, tend to have high coordination numbers because their d and f orbitals are filled or semifilled with electrons.

Therefore, different resulting structures are the consequences of the coordination number. The geometries vary and depend on the coordination number and on the ligand.

In the particular case of macrocycle systems, such as, porphyrins and phthalocyanines, which are shown in Fig. 2.15, many of their properties are associated with the capability of recognizing molecules in their internal cavities. Furthermore, in those cases, transition

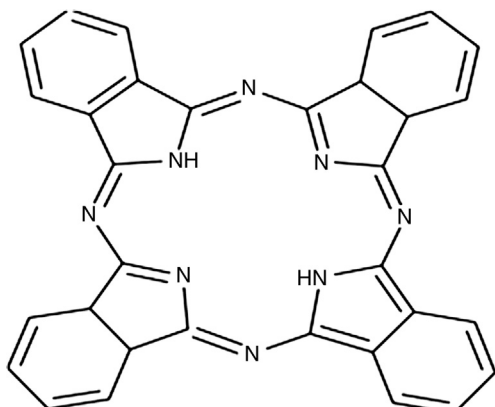
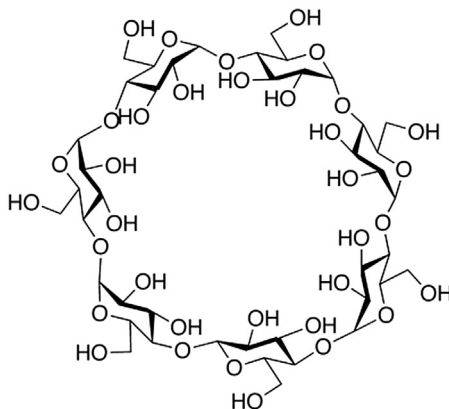


FIGURE 2.15 Chemical structure of phthalocyanine (right).



**FIGURE 2.16** Chemical structure of a cyclodextrin.

metals can covalently bond to the free electrons of nitrogen atoms of those molecules to form coordinated inorganic complexes. The classical example is porphyrin. It is a prosthetic (nonpolypeptide) element inside the hemoglobin protein, which is present in blood. Porphyrin has the capability of bonding to iron ions in the bloodstream and participating in the process of oxygen transport to biological tissues.

Many other more complex macrocycle compounds, such as, cyclodextrins (Fig. 2.16), act in more specific cases of molecular recognition. These compounds are cyclic oligosaccharides (sometimes called cycloamyloses) that are used in the pharmaceutical industry to increase the solubility of drugs in water. The active molecules are inserted in the molecule cavity and are transported to their performance location. Thus, the molecules are protected from oxidation and electromagnetic radiation, enabling their controlled release. Many studies in the literature have shown these applications for cyclodextrins [41–44].

In all examples that are mentioned in this study, there is a target substance on which the supramolecular system must act, which involves covalent and ionic interactions as well as intermolecular forces. Therefore, chemical and noncovalent interactions are key for these processes. Particularly, the study of noncovalent interactions is crucial for understanding many biological processes that involve cell structure and other biological interfaces. Biological systems are often the inspiration for supramolecular research. [2,45]

Thus, supramolecular chemistry and molecular self-assembly have been applied to develop new materials. Large-dimension structures can be readily obtained using small molecules that require fewer synthetic steps.

Catalysis is one of the applications of supramolecular chemistry. An example is template-driven synthesis, which is a special case of supramolecular catalysis. Other examples are encapsulating systems such as micelles. More examples can be found in recent bibliographic reviews.

## References

- [1] P.A. Gale, J.W. Steed, *Supramolecular Chemistry: From Molecules to Nanomaterials*, EUA, Hoboken, (2012).
- [2] Z.G. Zhang, Fabrication of novel biomaterials through molecular self-assembly, *Nat. Biotechnol.* 21 (2003) 1171–1178.
- [3] Ariga Katsuhiko, J.P. Hill, M.V. Lee, A. Vinu, R. Charvet, S. Acharya, Challenges and breakthroughs in recent research on self-assembly, *Sci. Technol. Adv. Mater.* 9 (2008) 014109.
- [4] M. Lehn, Perspectives in supramolecular chemistry—from molecular recognition towards molecular information-processing and self-organization, *Angew. Chem. Int. Ed. (English)* 29 (1990) p1304–1319.
- [5] E. Fischer, A. Speier, Darstellung der Ester, *Chemische Berichte* 28 (1895) p.3252–3258.
- [6] C.J. Pedersen, The discovery of crown ethers, *Chem. Scr.* 28 (1988) 229–235.
- [7] R.M. Pashley, M.E. Karaman, *Applied Colloid and Surface Chemistry*, J. Wiley, Chichester, West Sussex, England; Hoboken, N.J., (2004).
- [8] A.W. Adamson, A.P. Gast, *Physical Chemistry of Surfaces*, Wiley, New York, (1997).
- [9] J.N. Israelachvili, *Intermolecular and Surface Forces*, Academic Press, Burlington, MA, (2011).
- [10] B. Lindman, H.M. Wennerström, Topics in current chemistry, *Springer-Verlag, Berlin*, 87 (1980) 1–87.
- [11] W. Al-Soufi, L.P. Mercedes Novo, A model for monomer and micellar concentrations in surfactant solutions: application to conductivity, NMR, diffusion, and surface tension data, *J. Colloid Interface Sci.* 370 (2012) 102–110.
- [12] A.B. Mandal, B.U. Nair, D. Ramaswamy, Determination of the critical micelle concentration of surfactants and the partition coefficient of an electrochemical probe by using cyclic voltammetry, *Langmuir* 4 (3) (1988) 736–739.
- [13] K. Khougas, Z. Gao, A. Eisenberg, Determination of the critical micelle concentration of block copolymer micelles by static light scattering, *Macromolecules* 27 (1994) 6341–6346.
- [14] C.-H. Chang, E.I. Franses, Adsorption dynamics of surfactants at the air/water interface: a critical review of mathematical models, data, and mechanisms, *Colloids Surf. A: Physicochem. Eng. Asp.* 100 (1995) 1–45.
- [15] A.D. Bangham, R.W. Horne, Negative staining of phospholipids and their structural modification by surface-active agents as observed in the electron microscope, *J. Mol. Biol.* 8 (5) (1964) 660–710.
- [16] J.R. Silvius, Thermotropic phase transitions of pure lipids in membranes and their modification by membrane proteins, in: P.C. Jost, O.H. Griffith (Eds.), *Lipid-Protein Interactions*, vol. 2, Wiley, New York, NY, 1982, pp. 235–281.
- [17] S.C. Basu, M. Basu, *Liposome Methods and Protocols*, Humana Press, Totowa, N.J, (2002).
- [18] F. Szoka, Comparative properties and methods of preparation of lipid vesicles (liposomes), *Ann. Rev. Biophys. Bioeng.* 9 (1980) 467–508.
- [19] M.L. Moares, M.S. Baptista, R. Itri, V. Zucolotto, O.N. Oliveira, Immobilization of liposomes in nanostructured layer-by-layer films containing dendrimers, *Mater. Sci. Eng. C* 28 (4) (2008) 467–471.
- [20] J. De Gier, C.W.M. Haest, J.G. Mandersloot, L.L.M. Van Deenen, Valinomycin-induced permeation of  $86\text{Rb}^+$  of liposomes with varying composition through the bilayers, *Biochim. Biophys. Acta* 211 (1970) 373–375.
- [21] V.P. Torchilin, Recent advances with liposomes as pharmaceutical carriers, *Nat. Rev. Drug Discov.* 4 (2005) 145–160.
- [22] W.T. Al-Jamal, K. Kostarelos, Liposomes: from a clinically established drug delivery system to a nanoparticle platform for theranostic nanomedicine, *Acc. Chem. Res.* 44 (2011) 1094–1104.
- [23] A.I. Rahis-Uddin, K. Salim, M.A. Rather, W.A. Wani, A. Haque, Advances in nano drugs for cancer chemotherapy, *Curr. Cancer Drug Targets* 11 (2011) 135–146.

- [24] V.P.N. Geraldo, et al. Immobilization of ibuprofen-containing nanospheres in layer-by-layer films, *J. Nanosci. Nanotechnol.* 11 (2) (2011) 1167–1174.
- [25] A.C.F. Xavier, M.L. de Moraes, M. Ferreira, Immobilization of aloin encapsulated into liposomes in layer-by-layer films for transdermal drug delivery, *Mater. Sci. Eng. C* 33 (3) (2013) 1193–1196.
- [26] Petri, et al. Toward preserving the structure of the antigenic peptide p17-1 from the HIV-1 p17 protein in nanostructured films, *J. Nanosci. Nanotechnol.* 11 (8) (2011) 6705–6709.
- [27] T. Tanner, R. Marks, Delivering drugs by the transdermal route: review and comment, *Skin Res. Technol.* 14 (2008) 249–260.
- [28] H. Harde, K. Siddhapura, A.K. Agrawal, S. Jain, Development of dual toxoid-loaded layersomes for complete immunostimulatory response following peroral administration, *Nanomedicine* 10 (2015) 1077–1091.
- [29] M.X. Chen, B.K. Li, D.K. Yin, J. Liang, S.S. Li, D.Y. Peng, Layer-by-layer assembly of chitosan stabilized multilayered liposomes for paclitaxel delivery, *Carbohydr. Polym.* 13 (2014) 298–304.
- [30] S. Jeon, C.Y. Yoo, S.N. Park, Improved stability and skin permeability of sodium hyaluronate-chitosan multilayered liposomes by layer-by-layer electrostatic deposition for quercetin delivery, *Colloids Surf. B: Biointerfaces* 129 (2015) 7–14.
- [31] H. Lodish, A. Berk, L.S. Zipursky, et al., *Molecular Cell Biology*, fourth ed., W.H. Freeman New York, USA, 2007.
- [32] F.M. Goñi, The basic structure and dynamics of cell membranes: an update of the Singer–Nicolson model, *Biochim. Biophys. Acta* 1838 (2014) 1467–1476.
- [33] S.J. Singer, G.L. Nicolson, The fluid mosaic model of the structure of cell membranes, *Science* 175 (1972) 720–731.
- [34] J.F. Danielli, H. Davson, A contribution to the theory of permeability of thin films, *J. Cell. Comp. Physiol.* 5 (1935) 495–508.
- [35] E.G. Zalduondo, D.a. Rintoul, J.C. Carlson, W. Hansel, Luteolysis-induced changes in phase composition and fluidity of bovine luteal cell membranes, *Proc. Natl. Acad. Sci. USA* 79 (1982) 4332–4336.
- [36] I. Langmuir, The constitution and fundamental properties of solids and liquids. II. Liquids, *J. Am. Chem. Soc.* 39 (1917) 1848–1906.
- [37] L. Caseli, et al. Enzymatic activity of alkaline phosphatase adsorbed on dimyristoylphosphatidic acid Langmuir–Blodgett films, *Colloids Surf. B Biointerfaces* 25 (2002) 119–128.
- [38] L. Caseli, et al. Effect of molecular surface packing on the enzymatic activity modulation of an anchored protein on phospholipid Langmuir monolayers, *Langmuir* 21 (9) (2005) 4090–4095.
- [39] L. Caseli, et al. Probing the interaction between heparan sulfate proteoglycan with biologically relevant molecules in mimetic models for cell membranes: a Langmuir film study, *Biochim. Biophys. Acta. Biomembranes* 1818 (2012) 1211–1217.
- [40] N. Hussein, et al. , Surface chemistry and spectroscopy studies on 1,4-naphthoquinone in cell membrane models using Langmuir monolayers, *J Colloid Interface Sci.* 402 (2013) 300–306.
- [41] Pascholati, et al. , The interaction of an antiparasitic peptide active against African sleeping sickness with cell membrane models, *Colloids Surf. B Biointerfaces* 74 (2009) 504–540.
- [42] D. Ma, H.B. Zhang, Y.Y. Chen, J.T. Lin, L.M. Zhang, New cyclodextrin derivative containing poly(L-lysine) dendrons for gene and drug co-delivery, *J. Colloid Interface Sci.* 405 (2013) 305–311.
- [43] M.C. Hamoudi, J. Saunier, C. Gueutin, E. Fattal, A. Bochot, Beads made of alpha-cyclodextrin and soybean oil: the drying method influences bead properties and drug release, *Drug Dev. Ind. Pharm.* 39 (2013) 1305–1314.
- [44] T.S. Anirudhan, D. Dilu, S. Sandeep, Synthesis and characterisation of chitosan crosslinked- $\beta$ -cyclodextrin grafted silylated magnetic nanoparticles for controlled release of Indomethacin, *J. Magn. Magn. Mater.* 343 (2013) 149–156.
- [45] B. Alberts, A. Johnson, J. Lewis, et al. *Molecular Biology of the Cell*, fourth ed., Garland Science, New York, USA, 2002.

# Electrochemical Synthesis of Nanostructured Materials

F. Trivinho-Strixino\*, J.S. Santos\*, M. Souza Sikora\*\*

\*FEDERAL UNIVERSITY OF SÃO CARLOS, CENTER FOR SCIENCES AND TECHNOLOGY FOR SUSTAINABILITY, SOROCABA, SÃO PAULO, BRAZIL; \*\*FEDERAL TECHNOLOGICAL UNIVERSITY OF PARANÁ, PATO BRANCO, PARANÁ, BRAZIL

## CHAPTER OUTLINE

3.1	Introduction .....	53
3.2	Fundamental Aspects of Electrochemistry .....	54
3.2.1	Faradaic and Non-Faradaic Processes.....	54
3.2.2	Electrochemical Cells—Types and Definitions .....	56
3.3	Synthesis of Nanostructured Films by Electrodeposition.....	59
3.4	Oxide Formation by Anodization of Valve Metals .....	67
3.4.1	Anodization Under Strong Electric Fields.....	70
3.4.2	Self-Organization in Anodic Oxides: PAA.....	76
3.4.3	Electrochemical Synthesis of TiO <sub>2</sub> Nanotubes .....	85
3.4.4	Modification of the Oxide Properties by Anodic Doping.....	90
3.5	Conclusions .....	93
	List of Symbols .....	94
	References .....	94

## 3.1 Introduction

Nanotechnology associated with the design of surfaces for fabricating nanostructures and new materials has caught the attention of many researchers and has become a topic of intense scientific interest. The great progress observed in this area is a direct result of the modern advances in device miniaturization and the development of specialized instrumentation, which make it possible to visualize objects and surfaces with nanometric resolution. As a convention, nanostructured materials are those possessing structures smaller than 100 nm in any of their dimensions, including particle size, grain size, and layer width and thickness [1,2]. From a technological viewpoint, so-called *nanomaterials* have greater application potential and versatility than conventional materials, with micrometric and larger sizes. This is a consequence of a series of modifications in their physicochemical, mechanical, optical, and electronic properties, resulting from the miniaturization

process [1–4], and has raised great interest in the study and synthesis of these types of materials in recent years.

A large number of sophisticated nanomaterials have been fabricated on various types of surfaces using electrochemical techniques. The electrochemical method presents a series of advantages with respect to traditional chemical methods: ease of fabrication, low cost, homogeneity in the samples, control over the material properties, and good reproducibility. This method allows the fabrication of metallic [4] and bimetallic [5–8] nanomaterials and nanostructures; alloys [9,10], metallic oxides [11–13], etc. The main applications for these materials are in photocatalysis [14], electrocatalysis for fuel cells [15,16], photoelectric [17] and photovoltaic [18] devices, heterogeneous catalysis [16,19], thermoelectric energy converters [20], electrodes for batteries [21], and sensors [22–24].

Several experimental techniques may be employed for electrochemical synthesis, but theoretically, this process is based on the same classical foundations associated with reactions in conductor electrodes immersed in solutions containing ions [25]. It can also be performed in all types of materials (metals, oxides, and polymers), given that the “fuel” normally employed for the synthesis is the electron, which can reduce or oxidize atoms, ions, or molecules present in the solution or placed on a conductor substrate (electrode). This substrate may be part of the synthesis, or support the synthesized material. In the latter case, the synthesized material can be separated from substrate in a second stage, and it can be used for other applications of interest.

The great challenge for someone who wishes to perform electrochemical synthesis is mastering all the fundamental aspects of electrochemistry. Thus, it is imperative that whoever wants to benefit from the advances of this technique have a solid knowledge of the foundations of electrochemistry and materials science. The goal of this chapter is to survey the field of electrochemistry with a focus on the production of nanoscale metals and oxides. We do not aim to cover all of the fundamental aspects of electrochemistry and the disciplines that derive from it. Therefore, the reader eager to achieve a deeper understanding on the topic should consult further references. Detailed discussions can be found in the publications cited in this chapter, as well as in textbooks on electrochemistry and materials science.

The reader will find the content of this chapter divided into the fundamental aspects of electrochemistry, the electrodeposition of metals, and anodic oxidation. In the specific content of electrochemical synthesis of anodic oxides the focus is the synthesis of aluminum and titanium anodic oxides with high morphological control at the nanoscale, and the manipulation of the properties of the materials formed.

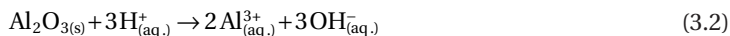
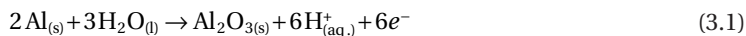
## 3.2 Fundamental Aspects of Electrochemistry

### 3.2.1 Faradaic and Non-Faradaic Processes

Two types of electrochemical processes can occur in a conductor substrate submerged in a solution containing ions. One of them comprises charge/electronic transfer reactions

through the surface between the conductor substrate and the electrolyte. In this case, the transfer of electrons through the interface promotes oxidation or reduction processes, known as *faradaic* processes. By contrast, under certain boundary conditions, this same interface may contain a region of potentials where no redox reactions take place. Consequently, in this region, it may occur physical adsorption processes that modify the chemical molecular structure of the electrode/electrolyte interface, and which depend on the applied potential and the composition of the electrolytic solution. These processes are described as *non-faradaic*.

In faradaic processes, Faraday's law states that the amount of product formed or reagent consumed by an electric current is stoichiometrically equivalent to the number of electrons provided. For example, in the case of a positive electric current (electrons removed from the electrode) going through an aluminum metallic plate submerged in an acid aqueous solution, electrons flow through that interface in the opposite direction to the applied current. Simultaneously, aluminum ions are transferred to the acid electrolyte, according to the reactions:



If the solution is composed of an acid that does not dissolve the oxide formed on metallic surface, only the reaction described by Eq. 3.1 will be favored. According to Faraday, the magnitude of the effect of an electrochemical reaction is the same in both the metallic surface and the electrolytic solution, and it is a function only of the amount of electricity crossing the system. This means that the amount (in grams) of species oxidized or reduced on the electrode surface is proportional to the number (in moles) of electrons involved. The charge corresponding to 1 mol of electrons is denominated 1 Faraday ( $F$ ), and mathematically it corresponds to:

$$F = Ne \quad (3.3)$$

where  $F$  is Faraday's constant,  $N$  is Avogadro's number, and  $e$  corresponds to the elementary charge. Substituting these values into Eq. 3.3, we obtain a good approximation for the value of  $F = 96,485$  C per mol of electrons. Therefore, in an electrodic process kept at constant current  $I$ , the variation in the theoretical mass of the oxidized or reduced material,  $dm$ , can be calculated as a function of the charge variation in the process,  $dQ$ , according to the following equation:

$$\left( \frac{dm}{dQ} \right)_I = \frac{MM}{z \cdot F} \quad (3.4)$$

where  $MM$  is the molecular mass of the species being oxidized or reduced,  $z$  is the amount (in moles) of electrons involved in the process, and  $F$  is the Faraday constant. Thus, it is

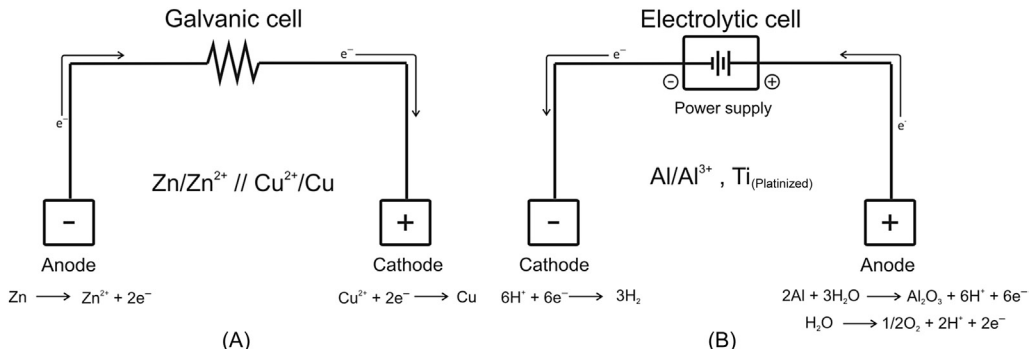


**FIGURE 3.1** Schematic representation of (A) galvanic and (B) electrolytic cells. Adapted from F. Trivinho-Strixino, J.S. Santos, M.S. Sikora, *Síntese Eletroquímica de Materiais Nanoestruturados* [electrochemical synthesis of nanostructured materials], In: A.L. Da Róz, F.L. Leite, et al. (Eds.), *Nanoestruturas: Princípios e Aplicações*, vol. 1, Elsevier, Rio de Janeiro, 2015, pp. 63–110 (Chapter 3) [26].

ideally possible to predict the theoretical deposited mass of a metallic ion being reduced in a conductor substrate under faradaic processes.

### 3.2.2 Electrochemical Cells—Types and Definitions

Electrochemical cells presenting a faradaic current flowing through its electrodes are classified as galvanic or electrolytic cells. In a galvanic cell, spontaneous reactions occur in the electrodes when they are externally connected through a conductor (Fig. 3.1A). These reactions are commonly employed in the conversion of chemical energy to electric energy. By contrast, the chemical reactions in electrolytic cells are affected by the application of an external voltage larger than the open-circuit potential of the cell (Fig. 3.1B).

In general, the term *electrolysis* is given to the process associated with the chemical changes accompanied by faradaic reactions over the electrode of interest, in contact with an electrolytic solution. In electrochemistry, by definition, the reactions that take place at the cathode are reduction reactions, and those occurring at the anode are oxidation reactions. In the former case, the transport of electrons from the electrode interface to the species in solution generates a cathodic current. In the latter case, the transport of electrons from the species in solution to the electrode interface generates an anodic current. In an electrolytic cell, the cathode is negative with respect to the anode, and, in a galvanic cell, the cathode is positive with respect to the anode.

In an electrochemistry experiment, the electrolytic cell is inserted into an electrochemical circuit consisting of a voltage or current source, metallic connectors, an ohmic resistor, an ammeter and a voltmeter, and a switch. Fig. 3.2 shows the schematic of a simple electrochemical system, where *S* corresponds to the voltage or current source, *R* is the ohmic resistor, *V* is the voltmeter, *A* the ammeter, *C* is the electrochemical cell, and *K* is the circuit on/off switch.

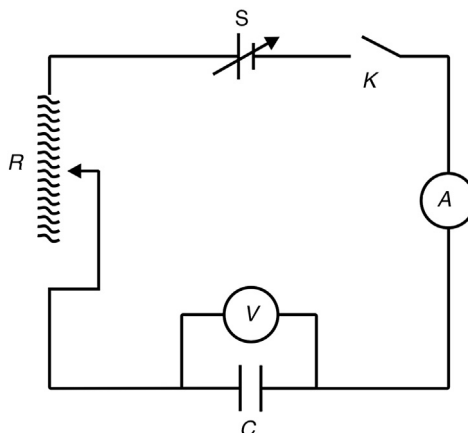


**FIGURE 3.2** Electrochemical circuit commonly used in electrochemistry experiments. Adapted from F. Trivinho-Strixino, J.S. Santos, M.S. Sikora, *Síntese Eletroquímica de Materiais Nanoestruturados [electrochemical synthesis of nanostructured materials]*, In: A.L. Da Róz, F.L. Leite, et al. (Eds.), *Nanoestruturas: Princípios e Aplicações*, vol. 1, Elsevier, Rio de Janeiro, 2015, pp. 63–110 (Chapter 3) [26].

A simplified way of visualizing an electrochemistry experiment consists of imagining a system that responds to a given perturbation. When a given excitation function (e.g., a potential step) is applied to the electrochemical cell, a response function to that perturbation is recorded (e.g., the produced current variation as a function of time), keeping all other system variables constant. Thus, the main goal of an electrochemistry experiment is to obtain information (thermodynamic, kinetic, analytic, etc.) from the observation of perturbation and response processes, which may contribute to the construction of appropriate models, and the comprehension of the fundamentals aspects of the investigated system. This allows a better control of the variables influencing the electrochemical synthesis.

In electrochemical experiments, a typical electrochemical cell is formed by a vessel commonly made of glass where the electrolyte is inserted. The electrodes are then immersed in this solution. The cell can be covered by an external and isolated glass wall jacket connected to a thermostatic bath to maintain the electrolyte temperature constant. Other ways of developing the cell and controlling the electrolyte temperature during the process can also be employed. Generally, three types of electrodes are used in this type of experiment: working, reference, and auxiliary electrodes (the last one is also called counter electrode). The working electrode is the conductor substrate where the chemical reaction of interest takes place. The working electrode potential is measured in relation to the reference electrode, which must present a known constant potential with respect to the standard hydrogen electrode within the potential window analyzed. An auxiliary or counter electrode is necessary for the flow of electric and ionic current; it closes the electrical circuit of the system and allows for the passing of a current through the external system. A magnetic stirrer can also be used to keep constant the transport process of species at

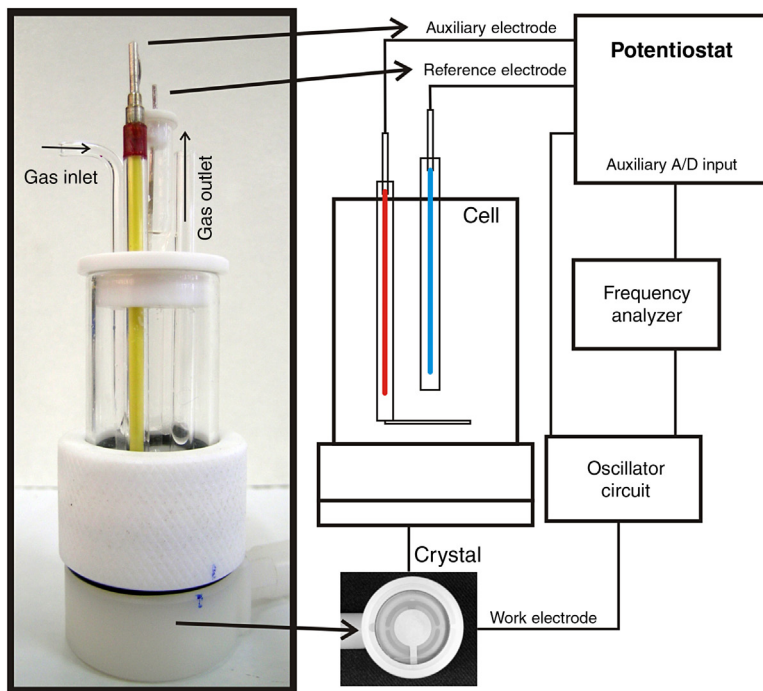


**FIGURE 3.3** Experimental configuration of a conventional three-electrode electrochemical cell used in measurements coupled to the electrochemical quartz-crystal microbalance (EQCM). Adapted from F. Trivinho-Strixino, J.S. Santos, M.S. Sikora, *Síntese Eletroquímica de Materiais Nanoestruturados* [electrochemical synthesis of nanostructured materials], In: A.L. Da Róz, F.L. Leite, et al. (Eds.), *Nanoestruturas: Princípios e Aplicações*, vol. 1, Elsevier, Rio de Janeiro, 2015, pp. 63–110 (Chapter 3) [26].

the electrode/electrolyte interface. A bubbler for N<sub>2</sub> input and a saturator can also be employed for removal of the oxygen dissolved in the electrolyte, and the maintenance of an inert gaseous phase inside the cell. This type of cell configuration is commonly used in electrodeposition reactions, which are reactions where the ions present in the electrolyte are deposited over the substrate surface by means of a reduction reaction. A typical cell used in these types of reactions is shown in Fig. 3.3.

By contrast, in anodization (anodic oxidation) reactions, which are characterized by the growth of an oxide film on the working electrode surface due to oxidation of the metallic substrate, the reference electrode is often not used. In such cases, one considers the potential difference between the working electrode and the counter electrode. This approximation can be taken once the potential difference between the electrodes is very high (exceeding 40 V) and there is no reference electrode that behaves as an ideal unpolarizable electrode, under the experimental conditions in which anodization is usually carried out. However, there are books that describe experimental configurations for adequately measuring the working electrode potential with respect to the reference electrode, in anodization reactions where the potential range allows the use of these electrodes [27].

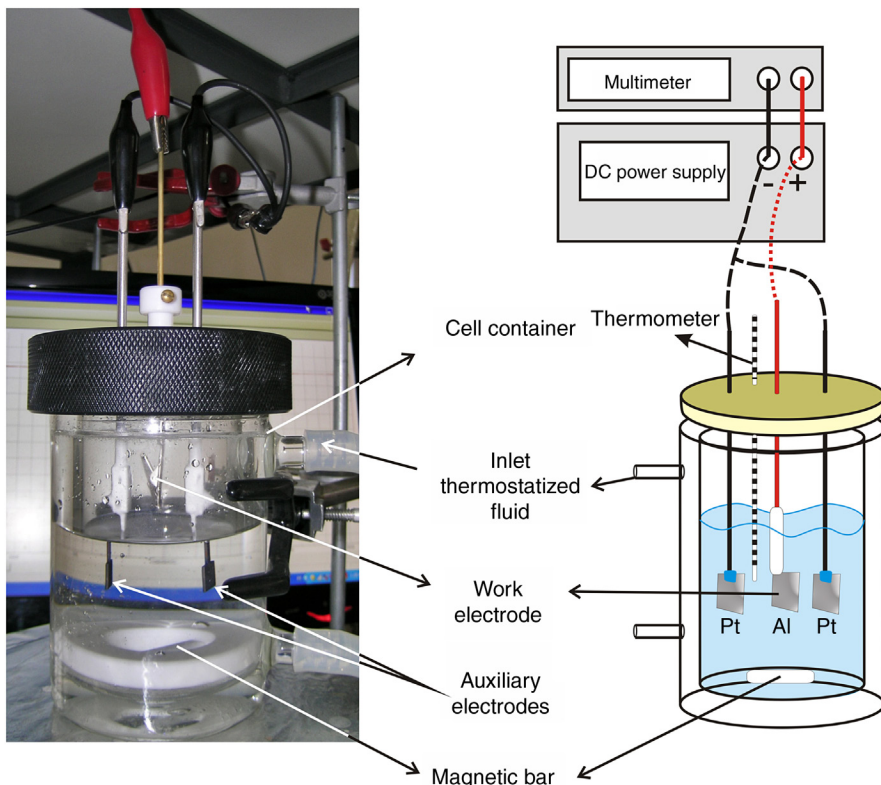


**FIGURE 3.4 Schematic representation of an electrochemical cell used for anodization.** Adapted from F. Trivinho-Strixino, J.S. Santos, M.S. Sikora, *Síntese Eletroquímica de Materiais Nanoestruturados [electrochemical synthesis of nanostructured materials]*, In: A.L. Da Róz, F.L. Leite, et al. (Eds.), *Nanoestruturas: Princípios e Aplicações*, vol. 1, Elsevier, Rio de Janeiro, 2015, pp. 63–110 (Chapter 3) [26].

Furthermore, the use of two counter electrodes placed parallel and symmetrically by the working electrode to maintain a homogeneous electric field at the faces of the electrode being anodized is common in this type of experiment. Fig. 3.4 shows a picture of this type of cell used for anodization.

The fundamental aspects of these two widely used electrochemical processes for the synthesis of nanostructured materials, namely, electrodeposition and anodic oxidation, are described in the following sections.

### 3.3 Synthesis of Nanostructured Films by Electrodeposition

Electrochemical reactions can easily be controlled by the potential applied to the electrolytic cell. These reactions take place at the interface between the electrode and the electrolyte and are stimulated by the gradients formed by the chemical and electric potentials of the species involved [28]. One of early models used for describing the electrode/electrolytic

interface is the Helmholtz model [28,29]. According to this model, the positive and negative species can be represented as a simple parallel-plate capacitor. Due to the simplistic nature of this model, other models were proposed for description of the charge distribution of the electrical double layer, as Gouy–Chapman and Stern models [28]. The Gouy–Chapman model considers the influence of the electrolyte and the applied potential on the capacitance of the double layer; consequently, the double layer is diffuse with a variable thickness. The Stern model is a combination of the previous models: the double layer is formed by a compact layer close to the electrode, and a diffuse layer that extends into the solution. Fig. 3.5 exhibits a refined model of the metal/electrolyte interface, considering the adsorption of fully and partially solvated ions on metal surface [29].

Fig. 3.5A illustrates the adsorption process of ionic species at the electrode surface. The potential variation as a function of the distance from the electrode surface, located at  $x = 0$ , is shown in Fig. 3.5B. In this figure, the plane parallel to the electrode located at a distance that passes through the center of the adsorbed ion is called the inner Helmholtz plane, whereas the parallel plane situated at a distance  $x_2$ , passing through the center of the fully dissolved ion, is called the outer Helmholtz plane. The distance between the electrode/solution interface at  $x = 0$  and the outer Helmholtz plane is called the electrical double layer and is represented schematically in the electrochemical cell of Fig. 3.5C.

During the electrodeposition, the working electrode is negatively polarized with respect to the reference electrode, so the positively charged metallic ions present in the electrolytic solution are attracted toward the metallic substrate and reduced to their metallic form at the electrode surface. The result is the formation of a compact film, dense and strongly adhered to the substrate, whose thickness can be monitored by the amount of charged consumed.

To control the process of electrodeposit fabrication at the nanoscale, it is necessary to know the fundamentals of the processes of nucleation, film growth, and kinetics of electrochemical reactions. These processes are influenced by a series of factors, such as the electrochemical technique used, the type of substrate, temperature, composition, and concentration of the electrolyte.

The first stage of metallic film formation is the nucleation of the metal, which tends to occur preferentially at regions of electrode surface containing defects and imperfections, such as grain contour regions, holes, inclusions, oxide layers, and adsorbed molecules [3]. Consequently, the presence of adsorbed impurities and the crystallographic structure and orientation of the substrate tend to influence the nucleation process, altering the characteristics of the formed film. Therefore, an adequate choice of substrate where the film will be deposited is of great importance. Among the materials most commonly used as working electrodes in electrodeposition are platinum [30–32], gold [33,34], copper [35,36], stainless steel [37–39], vitreous carbon [39–41], ITO [42,43], and FTO [44]. These materials exhibit chemical stability, good resistance to corrosion, ease to clean up surface, and possible functionalization of the surface for various applications.

The electrochemical reaction can be controlled through four types of mechanisms: charge-transfer reaction, diffusion, chemical reaction, and crystallization [45]. The

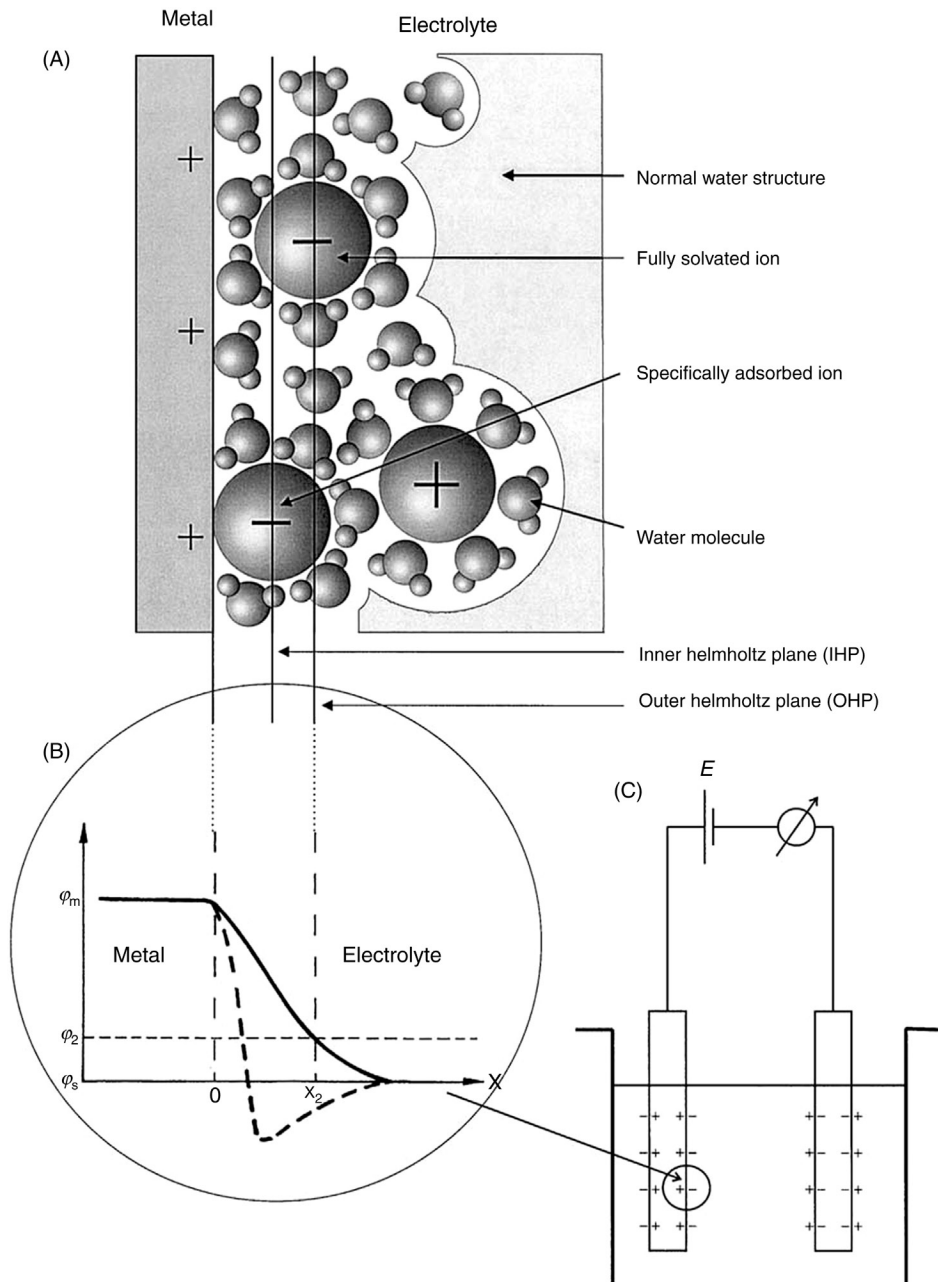


**FIGURE 3.5** The metal/electrolyte interface: (A) Adsorption process of the ionic species at the electrode surface. (B) Potential variation,  $\varphi$ , as a function of the distance,  $X$ . (C) Schematic representation of the electrical double layer in the electrochemical cell. [29]

charge-transfer reaction involves the transfer of charge carriers, such as ions and electrons, through the electrical double layer. In the case of diffusion, the species consumed or formed during the reaction are transported from the solution to the substrate interface and vice versa. Chemical reactions correspond to homogeneous reactions in solution or heterogeneous reactions at the electrode surface and do not involve charge transfer. Thus, they are not affected by the applied potential. In crystallization, atoms are incorporated into or removed from the crystal lattice of the metal being formed.

To select an electrolyte, one must consider the composition of the electrolytic bath, the pH, and the presence of additives since these factors can strongly affect the structure of the electrolyte/substrate interface, the charge, and mass transfer kinetics, as well as the kinetics of secondary chemical reactions that may occur simultaneously with the process. During the electrodeposition of certain metals, such as, cobalt, nickel, and iron, acid solutions containing sulfur and chlorine ions are commonly utilized to avoid passivation of the metal [46–48]. One example of additive use is during the electrodeposition of Co and Ni films and their alloys, which are normally carried out in an acid saline solution containing the metallic ion. Among the additives most used in the electrolyte in this process are boric acid and saccharin. In the former case, boric acid is used as a buffer during the electrodeposition of cobalt and nickel films. This prevents pH variation near the electrode surface and inhibits the formation of hydroxylated species that can precipitate together with the metallic film, forming a porous structure [49,50] and making the material unusable for technological applications. On the other hand, saccharin is used as an additive during electrodeposition of the Ni–Co alloy to decrease the internal tension and to reduce the grain size of the electrodeposits [48]. In the study performed by Mascaro et al. [44], glycerol was used as an additive to improve the crystallinity and to reduce the number of defects on Cu, In, Ga, and Se films deposited on the FTO substrate in acid medium.

The nucleation and crystallization processes are represented in Fig. 3.6. Nucleation (Fig. 3.6A) is a process characterized by the following stages: (i) diffusion of the ions onto the electrolyte/substrate interface, (ii) partial desolvation, (iii) adsorption in the substrate surface, and (iv) complete desolvation and nucleation [51]. Fig. 3.6B displays a possible ion attachment sites during the crystallization stage on a metallic surface with crystalline plane dislocation. In this case, when the ion at position (a) approaches the substrate, it can be incorporated into the following sites: on the crystal lattice, as an ad-ion (b), on a step (c), or in a corner (d) [51].

Another important variable that affects the electrodeposition process and the electro-deposited film properties is the electrolyte temperature, which interferes with the reaction speed, the diffusion processes, and the viscosity of the medium. However, it should be emphasized that in contrast with other methods used to fabricate nanostructured materials, electrochemical synthesis does not require high temperatures. Nanostructured films obtained by electrodeposition are generally produced at room temperature, although records can be found in the literature where such materials have been synthesized at temperatures ranging from 20–90°C [9,52,53].

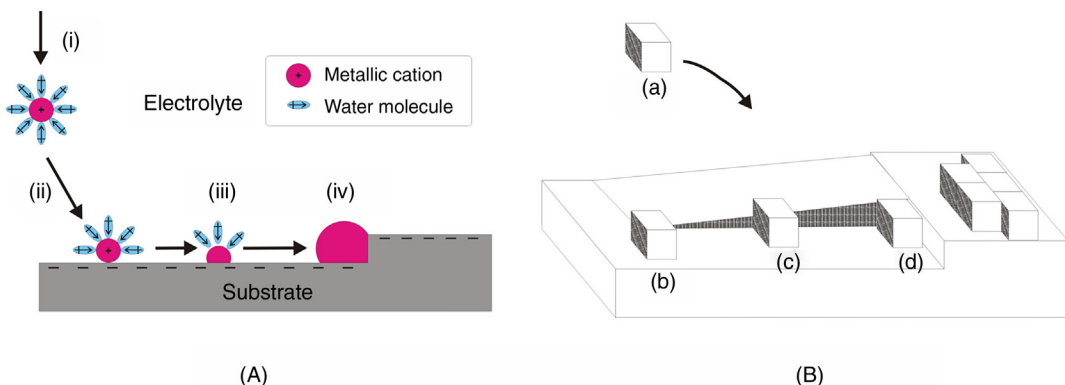


**FIGURE 3.6** Schematic representation of the (A) nucleation and (B) crystallization processes on a surface with crystal plane dislocation. Adapted from F. Trivinho-Strixino, J.S. Santos, M.S. Sikora, *Síntese Eletroquímica de Materiais Nanoestruturados [electrochemical synthesis of nanostructured materials]*, In: A.L. Da Róz, F.L. Leite, et al. (Eds.), *Nanoestruturas: Princípios e Aplicações*, vol. 1, Elsevier, Rio de Janeiro, 2015, pp. 63–110 (Chapter 3) [26].

Among the electrochemical techniques commonly used for electrodeposition are cyclic voltammetry, chronoamperometry, chronopotentiometry, and pulsed methods [45,54], which are chosen according to the type and properties of the desired material. Cyclic voltammetry is a potentiodynamic method, which involves the simultaneous variation of voltage and current. It consists of a triangular potential scanning within a specific interval and at a constant speed, while the current is monitored. Chronoamperometry is a potentiostatic method in which the voltage is kept constant, then the reactions tend to be limited by the applied voltage, and the observed response is the current variation as a function of time. Chronopotentiometry is a galvanostatic method in which the applied current density is fixed and the potential variation is observed during the process. Pulsed methods involve the application of current or voltage pulses over a specific time interval. The frequency of pulses can be controlled.

The film nucleation processes and growth kinetics will change depending on the technique used, leading to the formation of nanostructured electrodeposits with distinct properties and characteristics. Notably, these techniques do not provide morphological details of the film surface area and thickness, which can be monitored by complementary analysis techniques, such as, scanning tunneling microscopy (STM) and atomic force microscopy (AFM) [45,54]. As an example, Fig. 3.7A–B present STM and AFM images, respectively, of PbS films obtained by potentiostatic techniques under different experimental conditions. The corresponding rugosity variations in certain sample regions can be observed.

The electrochemical quartz-crystal microbalance (EQCM) is another technique that can be coupled with electrochemical techniques. This is an *in situ* method that provides information such as mass variation during the experiment, obtained from changes in oscillation frequency of the Pt- or Au-coated quartz crystal, generally used as a working

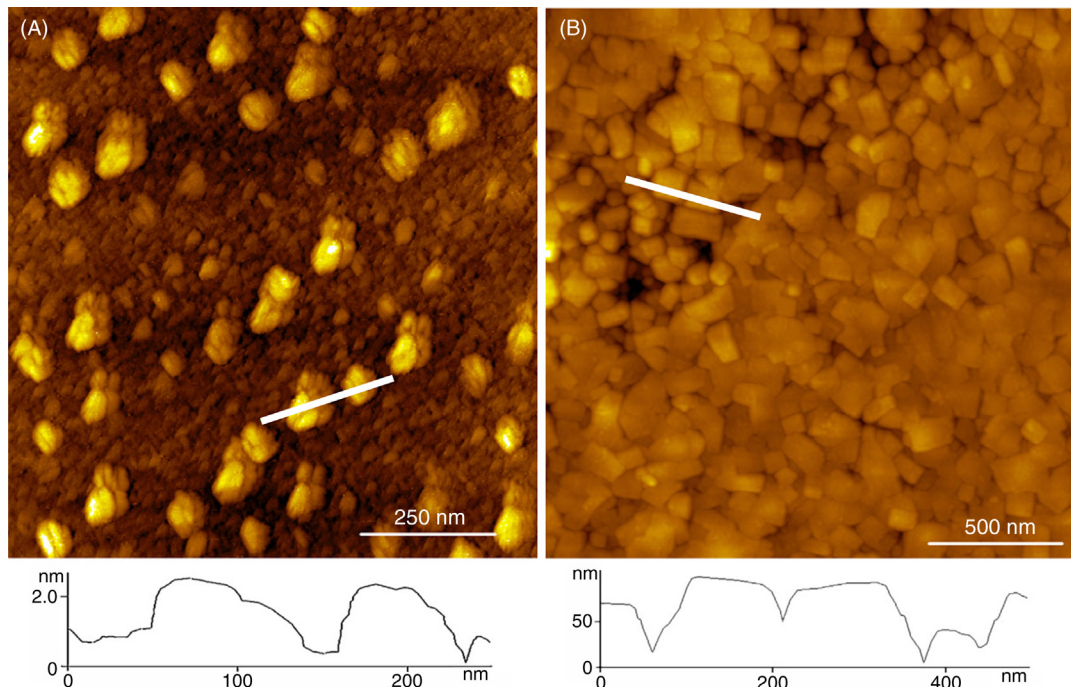


**FIGURE 3.7** Scanning tunneling microscopy (STM) (A) and atomic force microscopy (AFM) (B) images of the PbS surface on Au, obtained through potentiostatic deposition under the following conditions: (A) 6 min at 30°C and (B) 30 min at 90°C. The rugosity profiles corresponding to the film sections marked in white are shown at the bottom of each image [9].

electrode in this system [46,49]. Fig. 3.8 shows the results of cyclic voltammetry, illustrating the Co deposition process, followed by its oxidation and the corresponding mass variation on the electrode, as a function of the potential during experiments carried out at different pH values.

In addition to the formation of single-constituent metallic films, the electrodeposition technique also facilitates the formation of nanostructured films containing more than one type of metal, such as alloys [9,10,20,48,55] and multilayered films [15,16,56–58]. An alloy consists of a mixture of different compounds miscible in various proportions, which can be classified as a solid solution. On the other hand, the multilayered films correspond to a series of thin layers with thicknesses of a few nanometers, constituted by different metals. Due to small sizes of the alternating metallic layers, the resultant material acquires interesting properties that would not be observed if the same material were synthesized in larger dimensions [15,57]. Fig. 3.9 presents a cross-sectional image of a multilayered film obtained by transmission electron microscopy (TEM). The multiple layers are obtained through repetition of 10-nm-thick Cu and Ni nanolayers.

In the case of alloys, the electrolytic bath is composed of different salts containing the metallic ions that will be simultaneously deposited. As an example, in the codeposition

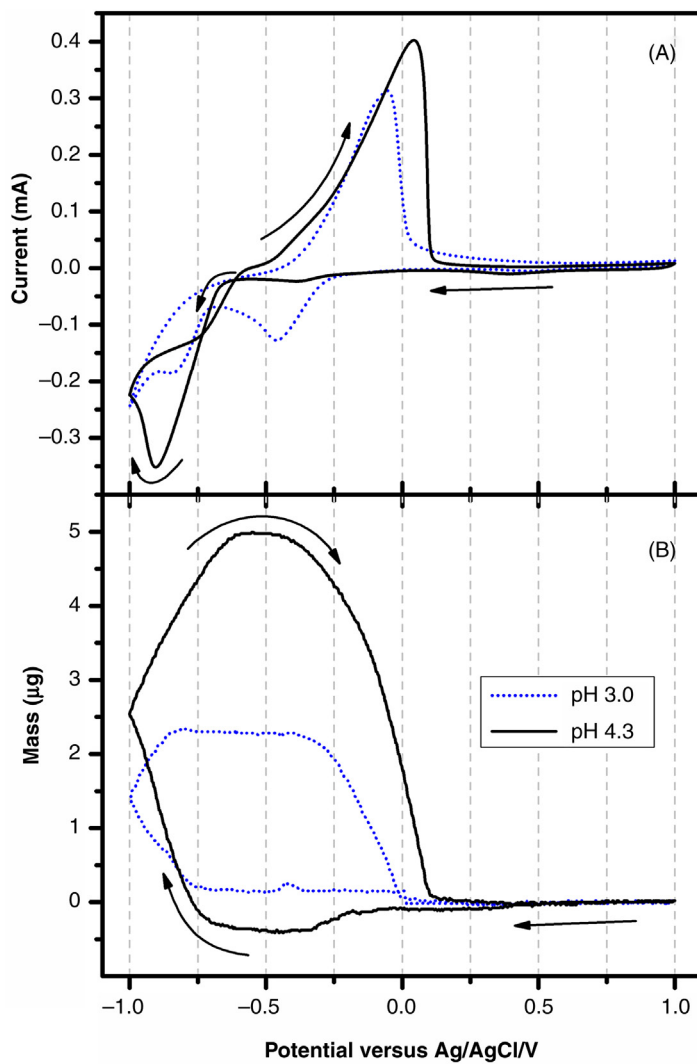


**FIGURE 3.8** (A) Cyclic voltammogram obtained in a solution containing  $0.01 \text{ mol L}^{-1} \text{ CoSO}_4 + 0.2 \text{ mol L}^{-1} \text{ Na}_2\text{SO}_4$  and (B) mass variation as a function of potential. Scanning rate =  $50 \text{ mV s}^{-1}$ . Adapted from F. Trivinho-Strixino, J.S. Santos, M.S. Sikora, *Síntese Eletroquímica de Materiais Nanoestruturados* [electrochemical synthesis of nanostructured materials], In: A.L. Da Róz, F.L. Leite, et al. (Eds.), *Nanoestruturas: Princípios e Aplicações*, vol. 1, Elsevier, Rio de Janeiro, 2015, pp. 63–110 (Chapter 3) [26].

process of nickel and cobalt ions for the formation of a Ni–Co alloy, Qiao et al. [48] used a solution containing salts of cobalt sulfate and nickel chloride, and boric acid as an additive. The final composition of the alloy is controlled by the ratio of the metallic ions in solution and the applied current. Comparing the alloys to their constituent materials in pure form, the alloys present certain properties that their individual constituents do not. Furthermore, an improvement in the mechanical, optical, and magnetic properties can be

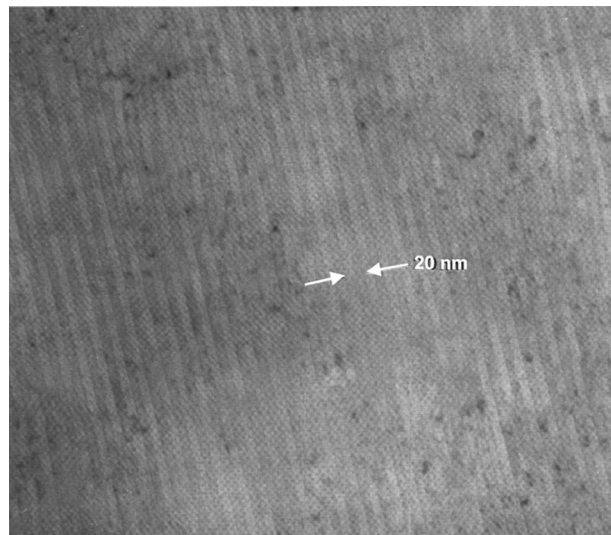


**FIGURE 3.9** Transmission electron microscopy (TEM) image of the cross section of a multilayered Cu and Ni film; each layer is 10 nm thick [58].

observed in the mixed material. Notably, it is not necessary that all constituents of an alloy be metals. Significant amounts of nonmetallic elements are also used in certain types of nanostructured alloys, such as  $\text{Bi}_2\text{Se}_3$  [20], CoNiP [55], PbS [9], and TiN [59] which are used in thermoelectric materials, magnetic devices, and optoelectronic devices.

In contrast with the process of alloy production, during the formation of multilayered films by electrodeposition, different cations that will form each layer are deposited separately, such that either a single electrolytic bath or two different and subsequent electrolytes can be used. In the former case, each layer is formed in the same electrolyte by controlling the applied voltage. This method can be used when the difference between the reduction potentials of the ionic species is large, and the electrolytes are similar. For example, nickel and copper can be deposited in acidic solutions containing both sulfide and sulfamate ions, and even then, the difference between their electrode potentials is 0.5 V. In the latter case, the layers are formed in different electrolytes, with the working electrode being removed from one solution after the formation of the first layer, and subsequent transferred to another electrolyte, where the deposition of a new layer will take place on top of the first one. This method is used when the reduction potentials of the different ions are very similar, and simultaneous deposition may occur. However, this approach may become impractical if the number of layers deposited is large.

Independently of the electrodeposition method, most multilayered films are formed by metallic compounds; they display a crystalline structure and preferential crystallographic orientation [56]. The first works about electrochemical synthesis of multilayers in the literature describe the magnetic properties of the systems Cu-Ni, Co-P, Co-W, and Co-Pt [56]. Recently, there has been great interest in the synthesis of these types of materials for

applications in fuel cells, using the systems Pt/Ir/Pt [15], Pt/Rh/Pt [16], and Pt/Bi/Pt [57] as substrate for the oxidation of small organic molecules, such as methanol. In comparison with traditional Pt electrodes, which are normally used for this type of application, the electrooxidation of methanol is much faster in the Pt/Ir/Pt multilayered films than for Pt electrodes, although both systems present the same electroactive area. This indicates a significant increase in the catalytic process efficiency [15]. Another interesting characteristic of this method is its great economy in the amount of reagent used to achieve a desired property. In the case of Pt, a significantly expensive noble metal, the use of this multilayer film offers great economic advantages.

In addition to metallic films, it is also possible to obtain metallic oxides by electrodeposition of the metal onto the substrate, followed by its oxidation. A negative potential is initially applied for the reduction of the ions in the solution; then, the polarization is inverted, applying a positive potential for the oxidation of the material previously deposited on the surface. An example of this method is the formation of zinc oxide on gold electrodes, obtained from the prior reduction of the  $Zn^{4+}$  ions present in a solution of  $ZnCl_2$  and KCl, and followed by the oxidation of metallic Zn into  $ZnO$  [60]. However, the most common form of electrochemical synthesis of oxides is the oxidation of the working electrode itself. This method, known as anodization, will be described in the following section.

### 3.4 Oxide Formation by Anodization of Valve Metals

The term “valve metal” has been used for a long time, but eventually, some confusion related to the nomenclature emerged in the literature because of the types of diodes used as “thermionic valves.” In fact, there was technological interest in developing alternatives based on semiconductor oxides for the already-discovered silicon-oxide-based devices. However, valve metal oxides exhibited high densities of structural defects that discouraged their application for electronic properties similar to those of silicon oxide. Therefore, it is more accurate to state that the nomenclature “valve metals” comes from their characteristic property as a group: the tendency to allow the passing of current in only one direction of the polarization. This is analogous to a hydraulic valve, whose flow can go only in one direction.

Some metals, including Ta, Nb, Al, Zr, Ti, Hf, Bi, Sb, and W, can be classified as valve metals: when they are cathodically polarized in the appropriate electrolytic solution, the current flows easily, whereas when it is polarized anodically, the current falls until it reaches a stationary state value [61]. Its surface is always covered by a thin oxide layer with a thickness of only a few nanometers. This layer is denominated native oxide, given that it forms spontaneously when the metal is exposed to a medium containing  $O_2$  or  $H_2O$  [62]. Other metals such as Be, Mg, Si, Ge, Ti, and U also form an insulating oxide layer under specific boundary conditions when anodically polarized, displaying very similar characteristics to those observed in valve metals. These metals present a tendency to form a highly resistive oxide film that protects the substrate when anodically polarized. The current decay during anodic polarization is due to the formation and growth of these oxides; this process is called anodic oxidization or anodization.

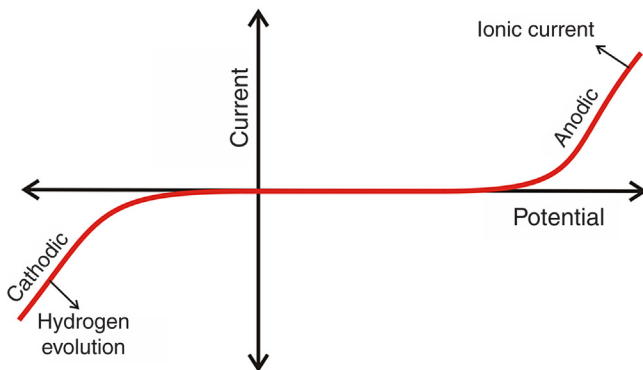


**FIGURE 3.10** Current versus voltage profile for a valve metal on which an oxide layer has already formed over the electrode. Adapted from F. Trivinho-Strixino, J.S. Santos, M.S. Sikora, *Síntese Eletroquímica de Materiais Nanoestruturados [electrochemical synthesis of nanostructured materials]*, In: A.L. Da Róz, F.L. Leite, et al. (Eds.), *Nanoestruturas: Princípios e Aplicações*, vol. 1, Elsevier, Rio de Janeiro, 2015, pp. 63–110 (Chapter 3) [26].

Fig. 3.10 shows a plot of the current as a function of potential for a valve metal with a previously formed oxide layer. The current increases rapidly in the direction of negative potentials, where the processes that allow the passing of current through the electrode/electrolyte interface are mostly related to and limited by the hydrogen evolution as water electrolysis. The behavior in this cathodic region depends on the duration of polarization, the method of preparation, and the nature of the oxide film. By contrast, the current going through the film during anodic polarization is small and cannot be reproduced until the voltage region where the ionic current begins to dominate over the electronic current. After this potential, the ionic current increases rapidly with the potential. Normally, the electronic current causes oxygen generation once the potential reaches values for which this process becomes thermodynamically favorable. Given that in most cases of valve metal anodization, the electric field is sufficiently large ( $10^6$ – $10^8 \text{ V m}^{-1}$ ) [63,64] to allow for preferential current passage of an ionic current, this behavior becomes time-dependent, since the thickness of the oxide film is continuously changing.

The characteristics of anodic oxide films are determined by the experimental conditions employed, such as the anodization regime, electrolyte composition and concentration, temperature, presence of dopant salts, microstructure and quality of the metal, previous surface treatment, and stirring of the solution. Regarding the anodization regime, there are two methods that can be employed for oxide production: potentiostatic and galvanostatic.

In the potentiostatic regime, the potential is kept constant during the process, and the observed response is the current variation as a function of time. In this case, the system energy is kept constant such that the processes tend to be limited by the applied potential. The current through the system tends to decrease up to a stationary value. This current decrease is related to the formation of a compact oxide layer over the electrode that increases the local electrical field intensity. Thus, the kinetic energy of the process is not held constant. Eventually, the observed growth rate of the oxide is so small that the film thickness can be considered to have reached a limit value. The total current associated

with this stage may or may not be small, given that it corresponds to the sum of the ionic and electronic currents. Therefore, the limit thickness hypothesis is acceptable in most cases. The idea of a limit thickness that is “proportional” to the applied voltage was transformed into a parameter commonly found on synthesis of anodic oxides, expressed in angstroms per volt ( $\text{\AA V}^{-1}$ ), and is related to a fully-formed film. This parameter may have practical applications during the experimental parameters selection for the synthesis, however its limitations must be known. Parallel electrochemical reactions that simultaneously occur during the formation of oxides are not considered, such as, oxygen generation and release or the combustion of organic compounds from the electrolyte. These reactions are known to consume charge during the anodization and to alter the kinetics constants of the overall process.

In the galvanostatic method, the oxide is grown by application of a constant current density, and the observed response is the potential as a function of time. In this method, it is possible to monitor oxide growth by observing the different processes occurring during synthesis. The growth rate is kept constant and the system is free to reach a stationary state characterized by a plateau in the potential versus time curve. As mentioned previously, the metallic substrate always presents an inhomogeneous thin film of native oxide, formed as soon as the metal is exposed to an oxygen-rich atmosphere. In this context, the heterogeneities of the oxide film play an important role because the electric field is inversely proportional to the film thickness. In other words, the oxidation reaction of the metal occurs locally, and the number of active areas is proportional to the applied current. Hence, in this constant current method, oxidation processes are more difficult to control and prevent local disruption of the formed oxide layer over the electrode.

The films produced by these two methods present significantly different characteristics. In the potentiostatic regime, the beginning of the process is marked by an increase in the electric current due to the metal oxidation. Nonetheless, as the oxide thickness increases, the current decreases until reaching a stationary value. If the electrolyte used is able to dissolve the oxide, there may be a competition between the oxide formation and dissolution reactions, leading to the formation of a highly ordered structure if a narrow window of specific experimental parameters are employed. This type of anodization is often applied in the synthesis of oxides with highly organized structures, such as porous anodic alumina (PAA), commonly used in templates for nanostructures, and  $\text{TiO}_2$  nanotubes, widely utilized in photocatalysis.

By contrast, in the galvanostatic method, the potential grows almost linearly at the beginning of the process, due to the formation of a barrier oxide film. The high electric field (approximately  $10^6\text{--}10^8 \text{ V m}^{-1}$ ) achieved during the anodic oxidation of these metals exceeds the critical values for electric breakdown in dielectric materials [63]. Therefore, the probability of a dielectric breakdown during the growth of these oxides is high. The dielectric breakdown observed during anodization under high electric field is also known as electrolytic breakdown. Thus, after reaching a critical thickness value, the electrolytic breakdown of the film takes place, characterized by potential oscillations resulting from localized oxide destruction and reconstruction processes [63]. Under those conditions, the formation of electric discharges on the electrode surface due to the intense localized

electric field is also observed. If the anodization time is relatively long, the potential fluctuations tend to stabilize, and the potential begins oscillating about a mean potential value, reaching a steady-state in which the rates of oxide film dissolution and reconstruction processes become constant. With this method, it is possible to obtain a porous crystalline material, although with a low pore ordering degree. Consequently, there is little interest in using this material for technological applications requiring a large available surface area, and this type of material is more commonly used as coatings.

A more detailed description of these anodization methods, synthesis conditions, influence of experimental parameters on the oxide film properties, and applications will be presented in the following sections.

### 3.4.1 Anodization Under High Electric Field

The process for obtaining anodic oxides by anodization under high electric field has received different names throughout time. Currently, the most common terms used are “Hard Anodization,” [65] “Spark Anodization,” [66,67] “Micro-Arc Oxidation,” [68,69] and “Plasma Electrolytic Oxidation” [70,71]. Normally, the term “Hard Anodization” is applied to the anodization of metals under high electric fields without reach the dielectric breakdown potential. This method is widely utilized for obtaining thick anodic oxides with self-organized structures, such as PAA and  $\text{TiO}_2$  nanotubes films. By contrast, the terms “Spark Anodization,” “Micro-Arc Oxidation,” and “Plasma Electrolytic Oxidation” refer to the anodization technique in which the oxide growth reaches the dielectric breakdown potential. In this case, the energy released is dissipated as heat and light that can be observed as electric discharges on the electrode surface. Depending on the emission characteristics and the experimental conditions, the electric discharges are classified as glow, spark, microdischarge, microarc, or arc [70–73]. This is the origin of the different names usually found for this technique.

[Fig. 3.11](#) shows current versus voltage curves corresponding to the different types of electric discharge observed in the anodization process [64]. According to Yerokhin et al. [64], the current versus voltage profile for type-A metals is observed in metals that do not form passive films, whereas the type-B profile is characteristic of metals that undergo passivation, such as, valve metals. Both systems obey Faraday's law at the beginning of the process; however, when the potential increases, a deviation from this behavior can be observed in both systems. The current increase with the potential is accompanied by the formation of electric discharges in the material. Nonetheless, for type-A metals, this current increase is limited by the gas evolution reaction along the surface of the metal, and the electrode is enveloped in plasma. A current drop due to the stabilization of the cloud surrounding the electrode is observed, and the electrical arcs are formed after the system reaches  $E_3$ . For type-B metals, the behavior is more complex. Initially, there is formation of the passive film, also known as a barrier film. However, after reaching the potential  $E_4$ , if the electrolyte is able to dissolve the oxide being formed, the dissolution process begins to compete with the oxide growth reaction, resulting in the formation of a porous oxide film.

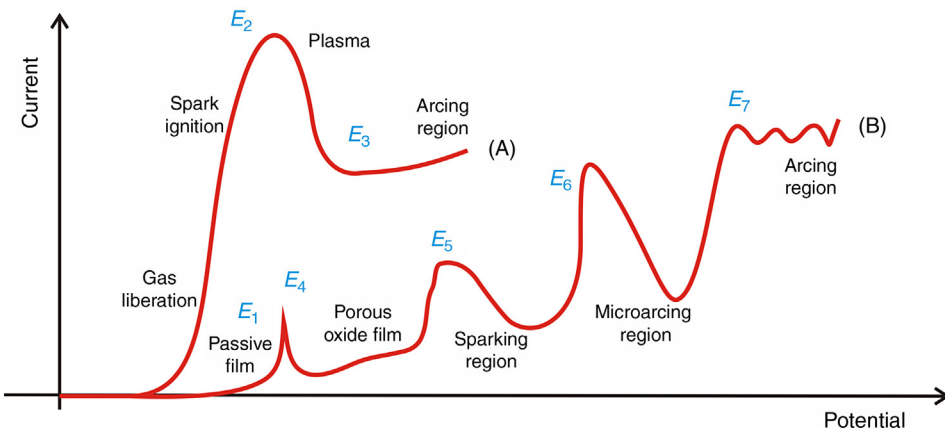


**FIGURE 3.11** Types of electric discharge observed in PEO processes (A) in the near-electrode area and (B) in the dielectric film on the electrode surface. Adapted from A.L. Yerokhin et al., *Plasma electrolysis for surface engineering*, *Surf. Coat. Technol.* 122 (2–3) (1999) 73–93 [64].

After the potential  $E_5$ , the electric field reaches a critical value, and there is a rupture of the oxide due to the ionization processes by impact or tunneling [64]. At this point, electric discharges (sparks) begin to appear along the entire surface of the electrode until reaching the potential  $E_6$ , at which point the longest-lasting electric microarcs begin to emerge on top of the electrode. After the potential  $E_7$ , once the system reaches the electric arc regime, the electric microarcs become larger, more intense and last longer and may have destructive effects on the oxide film (*thermal cracking*) [64].

Due to their characteristic electric, thermal, and wear resistance [74–76], materials fabricated using this technique have a variety of applications, mainly in the aerospace, textile, electronic, automotive, and biomedical industries [64,77–80]. These materials present various morphologies, which strongly depend on the experimental growth conditions of these films. A porous structure may form if the electrolyte used can dissolve the oxide being formed in an active oxide dissolution steady state. The diameter of these pores may vary from the nanometric to the micrometric scale.

Another remarkable characteristic of materials fabricated using this technique is the crystallization of the oxides films during their growth, forming crystallites with different sizes, depending on the anodization conditions employed [67,81]. The reason of film crystallization in PEO process has been extensively discussed in the literature [63,70,82–85]. There are two main theories that aim to explain the crystallization process of these materials. The first one ascribes crystallization to the compressive stress generated by the oxide growth [82,83]. The second one states that the electric discharges are responsible for the localized heating of the films, which would be the factor responsible for the oxide crystallization in regions neighboring the discharges sites [70,84,85].

With the advancement of experimental technologies, such as high-time-resolution signal acquisition, high-speed cameras, and optical emission spectroscopy equipment,

extensive development has been observed in the research, classification, and understanding of these phenomena [66,86]. In spectroscopic studies, Hussein et al. [85] observed a wide variation in the values of the plasma temperature of discharge events, ranging from  $4,500 \pm 450\text{K}$  to  $10,000 \pm 1,000\text{K}$ . Dunleavy et al. [87] attributed the wide temperature range to the existence of two distinct regions of plasma: a central nucleus at high temperature ( $\sim 16,000 \pm 3,500\text{K}$ ) with a high electronic density ( $N_e \sim 5 \times 10^{17} \text{ cm}^{-3}$ ), and a surrounding region extending in the direction towards the electrolyte, with a lower temperature ( $\sim 3,000\text{--}4,000\text{K}$ ) and electronic density ( $N_e \sim 10^{15} \text{ cm}^{-3}$ ). Computer modeling techniques have also been applied to investigate these phenomena. For example, Sikora et al. [88] used finite-element methods to simulate the effects of heat propagation from an electric discharge produced by a rupture event at a  $\text{TiO}_2$  pore and found that the heat propagation area is proportional to the spark temperature and the oxide thickness.

The anodization process under conditions of electrolytic breakdown (PEO) can be monitored through the galvanostatic anodization curves described by the potential variation as a function of time or applied charge. As an example, Fig. 3.12 presents the galvanostatic anodization curve of titanium in phosphoric acid, where the variation of the potential as a function of applied charge can be observed. At the beginning of the process (Region 1), a linear increase in the potential with the applied charge ( $q = I \times t$ ) can be observed, up until the beginning of the electrolytic breakdown of the film. The potential at which these oscillations begin is known as the breakdown potential [63]. Electrolytic breakdown is characterized by the appearance of the potential oscillations, resulting from localized rupture processes, growth, and dissolution of the oxide. In Region 2, the amplitude of the oscillations increases, and there is a decrease in the angular coefficient

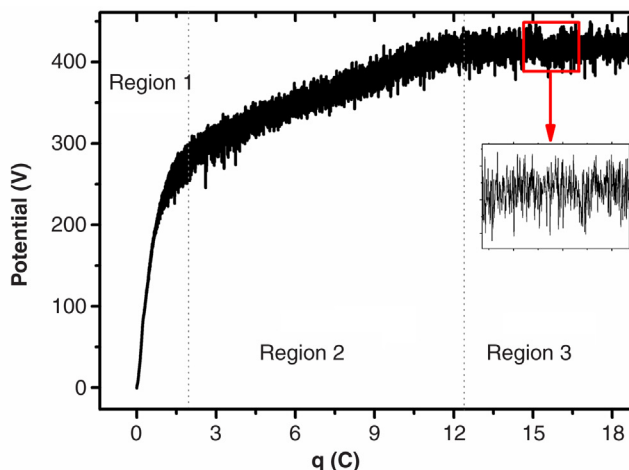


**FIGURE 3.12** Galvanostatic anodization curve for titanium in  $0.5 \text{ mol L}^{-1} \text{H}_3\text{PO}_4$  obtained at  $20 \text{ mA cm}^{-2}$  and  $T = 20^\circ\text{C}$ . Adapted from F. Trivinho-Strixino, J.S. Santos, M.S. Sikora, *Síntese Eletroquímica de Materiais Nanoestruturados [electrochemical synthesis of nanostructured materials]*, In: A.L. Da Róz, F.L. Leite, et al. (Eds.), *Nanoestruturas: Princípios e Aplicações*, vol. 1, Elsevier, Rio de Janeiro, 2015, pp. 63–110 (Chapter 3) [26].

$(dV/dq)$  of the anodization curve. In Region 3, the potential oscillations stabilize around a mean value.

The initial voltage increase is attributed to the enlargement of oxide thickness, which increases the resistive characteristics of the oxide layer. A high resistance of oxide film increases the potential and the local electric field. The potential at the oxide/electrolyte surface is given by [70]:

$$E = E_0 - IR \quad (3.5)$$

where  $E_0$  corresponds to the potential difference applied externally;  $R$  represents all the resistances in series within the system (contacts, electrolyte, film resistance, etc.); and  $I$  is the current applied to the system. Given that the current is kept constant during the entire process, the potential rises due to the increase in film resistance. This growth refers to the thickness increase or the decrease in the metallic area exposed to the material, as follows [70]:

$$R = \frac{\rho l}{A} \quad (3.6)$$

where  $\rho$  is the specific resistivity of the film,  $l$  is the thickness, and  $A$  is the surface area of the material. After this region of linear potential increase, where a high potential value is reached, potential oscillations can be observed. In this process, the appearance of spark discharges is observed at the electrode surface. This phenomenon can be observed on the surface of the titanium electrode during anodization in phosphoric acid, as can be seen in Fig. 3.13.

The potential oscillations are described in the literature as being a result of the film destruction and reconstruction processes [63]. As previously discussed, the potential increases due to the film thickening, therefore the angular coefficient  $dV/dq$  can also be described as the oxide film growth rate (anodization rate). In steady-state, the dissolution



**FIGURE 3.13** Titanium electrode surface before anodization under external lighting (A) and during anodization in  $0.5 \text{ mol L}^{-1} \text{ H}_3\text{PO}_4$ ,  $20 \text{ mA cm}^{-2}$  and  $T = 20^\circ\text{C}$ , in the absence of lighting. The images shown in (B) and (C) were acquired in Region 2 of the anodization curve (Fig. 3.12) Adapted from F. Trivinho-Strixino, J.S. Santos, M.S. Sikora, *Síntese Eletroquímica de Materiais Nanoestruturados* [electrochemical synthesis of nanostructured materials], In: A.L. Da Róz, F.L. Leite, et al. (Eds.), *Nanoestruturas: Princípios e Aplicações*, vol. 1, Elsevier, Rio de Janeiro, 2015, pp. 63–110 (Chapter 3) [26].

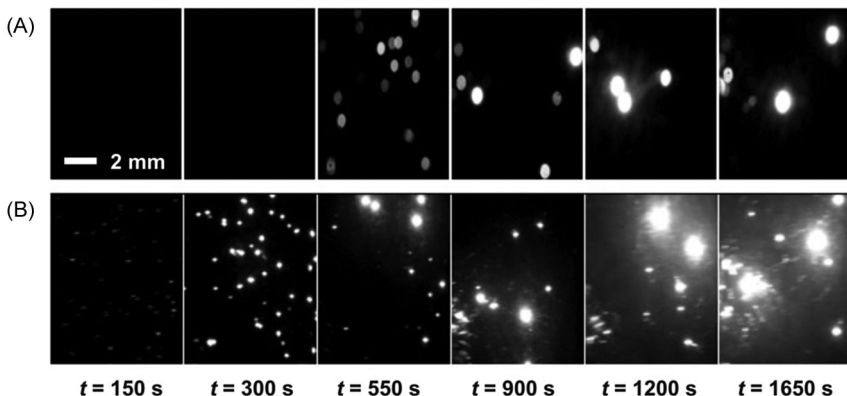


**FIGURE 3.14** Images of the electrode surface at different galvanostatic anodization stages of Zr at 20 mA cm<sup>-2</sup> in solutions of (A) 0.5 mol L<sup>-1</sup> H<sub>3</sub>PO<sub>4</sub> [1] and (B) 0.5 mol L<sup>-1</sup> H<sub>2</sub>C<sub>2</sub>O<sub>4</sub>. Adapted from J.S. Santos et al., Characterization of electrical discharges during spark anodization of zirconium in different electrolytes, *Electrochim. Acta* 130 (2014) 477–487 [66].

and growth processes of oxide film reach a constant diffusion rate due to the equivalence of the formation and dissolution rates, remaining in this condition until the end of the experiment. Depending on the metal and the experimental conditions, changes in the anodization rate, the amplitude of the potential oscillations, the oxide electrolytic rupture potential, and the spatial pattern of the electric discharges can be observed. Fig. 3.14 shows images of the Zr electrode surface during galvanostatic anodization at 20 mA cm<sup>-2</sup> in phosphoric acid and oxalic acid, where changes in the spatial distribution, sizes, and intensity of the electric discharges can be observed during the anodization.

The materials obtained through the PEO technique display different morphologies. A porous structure may be formed if the oxide is soluble or partially soluble in the electrolyte because the channels for electric charge propagation constitute the preferential sites for pore formation. If the oxide is not soluble in the electrolyte, the formation of a compact oxide film with fissures may occur due to the film breakdown [63]. In addition, the incorporation of electrolyte anions into the film affects the electrolytic breakdown process [89] and can also modify the morphology of the material. In acidic electrolytes, for example, the anionic incorporation tends to be favored, independently of the value of the applied current. This intensifies the breakdown process and leads to the formation of a porous structure if the oxide is soluble in the electrolyte.

In neutral and alkaline electrolytes, the oxide dissolution mechanism changes depending on the value of the applied current, and a homogeneous dissolution may occur. This leads to the formation of a pore-free barrier film with fractures throughout the surface. In porous films, depending on the experimental conditions, the pore size can change from a few nanometers up to a few micrometers. Fig. 3.15 shows micrographs obtained by scanning electron microscopy (SEM) of TiO<sub>2</sub> films prepared via PEO in phosphoric acid. The SEM images were obtained at different stages of the experiment.

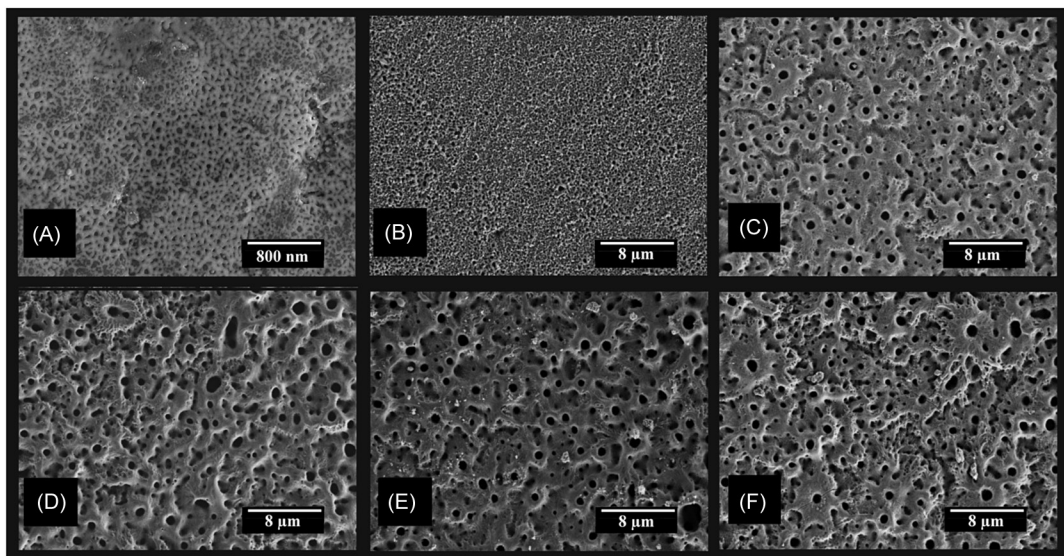


**FIGURE 3.15** SEM micrographs of the surfaces of  $\text{TiO}_2$  films obtained by PEO in  $0.3 \text{ mol L}^{-1} \text{ H}_3\text{PO}_4$ , after application of the following charges: (A) 1.8 C, (B) 4.6 C, (C) 25 C, (D) 108 C, (E) 180 C, and (F) 216 C [63].

One of the advantages that the PEO technique has over low-voltage anodization is the formation of a thick film with high mechanical resistance and crystallinity. These films are widely used as coatings in technological applications and as protection against corrosion. By contrast, materials obtained using this technique display a low degree of ordering and a variety of pore sizes at the same sample; for this reason, these oxide films prepared under high electric field are rarely explored in applications that demand well-ordered structures with high superficial area as photocatalysis or template formation. Nonetheless, one study can be found in the literature describing the photocatalytic properties of  $\text{TiO}_2$  in films produced by PEO from titanium in a phosphoric acid solution [67]. In that study, the authors observed the influence of morphology and the microstructure on the photocatalytic activity of the oxide, by analysis of the degradation of methyl orange dye. Their results demonstrated that when the number of pores was high the photocatalytic activity improved as a consequence of the increase in surface area. Also, the most relevant result revealed that the crystallite size strongly influenced the photocatalytic activity of  $\text{TiO}_2$  films since the grain boundary conditions acted as electron-hole recombination centers. This demonstrated that the photocatalytic activity is proportional to the sample crystallite size. The authors presents in this study the viability of using  $\text{TiO}_2$  films produced via PEO as an alternative to the traditional  $\text{TiO}_2$  nanotubes, which are normally used for this purpose but require a longer synthesis time and a subsequent thermal treatment for the film crystallization. A more detailed description of the electrochemical synthesis of  $\text{TiO}_2$  nanotubes will be presented in Section 3.4.3

One way of controlling the electric microdischarges to avoid superheating and localized destruction of the oxide film structure in the galvanostatic regime, is the use of an

alternating [90] or a pulsed current [85,91]. On the potentiostatic regime, by contrast, this control can be achieved by the application of a pulsed voltage. The choice of potential values depends on the characteristics of the desired oxide [92–94]. These methods, known also as *pulsed anodization* [93], constitute an alternative method because the potentiostatic method—mostly used to produce nanotubes and nanopores—requires a long anodization time, whereas the galvanostatic method, although faster, produces disordered porous structures and, in some cases, the local disruption of the oxide. Choosing an adequate pulse sequence, it is possible to control the composition, microstructure, and morphology of the oxide film.

### 3.4.2 Self-Organization in Anodic Oxides: PAA

Aluminum anodization is a widely explored process of great commercial impact. It represents one of the most important methods used to synthesize ordered nanostructures that exhibit an array of hexagonal cells containing nanopores in their centers [95] (Fig. 3.16). In general, aluminum anodization promotes the formation of two types of  $\text{Al}_2\text{O}_3$  (alumina) films: barrier-type oxide films and porous oxide films. The main factor that determines this type of growth on an Al surface is strongly related to the nature of the electrolyte being used [27,96,97]. Basically, the formation of barrier-type aluminum oxide is enabled by boric acid, ammonium borate, ammonium tartrate, phosphate aqueous solution, tetraborate in ethylene glycol medium, perchloric acid and ethanol, and organic electrolytes such as citric, succinic, and glycolic acid electrolytic solutions [97–100]. By contrast, obtaining porous oxide film requires the use of strongly acidic electrolytes; the oxide must be an effective solubility in the acid solution. Thus, the production of porous anodic alumina (PAA) is associated with an active and localized dissolution effect where the pores will originate.

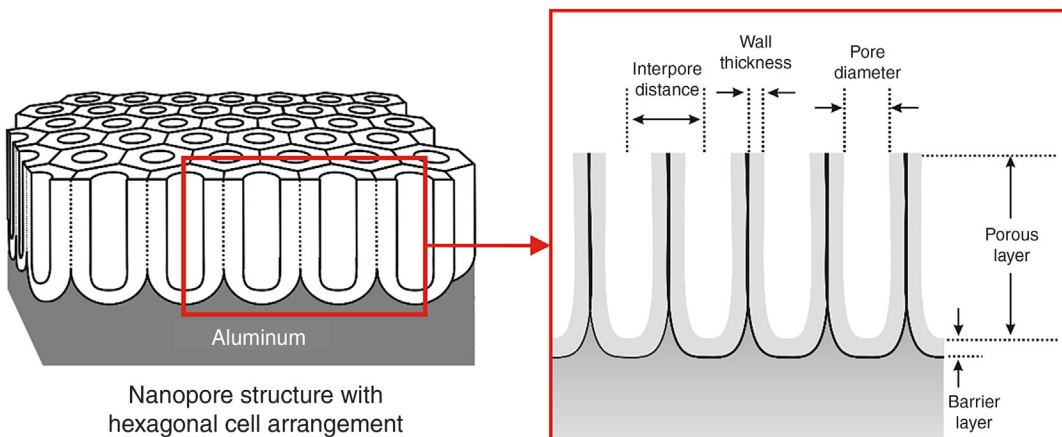


**FIGURE 3.16** Schematic representation of the hexagonal configuration of the self-organized porous anodic alumina (PAA) cells, grown on aluminum surface. Adapted from F. Trivinho-Strixino, J.S. Santos, M.S. Sikora, *Síntese Eletroquímica de Materiais Nanoestruturados* [electrochemical synthesis of nanostructured materials], In: A.L. Da Róz, F.L. Leite, et al. (Eds.), *Nanoestruturas: Princípios e Aplicações*, vol. 1, Elsevier, Rio de Janeiro, 2015, pp. 63–110 (Chapter 3) [26].

Normally, phosphoric acid or oxalic acid aqueous solutions are employed, although other electrolytes with the same described characteristics can also be used [95]. Another important factor for obtaining highly ordered layers of porous alumina is the anodization time. Anodization carried out during long periods allows the process to reach a steady-state where the oxide formation/dissolution processes stabilize. This promotes the growth of deep and well-organized pores [95].

The self-organized PAA obtained by Al anodization can be represented schematically by a compact array of hexagonal cells, with pores inside the cells, as illustrated in Fig. 3.16. The high ordering degree of the nanostructures and their morphology are described by geometric parameters, such as pore diameter, wall thickness, barrier layer thickness, and distance between pores (cell diameter). A uniform pore diameter—a factor that is strongly dependent on the experimental conditions of anodization—can vary from a few to several hundred nanometers. The depth of the pores' parallel channels can exceed 100  $\mu\text{m}$ , depending on the synthesis conditions [101]. Compared with other nanostructured fabrication techniques, this is one of the features that make PAA one of the most desired nanostructures with a high pore depth/diameter ratio, as well as a high nanopore density that can be obtained.

The growth of the oxide layer occurs at the metal/oxide interface at the pore base and involves the conversion of a preexisting barrier-type surface through a porous oxide layer. The pore formation mechanism can be briefly described as follows [101]: during growth of the porous oxide, a thin and compact barrier layer located at the pore base and in contact with the oxide/electrolyte interface is continuously dissolved by the action of the increasing local electric field. This process results from the increased resistance to the passage of excess current through the oxide formed. Simultaneously, there is a continuous formation of a new barrier oxide layer at the metal/oxide interface. The film growth in the steady-state requires equilibrium between the oxide growth rate and its dissolution rate at the bottom of the pores. In practice, what occurs is the consumption of aluminum oxide at the nanopore base simultaneously with the formation of additional oxide at the metal/oxide interface. The result is the erosion of the aluminum metal being consumed to form the oxide, and the penetration of the channels inside the oxide, originated by an active dissolution at the oxide bottom. In materials science, this phenomenon can be classified as a *top-down* design technology. Nonetheless, the origin of the self-organization is related to the precise control of the oxide formation and dissolution processes, so that the terms *bottom-up* and *top-down* can both be used in those cases, respectively. Various published works present proposals for mechanisms for the formation of self-organized anodic alumina hexagonal molecules [63,98,101–106].

Self-organized aluminum oxide cells can be easily fabricated by aluminum anodization under potentiostatic or galvanostatic regimes [101]. However, other anodization regimes, such as the hybrid pulsed methods, are also described in the literature and present advantages [93,107–109]. A typical growth transient curve for this oxide, analyzing the current or potential as a function of anodizing time, can be observed in Fig. 3.17. When a constant current is applied during the growth of porous alumina (constant current plot in Fig. 3.17), the measured potential increases linearly with time up to a maximum value.

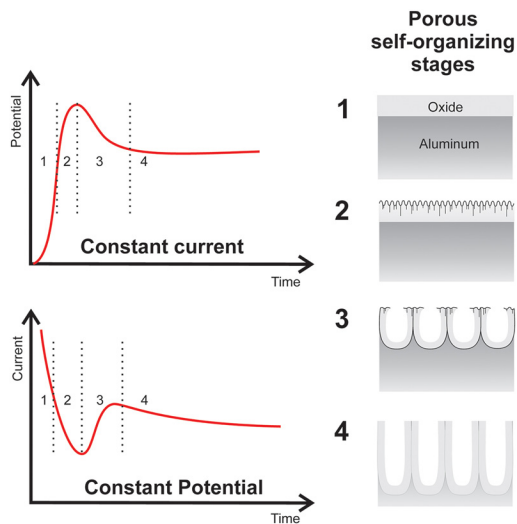


**FIGURE 3.17** Anodization curves illustrating the growth kinetics of anodic alumina under galvanostatic (constant current) and potentiostatic (constant potential) regimes, and related stages of porous oxide growth: (1) barrier film growth, (2) formation of pore precursors, (3) pore formation, and (4) pore growth. Adapted from F. Trivinho-Strixino, J.S. Santos, M.S. Sikora, *Síntese Eletroquímica de Materiais Nanoestruturados* [electrochemical synthesis of nanostructured materials], In: A.L. Da Róz, F.L. Leite, et al. (Eds.), *Nanoestruturas: Princípios e Aplicações*, vol. 1, Elsevier, Rio de Janeiro, 2015, pp. 63–110 (Chapter 3) [26].

Then, it gradually decreases until reaching a stationary potential. During the initial period (stage 1 in Fig. 3.17), the potential increase is associated with the linear growth of a highly resistive compact film (barrier film). Subsequently, the appearance of individual penetration channels occurs in the barrier layer (pore precursors, stage 2 in Fig. 3.17). The barrier film breaks at the maximum potential (stage 3 in Fig. 3.17), and the porous structure begins to form. Finally, the steady-state growth of the porous alumina continues (stage 4 in Fig. 3.17), and the potential becomes constant [101].

Currently, the potentiostatic method is preferred over the galvanostatic method for the fabrication of highly organized PAAs with precise control of the pore diameter. The current density decreases rapidly at the beginning of the PAA potentiostatic formation process (constant potential plot in Fig. 3.17), and immediately afterward, a minimum is reached. A linear increase of current follows up to a local maximum. After this maximum, the current smoothly decreases until the steady-state region, where the formation of the porous oxide proceeds (Fig. 3.17). When the system reaches this stage at which the value of the differential  $dj/dt$  decreases, the pore formation enters the steady-state regime. The self-ordering pore formation process directly depends on the anodization conditions. In general, the onset of pore formation, i.e., the current minimum, decreases with the increase in electric field. Therefore, the current minimum is usually low for anodization performed at high potential. The decrease in the observed current minimum is also verified in concentrated acid solutions [101].

Most anodic films are directly dependent on the applied potential. In addition, during oxide growth in the steady-state regime, both the current and potential measured during potentiostatic and galvanostatic anodization remain constant. Therefore, the anodic film morphology can be controlled by the anodization parameters. According to Sulka [101], the concentration and pH of the electrolyte, the potential, the anodization time, and the pore-widening time at the end of anodization, are parameters that directly influence the pore diameters in alumina films grown in the potentiostatic regime.

There are, in general, two PAA fabrication methods that can be used as templates: nanoindentation and two-step anodization (Fig. 3.18) [95,101]. It is also possible to apply lithographic methods [110]. In the first method, the anodization is performed on top of a prepatterned plate previously marked by nanoindentation, in order to guide and form a perfectly ordered network of nanopores during anodization. The second method consists of growing the oxide film on the metal during a sufficiently long time interval to mark the aluminium surface under the pore base. After finishing the first anodization, the formed oxide layer is chemically removed from substrate. Then, the film is anodized again under either the same or different conditions as the first anodization step. An aluminum metallic structure with marks at the nanoscale emerges after the oxide removal. This process aids and orients the formation of self-organized nanopores in the second anodization stage (Fig. 3.18).

The fabrication of alumina membranes with self-organized nanopores obtained from aluminum anodization is a multistage process. It involves the pretreatment of the substrate, the anodization process, and subsequent posttreatments related to the nanomanipulation of the templates, aiming toward the desired application. Thus, various aspects related to the adequate manipulation of nanoporous films must be verified to separate the oxide membrane from the metallic substrate without damaging it. One can also subsequently open the pore base to turn the structure into a nanosieve that can be used to fabricate a mold or other nanostructured materials.

The quality and purity of the aluminum substrates and the previous treatment of the surface significantly influence the self-organized pore formation process. The structure of the preexisting oxide film on the metal surface, which can be formed by exposure to air during chemical or electrochemical treatment, depends on the type of pretreatment employed. During aluminum anodization, the nucleation process of the self-organized pores depends on the defects present on the metal surface, such as imperfections and grain boundaries. The surface pretreatment procedure must have as a goal reducing the presence of these structural and surface defects. Thus, the ideal substrate for initiating the formation of self-organized nanopores must be high purity aluminium and must also have been previously processed by a thermal treatment to remove surface stress and increase the grain size.

The pretreatment procedure consists of a thermal treatment known as *annealing* of the aluminum metal, in the absence of oxygen and at high temperatures to relax the metal crystalline structure and remove structural stress [101]. In some cases, the *rapid thermal annealing* technique can be employed, which consists of applying a thermal

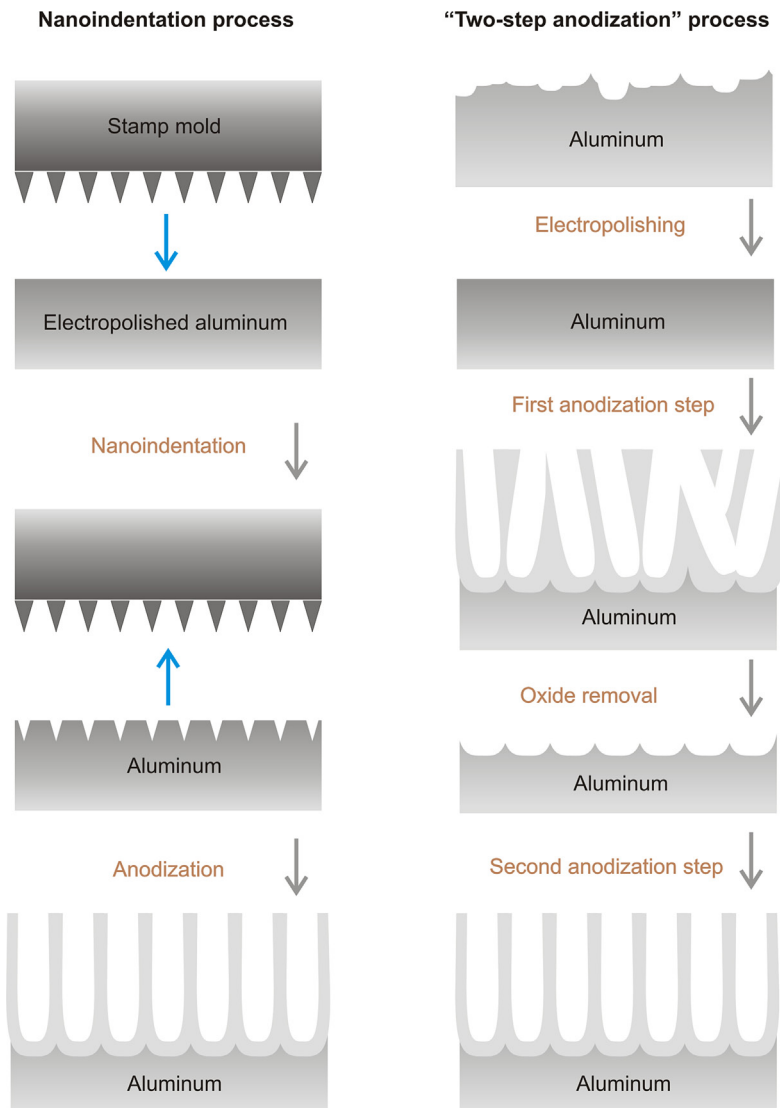


**FIGURE 3.18** Illustration of the two most common processes for the fabrication of nanoporous alumina. Adapted from F. Trivinho-Strixino, J.S. Santos, M.S. Sikora, *Síntese Eletroquímica de Materiais Nanoestruturados* [electrochemical synthesis of nanostructured materials], In: A.L. Da Róz, F.L. Leite, et al. (Eds.), *Nanoestruturas: Princípios e Aplicações*, vol. 1, Elsevier, Rio de Janeiro, 2015, pp. 63–110 (Chapter 3) [26].

shock to the sample using high-powered incandescent lamps for a brief period. Next, the samples are appropriately purified to remove any organic substance. Among the various solvents utilized for cleaning the substrate, acetone and ethyl alcohol are the most commonly employed. After this stage, the substrates undergo a mechanical, chemical, or electrochemical (electropolishing) polishing procedure to produce flat and mirror-finished

metallic substrates, depending on the desired application. Several tables can be found in Sulka et al. [101] describing examples of experimental conditions for the pretreatment of the aluminium surfaces.

As previously described, the two-step anodization consists of the usual anodization process, with the previous choice of experimental conditions (potential or current, temperature, and concentration/composition of the electrolyte), and the subsequent chemical dissolution of the oxide formed in the first anodization step. In the chemical attack for the oxide removal, a concave triangular profile is formed at the substrate base, where the formed pores used to be (Fig. 3.18). This structural profile will serve as a natural orientation for the formation of the oxide layer during the second anodization. Normally, this second step is carried out under the same conditions as the first anodization. Finally, using adequate chemical or physical methods [111], the porous structure can be separated from the substrate base to enable the desired manipulation of the membrane. Also, the pores diameter can be increased or their closed bases can be opened, thereby opening the membrane on both sides. The general scheme of the procedure for the fabrication of PAAs and their possible applications are illustrated in Fig. 3.19.

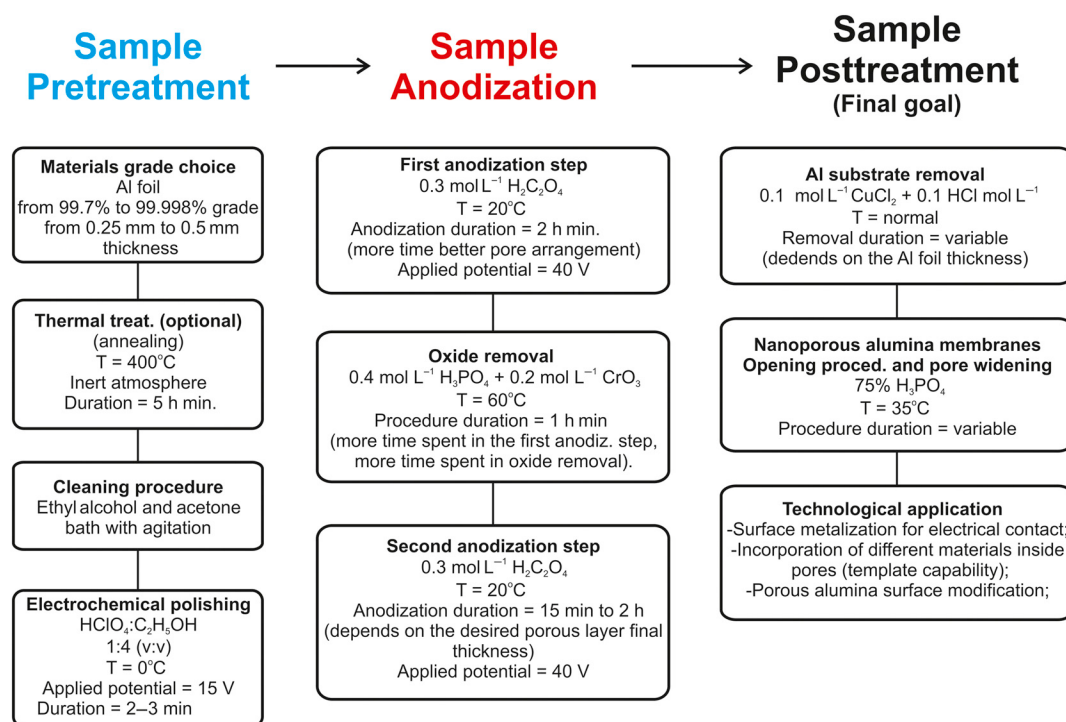


FIGURE 3.19 Schematic illustrating the experimental stages for obtaining anodic self-organized alumina for different applications.

The pore-opening process and the chemical erosion of the barrier oxide at its aluminium base depend on the chemical dissolution rate of anodic alumina. This procedure depends on the concentration and temperature of the electrolyte. Aqueous solutions of  $H_2SO_4$ ,  $H_2C_2O_4$ , and  $H_3PO_4$  are normally employed, and it is also possible to add small amounts of  $CrO_3$ , which increases the oxide dissolution rate. The procedure may be conducted in the same the electrolytic cell. Depending on the conditions used, the dissolution rate ranges from 0.02 to  $4.45\text{ nm min}^{-1}$  [101].

The separation of the nanoporous oxide from its aluminum base can be performed using an electrochemical method, in which inverted potential pulses are applied [93,107,109,112]. However, the most commonly used process is a chemical removal of aluminum [101]. This method consists of exposing the metal layer to chemical substances that oxidize the metal but not the oxide. The most used chemical substances are  $HgCl_2$ , copper (II) sulfates or chlorides, and mixtures of  $Br_2$  and ethanol. The solution temperature can also be varied between 5 and 40°C, as well as the exposure time of the metallic layer.

Surface images obtained by SEM of PAA samples prepared under galvanostatic and potentiostatic regimes are illustrated in Fig. 3.20 and Fig. 3.21, respectively. All samples were prepared using two-step anodization method, although under different conditions of electrolyte concentration, temperature, and growth regime.

The two-step anodization method is quite interesting from the practical viewpoint and useful when one does not have the experimental apparatus for nanoindentation. Nevertheless, to obtain self-organized structures with high morphologic homogeneity, a long anodization time is necessary for the first step, where the aluminum base is marked. For example, to produce a sample containing self-organized porous layers, with a thickness from 1 to 3  $\mu\text{m}$  using the galvanostatic method, using oxalic acid as electrolyte and temperature of 5°C, approximately 4 h are necessary for the experiment. This period is

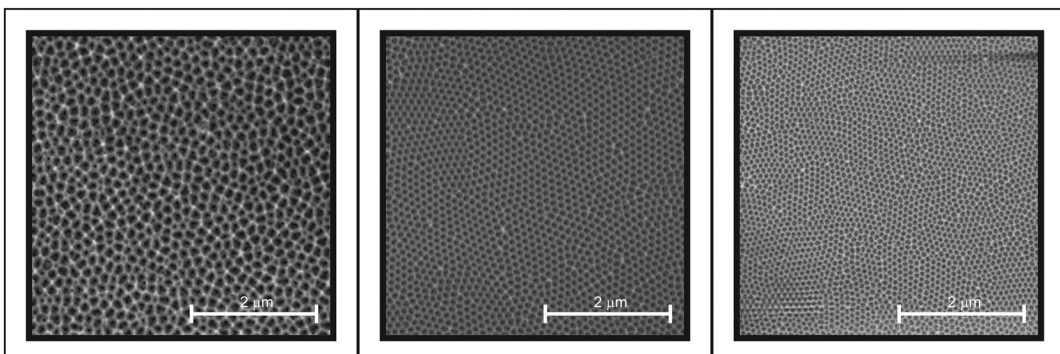


**FIGURE 3.20** Micrographs showing a top view of PAA films, obtained by two-step anodization method in the galvanostatic regime. Adapted from F. Trivinho-Strixino, J.S. Santos, M.S. Sikora, Síntese Eletroquímica de Materiais Nanoestruturados [electrochemical synthesis of nanostructured materials], In: A.L. Da Róz, F.L. Leite, et al. (Eds.), Nanoestruturas: Princípios e Aplicações, vol. 1, Elsevier, Rio de Janeiro, 2015, pp. 63–110 (Chapter 3) [26].

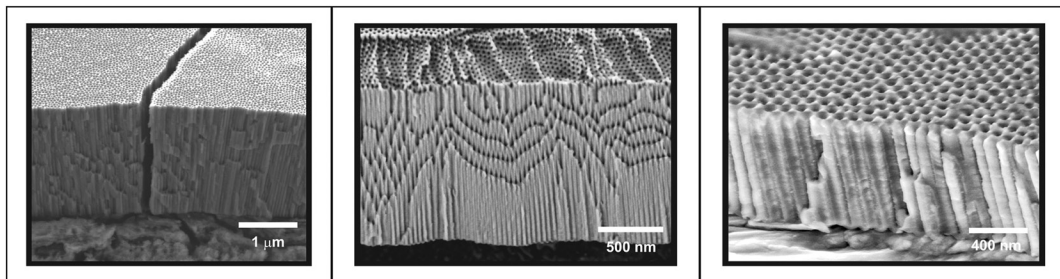


**FIGURE 3.21** Micrographs showing a lateral view of PAA films, obtained by two-step anodization method in the potentiostatic regime. Adapted from F. Trivinho-Strixino, J.S. Santos, M.S. Sikora, *Síntese Eletroquímica de Materiais Nanoestruturados [electrochemical synthesis of nanostructured materials]*, In: A.L. Da Róz, F.L. Leite, et al. (Eds.), *Nanoestruturas: Princípios e Aplicações*, vol. 1, Elsevier, Rio de Janeiro, 2015, pp. 63–110 (Chapter 3) [26].

distributed as follows: 2 h of anodization in the first step, 30 min for the removal oxide, and 1.5 h for the second anodization. The process is limited by the diffusional transport of the oxygenated species from the electrolytic solution to the metal/oxide interface, concentrated in the pores channels. This limits the oxide growth rate ( $2\text{--}6 \mu\text{m h}^{-1}$ ) and introduces a maximum value of 20 for the depth/diameter ratio [65].

A solution to this problem arose with the development of the so-called “Hard Anodization” method. In this method, aluminum substrates were anodized in oxalic acid in the high-field regime and in the potentiostatic mode, with applied potential values ranging from 100 to 150 V for oxalic acid electrolytes. Three-dimensional arrays of regular nanopores can be obtained through this method and utilized in nanotechnology applications such as photonic crystals, microfluidics, and template for nanowire and nanotube fabrication with diameter control [113]. However, to suppress the electrolytic breakdown produced by the high associated electric field, the existence on the aluminum substrate of a previously formed barrier-oxide layer larger than 400 nm is necessary before applying large anodization potentials ( $>100 \text{ V}$ ). This oxide layer can be growth using mild anodization conditions, for example, performing a potentiostatic anodization, applying 40 V in  $0.3 \text{ mol L}^{-1}$  oxalic acid for 5–10 min. Then, in sequence, the applied potential must be slowly increased up to values between 100 and 150 V at a rate of  $0.5\text{--}0.9 \text{ V s}^{-1}$  and be maintained at these values until the end of anodization. The hard anodization is accompanied by intense release of heat, which must be efficiently removed using an adequate experimental apparatus (Fig. 3.22).

Thus, “Hard Anodization” method offers great advantages compared with “Mild Anodization” method. This method accelerates the nanostructure fabrication of PAA films due to the high growth rate of the self-organized oxide arrays and it allows the fabrication of these arrays in larger areas and using only one side of the metal. This aspect increases its technological relevance. Some authors [65,114] have demonstrated the advantages of utilizing a hard anodization cell, as opposed to a conventional cell using the mild anodization mode. It is possible to obtain PAA films with aspect ratio 20 times larger than the conventional method using the same anodization time. This means pores with depths up to 110  $\mu\text{m}$ ,

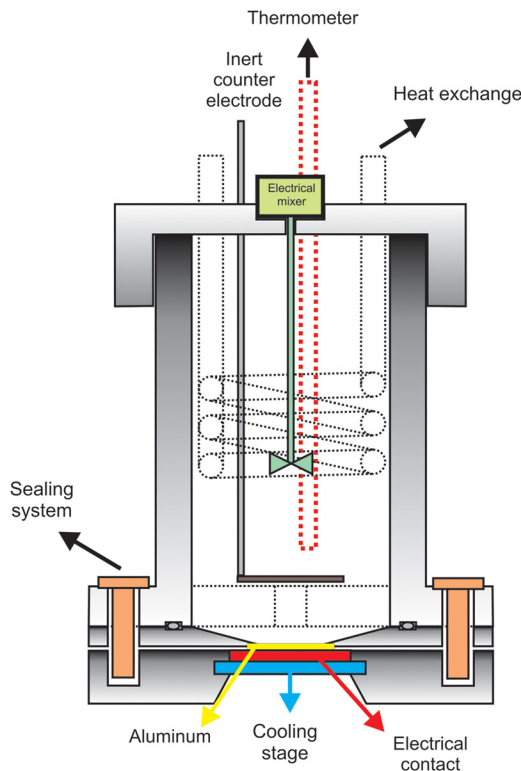


**FIGURE 3.22** Illustration of a cell used in the “Hard Anodization” method. Adapted from F. Trivinho-Strixino, J.S. Santos, M.S. Sikora, *Síntese Eletroquímica de Materiais Nanoestruturados* [electrochemical synthesis of nanostructured materials], In: A.L. Da Róz, F.L. Leite, et al. (Eds.), *Nanoestruturas: Princípios e Aplicações*, vol. 1, Elsevier, Rio de Janeiro, 2015, pp. 63–110 (Chapter 3) [26].

when compared with depths of 4 µm in average obtained by conventional anodization. Thus, the fabrication efficiency gains for self-organized structures are well established. Considering the same anodization time, the hard anodization technique allows obtaining self-organized alumina structures with much larger thicknesses and pore diameters.

The PAAs can also be modified by incorporation of specific ions. In addition to emitting in blue [115–121], these materials are particularly promising for use as a host material [118,122,123]. They have also been employed in the preparation of waveguides and in the fabrication process of nanoscopic luminescent devices that facilitate controlling the optical properties of the material at the molecular level. Applications of PAAs are countless. We can find studies that explore the advantages related to the porous alumina itself, as well as optical and mechanical properties [11,13,120,124–129]. Other studies report the use as templates to fabricate other nanostructured materials [101,128,130], and applications in biological systems [131–136], polymeric systems [137], and semiconductor devices [128].

### 3.4.3 Electrochemical Synthesis of TiO<sub>2</sub> Nanotubes

Since Gong and coworkers [138] electrochemically synthesized TiO<sub>2</sub> nanotubes for the first time in 2001, this material has been broadly investigated for applications in photocatalysis [14,139], photoelectric [17], and photovoltaic devices [18,140], sensors [22,141], and immunosensors [24]. This great interest is due to their large surface/volume ratio; consequently, the TiO<sub>2</sub> nanotube formation mechanism has been extensively investigated, as well as the experimental parameters involved in its preparation. The description of the electrochemical synthesis of other types of oxide nanotubes can be found in the literature, with materials such as ZrO<sub>2</sub> and WO<sub>2</sub> [142]. However, due to the intrinsic properties of TiO<sub>2</sub>, as well as its catalytic power [143] and biocompatibility with live tissues [144,145], this oxide has been widely studied, and it presents great advantages for technologic applications. TiO<sub>2</sub> nanotubes presenting pore sizes between 22 and 110 nm, width between 200 and 6,000 nm, and wall thickness between 7 and 34 nm are easily obtained via electrochemical methods by controlling the synthesis parameters [18,146]. In this section, we will present a brief review of the experimental conditions for the preparation of TiO<sub>2</sub> nanotubes and the influence of these parameters on the architecture of the produced nanomaterial.

As previously described, the formation of porous films using electrochemical methods is directly related to the solubility of the oxide in the electrolyte used. Anodic TiO<sub>2</sub> films can display either a porous structure with low spatial organization and a pore diameter measured in micrometers and nanometers or a highly organized structure in the form of nanotubes with well-defined walls, depending on the experimental conditions employed in the synthesis. In electrolytes in which the films present low solubility, such as phosphoric or sulfuric acid, or even alkaline media containing phosphates or aluminates [75], one generally obtains compact or porous structures with low spatial organization [67,147]. By contrast, highly organized structures in the form of nanotubes with well-defined walls can be obtained through anodization in media containing fluoride [14,75,138,143,144,148,149], or even perchlorate or chloride [142].

The electrochemical synthesis of TiO<sub>2</sub> nanotubes is generally carried out employing the galvanostatic or the potentiostatic method in electrolytes in which the oxide presents high solubility. Under these conditions, the potential reached by the galvanostatic system is smaller than the oxide breakdown potential (Section 4.1). In the potentiostatic method, a potential lower than the breakdown potential is applied, for the purpose of forming a homogeneous and self-organized structure, free of heterogeneities promoted by the phenomenon of electrolytic breakdown.

There is also the titanium oxidation technique using a pulsed charge, where the efficiency of the current related to the oxide formation is approximately 100%, eliminating parallel reactions such as O<sub>2</sub> evolution, commonly observed in potentiostatic and galvanostatic methods. In addition, according to Poznyak et al. [148], the formed material exhibits better electrocatalytic activity than the titanium oxide obtained through the galvanostatic method.

Considering potentiostatic anodization, it is observed that at the beginning of anodization, there is an abrupt potential drop due to the formation of a high-resistance compact oxide film that reduces the current intensity. In the sequence, a current increase due to the oxide dissolution process is observed, and then, it occurs the random growth of the nanoporous structure. The competition between the increase in oxide thickness and the formation of self-organized nanotubes (local film dissolution) promotes the slow decrease of the current intensity. Regular fluctuations can be observed, which are related to the growth and dissolution of the oxide film formed.

The first synthesis of  $\text{TiO}_2$  nanotubes films were carried out in a hydrofluoric acid medium. According to Regonini et al. [150], these films consisted the first generation of  $\text{TiO}_2$  nanotubes. The presence of fluoride in the reaction medium produces the partial dissolution of the formed film and promotes the formation of titanium dioxide nanotubes after the system achieves dynamic equilibrium between the formation and dissolution processes of the oxide layer. The chemical dissolution of  $\text{TiO}_2$  occurs because of the formation of the soluble complex  $\text{TiF}_6^{2-}$ , and the dynamic equilibrium between the formation and dissolution rates is reached after a long anodization period [151]. The formation mechanism of  $\text{TiO}_2$  nanotubes has been thoroughly discussed in the literature and is based on the existing proposals for PAA growth, considering the appropriate differences between the systems [152–158].

In potentiostatic anodization conducted at low potentials, an analogous morphology to porous alumina structures [159] is frequently observed. With the increased potential, a particulate surface is obtained. For potentials above 10 V, the particulate appearance is lost, with the initial formation of nanotubes [18]. If anodization is performed for a long period, there will be a uniform growth of the titanium nanotube array with an insulating barrier film in the lower portion of the films, separating the nanometric array from the titanium electrode, similarly to the barrier film observed in nanoporous alumina. At high potentials, the highly organized structure is lost and replaced by a randomly porous structure, due to the breakdown of the previously formed nanotubular structure [160].

The effect of the applied potential on  $\text{TiO}_2$  nanotube formation has been investigated by several researchers. According to Yahia et al. [161], the applied potential can strongly influence the nanotube growth and their properties. These researchers [161] observed a linear dependence of the barrier film thickness with the applied potential within the interval from 20 to 50 V. Similarly, by analysis of the applied voltage and the anodization time, Matykina et al. [160] confirmed a barrier layer increase proportional to this voltage. Furthermore, the authors [160] also observed the incorporation of fluoride ions into the barrier film, proportional to the potential. A percentile of 4–6% was detected in the films grown at 20 V, whereas up to 13% of fluoride was identified in the films grown at 60 V. In another study, Alivov et al. [162] demonstrated the growth of  $\text{TiO}_2$  nanotubes in a wide potential range (10–240 V) by electrolyte modification. According to the authors [162], the resistivity of the formed films was found to be proportional to the applied potential, with an observed increase of eight orders of magnitude for the films obtained at 240 V, with respect to those obtained at 10 V. In addition, at potentials lower than 60 V, well-ordered

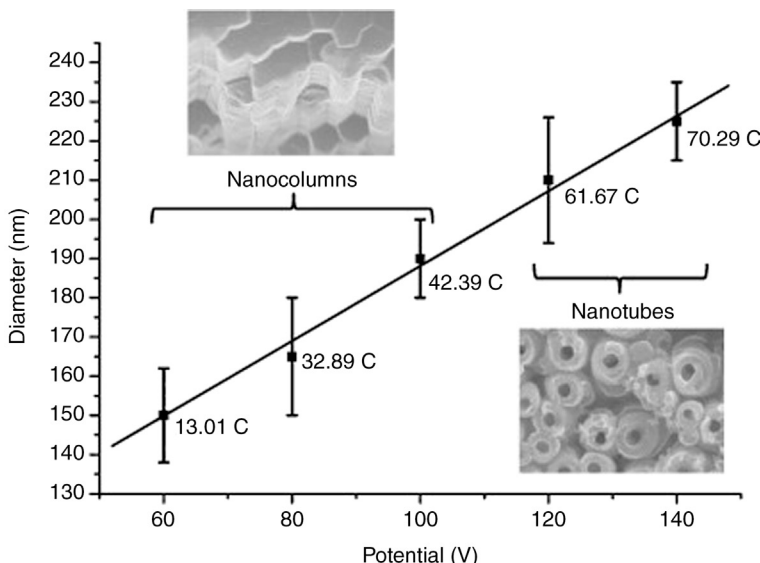


**FIGURE 3.23** Nanostructure diameter versus anodization potential at 10°C. The insets display SEM micrographs of the nanocolumn and nanotube structures of TiO<sub>2</sub> films [163].

structures were obtained for a solution of NaF + glycerol + H<sub>2</sub>O, with a NaF concentration of 0.7%, and for media containing NH<sub>4</sub>F + ethylene glycol + H<sub>2</sub>O, in different proportions of NH<sub>4</sub>F (0.5–1%) and water. For potentials higher than 60 V, the same result was obtained by diluting the solution to 0.1%. According to the authors, the increase in the water-electrolyte ratio promotes an increase in the nanotube growth rate, which modifies the morphology and increases the resistivity of the films.

Complex structures, such as hexagonal nanostructures formed at high potentials and low temperatures, have been reported by Ruff et al. [163] Fig. 3.23 reveals that the transition from a nanocolumn structure to nanotubes is caused by modification of the applied potential, among other factors. The authors also suggest that the formation of the nanocolumns results from the enlargement of the inner nanotube walls due to intensification of the oxide formation reaction, when compared with the dissolution reaction.

The pH of the electrolyte is also an important factor that affects the morphology of TiO<sub>2</sub> films. At pH = 1.0, well-defined nanotubes are produced with a length and diameter proportional to the anodization potential. The formation of a conical structure may occur after the formation of the nanometric array due to the increase of pore base [164]. According to Mor [18], the optimal pH range for obtaining relatively long nanotubes is between 3.0 and 5.0. However, a reduction in the acidity and the use of salts containing fluoride promote a decrease in the oxide dissolution rate, and it is possible to obtain nanotubes with lengths between 2 and 4 μm. [165] The oxide synthesis in aqueous medium with fluoride salt solutions forms the second generation of TiO<sub>2</sub> nanotubes [150].

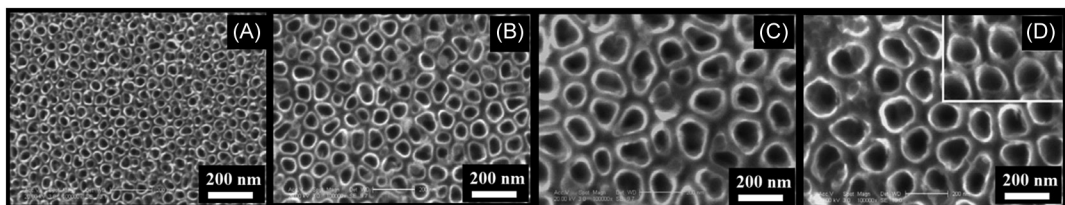


**FIGURE 3.24** SEM images of  $\text{TiO}_2$  nanotubes obtained in a mixture of methanol 50% vol. + HF 1% mass, under the following current densities: (A)  $10 \text{ mA cm}^{-2}$ , (B)  $15 \text{ mA cm}^{-2}$ , (C)  $20 \text{ mA cm}^{-2}$ , (D)  $30 \text{ mA cm}^{-2}$ . Adapted from S. Kaneko et al., *Fabrication of uniform size titanium oxide nanotubes: impact of current density and solution conditions*, *Scr. Mater.* 56 (5) (2007) 373–376 [166].

Kaneko et al. [166] performed galvanostatic anodizations in a solution containing methanol and HF in order to study the effect of methanol and the influence of the current density on  $\text{TiO}_2$  nanotube formation. Their results demonstrated that an increased current density promotes an enlargement of nanotube diameter and the formation of channels between them, as can be observed in Fig. 3.24. The changes in the nanotube diameter is promoted by the increase of dissolution rate and of magnitude of the electric field. In addition, the authors concluded that adding methanol to the electrolyte eliminated the current oscillations related to the gaseous evolution and produced a spacing between the nanotubes. This led to obtaining standardized nanomaterials with high surface area.

The synthesis of nanotubes in organic media containing fluoride salts and small amounts of water comprises the third and fourth generations of  $\text{TiO}_2$  nanotubes [150]. Nanotubes grown under these conditions can display thicknesses of 100–1000  $\mu\text{m}$  [146,165,167–169], and are more homogeneous than nanotubes of the first and second generations. Studying viscous electrolytes, such as glycerol or ethylene glycol containing  $\text{NaF}$  Macak and Schmuki [167] observed the formation of self-organized  $\text{TiO}_2$  nanotubes with smooth walls and lengths in micrometers. According to the authors, diffusion is limited in viscous electrolytes, causing local acidification in the pore, which promotes a high current efficiency compared with aqueous electrolytes. Due to the simplicity of the synthesis and reproducibility of the  $\text{TiO}_2$  nanotubes in organic media, great attention is currently being paid to these synthesis conditions.

Fourth-generation nanotubes are synthesized at the same electrolytic medium. However, the anodization parameters, such as anodizing time, applied potential, and concentration of fluoride ions, are carefully controlled to obtain a highly homogeneous and well-organized structure [150].

$\text{TiO}_2$  nanotubes formed during the electrochemical synthesis from first to fourth generation are amorphous. A thermal treatment known as annealing is required for their conversion to crystalline oxide. After annealing, the titanium dioxide can exist in three different crystalline phases: anatase (tetragonal), rutile (tetragonal), and brookite (orthorhombic) [150]. Generally, the anatase phase is predominant after the thermal treatment of this material. This characteristic, the large surface area, makes  $\text{TiO}_2$  nanotubes excellent photocatalysts [14]. In absence of fluoride in the electrolyte, there is usually no formation

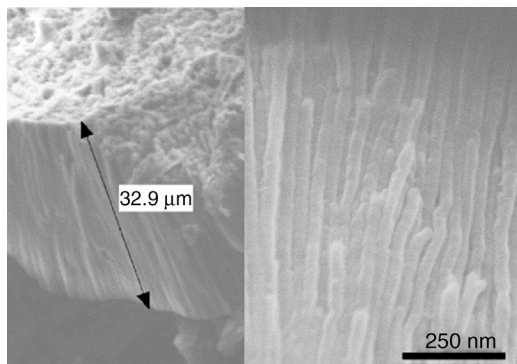


**FIGURE 3.25** SEM micrographs of the lateral view of  $\text{TiO}_2$  nanotubes prepared in  $0.1 \text{ mol L}^{-1} \text{ HClO}_4$  at  $30 \text{ V}$  for  $60 \text{ s}$ .  
Adapted from R. Hahn, J.M. Macak, P. Schmuki, Rapid anodic growth of  $\text{TiO}_2$  and  $\text{WO}_3$  nanotubes in fluoride free electrolytes. *Electrochim. Commun.* 9 (5) (2007) 947–952 [142].

of a tubular structure, but the formation of a porous structure caused by the electrical discharges at the surface during the oxide growth [67]. Studies carried out in media where  $\text{TiO}_2$  is poorly soluble, such as sulfuric acid [84,167] and phosphoric acid [67], show a transition from amorphous oxide to the crystalline anatase phase during the film growth.

In potentiostatic studies performed in electrolytes containing perchlorate and chloride ions, Hahn et al. [142] observed that, contrary to common sense, there is formation of a tubular array in the absence of fluoride, as shown in Fig. 3.25. Furthermore, this structure is obtained in a relatively short time. However, since the formation of this structure is induced by local breakdown—that is, by the formation of pitting corrosion [142]—the array does not display rigorous self-organization, such as that obtained in fluoride medium.

Temperature is another experimental parameter of great importance in the growth of nanotubular  $\text{TiO}_2$  arrays. A reduction of the electrolyte temperature tends to increase the wall thickness of the pore. As result, the formed material presents a sponge-like structure [18]. According to Prida et al. [151], low temperatures inhibit the formation of self-organized  $\text{TiO}_2$  nanotubes, favoring the formation of a randomly disordered structure due to the internal growth of the nanotubes. This effect is promoted by the direct influence of temperature on the oxide solubility in the electrolyte. The decrease in temperature reduces the solubility and alters the viscosity of the solution, promoting disequilibrium in the steady-state reached between the oxide formation and dissolution reactions. This way, a new steady-state is achieved. Consequently, there is an increase in the film resistivity and the formation of a structure with a higher or lower degree of ordering, depending on the electrolyte and the temperature used.

The effect of temperature becomes more pronounced in the growth of homogeneous nanotubes in viscous electrolyte, since the viscosity is inversely proportional to the temperature. According to Macak and Schmuki [167], the high temperature promotes the enlargement of the diameter and length of the tubes; and the limiting factor of nanotube

growth is the diffusion of the reagents to the inside of the pore (barrier oxide/electrolyte interface) or of the reaction products to the outside of the tubes.

Despite the experimental aspects of the electrochemical synthesis of  $\text{TiO}_2$  nanotubes being widely disseminated and discussed in the literature, great effort has been recently observed to improve the optical properties of  $\text{TiO}_2$  for applications as photocatalysts under sunlight irradiation. The absorption band of  $\text{TiO}_2$  can be shifted to the visible light region by the incorporation of other species into the oxide. In addition, the insertion of doping ions can promote different effects to improve the photocatalytic properties of  $\text{TiO}_2$ , such as a bandgap reduction, increased crystallization of the material, and increased surface area [170–172]. Considering the method of fabrication of these nanostructures by electrochemical techniques, the introduction of dopants into the oxide crystal lattice—a process known as anodic doping—enables the formation of doped anodic oxides with various interesting properties. The main characteristics of this process will be discussed in the next section.

### 3.4.4 Modification of the Oxide Properties by Anodic Doping

As previously discussed, the growth of anodic films in valve metals is determined by a high-field mechanism [63]. This means that the ion transport inside the oxide, which depends exponentially on magnitude of the electric field, is the determinant stage of the oxide-forming reaction. Consequently, a linear increase of the barrier-oxide thickness with the electrode potential in the galvanostatic regime is observed. During this process, impurities in the solution can migrate into the film and be incorporated into the oxide crystal lattice during its growth. According to some authors [89,173], the incorporation of anions into the electrolyte and their ability to release electrons for the conduction band are the main factors that cause anodic oxide film breakdown. In general, the adsorption of ions from the electrolyte will be preferred in positively polarized electrodes and will compete with the  $\text{OH}^-$  anions generated during electrolysis of the water.

In this sense, the modification of the oxide properties can be performed by introduction of dopant salts into the electrolyte, using the technique known as anodic doping [12,174–177]. In this technique, the doping ions present in the electrolyte can migrate into the film and be incorporated into the oxide crystal lattice during the anodization reactions. Various works in the literature describe the doping of oxides by chemical methods [178–185]; however, the doping process by electrochemical techniques, as the anodic doping method, is seldom explored.

A dopant can be defined as an atom that is originally not part of the crystal structure of the material. It can be intentionally introduced as an impurity to modify the properties of the material in question. In the case of doping by substitution at the reticule, the dopant atom can have a different number of valence atoms than the atom it substitutes, which enables forming extra energy levels and modifying the material properties. The type of dopant used and its location in the host structure (substitutional and interstitial defects, vacancies, etc.) can produce different effects during the capture of electrons and/or holes

at the surface, or during charge transfer. This way, the dopant nature exerts a great influence in the properties and characteristics of the resulting oxide.

The dopant atoms can be of two types: acceptors and donors. Acceptor dopants are ions that present a lower valence than the ions of the host material. By contrast, donor dopants are ions with a higher valence than those of the host material. An example of doping with acceptors is the case of  $\text{ZrO}_2$  doped with  $\text{Eu}^{3+}$  atoms [174], where the  $\text{Eu}^{3+}$  ions substitute the  $\text{Zr}^{4+}$  ion in the oxide crystal lattice, altering the defect density in its microstructure. The acceptor species presents an effective negative charge, represented by the notation  $\text{Eu}'_{\text{Zr}}$ . The introduction of acceptor species tends to add balancing holes to the structure. The inclusion of lower-valence impurities will influence the stoichiometry and the charge balance of the host material, so they must be counterbalanced by a series of defects. Acceptor doping can be done by addition of interstitial cations, anionic vacancies, and holes ( $h^+$ ) [186].

An example of donor dopant is the doping of  $\text{ZrO}_2$  with  $\text{Nb}^{5+}$  ions [12]. In this case, the  $\text{Nb}^{5+}$  ions substitute the  $\text{Zr}^{4+}$  ion in the oxide matrix. The donor species have a positive effective charge ( $\text{Nb}'_{\text{Zr}}$ ), and their introduction to the oxide matrix produces counterbalanced electrons in the structure. Such electrons also affect the material stoichiometry, which is balanced by defects. Donor doping can be performed through cationic vacancies, interstitial anions, and electrons ( $e^-$ ).

The  $\text{ZrO}_2$  in its most abundant crystalline phase (monoclinic [81]) have a large bandgap of approximately 5.2 eV and can present localized electronic states inside the bandgap, normally associated with irregularities of the crystal lattice or the presence of structural defects. This characteristic makes it an optimal candidate for use in photophysical and photochemical processes [19,187,188]. Furthermore, this oxide presents low phonon energy, i.e., electronic recombination processes that may take place during decay are mostly radioactive processes. Furthermore, nonradioactive recombination or vibrational processes are less probable due to the “harder” nucleus of Zr, which enables its use as a host in materials with luminescent properties. Thus, rare-earth elements can be incorporated into this oxide and have their luminescence signals intensified, creating probes of technological interest [178,188]. One example of this application was verified by Trivinho-Strixino et al. [174], who produced zirconium oxides doped with  $\text{Eu}^{3+}$  ions, using the anodic doping technique. Fig. 3.26 presents the photoluminescence spectra of pure  $\text{ZrO}_2$  and of  $\text{ZrO}_2$  doped with  $\text{Eu}^{3+}$ . A wide emission band is observed between 350 nm (3.5 eV) and 740 nm (1.7 eV), presenting two shoulders centered at 3.1 eV and 2.7 eV, as well as a maximum at 2.3 eV. These bands are related to emission in the oxide matrix, most likely originating from the structural defects introduced during the oxide film growth [19,63,189–192]. The photoluminescence spectrum of the  $\text{ZrO}_2$  sample doped with  $\text{Eu}^{3+}$  exhibits emission lines corresponding to the transition from the Eu(III)  ${}^5\text{D}_0$  level to various sublevels of the  ${}^7\text{F}_{0, 1, 2, 3, 4}$  ground state ( $e_{\max} = 2.09$  eV, 2.07 eV, 2.02 eV, 1.98 eV, and 1.74 eV, respectively) [193], where the emission line with  $e_{\max} = 2.02$  eV ( ${}^5\text{D}_0 \rightarrow {}^7\text{F}_2$  transition) is the most intense. In addition, Fig. 3.26 also illustrates that the emission lines of  $\text{Eu}^{3+}$  are asymmetric, which may be related to the fact that these ions are incorporated into the host matrix ( $\text{ZrO}_2$ ) at

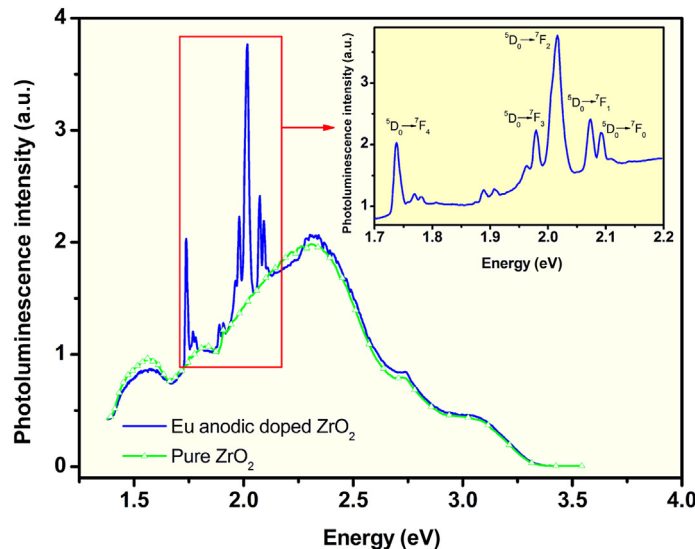


**FIGURE 3.26** Emission spectrum of  $\text{ZrO}_2$  doped with  $\text{Eu}^{3+}$  ions prepared in an electrolytic solution containing  $0.04 \text{ mol L}^{-1} \text{H}_3\text{PO}_4 + 0.05 \text{ mol L}^{-1}$  citric acid +  $5.3 \times 10^{-4} \text{ mol L}^{-1} \text{EuCl}_3$ ,  $I = 16 \text{ mA cm}^{-2}$ ,  $T = 20^\circ\text{C}$ . Laser  $\lambda_{\text{exc}} = 325 \text{ nm}$  (3.85 eV) and  $T = 4.7\text{K}$ . Inset: zoom-in of the  $\text{Eu}^{3+}$  ion emission lines.

substitutional defects of the crystal, causing an increase in the lattice microdeformation (inset in Fig. 3.26). Since the absorption region for the  $\text{Eu}^{3+}$  ion is smaller than the excitation of laser light at 325 nm (3.85 eV), it is assumed that the intense emissions of the europium are a consequence of the electronic energy transfer from the  $\text{ZrO}_2$  host matrix, which are superimposed onto the electronic states of the  $\text{Eu}^{3+}$  ions in the energy range below 3.85 eV [174].

Other dopants such as  $\text{Ca}^{2+}$  and  $\text{Nb}^{5+}$  ions modify the microstructural properties of  $\text{ZrO}_2$ . The zirconia films produced by galvanostatic anodization under PEO conditions crystallize predominantly in the monoclinic phase. Incorporation of these dopants to the oxide can lead to the stabilization of the tetragonal and cubic phases at room temperature. In pure  $\text{ZrO}_2$ , these crystalline phases are stable only at high temperatures (above  $1,200^\circ\text{C}$ ) [12,81,174,175]. Depending on the anodization conditions, such as the electrolyte concentration, composition, and temperature, as well as the applied current density, the incorporation of these doping species allows the partial or full stabilization of the cubic zirconia, turning the material into a good conductor and increasing its mechanical resistance. X-ray diffractometry results demonstrated the stabilization of  $\text{ZrO}_2$  films at room temperature, with 80% in the tetragonal or cubic phases, produced by galvanostatic anodization of Zr in phosphoric acid in the presence of  $\text{Ca}^{2+}$  ions [175].

In the synthesis of  $\text{TiO}_2$  nanotubes, the  $\text{Nb}^{5+}$  ions are widely used as dopants due to the easy insertion into the oxide crystal structure. Several studies show that doping with niobium produces materials that absorb in a wider band of the visible light spectrum [194–196]. According to Depero et al. [194], adding niobium to  $\text{TiO}_2$  presents a series of advantages

over the pure material. The formed crystallites become smaller, increasing the photoactive area of the material. In addition, the presence of the dopant promotes increased stress in the anatase phase, thus favoring the conversion to the rutile phase. Nonetheless, some authors have observed that although the mixed material absorbs a larger amount of visible light than the pure material, its photocatalytic activity is equal or lower than that of the pure oxide. This is because the formation of oxygenated Nb clusters promotes an increase in the rate of electron-hole recombination, decreasing the photoactivity.

Another way to dope the material without necessarily introducing dopant ions into the electrolyte is using the reanodization technique, in which the dopant metal is cathodically deposited over the previously anodized porous oxide. After electrodeposition of the dopant, the material is reanodized in order to introduce the metallic ions to the oxide crystal lattice [171]. Studies with copper, manganese, and chromium as dopants in  $\text{TiO}_2$  nanotubes demonstrate that the photocurrent is greater in the doped electrodes, and the electrocatalytic efficiency increases with the dopant concentration, up to an optimum value of approximately 1%, due to the decrease in the electron-hole recombination. Above this optimum concentration value, the metal behaves as a recombination center for electron-hole pairs, decreasing the electrocatalytic efficiency of the doped material.

### 3.5 Conclusions

In this chapter, the use of electrochemical methods was discussed with a focus on the preparation of nanostructured materials. The approaches described present a robust method of nanomaterials fabrication, which is easy to use, produces results that are easy to interpret, is faster, and has a lower cost than other fabrication techniques, such as lithography.

Furthermore, a wide range of materials with a variety of properties can be easily obtained by electrochemical methods, given that the film properties can be controlled by the experimental conditions employed in the synthesis. Different types of materials can be obtained simply by changing voltage, current, temperature, pH, and/or the electrolyte used. In addition to obtaining electrodeposited films with different compositions, morphologies, and microstructures, it is possible to obtain highly organized structures. Examples of this are the cases of porous anodic alumina and  $\text{TiO}_2$  nanotubes, as well as the formation of concave nanotubes, nanocolumns, and other structures. It is important to emphasize that structures with a lower order degree but large surface area and high degree of crystallinity can also be produced, and they present interesting complex phenomena during film growth, which are extensively used but yet poorly understood. An example is the case of oxide films obtained by anodization under high electric field, i.e., in conditions of dielectric breakdown of the anodic oxide.

Finally, electrochemistry also presents an interesting technique for the modification of material properties: the method of anodic doping. As discussed previously, the addition of doping ions to the electrolyte promotes significant modifications in the host material, which will depend on the nature of the inserted species. These modifications can change

the material properties, such as: increased photocatalytic activity; increased biocompatibility; increased corrosion resistance; improved thermal conductivity in oxides; improved photoluminescent materials, etc. After an appropriate development time, these new materials with interesting properties can be introduced into technological niches, gaining a space in practical and commercially viable applications and becoming part of the daily life of the entire society, from the scientist to the common citizen.

## List of Symbols

<b>A</b>	Area
<b>e</b>	Electron charge
<b>e<sup>-</sup></b>	Electron
<b>E</b>	Potential
<b>E<sub>0</sub></b>	Externally applied potential
<b>F</b>	Faraday constant
<b>h<sup>+</sup></b>	Vacancy
<b>I</b>	Electric current
<b>j</b>	Electric density
<b>l</b>	Thickness
<b>q</b>	Qcharge
<b>R</b>	Ohmic resistance
<b>T</b>	Temperature
<b>t</b>	Time
<b>z</b>	Number of moles of electrons
<b>λ</b>	Wavelength
<b>ρ</b>	Resistivity

## References

- [1] L.P. Bicelli, et al. A review of nanostructural aspects of metal electrodeposition, *Int. J. Electrochem. Sci.* 3 (4) (2008) 356–408.
- [2] A. Mukhopadhyay, B. Basu, Consolidation–microstructure–property relationships in bulk nanoceramics and ceramic nanocomposites: a review, *Int. Mater. Rev.* 52 (2007) 257–288.
- [3] I. Gurrappa, L. Binder, Electrodeposition of nanostructured coatings and their characterization—a review, *Sci. Technol. Adv. Mater.* 9 (4) (2008) 043001.
- [4] G. Cao, Y. Wang, *Nanostructures and Nanomaterials: Synthesis, Properties, and Applications*, second ed., World Scientific Publishing Co. Pte. Ltd, Singapore, (2011) 596.
- [5] J. Briggle, P.D. Nolidin, T.D. Golden, Multilayer film fabrication using flow injection coupled with electrochemical deposition, *Electroanalysis* 22 (19) (2010) 2157–2161.
- [6] B. Jang, et al. Fabrication of Segmented Au/Co/Au nanowires: insights in the quality of Co/Au junctions, *ACS Appl. Mater. Interfaces* 6 (16) (2014) 14583–14589.
- [7] H. Chen, et al. Electrochemical construction of porous gold nanostructures on DVD substrate and its application as nonenzymatic hydrogen peroxide sensor, *Sci. China-Chem.* 58 (10) (2015) p1585–1592.

- [8] A. Uzunoglu, A.D. Scherbarth, L.A. Stanciu, Bimetallic PdCu/SPCE non-enzymatic hydrogen peroxide sensors, *Sens. Actuat B-Chem.* 220 (2015) 968–976.
- [9] M. Alanyalioglu, F. Bayrakceken, U. Demir, Preparation of PbS thin films: a new electrochemical route for underpotential deposition, *Electrochim. Acta* 54 (26) (2009) 6554–6559.
- [10] N.M.N. Rozlin, A.M. Alfantazi, Nanocrystalline cobalt–iron alloy: synthesis and characterization, *Mater. Sci. Eng. A-Struct. Mater.* 550 (2012) 388–394.
- [11] F. Trivinho-Strixino, et al. Active waveguide effects from porous anodic alumina: an optical sensor proposition, *Appl. Phys. Lett.* 97 (1) (2010).
- [12] J.S. Santos, F. Trivinho-Strixino, E.C. Pereira, The influence of experimental conditions on microstructure and morphology of Nb-doped ZrO<sub>2</sub> films prepared by spark anodization, *Corros. Sci.* 73 (2013) 99–105.
- [13] H.A. Guerreiro, et al. Grazing angle photoluminescence of porous alumina as an analytical transducer for gaseous ethanol detection, *J. Nanosci. Nanotechnol.* 14 (9) (2014) 6653–6657.
- [14] J.L. Zhao, et al. Crystal phase transition and properties of titanium oxide nanotube arrays prepared by anodization, *J. Alloy. Compd.* 434 (2007) 792–795.
- [15] R.G. Freitas, E.P. Antunes, E.C. Pereira, CO and methanol electrooxidation on Pt/Ir/Pt multilayers electrodes, *Electrochim. Acta* 54 (7) (2009) 1999–2003.
- [16] R. Nagao, et al. Oscillatory electro-oxidation of methanol on nanoarchitected Ptpc/Rh/Pt metallic multilayer, *ACS Catal.* 5 (2) (2015) 1045–1052.
- [17] M. Gratzel, Photoelectrochemical cells, *Nature* 414 (6861) (2001) 338–344.
- [18] G.K. Mor, et al. A review on highly ordered, vertically oriented TiO<sub>2</sub> nanotube arrays: fabrication, material properties, and solar energy applications, *Sol. Energy Mater. Sol. Cells* 90 (14) (2006) 2011–2075.
- [19] A. Emeline, et al. Spectroscopic and photoluminescence studies of a wide band gap insulating material: powdered and colloidal ZrO<sub>2</sub> sols, *Langmuir* 14 (18) (1998) 5011–5022.
- [20] F. Xiao, et al. Recent progress in electrodeposition of thermoelectric thin films and nanostructures, *Electrochim. Acta* 53 (28) (2008) 8103–8117.
- [21] P.G. Bruce, B. Scrosati, J.M. Tarascon, Nanomaterials for rechargeable lithium batteries, *Angew. Chem. Int. Ed.* 47 (2008) 2930–2946.
- [22] G.K. Mor, et al. Fabrication of hydrogen sensors with transparent titanium oxide nanotube-array thin films as sensing elements, *Thin Solid Films* 496 (1) (2006) 42–48.
- [23] J.J. Gooding, L.M.H. Lai, I.Y. Goon, Nanostructured electrodes with unique properties for biological and other applications, in: R.C. Alkire, D.M. Kolb, et al. (Eds.), *Chemically Modified Electrodes*, vol. 11, Wiley-VCH, Weinheim, 2009, pp. 1–56.
- [24] A.G. Mantzila, M.I. Prodromidis, Development and study of anodic Ti/TiO<sub>2</sub> electrodes and their potential use as impedimetric immunosensors, *Electrochim. Acta* 51 (17) (2006) 3537–3542.
- [25] K.I. Popov, S.S. Djokic, B.N. Grgur, *Fundamentals Aspects of Electrometallurgy*, Kluwer Academic Publishers, New York, (2002).
- [26] F. Trivinho-Strixino, J.S. Santos, M.S. Sikora, Síntese Eletroquímica de Materiais Nanoestruturados [electrochemical synthesis of nanostructured materials], in: A.L. Da Róz, F.L. Leite, et al. (Eds.), *Nanoestruturas: Princípios e Aplicações*, vol. 1, Elsevier, Rio de Janeiro, 2015, pp. 63–110 Chapter 3.
- [27] L. Young, *Anodic Oxide Films*. 1, Academic Press, New York, (1961) p. 377.
- [28] J.O. Bockris, A.K.N. Reddy, *Modern Electrochemistry*, Plenum Press, New York, (1973) pp. 1231–1251.
- [29] D.M. Kolb, An atomistic view of electrochemistry, *Surf. Sci.* 500 (1–3) (2002) 722–740.
- [30] V.P. Santos, G. Tremiliosi, The correlation between the atomic surface structure and the reversible adsorption-desorption of hydrogen on single crystal Pt(111), Pt(100) e Pt(110), *Quim. Nova* 24 (2001) 856–863.

- [31] C. Lebouin, et al. Electrochemically elaborated palladium nanofilms on Pt(111): characterization and hydrogen insertion study, *J. Electroanal. Chem.* 626 (1–2) (2009) 59–65.
- [32] N.M. Markovic, H.A. Gasteiger, P.N. Ross, Copper electrodeposition on Pt(111) in the presence of chloride and (bi)sulfate—rotating-ring Pt(111) disk electrode studies, *Langmuir* 11 (10) (1995) 4098–4108.
- [33] I. Flis-Kabulska, Electrodeposition of cobalt on gold during voltammetric cycling, *J. Appl. Electrochem.* 36 (2006) 131–137.
- [34] L.H. Mendoza-Huizar, J. Robles, M. Palomar-Pardavé, Nucleation and growth of cobalt onto different substrates Part I. Underpotential deposition onto a gold electrode, *J. Electroanal. Chem.* 521 (2002) 95–106.
- [35] M.C. Vilchenski, et al. Electrodeposition of Co and Co-Fe Films on platinum and on copper substrates, *Portugaliae Electrochim. Acta* 21 (2003) 33–47.
- [36] B. Losiewicz, et al. The structure, morphology and electrochemical impedance study of the hydrogen evolution reaction on the modified nickel electrodes, *Int. J. Hydrogen Energ.* 29 (2) (2004) 145–157.
- [37] L. Bonou, M. Eyraud, J. Crousier, Nucleation and growth of copper on glassy-carbon and steel, *J. Appl. Electrochem.* 24 (9) (1994) 906–910.
- [38] C.L. Fan, D.L. Piron, P. Paradis, Hydrogen evolution on electrodeposited nickel cobalt molybdenum in alkaline water electrolysis, *Electrochim. Acta* 39 (18) (1994) 2715–2722.
- [39] D. Stoychev, et al. Electrodeposition of platinum on metallic and nonmetallic substrates—selection of experimental conditions, *Mater. Chem. Phys.* 72 (3) (2001) 360–365.
- [40] J.H. Marsh, S.W. Orchard, Voltammetric studies of glassy-carbon electrodes activated in air and steam, *Carbon* 30 (6) (1992) 895–901.
- [41] S. Ranganathan, T.C. Kuo, R.L. McCreery, Facile preparation of active glassy carbon electrodes with activated carbon and organic solvents, *Anal. Chem.* 71 (16) (1999) 3574–3580.
- [42] Y.-J. Song, J.-Y. Kim, K.-W. Park, Synthesis of Pd dendritic nanowires by electrochemical deposition, *Crys. Growth Des.* 9 (1) (2009) 505–507.
- [43] X. Su, C. Qiang, Influence of pH and bath composition on properties of Ni–Fe alloy films synthesized by electrodeposition, *Bull. of Mater. Sci.* 35 (2) (2012) 183–189.
- [44] F.W.S. Lucas, A.R.F. Lima, L.H. Mascaro, Glycerol as additive in copper indium gallium diselenide electrodeposition: morphological, structural and electronic effects, *RSC Adv.* 5 (24) (2015) 18295–18300.
- [45] A.J. Bard, L.R. Faulkner, *Electrochemical Methods—Fundamentals and Applications*, John Wiley & Sons, New York, (1980) p. 51.
- [46] J.T. Matsushima, F. Trivinho-Strixino, E.C. Pereira, Investigation of cobalt deposition using the electrochemical quartz crystal microbalance, *Electrochim. Acta* 51 (2006) 1960–1966.
- [47] I.L. Rakityanskaya, A.B. Shein, Anodic behavior of iron, cobalt, and nickel silicides in alkaline electrolytes, *Russ. J. Electrochem.* 42 (2006) 1208–1212.
- [48] G.Y. Qiao, et al. High-speed jet electrodeposition and microstructure of nanocrystalline Ni–Co alloys, *Electrochim. Acta* 51 (1) (2005) 85–92.
- [49] J.S. Santos, et al. Effect of temperature in cobalt electrodeposition in the presence of boric acid, *Electrochim. Acta* 53 (2007) 644–649.
- [50] K.D. Song, et al. A study on effect of hydrogen reduction reaction on the initial stage of Ni electrodeposition using EQCM, *Electrochim. Commun.* 5 (2003) 460–466.
- [51] A.R. Despic, Deposition and dissolution of metals and alloys. Part. B: mechanisms, kinetics, texture and morphology, in: B.E. Conway, J.O.M. Bockris, et al. (Eds.), *Comprehensive Treatise of Electrochemistry*, vol. 7, Plenum Press, New York, 1973, pp. 483.

- [52] J.M. Elliott, et al. Nanostructured platinum (H-I-ePt) films: effects of electrodeposition conditions on film properties, *Chem. Mater.* 11 (12) (1999) 3602–3609.
- [53] W.Q. Yang, et al. Nanostructured palladium-silver coated nickel foam cathode for magnesium-hydrogen peroxide fuel cells, *Electrochim. Acta* 52 (1) (2006) 9–14.
- [54] C.M.A. Brett, A.M.O. Brett, *Electrochemistry: Principles, Methods and Applications*, Oxford University Press, New York, (1993).
- [55] D.Y. Park, et al. Nanostructured magnetic CoNiP electrodeposits: structure-property relationships, *Electrochim. Acta* 47 (18) (2002) 2893–2900.
- [56] C.A. Ross, Electrodeposited multilayer thin films, *Annu. Rev. Mater. Sci.* 24 (1994) 159–188.
- [57] R.G. Freitas, E.C. Pereira, Giant multilayer electrocatalytic effect investigation on Pt/Bi/Pt nanostructured electrodes towards CO and methanol electrooxidation, *Electrochim. Acta* 55 (26) (2010) 7622–7627.
- [58] D.S. Lashmore, R. Thomson, Cracks and dislocations in face-centered cubic metallic multilayers, *J. Mater. Res.* 7 (9) (1992) 2379–2386.
- [59] P.N. Bartlett, et al. Non-aqueous electrodeposition of p-block metals and metalloids from halometallate salts, *RSC Adv.* 3 (36) (2013) 15645–15654.
- [60] R. Liu, et al. Epitaxial electrodeposition of zinc oxide nanopillars on single-crystal gold, *Chem. Mater.* 13 (2) (2001) 508–512.
- [61] M.J. Chappell, J.S.L. Leach, Passivity and breakdown of passivity of valve metals, in: R.P. Frankenthal, J. e Kruger (Eds.), *The Electrochemical Society*, Princeton, New Jersey, 1978.
- [62] S. Ikonopisov, Theory of electrical breakdown during formation of barrier anodic films, *Electrochim. Acta* 22 (10) (1977) 1077–1082.
- [63] V.P. Parkhutik, J.M. Albella, J.M. Martinez-Duart, Electric breakdown in anodic oxide films, in: B.E. Conway, J.O.M. Bockris, et al. (Eds.), *Modern Aspects of Electrochemistry*, vol. 23, Plenum Press, New York, 1992, pp. 315–391 Chapter 5.
- [64] A.L. Yerokhin, et al. Plasma electrolysis for surface engineering, *Surf. Coat. Technol.* 122 (2–3) (1999) 73–93.
- [65] W. Lee, et al. Fast fabrication of long-range ordered porous alumina membranes by hard anodization, *Nat. Mater.* 5 (9) (2006) 741–747.
- [66] J.S. Santos, et al. Characterization of electrical discharges during spark anodization of zirconium in different electrolytes, *Electrochim. Acta* 130 (2014) 477–487.
- [67] M.S. Sikora, et al. Influence of the morphology and microstructure on the photocatalytic properties of titanium oxide films obtained by sparking anodization in H<sub>3</sub>PO<sub>4</sub>, *Electrochim. Acta* 56 (9) (2011) 3122–3127.
- [68] B.H. Long, et al. Characteristics of electric parameters in aluminium alloy MAO coating process, *J. Phys. D: Appl. Phys.* 38 (18) (2005) 3491–3496.
- [69] G. Sundararajan, L. Rama Krishna, Mechanisms underlying the formation of thick alumina coatings through the MAO coating technology, *Surf. Coat. Technol.* 167 (2–3) (2003) 269–277.
- [70] A.L. Yerokhin, et al. Discharge characterization in plasma electrolytic oxidation of aluminium, *J. Phys. D: Appl. Phys.* 36 (17) (2003) 2110.
- [71] S. Moon, Y. Jeong, Generation mechanism of microdischarges during plasma electrolytic oxidation of Al in aqueous solutions, *Corros. Sci.* 51 (7) (2009) 1506–1512.
- [72] A.I. Maximov, A.V. Khlustova, Optical emission from plasma discharge in electrochemical systems applied for modification of material surfaces, *Surf. Coat. Technol.* 201 (21) (2007) 8782–8788.
- [73] R.O. Hussein, et al. Spectroscopic study of electrolytic plasma and discharging behaviour during the plasma electrolytic oxidation (PEO) process, *J. Phys. D: Appl. Phys.* 43 (2010) 105203.

- [74] F. Monfort, et al. Development of anodic coatings on aluminium under sparking conditions in silicate electrolyte, *Corros. Sci.* 49 (2) (2007) 672–693.
- [75] H. Habazaki, et al. Spark anodizing of [beta]-Ti alloy for wear-resistant coating, *Surf. Coat. Technol.* 201 (21) (2007) 8730–8737.
- [76] A. Yerokhin, et al. Spatial characteristics of discharge phenomena in plasma electrolytic oxidation of aluminium alloy, *Surf. Coat. Technol.* 177 (2004) 779–783.
- [77] P. Gupta, et al. Electrolytic plasma technology: science and engineering—an overview, *Surf. Coat. Technol.* 201 (21) (2007) 8746–8760.
- [78] W. Ma, et al. Preparation and in vitro biocompatibility of hybrid oxide layer on titanium surface, *Surf. Coat. Technol.* 205 (6) (2010) 1736–1742.
- [79] X. Shi, L. Xu, Q. Wang, Porous TiO<sub>2</sub> film prepared by micro-arc oxidation and its electrochemical behaviors in Hank's solution, *Surf. Coat. Technol.* 205 (6) (2010) 1730–1735.
- [80] Y. Yan, et al. Microstructure and bioactivity of Ca, P and Sr doped TiO<sub>2</sub> coating formed on porous titanium by micro-arc oxidation, *Surf. Coat. Technol.* 205 (6) (2010) 1702–1713.
- [81] F. Trivinho-Strixino, et al. Tetragonal to monoclinic phase transition observed during Zr anodisation, *J. Solid State Electrochem.* 1–9 (2012).
- [82] J.S.L. Leach, B.R. Pearson, The Effect of foreign ions upon the electrical characteristics of anodic ZrO<sub>2</sub> films, *Electrochim. Acta* 29 (9) (1984) 1271–1282.
- [83] J.S.L. Leach, B.R. Pearson, Crystallization in anodic oxide-films, *Corros. Sci.* 28 (1988) 43.
- [84] M.V. Diamanti, M.P. Pedeferrri, Effect of anodic oxidation parameters on the titanium oxides formation, *Corros. Sci.* 49 (2) (2007) 939–948.
- [85] R.O. Hussein, et al. Spectroscopic study of electrolytic plasma and discharging behaviour during the plasma electrolytic oxidation (PEO) process, *J. Phys. D-Appl. Phys.* 43 (10) (2010).
- [86] S. Stojadinović, et al. Spectroscopic and real-time imaging investigation of tantalum plasma electrolytic oxidation (PEO), *Surf. Coat. Technol.* 205 (23–24) (2011) 5406–5413.
- [87] C.S. Dunleavy, et al. Characterisation of discharge events during plasma electrolytic oxidation, *Surf. Coat. Technol.* 203 (22) (2009) 3410–3419.
- [88] M.S. Sikora, et al. Theoretical calculation of the local heating effect on the crystallization of TiO<sub>2</sub> prepared by sparking anodization, *Curr. Nanosci.* 11 (3) (2015) 263–270.
- [89] J.M. Albella, I. Montero, J.M. Martinez-Duart, Electron injection and avalanche during the anodic oxidation of tantalum, *J. Electrochem. Soc.: Solid-State Sci. Technol.* 131 (5) (1984) 1101–1104.
- [90] E. Matykina, et al. Investigation of the growth processes of coatings formed by AC plasma electrolytic oxidation of aluminium, *Electrochim. Acta* 54 (27) (2009) 6767–6778.
- [91] A. Yerokhin, A. Pilkington, A. Matthews, Pulse current plasma assisted electrolytic cleaning of AISI 4340 steel, *J. Mater. Process. Technol.* 210 (1) (2010) 54–63.
- [92] W. Chanmanee, et al. Titania nanotubes from pulse anodization of titanium foils, *Electrochim. Commun.* 9 (8) (2007) 2145–2149.
- [93] W. Lee, et al. Structural engineering of nanoporous anodic aluminium oxide by pulse anodization of aluminium, *Nat. Nanotechnol.* 3 (2008) 234–239.
- [94] L. Sottovia, et al. Thin films produced on 5052 aluminum alloy by plasma electrolytic oxidation with red mud-containing electrolytes, *Mater. Res.* 17 (6) (2014) 1404–1409.
- [95] D. Losic, A. Santos, Nanoporous Alumina Fabrication, Structure, Properties and Applications, Springer, New York, (2015) p. 362.
- [96] F. Keller, M.S. Hunter, D.L. Robinson, Structural features of oxide coatings on aluminum, *J. Electrochem. Soc.* 100 (9) (1953) 411–419.

- [97] A. Despic, V.P. Parkhutik, *Electrochemistry of aluminum in aqueous solution and physics of its anodic oxide*, in: J.O.M. Bockris, R.E. White, et al. (Eds.), *Modern Aspects of Electrochemistry*, vol. 20, Plenum Press, New York and London, 1989, pp. 518 Chapter 6.
- [98] J.W. Diggle, T.C. Downie, C.W. Goulding, Anodic oxide films on aluminum, *Chem. Rev.* 69 (3) (1969) 365–382.
- [99] G.E. Thompson, G.C. Wood, *Treatise on Materials Science and Technology*, Academic Press, New York, (1983).
- [100] H. Takahashi, K. Fujimoto, M. Nagayama, Effect of pH on the distribution of anions in anodic oxide-films formed on aluminum in phosphate solutions, *J. Electrochem. Soc.* 135 (6) (1988) 1349–1353.
- [101] G.D. Sulka, Highly ordered anodic porous alumina formation by self-organized anodizing, in: A. Eftekhari (Ed.), *Nanostructured Materials in Electrochemistry*, first ed., Wiley-VCH, Berlin, 2008, pp. 1–116.
- [102] G. Patermarakis, K. Masavetas, Aluminium anodising in oxalate and sulphate solutions. Comparison of chronopotentiometric and overall kinetic response of growth mechanism of porous anodic films, *J. Electroanal. Chem.* 588 (2) (2006) 179–189.
- [103] G. Patermarakis, J. Chandrinos, K. Masavetas, Formulation of a holistic model for the kinetics of steady state growth of porous anodic alumina films, *J. Solid State Electrochem.* 11 (9) (2007) 1191–1204.
- [104] G. Patermarakis, The origin of nucleation and development of porous nanostructure of anodic alumina films, *J. Electroanal. Chem.* 635 (1) (2009) 39–50.
- [105] G. Patermarakis, K. Moussoutzanis, Development and application of a holistic model for the steady state growth of porous anodic alumina films, *Electrochim. Acta* 54 (9) (2009) 2434–2443.
- [106] G. Patermarakis, J. Diakonikolaou, Mechanism of aluminium and oxygen ions transport in the barrier layer of porous anodic alumina films, *J. Solid State Electrochem.* 16 (9) (2012) 2921–2939.
- [107] M. Pashchanka, J.J. Schneider, Uniform contraction of high-aspect-ratio nanochannels in hexagonally patterned anodic alumina films by pulsed voltage oxidation, *Electrochim. Commun.* 34 (2013) 263–265.
- [108] Y. Chen, et al. On the generation of interferometric colors in high purity and technical grade aluminum: an alternative green process for metal finishing industry, *Electrochim. Acta* 174 (2015) 672–681.
- [109] S.-Y. Li, et al. Fabrication of one-dimensional alumina photonic crystals by anodization using a modified pulse-voltage method, *Mater. Res. Bull.* 68 (2015) 42–48.
- [110] J.M.M. Moreno, et al. Constrained order in nanoporous alumina with high aspect ratio: smart combination of interference lithography and hard anodization, *Adv. Funct. Mater.* 24 (13) (2014) 1857–1863.
- [111] T. Kumeria, A. Santos, Nanoporous alumina membranes for chromatography and molecular transporting, In: A. Santos, D. Lasic, (Eds.), *Nanoporous Alumina: Fabrication, Structure, Properties and Applications*, vol. 219, Springer, 2015, p. 362 (Chapter 10), Switzerland.
- [112] A. Brudzisz, A. Brzozka, G.D. Sulka, Effect of processing parameters on pore opening and mechanism of voltage pulse detachment of nanoporous anodic alumina, *Electrochim. Acta* 178 (2015) 374–384.
- [113] W. Lee, The anodization of aluminum for nanotechnology applications, *Jom* 62 (6) (2010) 57–63.
- [114] U.M. Garcia, et al. Comparison and construction of “mild” and “hard” anodisation reactors for the synthesis of porous alumina, *Quím. Nova* 38 (8) (2015) 1112–1116.
- [115] Y. Li, et al. Photoluminescence and optical absorption caused by the F+ centres in anodic alumina membranes, *J. Phys. Condens. Matter* 13 (11) (2001) 2691–2699.
- [116] G.H. Li, et al. Wavelength dependent photoluminescence of anodic alumina membranes, *J. Phys. Condens. Matter* 15 (49) (2003) 8663–8671.

- [117] G.S. Huang, et al. Strong blue emission from anodic alumina membranes with ordered nanopore array, *J. Appl. Phys.* 93 (1) (2003) 582–585.
- [118] G.S. Huang, et al. Dependence of blue-emitting property on nanopore geometrical structure in Al-based porous anodic alumina membranes, *Appl. Phys. A: Mater. Sci. Process.* 81 (2005) 1345.
- [119] J.H. Chen, et al. The investigation of photoluminescence centers in porous alumina membranes, *Appl. Phys. A-Mater. Sci. Process.* 84 (3) (2006) 297–300.
- [120] Z. Li, K. Huang, Optical properties of alumina membranes prepared by anodic oxidation process, *J. Lumin.* 127 (2) (2007) 435–440.
- [121] T. Gao, G.M. Meng, L.D. Zhang, Blue luminescence in porous anodic alumina films: the role of the oxalic impurities, *J. Phys. Conden. Matter* 15 (12) (2003) 2071–2079.
- [122] S. Wang, et al. The effect of nanometer size of porous anodic aluminum oxide on adsorption and fluorescence of tetrahydroxyflavanol, *Spectrochim. Acta A-Mol. Biomol. Spectrosc.* 59 (2003) 1139.
- [123] G.S. Huang, et al. On the origin of light emission from porous anodic alumina formed in sulfuric acid, *Solid State Commun.* 137 (2006) 621.
- [124] X. Liu, et al. Photoluminescence of poly(thiophene) nanowires confined in porous anodic alumina membrane, *Polymer* 49 (9) (2008) 2197–2201.
- [125] C.-S. Hsiao, et al. Synthesis and luminescent properties of strong blue light-emitting  $\text{Al}_2\text{O}_3/\text{ZnO}$  nanocables, *J. Electrochem. Soc.* 155 (5) (2008) K96–K99.
- [126] Y.Q. Cheng, et al. Photoluminescence characteristics of several fluorescent molecules on nanometer porous alumina film, *Acta Chim. Sinica* 62 (2) (2004) 183–187.
- [127] D.F. Qi, et al. Optical emission of conjugated polymers adsorbed to nanoporous alumina, *Nano Lett.* 3 (9) (2003) 1265–1268.
- [128] X.-J. Wu, et al. Electrochemical synthesis and applications of oriented and hierarchically quasi-1D semiconducting nanostructures, *Coord. Chem. Rev.* 254 (9–10) (2010) 1135–1150.
- [129] Y.M. Park, et al. Artificial petal surface based on hierarchical micro- and nanostructures, *Thin Solid Films* 520 (1) (2011) 362–367.
- [130] R.E. Sabzi, K. Kant, D. Lasic, Electrochemical synthesis of nickel hexacyanoferrate nanoarrays with dots, rods and nanotubes morphology using a porous alumina template, *Electrochim. Acta* 55 (5) (2010) 1829–1835.
- [131] A. Hoess, et al. Self-supporting nanoporous alumina membranes as substrates for hepatic cell cultures, *J. Biomed. Mater. Res. A* 100 (9) (2012) 2230–2238.
- [132] S. Thakur, et al. Depth matters: cells grown on nano-porous anodic alumina respond to pore depth, *Nanotechnology* 23 (25) (2012).
- [133] I. Sopyan, A. Fadli, M. Mel, Porous alumina-hydroxyapatite composites through protein foaming-consolidation method, *J. Mech. Behav. Biomed. Mater.* 8 (2012) 86–98.
- [134] E. Bernardo, et al. Porous wollastonite hydroxyapatite bioceramics from a preceramic polymer and micro- or nano-sized fillers, *J. Eur. Ceram. Soc.* 32 (2) (2012) 399–408.
- [135] B. Yuan, et al. Fabrication of porous alumina green bodies from suspension emulsions by gel casting, *Mater. Lett.* 81 (2012) 151–154.
- [136] I. Sopyan, A. Fadli, Floating porous alumina from protein foaming-consolidation technique for cell culture application, *Ceram. Int.* 38 (6) (2012) 5287–5291.
- [137] J. Martin, et al. Tailored polymer-based nanorods and nanotubes by “template synthesis”: from preparation to applications, *Polymer* 53 (6) (2012) 1149–1166.
- [138] D. Gong, et al. Titanium oxide nanotube arrays prepared by anodic oxidation, *J. Mater. Res.* 16 (12) (2001) 3331–3334.

- [139] J. Podporska-Carroll, et al. Antimicrobial properties of highly efficient photocatalytic TiO<sub>2</sub> nanotubes, *Appl. Catal. B: Environ.* 176-177 (2015) 70–75.
- [140] N. Shahzad, et al. Silver-copper nanoalloys—an efficient sensitizer for metal-cluster-sensitized solar cells delivering stable current and high open circuit voltage, *J. Power Sources* 294 (2015) 609–619.
- [141] Z.P. Yang, et al. A high-performance nonenzymatic piezoelectric sensor based on molecularly imprinted transparent TiO<sub>2</sub> film for detection of urea, *Biosens. Bioelectron.* 74 (2015) 85–90.
- [142] R. Hahn, J.M. Macak, P. Schmuki, Rapid anodic growth of TiO<sub>2</sub> and WO<sub>3</sub> nanotubes in fluoride free electrolytes, *Electrochem. Commun.* 9 (5) (2007) 947–952.
- [143] V. Stengl, et al. Preparation, characterization and photocatalytic activity of optically transparent titanium dioxide particles, *Mater. Chem. Phys.* 105 (1) (2007) 38–46.
- [144] A. Kar, K.S. Raja, M. Misra, Electrodeposition of hydroxyapatite onto nanotubular TiO<sub>2</sub> for implant applications, *Surf. Coat. Technol.* 201 (6) (2006) 3723–3731.
- [145] M. Kulkarni, et al. Titanium nanostructures for biomedical applications, *Nanotechnology* 26 (6) (2015) 062002.
- [146] K. Syrek, et al. Effect of electrolyte agitation on anodic titanium dioxide (Ato) growth and its photoelectrochemical properties, *Electrochim. Acta* 180 (2015) 801–810.
- [147] H.-J. Song, et al. The effects of spark anodizing treatment of pure titanium metals and titanium alloys on corrosion characteristics, *Surf. Coat. Technol.* 201 (21) (2007) 8738–8745.
- [148] S.K. Poznyak, D.V. Talapin, A.I. Kulak, Electrochemical oxidation of titanium by pulsed discharge in electrolyte, *J. Electroanal. Chem.* 579 (2) (2005) 299–310.
- [149] S. Daothong, et al. Size-controlled growth of TiO<sub>2</sub> nanowires by oxidation of titanium substrates in the presence of ethanol vapor, *Scr. Mater.* 57 (7) (2007) 567–570.
- [150] D. Regonini, et al. A review of growth mechanism, structure and crystallinity of anodized TiO<sub>2</sub> nanotubes, *Mater. Sci. Eng. R-Rep.* 74 (12) (2013) 377–406.
- [151] V.M. Prida, et al. Temperature influence on the anodic growth of self-aligned Titanium dioxide nanotube arrays, *J. Magn. Magn. Mater.* 316 (2) (2007) 110–113.
- [152] Q. Cai, L. Yang, Y. Yu, Investigations on the self-organized growth of TiO<sub>2</sub> nanotube arrays by anodic oxidation, *Thin Solid Films* 515 (4) (2006) 1802–1806.
- [153] G.A. Crawford, N. Chawla, Porous hierarchical TiO<sub>2</sub> nanostructures: processing and microstructure relationships, *Acta Mater.* 57 (3) (2009) 854–867.
- [154] S. Berger, et al. The origin for tubular growth of TiO<sub>2</sub> nanotubes: a fluoride rich layer between tube-walls, *Surf. Sci.* 605 (19–20) (2011) L57–L60.
- [155] L.V. Taveira, et al. Voltage oscillations and morphology during the galvanostatic formation of self-organized TiO<sub>2</sub> nanotubes, *J. Electrochem. Soc.* 153 (4) (2006) B137–B143.
- [156] L.V. Taveira, et al. Initiation and growth of self-organized TiO<sub>2</sub> nanotubes anodically formed in NH<sub>4</sub>F/(NH<sub>4</sub>)<sub>2</sub>SO<sub>4</sub> electrolytes, *J. Electrochem. Soc.* 152 (10) (2005) B405–B410.
- [157] F. Thebault, et al. Modeling of growth and dissolution of nanotubular Titania in fluoride-containing electrolytes, *Electrochem. Solid State Lett.* 12 (3) (2009) C5–C9.
- [158] K. Yasuda, et al. Mechanistic aspects of the self-organization process for oxide nanotube formation on valve metals, *J. Electrochem. Soc.* 154 (9) (2007) C472–C478.
- [159] G.E. Thompson, et al. Nucleation and growth of porous anodic films on aluminum, *Nature* 272 (5652) (1978) 433–435.
- [160] E. Matykina, et al. Morphologies of nanostructured TiO<sub>2</sub> doped with F on Ti-6Al-4V alloy, *Electrochim. Acta* 56 (5) (2011) 2221–2229.

- [161] S.A.A. Yahia, et al. Effect of anodizing potential on the formation and EIS characteristics of TiO<sub>2</sub> nanotube arrays, *J. Electrochem. Soc.* 159 (4) (2012) K83–K92.
- [162] Y. Alivov, Z.Y. Fan, D. Johnstone, Titanium nanotubes grown by titanium anodization, *J. Appl. Phys.* 106 (3) (2009).
- [163] T. Ruff, R. Hahn, P. Schmuki, From anodic TiO<sub>2</sub> nanotubes to hexagonally ordered TiO<sub>2</sub> nanocolumns, *Appl. Surf. Sci.* 257 (19) (2011) 8177–8181.
- [164] G.K. Mor, et al. Fabrication of tapered, conical-shaped titania nanotubes, *J. Mater. Res.* 18 (11) (2003) 2588–2593.
- [165] J.M. Macák, H. Tsuchiya, P. Schmuki, High-aspect-ratio TiO<sub>2</sub> nanotubes by anodization of titanium, *Angew. Chem. Int. Ed.* 44 (14) (2005) 2100–2102.
- [166] S. Kaneco, et al. Fabrication of uniform size titanium oxide nanotubes: impact of current density and solution conditions, *Scr. Mater.* 56 (5) (2007) 373–376.
- [167] J.M. Macák, P. Schmuki, Anodic growth of self-organized anodic TiO<sub>2</sub> nanotubes in viscous electrolytes, *Electrochim. Acta* 52 (3) (2006) 1258–1264.
- [168] A. Roguska, et al. Synthesis and characterization of ZnO and Ag nanoparticle-loaded TiO<sub>2</sub> nanotube composite layers intended for antibacterial coatings, *Thin Solid Films* 553 (2014) 173–178.
- [169] B. Yuan, et al. Nitrogen doped TiO<sub>2</sub> nanotube arrays with high photoelectrochemical activity for photocatalytic applications, *Appl. Surf. Sci.* 280 (2013) 523–529.
- [170] C. Das, et al. Photoelectrochemical and photocatalytic activity of tungsten doped TiO<sub>2</sub> nanotube layers in the near visible region, *Electrochim. Acta* 56 (28) (2011) 10557–10561.
- [171] E.B. Gracien, et al. Photocatalytic activity of manganese, chromium and cobalt-doped anatase titanium dioxide nanoporous electrodes produced by re-anodization method, *Thin Solid Films* 515 (13) (2007) 5287–5297.
- [172] A. Kubacka, G. Colón, M. Fernández-García, Cationic (V, Mo, Nb, W) doping of TiO<sub>2</sub>-anatase: a real alternative for visible light-driven photocatalysts, *Catal. Today* 143 (3–4) (2009) 286–292.
- [173] J.S.L. Leach, B.R. Pearson, The conditions for incorporation of electrolyte ions into anodic oxides, *Electrochim. Acta* 29 (9) (1984) 1263–1270.
- [174] F. Trivinho-Strixino, F.E.G. Guimaraes, E.C. Pereira, Luminescence in anodic ZrO<sub>2</sub> doped with Eu(III) ions, *Mol. Cryst. Liq. Cryst.* 485 (2008) 766–775.
- [175] E.O. Bensadon, et al. Cubic stabilized zirconium oxide anodic films prepared at room temperature, *Chem. Mater.* 11 (1999) 277–280.
- [176] K. Smits, et al. Luminescence of Eu ion in alumina prepared by plasma electrolytic oxidation, *Appl. Surf. Sci.* 337 (2015) 166–171.
- [177] D. Shen, et al. Effect of cerium and lanthanum additives on plasma electrolytic oxidation of AZ31 magnesium alloy, *J. Rare Earth.* 31 (12) (2013) 1208–1213.
- [178] E. De La Rosa-Cruz, et al. Luminescence and visible upconversion in nanocrystalline ZrO<sub>2</sub>:Er<sup>3+</sup>, *Appl. Phys. Lett.* 83 (24) (2003) 4903–4905.
- [179] R. Naccache, et al. Visible upconversion emission of Pr<sup>3+</sup> doped gadolinium gallium garnet nanocrystals, *J. Nanosci. Nanotechnol.* 4 (8) (2004) 1025–1031.
- [180] H. Eilers, Synthesis and characterization of nanophase yttria co-doped with erbium and ytterbium, *Mater. Lett.* 60 (2) (2006) 214–217.
- [181] A. Boukhachem, et al. Structural, optical, vibrational and photoluminescence studies of Sn-doped MoO<sub>3</sub> sprayed thin films, *Mater. Res. Bull.* 72 (2015) 252–263.
- [182] D. Chandran, et al. Structural, optical, photocatalytic, and antimicrobial activities of cobalt-doped tin oxide nanoparticles, *J. Sol–Gel Sci. Technol.* 76 (3) (2015) 582–591.

- [183] G. Nam, B. Kim, J.-Y. Leem, Facile synthesis and an effective doping method for ZnO:In<sup>3+</sup> nanorods with improved optical properties, *J. Alloy. Compd.* 651 (2015) 1–7.
- [184] W.A. Pisarski, et al. Enhancement and quenching photoluminescence effects for rare earth—doped lead bismuth gallate glasses, *J. Alloy. Compd.* 651 (2015) 565–570.
- [185] S. Shakir, et al. Development of copper doped titania based photoanode and its performance for dye sensitized solar cell applications, *J. Alloy. Compd.* 652 (2015) 331–340.
- [186] R.J.D. Tilley, *Defects in Solids*, John Wiley & Sons Ltda, Hoboken, New Jersey, (2008).
- [187] A.V. Emeline, et al. Photostimulated generation of defects and surface reactions on a series of wide band gap metal-oxide solids, *J. Phys. Chem. B* 103 (43) (1999) 9190–9199.
- [188] E. De La Rosa, et al. Visible light emission under UV and IR excitation of rare earth doped ZrO<sub>2</sub> nano-phosphor, *Opt. Mater.* 27 (7) (2005) 1320–1325.
- [189] P.A. Arsenev, et al. X-ray and thermostimulated luminescence of 0.9ZrO<sub>2</sub>-0.1Y<sub>2</sub>O<sub>3</sub> single-crystals, *Phys. Status Solidi A-Appl. Res.* 62 (2) (1980) 395–398.
- [190] E.D. Wachsman, et al. Spectroscopic investigation of oxygen vacancies in solid oxide electrolytes, *Appl. Phys. A-Mater. Sci. Process.* 50 (6) (1990) 545–549.
- [191] R. Reisfeld, M. Zelner, A. Patra, Fluorescence study of zirconia films doped by Eu<sup>3+</sup>, Tb<sup>3+</sup> and Sm<sup>3+</sup> and their comparison with silica films, *J. Alloy. Compd.* 300 (2000) 147–151.
- [192] H.K. Yueh, B. Cox, Luminescence properties of zirconium oxide films, *J. Nucl. Mater.* 323 (1) (2003) 57–67.
- [193] R. Reisfeld, et al. Rare earth ions, their spectroscopy of cryptates and related complexes in sol-gel glasses, *Opt. Mater.* 24 (1–2) (2003) 1–13.
- [194] L.E. Depero, et al. Correlation between crystallite sizes and microstrains in TiO<sub>2</sub> nanopowders, *J. Cryst. Growth* 198–199 (Part I) (1999) 516–520.
- [195] V. Guidi, et al. Effect of dopants on grain coalescence and oxygen mobility in nanostructured titania anatase and rutile, *J. Phys. Chem. B* 107 (2003) 120–124.
- [196] A. Mattsson, et al. Adsorption and solar light decomposition of acetone on anatase TiO<sub>2</sub> and niobium doped TiO<sub>2</sub> thin Films, *J. Phys. Chem. B* 110 (3) (2006) 1210–1220.

# Nanostructured Films: Langmuir–Blodgett (LB) and Layer-by-Layer (LbL) Techniques

R.F. de Oliveira\*, A. de Barros\*\*, M. Ferreira<sup>†</sup>

\*BRAZILIAN CENTER FOR RESEARCH IN ENERGY AND MATERIALS, BRAZILIAN NANOTECHNOLOGY NATIONAL LABORATORY, CAMPINAS, SÃO PAULO, BRAZIL;

\*\*STATE UNIVERSITY OF CAMPINAS, INSTITUTE OF CHEMISTRY, CAMPINAS, SÃO PAULO, BRAZIL; <sup>†</sup>FEDERAL UNIVERSITY OF SÃO CARLOS, CENTER FOR SCIENCES AND TECHNOLOGY FOR SUSTAINABILITY, SOROCABA, SÃO PAULO, BRAZIL

## CHAPTER OUTLINE

<b>4.1</b>	<b>Introduction .....</b>	<b>106</b>
<b>4.2</b>	<b>Langmuir–Blodgett Technique.....</b>	<b>106</b>
4.2.1	History.....	106
4.2.2	Description of the Technique .....	108
4.2.3	Pressure and Surface Potential.....	109
4.2.4	Langmuir Monolayer Deposition: Transfer Ratio.....	111
4.2.5	Applications.....	113
<b>4.3</b>	<b>Layer-by-Layer Technique .....</b>	<b>114</b>
4.3.1	History.....	114
4.3.2	Description of the Technique .....	114
4.3.3	Mechanisms of LbL Film Formation .....	115
4.3.4	Spray- and Spin-LbL Methods.....	117
4.3.5	Characterization Methods .....	118
4.3.6	Applications.....	118
<b>4.4</b>	<b>Final Considerations.....</b>	<b>119</b>
<b>Acknowledgment.....</b>		<b>119</b>
<b>References .....</b>		<b>120</b>

## 4.1 Introduction

Ultrathin film fabrication is an important process in nanoscience and nanotechnology, as demonstrated by the large number of publications about manufacturing new thin-film materials and their applications in a wide range of fields, such as biotechnology, electronics, medicine, and so on [1–3]. Of the existing film fabrication methods, Langmuir–Blodgett (LB) and layer-by-layer (LbL) techniques are notable because they allow the film thickness and architecture to be controlled at the molecular level. For example, films with a high degree of molecular organization can be obtained, and the spatial arrangement of the film material can be investigated by the LB technique. The LbL method, in turn, is advantageous because of the simplicity of the film deposition process and the large variety of materials that can be used.

In addition to the technological importance of nanostructured films, fundamental questions about their formation are of great scientific interest because a wide variety of materials and film architectures are possible. The LB technique, which was developed in the mid-1900s, and the LbL method, which was discovered just over 20 years ago, are still attracting the interest of specialized research groups worldwide.

In this chapter, the key aspects of the LB and LbL techniques in ultrathin film fabrication, including the film formation mechanisms, main characterization techniques and applications, are addressed to provide the reader with an overview of these important nanotechnological processes.

## 4.2 Langmuir–Blodgett Technique

### 4.2.1 History

The first surface chemistry experiments that stimulated further research on ultrathin film formation were performed in the 18th century. According to Behroozi et al. [4], during one of his overseas journeys, Benjamin Franklin (1706–90) noted that the waves near ships with oil leakages appeared to be damped. To investigate this phenomenon, he performed experiments on the damping effect of oil on water, which resulted in the first publication in the field in 1774. In one of these experiments, Franklin poured a small known amount of oil on a water surface and observed a decrease in the wind turbulence within a certain distance of the oil-coated area [5].

At that time, Franklin focused only on the wave-damping phenomenon and did not realize that this effect was related to the formation of a monomolecular layer at the surface. Dividing the oil volume by the area it occupies gives the oil layer thickness, which is on the nanometer scale [6]. This simple calculation was not performed until years later, when Lord Rayleigh (1842–1919) determined the thickness of oil layers. However, he did not know that the calculated value corresponded exactly to the length of the molecule used in the experiments, indicating that the layer was one molecule thick [6].

During the same period, Agnes Pockels (1862–1935) made an important advance in the science of monolayer formation by creating a prototype of the Langmuir trough (Fig. 4.1). This prototype was a primitive device in which barriers were used both to compress oil molecules scattered on a water surface and to remove impurities from the surface. Pockles also developed a method for measuring the surface tension of water in a container [5]. In recognition of these important contributions, Rayleigh helped Pockles publish her results in the prestigious journal *Nature*. A few years later, Irving Langmuir (1881–1957) introduced the concept of molecular conformations.

For Langmuir, molecules were asymmetrical and would therefore have identical orientations on the water surface, depending on their hydrophilic or hydrophobic character. Langmuir also estimated the size of the molecule used in his experiments, which had a large impact on the scientific community at the time. These studies motivated Langmuir to investigate monolayer formation on water surfaces, and he was awarded the Nobel Prize in Chemistry for this work in 1932. Langmuir suggested that the monolayers formed on a water surface could be transferred to a solid surface. His assistant Katherine Blodgett (1898–1979) performed the corresponding experiments, and the initial results were published in 1934 and 1935. Blodgett was awarded her own Nobel Prize for this work. During this period, the LB monolayer deposition method was developed. Several years later, Langmuir and Vincent Schaefer (1906–93) studied protein deposition on solid substrates and discovered a new approach called the Langmuir–Schaefer (LS) method for depositing Langmuir monolayers. In the LS method, a Langmuir monolayer is deposited on a surface horizontally instead of vertically, as in LB films [5,7].

The formation of Langmuir monolayers and LB and LS films was not actively studied for a long time because they had no practical application. Around 1980, research interest

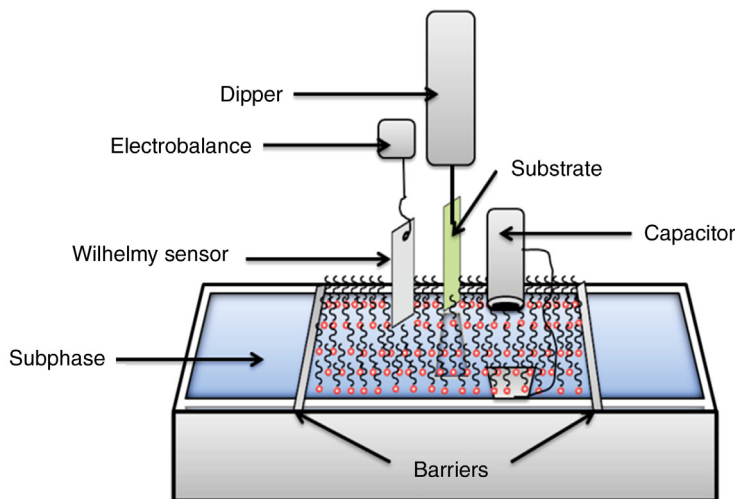


**FIGURE 4.1** Schematic representation of a Langmuir trough and its accessories.

in this area was renewed by the use of LB films in organic electronics. Since then, physicists, chemists, biologists, and engineers have actively collaborated to develop this technique using various types of materials for a wide range of applications.

#### 4.2.2 Description of the Technique

As illustrated in Fig. 4.1, the Langmuir trough is composed of an inert material, typically Teflon. The trough accessories include mobile barriers that compress the molecules spread at the air–water interface, a device (dipper) that immerses the substrate for the monolayer deposition, a Wilhelmy sensor that measures the surface tension of the subphase, and a capacitor that measures the surface potential.

Langmuir monolayers and LB films are fabricated by pouring a known volume of a given solution at the air–water interface. Ideally, the material in the solution is soluble in an organic solvent or solvent mixture. During film fabrication, the solvent is evaporated after a given amount of time, and the molecules are then compressed until maximum order is achieved.

Initially, the materials employed in the Langmuir technique were necessarily amphiphilic compounds, that is, molecules with a polar head group (hydrophilic) and a non-polar tail group (hydrophobic) essentially insoluble in polar solvents. These compounds self-organize with their polar part in the water and nonpolar part in the air. The hydrophobic portion of these molecules generally consists of aliphatic chains, which reduce its solubility in the aqueous subphase. The hydrophilic part is responsible for spreading the molecules because it interacts strongly with the water. The molecular orientation of these molecules at the air–water interface minimizes their free energy [5,7–9].

A typical isotherm for amphiphilic molecules is illustrated in Fig. 4.2. Before compression by the barriers, the molecules are initially in the gas phase (stage A); they are fully

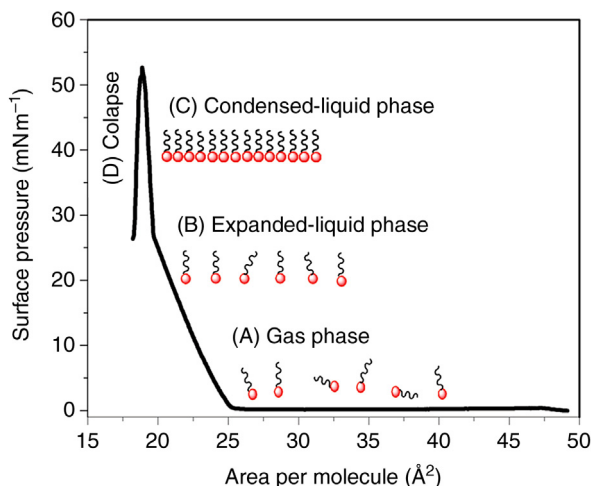


**FIGURE 4.2** Typical surface pressure isotherm for a stearic acid monolayer.

dispersed and do not interact. As the molecules are compressed, their proximity leads to the formation of an expanded liquid phase (stage B). When the molecule surface density increases, the regular arrays in the film form, resulting in a compact structure called the condensed-liquid phase (stage C). However, further compression of the monolayer causes molecular disorder and a phenomenon commonly called collapse (stage D) [5,7–9].

The use of LB films composed of common amphiphilic molecules is limited by their properties. To search for new technological applications of LB films, researchers have investigated the use of various materials, including polymers [10–13], phospholipids [14–16], enzymes [17–20], and peptides [21,22]. However, the formation of monolayers of other types of molecules is not trivial because they might not be completely soluble in volatile organic solvents or might be unstable, making them difficult to spread at the surface and consequently deposit homogeneously on a substrate [8].

To minimize these difficulties, several strategies have been employed depending on the type of film material. For example, miscible solvents can be used, or the material can be spread in the subphase [10,23]. The organization, homogeneity, deposition quality, and formation of Langmuir monolayers and LB films can be evaluated experimentally by characterization methods such as Brewster angle microscopy [24,25], polarization modulation infrared reflection-absorption spectroscopy [24,26,27], and atomic force microscopy (AFM) [28,29].

#### 4.2.3 Pressure and Surface Potential

The pressure and surface potential of LB monolayers are measured as a function of the average molecular area occupied at the air–water interface to assess molecular packing and order [5,7,9]. These characterizations are fundamental and necessary for evaluating the quality of the Langmuir film formed at the interface. To determine the surface pressure of a Langmuir monolayer, the material is spread on an aqueous subphase, and the surface pressure is measured by detecting variations in the liquid surface tension, as shown by the following equation:

$$\pi = \gamma_0 - \gamma_A \quad (4.1)$$

where  $\gamma_0$  and  $\gamma_A$  are the surface tensions of pure water and due to the monolayer, respectively [5,7].

The surface pressure isotherms are obtained using a Wilhelmy sensor, which is suspended by a wire from an electrobalance and partially immersed in the water. The electrobalance measures the force exerted to keep the sensor stationary as the surface tension varies. The vertical force exerted by the surface tension is detected by the balance and converted into a voltage [5,7]. A typical isotherm of an amphiphilic material (stearic acid) is illustrated in Fig. 4.2.

One disadvantage of this technique is related to the contact angle ( $\theta$ ) formed between the liquid subphase and the balance sensor, as shown in Fig. 4.3 [5,7]. Another disadvantage is that the position of the Wilhelmy sensor relative to the barrier positions can affect the pressure isotherm during monolayer formation. These problems can be minimized by placing the sensor in the center of the trough [8].

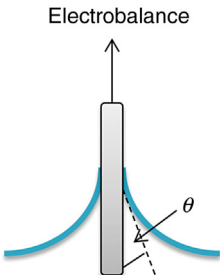


**FIGURE 4.3 Schematic representation of the contact angle between the Wilhelmy sensor and the subphase.**

The surface pressure isotherms might exhibit hysteresis. This phenomenon arises due to differences in the molecular behavior during compression and decompression. Specifically, as the barriers compress the molecules, the area that they occupy decreases, resulting in an increase in their interactions and consequently an increase in the surface pressure. When the monolayer is decompressed, the surface pressure gradually decreases, but not in the same way that it increases during the initial compression. The hysteresis in the area occupied by the molecules indicates that some of the material is lost to the aqueous subphase or to aggregation. A large hysteresis implies that the stability of the monolayer is low. Another method for characterizing monolayer stability is based on compressing the monolayer to the maximum pressure at which molecule order is observed for long periods of time. If large variations in the area are observed during this period, the monolayers are unstable and therefore unsuitable for film deposition [7–9].

Another widely used technique for characterizing Langmuir films is surface potential ( $\Delta V$ ) measurements. Surface potential is defined as the difference in the potentials of the aqueous subphase covered with the monolayer and the pure aqueous subphase. Surface potential can be measured using a Kelvin probe or a vibrating plate capacitor, which is more common [5,7–9,30]. In the vibrating capacitor method, surface potential is measured by a plate positioned above the water that detects the vibrations of the spread molecules. The potential of the pure water is used as a reference and is measured by a metal plate immersed in the subphase. The  $\Delta V$  value is the change in the permanent electric dipoles at the air–water interface due the presence of a partially or fully ionized film. To gain insight into the effect, theoretical models were developed to relate the measured potential to the dipole moments of the film material. The most commonly used model was developed by Demchak and Fort (DF) [30]. In this model, the Langmuir monolayer is considered to be a three-layer capacitor in which each layer has a different relative permittivity, as illustrated in Fig. 4.4 [8,9,30].

According to the DF model, the surface potential is given by:

$$\Delta V = \frac{1}{A\epsilon_0} \left( \frac{\mu_1}{\epsilon_1} + \frac{\mu_2}{\epsilon_2} + \frac{\mu_3}{\epsilon_3} \right) + \Psi_0 \quad (4.2)$$

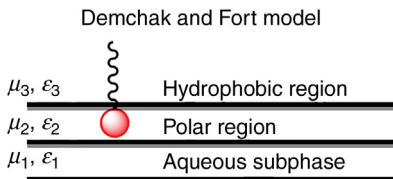


**FIGURE 4.4 Capacitor model of Demchak and Fort for a Langmuir monolayer.** Adapted from P. Dynarowicz-Latka, A. Dhanabalan, O.N. Oliveira Jr., Modern physicochemical research on Langmuir monolayers, *Adv. Colloid Interface Sci.* 91 (2) (2001) 221–293 [8].

where  $A$  is the average area per molecule;  $\epsilon_0$  is the vacuum permittivity;  $\mu_1$ ,  $\mu_2$ , and  $\mu_3$  are the dipole moments attributed to the polarization and reorientation of the molecules; and  $\epsilon_1$ ,  $\epsilon_2$ , and  $\epsilon_3$  are the permittivities due to changes in the dipole moments of the hydrophilic and hydrophobic groups. More specifically, the component  $\mu_1/\epsilon_1$  corresponds to the reorientation of water molecules that is induced by the presence of the monolayer,  $\mu_2/\epsilon_2$  is the contribution of the hydrophilic portion of the molecule,  $\mu_3/\epsilon_3$  is the contribution of the hydrophobic portion, and  $\Psi_0$  is attributed to the electrical double layer that forms when the film is partially or fully ionized [5,7–9]. In polymer films, for example, it is impossible to estimate values for  $\mu_1/\epsilon_1 + \mu_2/\epsilon_2 + \mu_3/\epsilon_3$  and  $\Psi_0$ , mainly because the polymer is often processed under different conditions, which induce structural changes in the polymer chain. These changes make it difficult to explain the experimental results using a theoretical surface potential model.

Molecular behavior during the surface potential measurement can be described as follows. Initially, the molecules spread on the subphase cover an area so large that their interactions are too weak to induce a detectable change in the surface potential of the aqueous subphase. During compression, the area covered by the molecules reaches a critical value at which the potential is no longer zero, and it increases sharply as the area per molecule is further decreased. Due to this critical area, surface potential measurements are more sensitive to the film organization than surface pressure measurements [5,7–9]. Fig. 4.5 shows a typical surface potential curve for stearic acid based on the DF model, which considers the changes in the dielectric constants of the three layers as functions of the area per molecule.

#### 4.2.4 Langmuir Monolayer Deposition: Transfer Ratio

Langmuir monolayers can be deposited by two methods, the vertical (LB) and horizontal (LS) methods, which are as illustrated in Fig. 4.6. The vertical method is more commonly used because the amount of material deposited on the substrate cannot be effectively controlled during horizontal deposition, that is, it is unknown if the entire surface is actually covered by the monolayer [5,31]. The effectiveness of the monolayer deposition process is described by the transfer ratio (TR). A TR of close to 1.0 implies that the material exhibits good adhesion to the substrate when it is immersed in and then removed from the subphase. However, a low TR value indicates that the material does not adhere to the

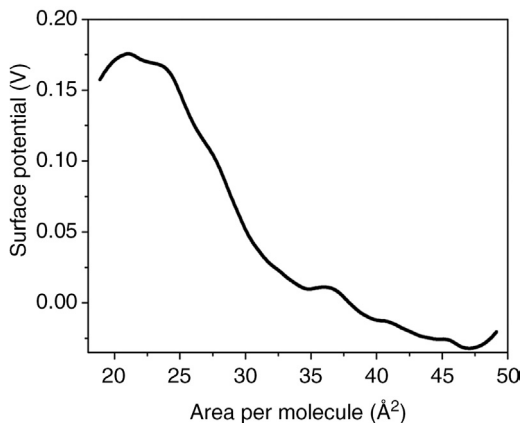


FIGURE 4.5 Typical surface potential isotherm for a stearic acid monolayer.

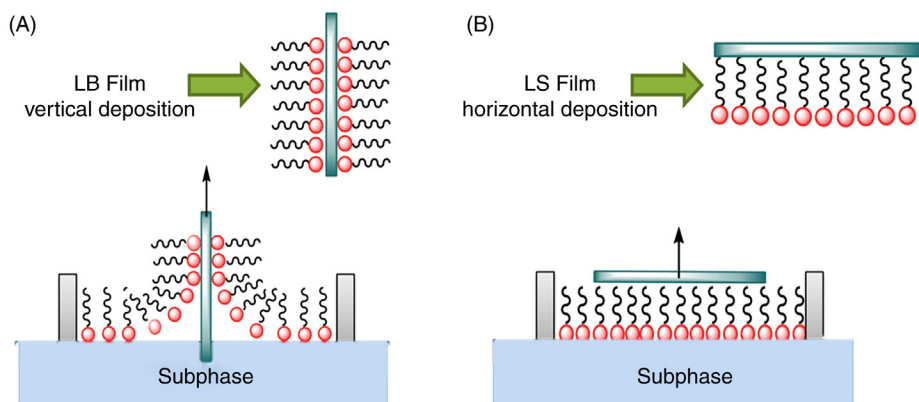


FIGURE 4.6 Schematic representation of the different Langmuir monolayer deposition methods. (A) Vertical deposition (LB) and (B) horizontal deposition (LS).

substrate well, and consequently, the second monolayer deposited on the film might be easily removed, resulting in a low-quality film [7]. The TR value is calculated using the following equation:

$$\tau = \frac{A_L}{A_S} \quad (4.3)$$

where  $A_L$  is the decrease in the area occupied by the molecules at the air/water interface (at constant pressure) and  $A_S$  is the area of the substrate covered with the monolayer [7].

Different LB film architectures can be obtained by varying the deposition parameters, substrate characteristics, and film material. The possible architectures are called X-, Y-, and Z-type films and are illustrated in Fig. 4.7. Y-type LB films are generally obtained when substrates with hydrophilic surfaces are used. For the X- and Z-type films, deposition

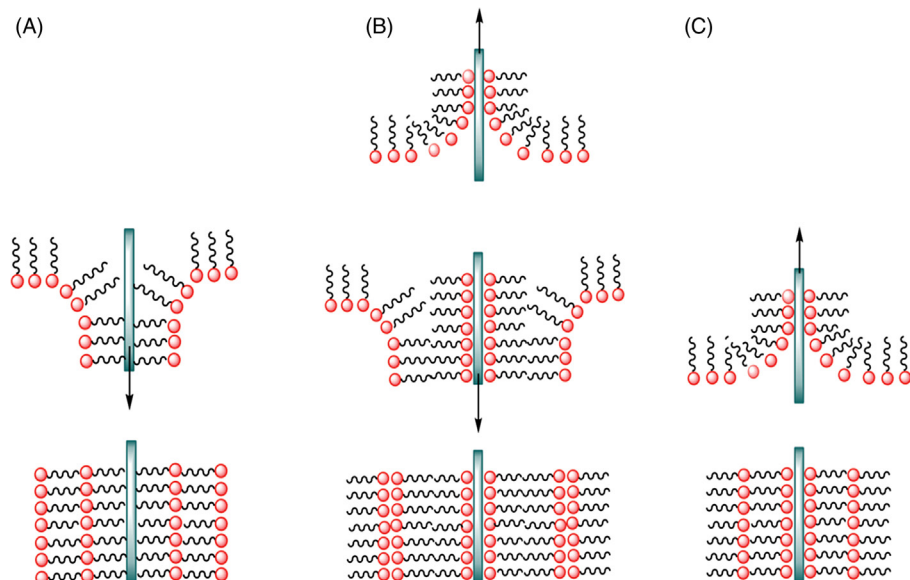


FIGURE 4.7 Different LB film types: X (A), Y (B), and Z (C).

occurs preferentially during substrate immersion and removal from the subphase, which favors the formation of films in which the polar and nonpolar groups in adjacent monolayers interact. It is important to note that Z-type films form on hydrophilic substrates, whereas X-type films form onto hydrophobic substrates [5,7,32].

#### 4.2.5 Applications

Numerous applications of LB and LS films, such as nonlinear optical and piezoelectric devices [33,34], chemical sensors and biosensors [10,12,13,17–20], cell membrane applications [35–37], and so on [1,38–40] have been reported in the literature.

LB and LS films are widely used in sensors, biosensors, and cell membrane model studies because their molecular organization can be highly controlled, which results in satisfactory experimental results. In one study, enzymes were immobilized on lipid monolayers of LS films, and the catalytic activity of the biomolecule-containing films in sucrose hydrolysis was evaluated. The experimental results indicated that 78% of the invertase enzymatic activity was maintained in this system [17]. In another study, the interactions between mucin and chitosan were studied using dimyristoyl phosphatidic acid (DMPA) Langmuir monolayers as cell membrane models. The experimental results for the DMPA–chitosan–mucin Langmuir and LB films indicated that a mucin–chitosan complex forms via electrostatic interactions that are crucial for the mucoadhesion mechanism [35].

De Barros et al. developed electrochemical sensors composed of polyaniline and montmorillonite clay using LB technique for the detection of copper, lead, and cadmium

metal ions. The Langmuir isotherms and ultraviolet-visible (UV-vis) absorption spectroscopy, Fourier transform infrared spectroscopy and Raman spectroscopy results indicated the existence of synergistic molecular-level interactions between the film materials, which were favorable for the sensor performance, that is, the sensors had high sensitivity and a low detection limit on the order of  $\mu\text{g L}^{-1}$  [10]. Thin films of polythiophene derivatives were fabricated using LS and spin-coating techniques to compare the effect of the deposition method on the electrical properties of the films. The experimental results revealed an electrochromic effect during analysis, and the electrical and electrochemical measurements revealed the effects of the film organization on its electrical properties [11].

For further reading on the theoretical concepts and applicability of this technique, the reader is referred to the work of M. Petty titled “Langmuir–Blodgett Films: An Introduction” and other texts in this field.

## 4.3 Layer-by-Layer Technique

### 4.3.1 History

The LbL method became widely spread during the 1990s due to several publications by G. Decher [41–46], including a paper in the prestigious journal *Science* [46] in 1997. This technique, however, was first described in 1966 by R.K. Iler as a study titled “Multilayers of Colloidal Particles” [47]. This study showed that multilayer films could be obtained by alternately immobilizing oppositely charged colloidal particles. Iler observed that the thicknesses of alternating cationic (alumina) and anionic (silica) layers on glass could be controlled and observed by the change in color of light reflected on the substrate surface [47].

The LbL technique was further developed in several subsequent studies that described, for example, the successive deposition of inorganic ionic compounds [48] and polyanion adsorption on cellulosic fibers containing preadsorbed polycations [49], among other systems [50]. Decher contributed not only to the rediscovery of this technique but also to its use as an alternative to the LB method for fabricating nanostructured films. He also demonstrated that it could be used to deposit films of various types of materials, including bipolar amphiphilic molecules [42], polyelectrolytes [42,44], and proteins and DNA [43,44]. According to Decher and Schlenoff [50], the field of nanostructure fabrication via the LbL method is still popular and growing more than 20 years after the technique was reintroduced.

### 4.3.2 Description of the Technique

As the terminology itself suggests, the LbL technique is a method for obtaining nanostructured films by successively depositing layers of different materials, such as polymers, nanoparticles, enzymes, cells, and so on, with highly controlled thicknesses at the molecular level. The ultrathin films fabricated using LbL method have nanostructures that can be used in optical devices, electronics, sensors, and biotechnological applications [2,3,51,52].

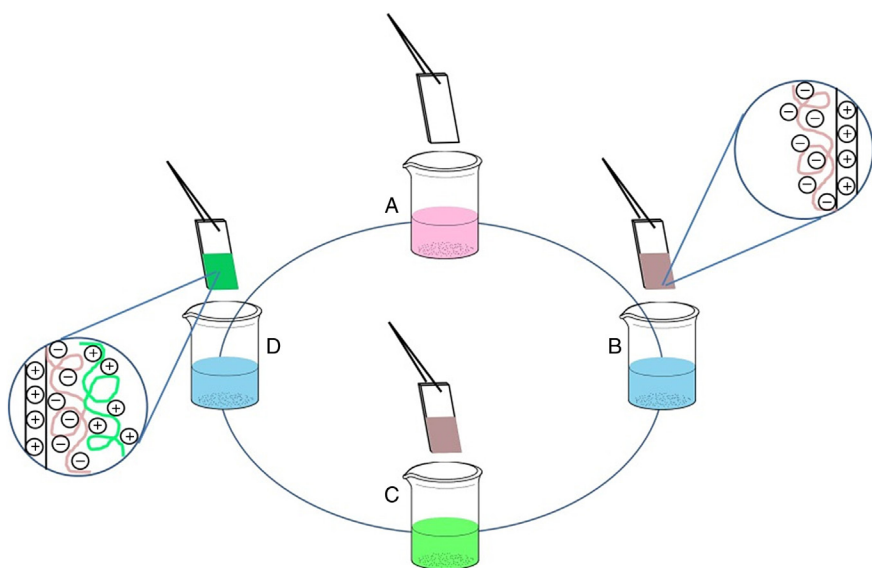


**FIGURE 4.8** Schematic representation of the traditional LbL deposition process.

Unlike the sophisticated LB method, the main advantages of the LbL technique are its simplicity and low cost. Fig. 4.8 illustrates the LbL deposition process and film formation.

Initially, a substrate is immersed in a solution containing charged species, for example, polyanions (step A). During this step, the anionic polyelectrolyte adsorbs on the substrate surface via simple electrostatic interactions, resulting in the formation of a negative charge network on the surface. Then, the substrate is immersed in a rinsing solution (step B) to remove weakly adsorbed material to prevent contamination of the next solution. The substrate is subsequently immersed in a polycation solution to generate a new network of positive charges on the surface (step C). Finally, the substrate is again immersed in a rinsing solution (step D). Thus, a bilayer of the ionic materials, in this case polyelectrolytes, is obtained. This procedure can be repeated as many times as desired to obtain multilayer films with controlled structures and thicknesses.

#### 4.3.3 Mechanisms of LbL Film Formation

The multilayer formation process can be divided into two stages: (1) the initial adsorption of the material on the surface (fast process) and (2) the relaxation of the adsorbed layer (slower process) [53]. In the first stage, the polyelectrolyte segments diffuse through the solution to adsorb on the surface until a repulsive electrical potential is generated, preventing the adsorption of more chains [54]. At this point, the polyelectrolyte layer has reached saturation, which is only possible when the adsorption rate is not limited, that is, when the species concentration in solution is much larger than the saturation concentration of the adsorbed species [46,53,54]. In this stage, the polyelectrolyte segments adsorb on the surface because of favorable electrostatic interactions, and the surface becomes

oppositely charged, which enables the adsorption of new polyions with opposite charges to the surface [46].

When the initial substrate charge density is small, multiplication of surface functionality occurs. In this process, the charge density of the first adsorbed layer is larger than that of the substrate, which favors the subsequent adsorption of oppositely charged species [46]. It should be noted that the surface charge and roughness of the substrate (glass, quartz, silicon, paper, cloth, etc.) might affect the deposition of the first few layers [53]. The influence of the substrate on the deposited layers becomes negligible after a few deposition cycles. Then, the film growth and structure are fundamentally governed by the film materials. This important feature allows a film to be fabricated on a different surface for a given application than on the substrate that was used to study the film properties [50].

During the second stage of the layer formation process, the conformations of the adsorbed polyelectrolyte chains change as they relax [54]. The relaxation process explains the interpenetration of adjacent polyelectrolyte chains observed in experimental studies. However, it is assumed that the adsorbed segments do not diffuse along the surface during LbL film formation because this process would involve the breaking of many electrostatic bonds simultaneously, which requires more energy than that gained by thermodynamic contributions to the system and is therefore highly improbable [54].

Although electrostatic interactions are involved in the formation of polyelectrolyte films (Fig. 4.8), they are not the only interactions that can be exploited in LbL film formation. Depending on the characteristics of the selected materials, covalent bonds, van der Waals forces, and hydrogen bonds can also govern the film formation mechanism, further enhancing the versatility of the LbL technique [55].

Hydrogen bonds, for example, are sensitive to the medium and can be broken and reformed by changing the pH. This phenomenon is observed in the production of some porous films, such as polyacid acrylic (PAA)/polyvinyl pyridine (PVP) multilayers. In a basic solution, the PAA layers dissolve, allowing the PVP layers to subsequently rearrange to yield the porous structure [56]. The film characteristics, such as the pore size and pore size distribution, can also be tuned by varying the pH and temperature of the solution and the immersion time and nature of the substrate during treatment in a basic solution [55,57]. Hydrogen bonds also enable the production of multilayers of a single material; for example, films can be fabricated from a dendrimer with carboxylic acid groups that can act as both hydrogen bond donors and acceptors [56]. Other examples of different multilayer film formation mechanisms include charge transfer reactions (electron donor and acceptor materials are alternately deposited) [58] and covalent bonding [59].

In addition to these different interactions, other strategies, such as using avidin–biotin biospecificity [60], DNA hybridization [61], and other interactions [2,55,62,63], have been employed to obtain LbL films. In LbL films, different interactions not only drive the film formation mechanism but also participate to a minor degree in films formed via electrostatic interactions, influencing their properties, such as their stability, morphology, and thickness [53].

Of all the characteristics of a film, its thickness might be one of the most important [50]. The thickness depends on the deposition conditions of each layer, which in turn influence the subsequently deposited layer and, consequently, the final film properties, including the roughness, uniformity, chemical resistance, and so on. The intrinsic film material properties, such as the nature and density of the charged groups; the solution characteristics, such as the concentration, pH, and ionic strength; the fabrication operating parameters, such as the deposition and rinse times; and many other factors affect the film formation. For example, studies indicate that in general, increasing the ionic strength of a polyelectrolyte solution causes the polymer chains to contract, which leads to an increase in the surface density of the adsorbed segments and thus to an increase in film thickness [54]. However, exposing a polyelectrolyte film to a concentrated salt solution after fabrication leads to a decrease in film roughness due to increased chain mobility [50]. Moreover, changing the solution pH can alter the degree of dissociation and the conformation of some polyelectrolytes and also the enzymatic activity of biological films. Although many factors in the deposition process affect the film properties, understanding their effects are crucial to optimizing the film deposition process.

#### 4.3.4 Spray- and Spin-LbL Methods

In addition to the conventional immersion method, other LbL film fabrication procedures have been reported in the literature. In the spin-assisted LbL method, the film materials are alternately added to a substrate rotating at a given speed, whereas in the spray-LbL method, the materials are sprayed in small liquid particles on the substrate surface. These methods are depicted in Fig. 4.9.

These techniques can be advantageous over the conventional method and therefore more appropriate, depending on the desired film characteristics and application. The

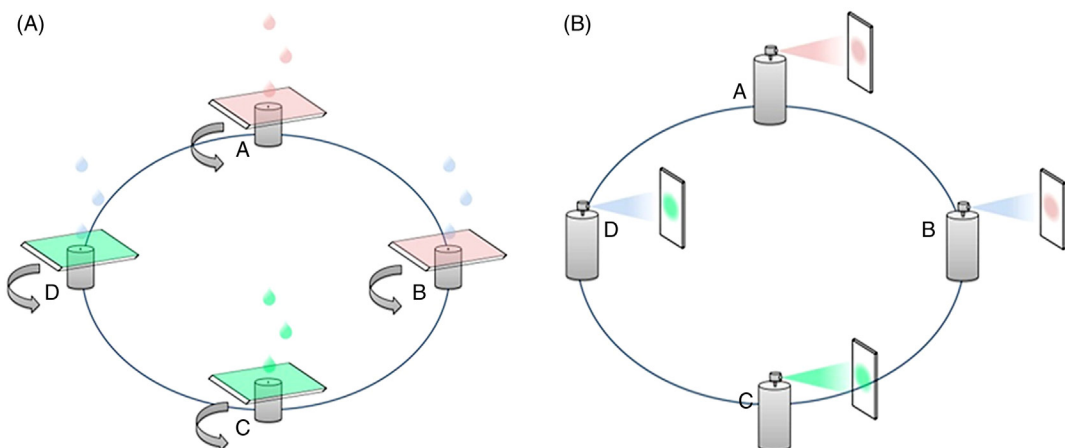


FIGURE 4.9 Novel LbL deposition strategies. (A) Spin-assisted LbL and (B) spray-LbL.

spin-assisted LbL and spray-LbL methods are faster than the conventional immersion method, particularly in the production of thick (micrometer) films because they do not depend on the diffusion kinetics of the species in the liquid medium. They also consume smaller amounts of material. However, the spin-assisted LbL method can only be used with flat substrates and produces nonuniform films on large-area substrates. The spray technique is more appropriate for these types of substrates [64]. The characteristics of films produced via the spray and conventional methods are very similar, whereas films produced by the spin-assisted LbL method are generally smoother due to decreased chain interpenetration, for example, in the case of polyelectrolytes [64]. It should be noted that all three deposition methods can be automated, which increases the reproducibility of the fabricated films [65].

### 4.3.5 Characterization Methods

Regardless of the deposition procedure, materials, and desired application, the characterization of LbL films is frequently necessary. In particular, UV-vis spectroscopy, zeta potential determination, and quartz crystal microbalances are commonly used to monitor the film during the deposition steps. For example, the amount of material adsorbed in each step can be determined by UV-vis monitoring in which the absorption band intensities of compounds with chromophore groups are measured as a function of the number of deposited layers. However, this and some other techniques require the film to be dried after rinsing, which might not be desirable depending on the application. Alternatively, film growth can be monitored *in situ* by a quartz crystal microbalance. In this method, the frequency of a resonant quartz crystal changes in response to changes in the material mass, enabling the amount of material adsorbed during each step to be measured. This technique allows film growth to be monitored when UV-vis spectroscopy is not possible, for example, when the material of interest absorbs only at frequencies outside the ultraviolet and visible regions [50].

Several other techniques, such as infrared spectroscopy, Raman spectroscopy, AFM, scanning electron microscopy (SEM), and transmission electron microscopy (TEM), are often used to characterize LbL films. Raman and infrared spectroscopies are used to determine the functional groups present in the film materials by recording their vibrational modes. Techniques such as AFM, SEM, and TEM are used to analyze film morphology, including its surface roughness, uniformity, and so on. The reader is referred to other chapters in this book for more information on various nanostructure characterization techniques.

### 4.3.6 Applications

Although the LbL technique has been widely used to fabricate polyelectrolyte films, it is currently employed for many different materials and applications. A few of the commonly used synthetic and natural materials include polypeptides, proteins,

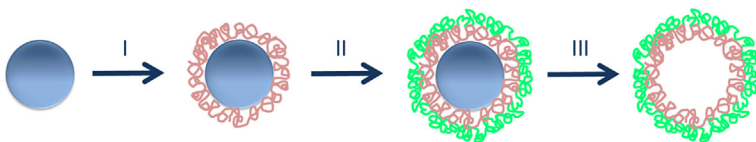


**FIGURE 4.10** Schematic illustration of the fabrication of spherical shells by the LbL method.

enzymes, polysaccharides, metallic nanoparticles, oxides and clays, DNA, biopolymers, dendrimers, and carbon nanotubes [2,50,66–71]. LbL films are employed in biotechnological applications, such as antibacterial and antiadhesive biopolymer surface coatings [72], sensors [66,71] and electrochemical biosensors [73–75], and also in biomedical applications, such as self-supporting polymeric shells for controlled drug delivery [53]. In the latter application, polystyrene, polylactic acid and silica particles are coated with polyelectrolyte or biopolymer multilayers (steps I and II, Fig. 4.10) and then decomposed in an appropriate solvent to obtain spherical shells (step III, Fig. 4.10). The drug of interest is introduced into the shells via a stimulus, such as a change in the temperature, magnetic field, or pH, and then released at the target using the same stimulus [53]. Fig. 4.10 illustrates the formation process of these spherical shells.

LbL films are also used in electronic devices; they serve as charge injection layers in light-emitting diodes [76], are employed in solar cells [77], constitute the active layer in field-effect transistors [78], and are used in memory applications [79]. In addition, these films are used as ion-exchange membranes in fuel cells [80] and as antireflective surface coatings in optical applications [81], among other applications [2,3,9].

For a more comprehensive study of the concepts and applicability of the LbL technique, the reader is referred to the publication of G. Decher titled “Multilayer Thin Films: Sequential Assembly of Nanocomposite Materials, 2nd Edition” and other texts in this field.

## 4.4 Final Considerations

The unique properties of nanostructured films constructed from various materials and the versatility of the LB and LbL methods have contributed considerably to the development of nanotechnology. LB and LbL methods have enabled the use of various materials with diverse architectures in many technological applications, from electronics to medicine. It should be noted that these methods have limitations and are thus complementary. Although ultrathin film fabrication has been extensively studied, it is a growing and popular field with many possibilities yet to be explored.

## Acknowledgment

The authors thank *Bianca Martins Estevão* for producing some of the figures.

## References

- [1] K. Ariga, et al. 25th anniversary article: what can be done with the Langmuir–Blodgett method? Recent developments and its critical role in materials science, *Adv. Mater.* 25 (45) (2013) 6477–6512.
- [2] K. Ariga, et al. Layer-by-layer nanoarchitectonics: invention, innovation and evolution, *Chem. Lett.* 43 (1) (2014) 36–68.
- [3] K. Ariga, et al. Thin film nanoarchitectonics, *J. Inorg. Organomet. Polym. Mater.* 25 (3) (2015) 466–479.
- [4] P. Behroozi, et al. The calming effect of oil on water, *Am. J. Phys.* 75 (2007) 407–414.
- [5] A. Ulman, Langmuir–Blodgett films, in: An Introduction to Ultrathin Organic Films from Langmuir–Blodgett to Self-Assembly, [s.I.] Academic Press, USA, 1991, pp. 101–219.
- [6] J.N. Israelachvili, Historical perspective, in: Intermolecular and Surface Forces, third ed., [s.I] Academic Press, USA, 2011, pp. 15–16.
- [7] M.C. Petty, Langmuir–Blodgett films: an introduction [s.I.], Cambridge University Press, Cambridge, England, (1996).
- [8] P. Dyrnowicz-Latka, A. Dhanabalan, O.N. Oliveira Jr., Modern physicochemical research on Langmuir monolayers, *Adv. Colloid. Interface Sci.* 91 (2) (2001) 221–293.
- [9] O.N. Oliveira Jr., F.J. Pavinatto, D.T. Balogh, Fundamentals and applications of organised molecular films, in: Nanomaterials and Nanoarchitectures. first ed., [s.I] Springer, 2015, pp. 301–343.
- [10] A. De Barros, et al. Synergy between polyaniline and OMt clay mineral in Langmuir–Blodgett films for the simultaneous detection of traces of metal ions, *ACS Appl. Mater. Interfaces* 7 (12) (2015) 6828–6834.
- [11] M.L. Brauner, et al. Electrical and electrochemical measurements in nanostructures films of poly-thiophenes derivates, *Electrochim. Acta* 164 (1–6) (2015).
- [12] X. Chen, et al. Enhanced of polymer solar cells with a monolayer of assembled gold nanoparticle films fabricated Langmuir–Blodgett technique, *Mater. Sci. Eng. B* 178 (1) (2013) 53–59.
- [13] S. Jayaraman, L.T. Yu, M.P. Srinivasan, Polythiphene-gold nanoparticle hybrid systems: Langmuir–Blodgett assembly of nanostructure films, *Nanoscale* 5 (2013) 2974–2982.
- [14] E. Guzmán, et al. DPPC-DOPC Langmuir monolayers modified by hydrophilic silica nanoparticles: phase behaviour, structure and rheology, *Colloids Surf. A Physicochem. Eng. Asp.* 413 (2012) 174–183.
- [15] H. Nakahara, et al. Interfacial properties in Langmuir monolayers and LB films of DPPC with partially fluorinated alcohol ( $F_8H_7OH$ ), *J. Oleo Sci.* 62 (12) (2013) 1017–1027.
- [16] M. Saha, S.A. Hussain, D. Bhattacharjee, Interaction of nano-clay platelets with a phospholipid in presence of a fluorescence probe, *Mol. Cryst. Liq. Cryst.* 608 (1) (2015) 198–210.
- [17] J. Cabaj, et al. Biosensing invertase-based Langmuir–Schaefer films: preparation and characteristic, *Sens. Actuators. B* 166/167 (2012) 75–82.
- [18] L. Caseli, J.R. Siqueira, High enzymatic activity preservation with carbon nanotubes incorporated in urease-lipid hybrid Langmuir–Blodgett films, *Langmuir* 28 (12) (2012) 5398–5403.
- [19] J.M. Rocha, L. Caseli, Adsorption and enzyme activity of sucrose phosphorylase on lipid Langmuir and Langmuir–Blodgett films, *Colloids Surf. B* 116 (2014) 497–501.
- [20] F.A. Scholl, L. Caseli, Langmuir and Langmuir–Blodgett films of lipids and penicillinase: studies on adsorption and enzymatic activity, *Colloids Surf. B* 126 (2015) 232–236.
- [21] K. Togashi, et al. Fabrication of Langmuir–Blodgett films using amphiphilic peptides, *J. Nanosci. Nanotechnol.* 12 (1) (2012) 568–572.
- [22] N. Kato, T. Sasaki, Y. Mukai, Partially induced transition from horizontal to vertical orientation of helical peptides at the air-water interface and the structure of their monolayers transferred on the solid substrates, *Biochim. Biophys. Acta* 1848 (4) (2015) 967–975.

- [23] S.A. Hussain, et al. Incorporation of nano-clay saponite layers in the organo-clay hybrid films using anionic amphiphile stearic acid by Langmuir–Blodgett technique, *Thin Solid Films* 536 (2013) 261–268.
- [24] L. Ballesteros, et al. Directionally oriented LB films of and OPE derivate: assembly, characterization and electrical properties, *Langmuir* 27 (7) (2011) 3600–3610.
- [25] A.C. Kucuk, J. Matsui, T. Miyashita, Langmuir–Blodgett films composed of amphiphilic double-decker shaped polyhedral oligomeric silsesquioxanes, *J. Colloid Interface Sci.* 355 (1) (mar 2011) 106–114.
- [26] M.J. Shultz, et al. Aqueous solution/air interfaces probed with sum frequency generation spectroscopy, *J. Phys. Chem. B* 106 (2002) 5313–5324.
- [27] D. Blaudez, et al. Polarization-modulated FT-IR spectroscopy of a spread monolayer at the air/water interface, *Appl. Spectrosc.* 47 (1993) 869–874.
- [28] S. Talu, N. Patra, N. Salerno, Micromorphological characterization of polymer-oxide nanocomposite thin films by atomic force microscopy and fractal geometry analysis, *Prog. Org. Coat.* 89 (2015) 50–56.
- [29] J. Makowiecki, et al. Molecular organization of perylene derivatives in Langmuir–Blodgett multilayers, *Opt. Mater.* 46 (2015) 555–560.
- [30] R.J. Demchak, T Fort Jr., Surface dipole moments of close-packed un-ionized monolayers at the air-water interface, *J. Colloid Interface Sci.* 46 (2) (1974) 191–202.
- [31] Y.S. Lee, Nanostructures films, in: Self Assembly and Nanotechnology, [s.I.] John Wiley & Sons, Inc., Hoboken, New Jersey, 2008, pp. 259–262.
- [32] G. Cao, Two-dimensional nanostructures: thin films, in: Nanostructures & Nanomaterials: Synthesis, Properties & Applications, [s.I.] Imperial College Press, United States, 2004, pp. 173–224.
- [33] G. Giancane, et al. Investigations and application in piezoelectric phenol sensor of Langmuir–Schaefer films of a copper phthalocyanine derivate functionalized with bulky substituents, *J. Colloid. Interface Sci.* 377 (2012) 176–183.
- [34] R. Fernández, et al. Optical storage in azobenzene –containing epoxy polymers process as Langmuir–Blodgett films, *Mater. Sci. Eng. C* 33 (3) (2013) 1403–1408.
- [35] C.A. Silva, et al. Interaction of chitosan and mucin in a biomembrane model environment, *J. Colloid Interface Sci.* 376 (1) (2012) 289–295.
- [36] M.T. Nobre, et al. Interaction of bioactive molecules and nanomaterials with Langmuir monolayers as cell membrane models, *Thin Solid Films* 593 (2015) 158–178.
- [37] A. Mangiarotti, B. Caruso, N. Wilke, Phase coexistence in films composed of DLPC and DPPC: a comparison between different model membrane system, *Biochim. Biophys. Acta* 1838 (7) (2014) 1823–1831.
- [38] V. Arslanov, et al. Designed and evaluation of sensory system based on amphiphilic anthraquinones molecular receptors, *Colloids Surf. A* 483 (2015) 193–203.
- [39] Z. Yin, et al. Real-time DNA detection using Pt nanoparticle-decorated reduced graphene oxide field-effect transistors, *Nanoscale* 4 (2012) 293–297.
- [40] L. Wang, et al. A new strategy for enhancing electrochemical sensing from MWCNTs modified electrode with Langmuir–Blodgett film and used in determination of methylparaben, *Sens. and Actuators B* 211 (2015) 332–338.
- [41] G. Decher, J. Hong, Buildup of ultrathin multilayer films by a self-assembly process: II. Consecutive adsorption of anionic and cationic bipolar amphiphiles and polyelectrolytes on charged surfaces, *Phys. Chem. Chem. Phys.* 95 (11) (1991) 1430–1434.
- [42] G. Decher, J.D. Hong, J. Schmitt, Buildup of ultrathin multilayer films by self-assembly process: III. Consecutively alternating adsorption of anionic and cationic polyelectrolytes on charged surfaces, *Thin Solid Films* 210 (1992) 831–835.

- [43] Y. Lvov, G. Decher, G. Sukhorukov, Assembly of thin films by means of successive deposition of alternate layers of DNA and poly(allylamine), *Macromolecules* 26 (20) (1993) 5396–5399.
- [44] G. Decher, Y. Lvov, J. Shimitt, Proof of multilayer structural organization in self-assembled polycation-polyanion molecular films, *Thin Solid Films* 244 (1) (1994) 772–777.
- [45] G. Decher, et al. New nanocomposite films for biosensors: layer-by-layer adsorbed films of polyelectrolytes, proteins or DNA, *Biosens. Bioelectron.* 9 (9) (1994) 677–684.
- [46] G. Decher, Fuzzy nanoassemblies: toward layered polymeric multicomposites, *Science* 277 (5330) (1997) 1232–1237.
- [47] R.K. Iler, Multilayers of colloidal particles, *J. Colloid Interface Sci.* 21 (6) (1996) 569–594.
- [48] Y.F. Nicolau, Solution deposition of thin solid compound films by a successive ionic-layer adsorption and reaction process, *Appl. Surf. Sci.* 22 (1985) 1061–1074.
- [49] R. Aksberg, L. Ödberg, Adsorption of anionic polyacrylamide on cellulosic fibers with pre-adsorbed polyelectrolytes, *Nord. Pulp. Pap. Res. J.* 5 (1990) 168–171.
- [50] G. Decher, E.F. Schlenoff, *Multilayer Thin Films: Sequential Assembly of Nanocomposite Materials*, second ed., John Wiley & Sons, Germany, 2012.
- [51] G. Decher, Layered nanoarchitectures via directed assembly of anionic and cationic molecules, in: J.P. Sauvage, M.W. Hosseini (Eds.), *Comprehensive supramolecular chemistry* [s.I.], 9, Pergamon Press, Oxford, 1996, pp. 507–528.
- [52] R.J. El-Khoury, et al. Multifunctional layer-by-layer architectures for biological applications, in: W. Knoll, R.C. Advincula (Eds.), *Functional polymer films* [s.I.], Wiley-VCH, Germany, 2011, pp. 11–72.
- [53] M.M. De Villiers, et al. Introduction to nanocoatings produced by layer-by-layer (LbL) self-assembly, *Adv. Drug Deliv. Rev.* 63 (9) (2011) 701–715.
- [54] M. Schönhoff, Layered polyelectrolyte complexes: physics of formation and molecular properties, *J. Phys. Condens. Matter* (2003) 1781–1808.
- [55] J. Borges, J.F. Mano, Molecular interactions driving the layer-by-layer assembly of multilayers, *Chem. Rev.* 114 (18) (2014) 8883–8942.
- [56] S. Bai, et al. Hydrogen-bonding-directed layer-by-layer polymer films: substrate effect on the micro-porous morphology variation, *Eur. Polym. J.* 42 (4) (2006) 900–907.
- [57] X. Zhang, H. Chen, H. Zhang, Layer-by-layer assembly: from conventional to unconventional methods, *Chem. Commun.* 14 (2007) 1395.
- [58] J. Zhang, et al. Layer-by-layer assembly of azulene-based supra-amphiphiles: reversible encapsulation of organic molecules in water by charge-transfer interaction, *Langmuir* 29 (2013) 6348–6353.
- [59] A.H. Broderick, U. Manna, D.M. Lynn, Covalent layer-by-layer assembly of water-permeable and water-impermeable polymer multilayers on highly water-soluble and water-sensitive substrates, *Chem. Mater.* 24 (2012) 1786–1795.
- [60] S. Takahashi, K. Sato, J.-I. Anzai, Layer-by-layer construction of protein architectures through avidin-biotin and lectin-sugar interactions for biosensor applications, *Anal. Bioanal. Chem.* 402 (2012) 1749–1758.
- [61] L. Lee, et al. Influence of salt concentration on the assembly of DNA multilayer films, *Langmuir* 26 (5) (2010) 3415–3422.
- [62] M. Matsusaki, et al. Layer-by-layer assembly through weak interactions and their biomedical applications, *Adv. Mater.* 24 (4) (2012) 454–474.
- [63] H. Xu, M. Schönhoff, X. Zhang, Unconventional layer-by-layer assembly: surface molecular imprinting and its applications, *Small* 8 (4) (2012) 517–523.
- [64] Y. Li, X. Wang, J. Sun, Layer-by-layer assembly for rapid fabrication of thick polymeric films, *Chem. Soc. Rev.* 41 (18) (2012) 5998.

- [65] J.J. Richardson, M. Björnholm, F. Caruso, Technology-driven layer-by-layer assembly of nanofilms, *Science* 348 (2015) 411–423.
- [66] Y. Kim, et al. Stretchable nanoparticle conductors with self-organized conductive pathways, *Nat. Lett.* 500 (2013) 59–64.
- [67] Q. Xi, et al. Gold nanoparticle-embedded porous graphene thin film fabricated via layer-by-layer self-assembly and subsequent thermal annealing for electrochemical sensing, *Langmuir* 28 (2012) 9885–9892.
- [68] A. De Barros, et al. Nanocomposites based on LbL films of polyaniline and sodium montmorillonite clay, *Synth. Met.* 197 (2014) 119–125.
- [69] A.Y.W. Sham, S.M. Notley, Graphene polyelectrolyte multilayer film formation driven by hydrogen bonding, *J. Colloid Interface Sci.* 456 (2015) 32–41.
- [70] X. Xu, et al. Multifunctional drug carriers comprised of mesoporous silica nanoparticles and polyamidoamine dendrimers based on layer-by-layer assembly, *Mater. Des.* 88 (2015) 1127–1133.
- [71] J.S. Silva, et al. Layer-by-layer films based on carbon nanotubes and polyaniline for detecting 2-chlorophenol, *J. Nanosci. Nanotechnol.* 14 (9) (2014) 6586–6592.
- [72] H.D.M. Follmann, et al. Anti-adhesive and antibacterial multilayer films via layer-by-layer assembly of TMC/heparin complexes, *Biomacromolecules* 13 (2012) 3711–3722.
- [73] R.F. De Oliveira, et al. Exploiting cascade reactions in bienzyme layer-by-layer films, *J. Phys. Chem. C* 115 (39) (2011) 19136–19140.
- [74] P.P. Campos, et al. Amperometric detection of lactose using  $\beta$ -galactosidase immobilized in layer-by-layer films, *ACS Appl. Mater. Interfaces* 6 (14) (2015) 11657–11664.
- [75] J.S. Graça, et al. Amperometric glucose biosensor based on layer-by-layer films of microperoxidase-11 and liposome-encapsulated glucose oxidase, *Bioelectrochemistry* 96 (2014) 37–42.
- [76] P.K.H. HO, et al. Molecular-scale interface engineering for polymer light-emitting diodes, *Nature* 404 (mar 2000) 481–484.
- [77] S.K. Saha, A. Guchhait, A.J. Pal, Organic/inorganic hybrid pn-junction between copper phthalocyanine and CdSe quantum dot layers as solar cells, *J. Appl. Phys.* 112 (4) (2012) 044507.
- [78] H. Hwang, et al. Highly tunable charge transportation in layer-by-layer assembled graphene transistor, *ACS Nano* 6 (3) (2012) 2432–2440.
- [79] B. Koo, H. Baek, J. Cho, Control over memory performance of layer-by-layer assembled metal phthalocyanine multilayers via molecular-level manipulation, *Chem. Mater.* 24 (6) (2012) 1091–1099.
- [80] L. Zhao, et al. Fabrication of ultrahigh hydrogen barrier polyethyleneimine/graphene oxide films by LbL assembly fine-tuned with electric field application, *Compos. Part A Appl. S.* 78 (2015) 60–69.
- [81] K. Katagiri, et al. Anti-reflective coatings prepared via layer-by-layer assembly of mesoporous silica nanoparticles and polyelectrolytes, *Polym. J.* 47 (2015) 190–194.

# Low-Dimensional Systems: Nanoparticles

C.M. Miyazaki\*, A. Riul Jr\*\*

\*FEDERAL UNIVERSITY OF SÃO CARLOS, CENTER OF SCIENCES AND TECHNOLOGY FOR SUSTAINABILITY, SOROCABA, SÃO PAULO, BRAZIL; \*\*"GLEB WATAGHIN" INSTITUTE OF PHYSICS, STATE UNIVERSITY OF CAMPINAS, CAMPINAS, SÃO PAULO, BRAZIL

## CHAPTER OUTLINE

5.1	Introduction .....	125
5.2	Synthesis Methods .....	126
5.2.1	Top-Down Methods .....	127
5.2.2	Bottom-Up Methods .....	129
5.3	Properties .....	133
5.4	Characterization Methods .....	135
5.4.1	X-Ray Diffraction .....	135
5.4.2	Transmission Electron Microscopy .....	136
5.4.3	Atomic Force Microscopy .....	137
5.5	Applications .....	139
5.5.1	Biosensors .....	139
5.5.2	Catalysis .....	140
5.5.3	Magnetic Nanoparticles in Biomedicine .....	141
5.6	Final Considerations .....	142
	List of Symbols .....	143
	References .....	143

## 5.1 Introduction

Nanoparticles have been extensively explored because of their unique properties, which are dependent on their size and shape and enable their application in an extensive variety of fields, such as, cancer treatment and diagnosis [1–3]. Nanoparticles also enable the exploitation and production of existing materials with novel properties that, combined with advances in the synthesis and characterization processes, facilitate the development of new products, such as fabrics, dyes, cosmetics, and sports products.

In the 4th century, the Romans employed metal nanoparticles (silver and gold) to produce colorful glasses. The Lycurgus cup is a classic example, with its variable coloration according to the incident light, which ranges from green to red. In the mid-18th century, photography was discovered based on the production of light-sensitive silver nanoparticles. In 1857, Michael Faraday synthesized and performed experiments with a colloidal suspension of gold via the reduction of  $[\text{AuCl}_4]^-$  salt using phosphorus as a reducing agent [4]. In 1951, Turkevitch et al. described a detailed syntheses study, using transmission electron microscopy (TEM), of the preparation of gold nanoparticles using different reducing agents to elucidate the processes of nucleation, growth and agglomeration of nanoparticles, and the synthesis of monodisperse and reproducible suspensions [4]. Richard Feynman, who was awarded the 1965 Nobel Prize in Physics, predicted the technological potential of nanostructures, which suggests that the manipulation of individual atoms can provide a new material with new properties, and their application in electronic circuits on a nanometric scale for more powerful computers, as well as the manipulation of biological systems. Currently, many examples and applications show that Feynman's vision was ahead of his time [5].

Nanoparticles are defined as materials with sizes that range from 1 to 100 nm in at least one of their dimensions [6]; by this definition, nanotubes, fullerene, and nanothreads are also considered to be nanoparticles. However, this chapter focuses on zero-dimensional nanostructures. The term cluster (or nanocluster) will be extensively applied to define colloidal particle aggregates and may sometimes refer to nanoparticles.

The synthesis of nanoparticles involves two different approaches: the top-down method and the bottom-up method; these approaches will be detailed in [Section 5.2](#). The important requirements for the practical application of nanoparticles are as follows: nanometric dimension, uniform size distribution, morphology, chemical composition, and identical crystal structure [7]. In addition to advancements in the synthesis of nanoparticles, the need for characterization techniques that can demonstrate the physico-morphological characteristics of these nanometric entities is evident. Currently, a range of tools are available to investigate these characteristics, including electronic microscopy and X-ray diffraction (XRD) techniques and spectroscopy.

Given the extent of the content that involves synthesis, properties, and applications of nanoparticles, this chapter will focus on the main synthesis processes, with a simplified approach to the nanoparticle properties, describe the main characterization methods, and indicate some applications in the literature.

## 5.2 Synthesis Methods

As previously mentioned, the unique properties of a nanoparticle are dependent on its shape and size, which are dependent on the synthesis process that is employed for the fabrication of nanoparticles. The process in which nanoparticles derive from atomic precursors that aggregate to form a cluster and subsequently form a nanostructure is referred to as a bottom-up process. The process in which nanoparticles are obtained by the physical

wear of a larger volume is referred to as a top-down process. The main top-down (mechanical attrition and lithography) and bottom-up (chemical synthesis via sol–gel and reduction of metal salts) techniques are described in the next section.

### 5.2.1 Top-Down Methods

The mechanical attrition and lithography are the most well-known top-down methods for the production of nanometric structures, in which the former is commonly applied in the industry for large-scale production and the latter is a more sophisticated technique for the production of electronic and optical devices.

#### 5.2.1.1 Mechanical Friction

Mechanical friction is extensively applied by the metallurgical industry for the production of new alloys and mixtures with different properties due to the incorporation of defects in the crystal lattice of a metal [8,9]. This technique enables syntheses that are impossible via traditional fusion routes, such as, the production of uniform dispersions of ceramic particles in a metal matrix or metal dispersions with different melting points [8,10]. Mechanical friction also allows the solubility of immiscible binary systems due to the segregation of solute in the grain boundaries [9].

In the high-energy grinding process, particles with diameters near 50 µm are placed together with steel balls or tungsten binary composites inside sealed chambers and subjected to intense agitation (Fig. 5.1). The high energy of the grinding process can be obtained by applying high-frequency and low-amplitude vibration [8]. The grain size decreases with the grinding time until a constant value is obtained depending on the melting point of the material. The high-energy grinding process enables the creation of mono- or multi-component nanoparticles at the industrial scale; however, contamination by the grinding medium is a major disadvantage [9]. Lam et al. produced Si nanoparticles via the milling process with stainless steel balls. The reaction on the solid phases between graphite and silicon oxide ( $C + SiO_2 \rightarrow Si + CO_2$ ) produces nanoparticles with a 5-nm Si nucleus and 1-nm external layer of amorphous silicon oxide [11]. Details about the process of nanoparticle production by mechanical friction are provided by Koch (1993).

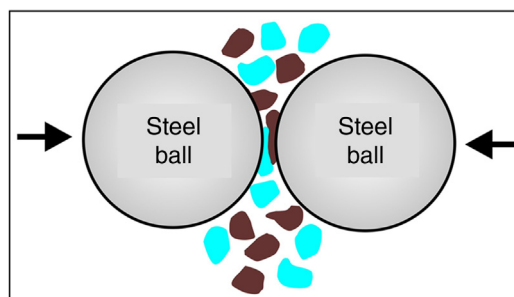


FIGURE 5.1 Schematic of the ball-milling process using steel balls.

### 5.2.1.2 Lithography

The lithographic process consists of the transfer of patterns to the desired substrate and is extensively applied for the production of electronic and optical devices due to the high resolution obtained [12]. Briefly, this process consists of the deposition of a photoresist, exposure of its specific areas using a mask, the exposure of the resist and consequently, the transfer of the desired pattern.

The first step includes the deposition of the resist on a substrate, using the controlled rotation of the substrate by a technique denominated as spin-coating [13]. The second step includes the irradiation of the photoresist using a polymeric material that undergoes chemical structural alterations when irradiated, such as, the rupture of the polymeric chain (positive resist) or the formation of cross-links (negative resist). In the case of the positive resist, the irradiated part will be dissolved during the exposure process due to the breakdown of the macromolecule into smaller parts; for the negative resist, the formation of cross-links render the irradiated parts insoluble [12].

Depending on the type of radiation that is used to sensitize the resist, such as ultraviolet, X-ray, electron or ion beam, different resolutions can be obtained. Patterns of up to 5 nm can be obtained with an electron beam, whereas 30-nm patterns are obtained using X-ray [12]. After the desired model is created, the transfer can be performed via the corrosion or the lift-off metallization process. The chemical corrosion involves the protection of certain areas by the pattern created in the resist and the corrosion of the other areas by specific chemical solution or plasma with reactive radicals [12]. Metal structures can be created by metallization followed by lift-off, that is, the substrate receives the resist with the desired pattern, and the metal is evaporated on top of it. The metal is fixed at the substrate-free zone, and the resist is removed using an appropriate solvent, leaving only the desired metal pattern, as illustrated in Fig. 5.2.

Lithography is an extensive process, including various details. For a better understanding of the technique, refer to Dobisz et al. (1996) and Hilleringmann (2005).

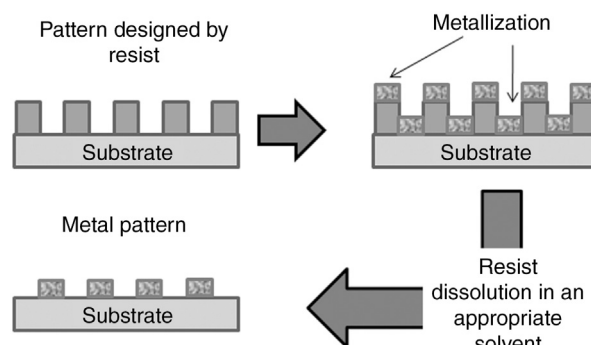


FIGURE 5.2 Schematic of the lift-off process for the production of metal patterns.

## 5.2.2 Bottom-Up Methods

In the bottom-up process, the starting points are the atomic or ionic precursors that unite to form larger particles. Initially, the discussion will cover the physicochemical aspects of the process of nanoparticle production in solution, the nanoparticle stabilization in suspensions, the synthesis of metal nanoparticles via metal reduction and the synthesis of oxide nanoparticles via the sol–gel method. Although we will only discuss the techniques based on chemical synthesis, other bottom-up methods, such as molecular beam epitaxy, chemical vapor deposition, pulse laser deposition, laser ablation and sputtering deposition, are extremely important in the semiconductor industry. However, these sophisticated techniques are dependent on specific equipment for temperature and pressure control; details are provided in Refs. [14–16]. We also emphasize the high control and quality of nanoparticles that are obtained by physical methods in relation to size and stoichiometric composition [17,18]. The metal nanoparticles should be protected against the oxidative effects of the environment for their subsequent technological applications. We also emphasize the complexity that is required by these experimental setups, which justify the selected descriptions of the chemical methods discussed in this paper.

For each application, the synthesis conditions should be well controlled to ensure that the product has well-defined characteristics, such as equivalent dimension (uniform size distribution), shape and morphology, and similar composition and crystal structure between particles to prevent the formation of agglomerates [7].

### 5.2.2.1 Physicochemical Aspects of Nanoparticle Formation

The mechanism of nanoparticle formation in a liquid phase can be explained by nucleation and growth phenomena [7,19]. According to the theory developed by Lamer [20], particle formation consists of the following steps:

1. increase in monomer concentration in the solution until supersaturation and the start of nuclei formation;
2. continuous aggregation of monomers in the nucleus, which causes a gradual decrease in the monomer concentration in the solution; and
3. stabilization of the surface of the resulting particles by surfactants.

If the solute concentration increases to the limit of solubility or the temperature decreases to a point that enables phase transformation, the system will have a high Gibbs free energy. To minimize the energy of the system, the solute aggregates and the variation of the Gibbs free energy per unit volume ( $\Delta G_v$ ) of the solid phase is given by Eq. 5.1, which is dependent on the solute concentration [7].

$$\Delta G_v = \frac{-KT}{\Omega} \ln \left( \frac{C}{C_0} \right) \quad (5.1)$$

where  $C$  is the solute concentration,  $C_0$  is the solubility,  $K$  is the Boltzmann constant,  $T$  is the temperature and  $\Omega$  is the atomic volume. Consider the supersaturation  $\sigma = (C - C_0)/C_0$ :

$$\Delta G_v = \frac{-KT}{\Omega} \ln(1 + \sigma) \quad (5.2)$$

From Eq. 5.2, when  $\sigma = 0$ , the Gibbs free energy will be zero and supersaturation will not occur. If  $C > C_0$ , the free energy will be negative and the nucleation process will be spontaneous.

A spherical nucleus of radius  $r$  can be assumed, with the Gibbs free energy given in Eq. 5.3 [7]:

$$\Delta\mu_v = \frac{4}{3}\pi r^3 \Delta G_v \quad (5.3)$$

In addition to the decrease in free energy, the total energy of the system will also be influenced by the appearance of the surface energy  $\Delta\mu_s$ . Thus, Eq. 5.4 indicates that the reduction in the free energy of the system is influenced by the appearance of the surface energy, which is expressed as  $4\pi r^2 \gamma$  [7].

$$\Delta G = \Delta\mu_v + \Delta\mu_s = \frac{4}{3}\pi r^3 \Delta G_v + 4\pi r^2 \gamma \quad (5.4)$$

where  $\gamma$  is the surface energy per unit area. The formed nuclei should have a minimum radius to be stable; otherwise, they dissolve and return to their volume [7,19]. This minimum radius is referred to as the critical radius  $r^*$ , and the nuclei with  $r \geq r^*$  will act as nucleation centers for the formation of particles. Fig. 5.3 illustrates the nucleation and growth processes.

After nucleation starts, the concentration of the species in solution and the free energy of the system decreases [7,21]. The concentration decreases to values below a specific

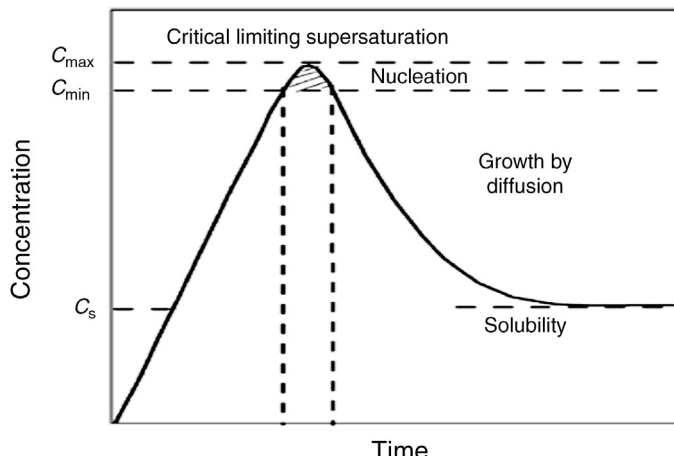


**FIGURE 5.3** Schematic of the nucleation and growth process by LaMer. Modified from V.K. LaMer, R.H. Dinegar, Theory, production and mechanism of formation of monodispersed hydrosols, *J. Am. Chem. Soc.* 72 (1950) 4847–4854 [20].

concentration when the nucleation stops, and the growth process continues until an equilibrium concentration  $C_s$  is attained. When a nucleus is formed, the growth process immediately starts, with larger particles that increase at the expense of the smaller particles by a process named Ostwald ripening, which reduces the surface energy. Above a minimum concentration, the nucleation and growth process simultaneously occur but at different rates.

#### 5.2.2.2 Nanoparticle Stabilization

Nanometric particles have a wider surface area and tend to form aggregates to minimize their surface energy. The agglomeration process can initiate during synthesis; thus, the use of different types of surfactants and stabilizers has been explored [22]. To minimize the surface energy of the particles and prevent the agglomeration process, two paths can be followed: (1) electrostatic repulsion between covered particles, which is effective in diluted aqueous or polar organic systems, and (2) steric effects, which are active in aqueous and nonaqueous systems, and dispersions at high concentration; however, they are less sensitive to impurities or additives when compared with electrostatic repulsion [4,22].

For example, when suspended, gold nanoparticles that are synthesized via sodium citrate are surrounded by an electron double layer, which is formed by the adsorbed citrate, chloride ions and cations that are attracted to the surface. In this case, any disturbance in the system, such as an increase in ionic force, may cause the formation of agglomerates. The protection by steric effects includes the adsorption of molecules, such as polymers, surfactants and other types of ligands, on the surface of nanoparticles. Polymers are commonly applied and selected according to the solubility of the precursor in the polymeric solution and the ability to stabilize the product [4]. Some natural polymers, such as chitosan [23,24] and cyclodextrins [25,26], as well as synthetic polymers, such as PVP (polyvinylpyrrolidone) [27–29] and PVA (polyvinyl alcohol) [30,31], have been employed.

#### 5.2.2.3 Sol–Gel Synthesis

Sol–gel synthesis is extensively employed for the production of colloidal dispersions of oxides and the production of core–shell nanostructures, which is also useful for the production of inorganic materials and organic–inorganic hybrids, particularly oxides [7,32]. The precursor can be an inorganic metal salt (acetate, chloride, nitrate, and sulfate) or a metal organic species, such as a metal alkoxide [33]. The precursor can be dissolved in an aqueous or organic solvent, and a catalyst is added to promote the hydrolysis and condensation reactions [7].

A typical sol–gel production process consists of the use of metal alkoxide as a precursor in an aqueous system that undergoes hydrolysis and condensation. The alkoxides are precursors for silica, alumina, titanium, and zirconium [32]. With hydrolysis, the metal alkoxide is transformed into sol (colloidal dispersion of particles in a liquid) and a gel after condensation [33]. The hydrolysis and condensation steps occur sequentially and in parallel with the condensation step, which frequently causes the formation of aggregates of oxides or metal hydroxides with incorporated or linked organic groups. These organic

groups may derive from incomplete hydrolysis or may be introduced as organic nonhydrolyzable ligands [7].

The synthesis in an aqueous medium has the disadvantage of different reactivities of metal alkoxides, which hinder the control of the composition and its homogeneity in the synthesis of multicomponent oxides [33,34]. The nonaqueous synthesis can be divided into synthesis by surfactant control or by synthesis controlled by solvents. In the first case, the precursor is commonly injected into a heated solvent that contains surfactants, with the surfactant molecules avoiding agglomeration, which produces reasonable colloidal stability in organic solvents [34]. Zeng et al. produced MnFe<sub>2</sub>O<sub>4</sub> magnetic nanoparticles with different sizes by controlling the stabilizers/Fe ratio. Depending on the proportion, the produced particles presented a spherical, polyhedron or cubic shaped [35].

In the case in which the presence of surfactants is undesirable, for example, when it affects the catalytic activity, the synthesis is performed via the solvent-control path. Ba et al. produced monodisperse tin oxide nanoparticles with a diameter of 3.5 nm. For the synthesis, a tin chloride solution was dripped into a benzyl alcohol solvent under agitation at 100°C for 24 h. The precipitate was collected, centrifuged, and suspended in tetrahydrofuran (THF) to form a suspension of transparent nanoparticles that are stable even in the absence of surfactants without the formation of agglomerates [36]. Additional information about the sol-gel hot-injection method is provided in Ref. [37].

#### 5.2.2.4 Metal Reduction

The reduction of salts to obtain colloidal suspensions of metal nanoparticles is the most common synthesis technique [4], with the use of an extensive variety of metal salts, surfactants, and reducing agents. The following materials can be applied as metal precursors: oxides, nitrates, chlorides, acetates, and acetyl ketones [38]. The following materials can be employed as reducing agents: hydrides (such as sodium borohydride), dehydrogenating gases, citrates, ascorbic acid, hydrazine, and ethylene glycol. Depending on the reduction potential of the reducing agents, a reaction may occur at room temperature or at high temperatures [19].

The reduction of gold by citrate is one of the most common examples of metal reduction. In 1951, Turkevitch demonstrated the synthesis of nanoparticles in the scale of 20 nm via the reduction of HAuCl<sub>4</sub> in an aqueous medium with sodium citrate [39]. Yonezawa et al. proposed a modification of the synthesis via citrate using 3-mercaptopropionate as a stabilizer. The nanoparticle size can be controlled by varying the stabilizer/precursor ratio [40]. Zhu et al. produced functionalized Au nanoparticles with carboxylic groups via reduction with citrate using 2-mercaptosuccinic acid [41], in which the product was more stable to pH changes.

Nanoreactors have been applied to improve the control of the synthesis processes. The dendrimers are extensively employed because they are macromolecules of tree-like morphology with regularly spaced ramifications, three-dimensional structures and an abundance in surface groups [42]. The advantages of their application are as follows: (1) uniform structure and composition; (2) the stabilization and encapsulation of nanoparticles inside

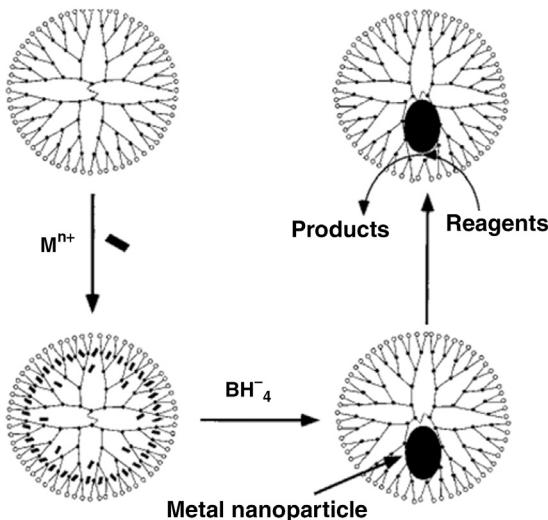


**FIGURE 5.4** Schematic of the synthesis of metal nanoparticles via reduction by borohydride inside a dendrimer.  
R.M. Crooks, M. Zhao, L. Sun, V. Chechik, L.K. Yeung, Dendrimer-encapsulated metal nanoparticles: synthesis, characterization, and applications to catalysis, *Acc. Chem. Res.* 34 (2001) 181–190 [43].

the dendrimers without the formation of agglomerates; (3) the encapsulation of nanoparticles by steric effects; thus, a large part of the particle surface is available to participate in the reactions; and (4) the peripheral groups of dendrimers can be adapted for the control of solubility, which helps in surface adsorption [43]. Fig. 5.4 illustrates the synthesis of metal nanoparticles inside the structure of a dendrimer via reduction by borohydride.

Polyamidoamine (PAMAM) is one of the most employed nanoreactors because it produces very small nanoparticles with diameters less than 4 nm. This type of method has been applied to the fields of biosensors and catalysis and the fabrication of electronic devices. Crespihlo et al. developed an enzymatic biosensor for the detection of glucose. Initially, PAMAM-Au was synthesized by reduction of  $KAuCl_4$  solution with formic acid in the presence of G4 PAMAM. PAMAM-Au were alternated with poly(vinylsulfonic acid) (PVS) on ITO electrodes using the self-assembly technique [layer-by-layer (LbL)] to form bilayers. The hexacyanoferrate was electrodeposited, which modified the gold nanoparticles, and the glucose oxidase enzyme was subsequently immobilized on the self-assembled film to form the biosensor [44].

### 5.3 Properties

As predicted by Feynman, new phenomena govern the characteristics of materials that affect their properties at the nanoscale, which can be properly explored in many applications. When the size of a nanoparticle or nanocrystal is smaller than the wavelength of the incident radiation, its de Broglie wavelength will be comparable to its diameter.

Consequently, the conduction electrons can become trapped in the nanoparticles; this effect is known as quantum trapping, which induces alterations in the bandgap and in the electron energy levels of the material. This effect is more pronounced in semiconductor nanoparticles due to an increase in the bandgap that is caused by a decrease in their size, which generates interband transitions that cause electron displacements to higher frequencies. In a simplistic manner, different electronic configurations exist compared with the configurations observed in the same materials at the macroscopic scale. The control of the nanostructure size generates control of the wavelength of the scattered light and, consequently, of the color of the observed sample [6,7,45].

A nanoparticle with a diameter of 10 nm, for example, contains ~10% of its atoms at the surface, which become more active than the atoms in the volume due to the number of bonds that the volumetric atoms make with the closest neighbors. Consequently, the surface atoms in the nanoparticles have more electron energy levels due to the imperfections or active sites caused by the bonds that are not completed. When an electromagnetic wave is incident on the nanoparticle, these surface conduction electrons interact with the electric field of the incident wave, which induces the polarization of the free electrons in relation to the ions of the crystal structure of the material. These free electrons start to oscillate together from one side to the other side at the surfaces of the nanoparticles. When the incident radiation frequency approaches the oscillation frequency of the conduction electrons (dipolar resonance), strong energy absorption is induced at the surfaces of the nanoparticles (region in which the oscillation occurs), which is known as surface plasmon absorption (which is dependent on the nanoparticle size and shape). To illustrate this phenomenon, Fig. 5.5 (top panels) presents the micrographs of the seeds (a) that originate the rod-shaped gold nanoparticles (b–e) with different aspect ratios (length divided by width). The bottom panels show the optical spectra that correspond to each suspension [46].

The macroscopic metal materials have a continuous conduction band, and the nanoparticles have discrete electronic states that are dependent on their size. In nanometric scale, a significant percentage of the material surface is exposed, which intensifies the surface and interface effects, which, consequently, also produce a significant variation in their magnetic properties [45].

A magnetic field can be created due to the electron movement inside the material, whereas a magnetic model can arise due to the spin orientations inside the sample. Because small magnetic particles tend to form monodomains in the range of 20–2000 nm, the magnetic behavior of the majority of experimental systems can be attributed to the contributions of the effect of size and the interactions among the nanoparticles. The correlation between the nanostructure and its magnetic properties has isolated nanometric particles that generally have small interactions with magnetism due to the spin polarized tunneling effect and oscillatory coupling between magnetic/nonmagnetic multilayers and magnetoresistance. Conversely, volumetric materials with nanoscale structures (nanostructured films), whose magnetic properties are predominantly caused by the interactions involved in these systems, are observed. However, when the nanoparticle size is reduced to a size smaller than the critical diameter, the formation of domains is energetically unfavorable,

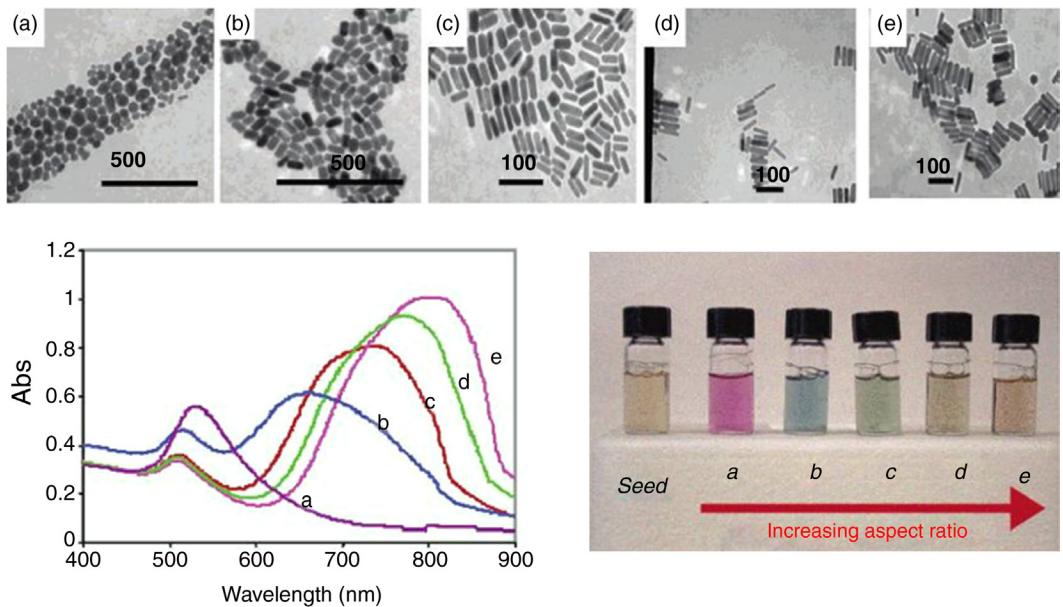


**FIGURE 5.5** Transmission electron micrographs (top), optical spectra (left) and photographs (right) of gold nanorod aqueous solutions of different aspect ratios (length divided by width). Scale: 500 nm for (a) and (b); 100 nm for (c–e). C.J. Murphy, T.K. Sau, A.M. Gole, C.J. Orendorff, J. Gao, L Gou, et al., Anisotropic metal nanoparticles: synthesis, assembly, and optical applications, *J. Phys. Chem. B* 109 (2005) 13857–13870 [46].

and the variations in the magnetization are not caused by the movement of domains but by the coherent rotation of spins, which is frequently affected by thermal fluctuations (the system starts to present paramagnetic behaviors) [45]. An example that is often cited in studies is the possibility of the application of magnetic nanoparticles for cancer treatment. The nanoparticles are encapsulated with specific chemical agents that bond in tumor regions; with the control of magnetization, they agitate, which heats the affected region by a hyperthermia process and selectively destroys cancer cells [19].

## 5.4 Characterization Methods

Various experimental techniques can be employed for the characterization of nanoparticles, such as spectroscopic methods (UV-vis and infrared), XRD, TEM, scanning electron microscopy, and atomic force microscopy (AFM). Some methods and examples of nanoparticle characterization by XRD, TEM, and AFM are presented in the next section.

### 5.4.1 X-Ray Diffraction

The XRD technique enables the investigation of the crystallinity degree and the size of the crystallites of different materials, including nanoparticles [47], according to the spaces between adjacent atomic planes [48]. With the incidence of X-rays of wavelength  $\lambda$ , with

the incidence angle  $\theta$  on a crystal, they can pass with no interruptions or interact with the atoms of the crystal lattice of the material. Bragg's law (Eq. 5.5) indicates that diffracted X-rays of various intensities, which represent a specific interplanar distance  $d$  in the lattice, can be detected when X-rays of known wavelength and incidence angle are directed to a crystal lattice.

$$n\lambda = 2ds\sin\theta \quad (5.5)$$

Scanning at different angles and a constant wavelength generates a diffraction pattern [48]. The determination of the unit cell size and interplanar atomic distances can be evaluated by the angle position of the peaks in the diffractogram, and the atomic arrangement inside each unit cell can be associated with the relative intensities of these peaks [49].

XRD has also been explored in the estimation of nanoparticle size with Scherrer's equation (Eq. 5.6), which relates the full width at half maximum (FWHM) of the diffraction peak with the crystallite size  $D$  [7].

$$D = \frac{k\lambda}{w\cos\theta} \quad (5.6)$$

where  $\lambda$  is the wavelength of the incidence photons (nm),  $\theta$  is Bragg's reflection angle,  $w$  is the FWHM and  $k$  is a constant that is dependent on geometrical factors [50]. The widening of the peaks represents crystallites of increasingly smaller sizes [51]; thus, nanoparticles present wide diffraction peaks that differ from the materials at the macroscopic scale, which present fine lines in the diffractograms. Note that Scherrer's equation can be applied to crystallites of average size in the range of approximately 100–200 nm; above these dimensions, the diffraction peak width can be affected by other factors than the crystallite size [52].

Borchert et al. investigated the nanoparticle size of CoPt<sub>3</sub> via three different methods: TEM, small-angle X-ray scattering (SAXS) and XRD. The correctly adapted Scherrer's equation for the near-spherical geometry of CoPt<sub>3</sub> nanoparticles provides diameters that are highly consistent with the diameters obtained by the other methods: 8.5 nm by TEM, 8.11 by SAXS and 8.4 with the adapted Scherrer's equation (Eq. 5.7), which yields a difference less than 5%.

$$D = \frac{4}{3} \frac{0.9\lambda}{w\cos\theta} \quad (5.7)$$

The method for the determination of the average crystallite size by XRD is indirect, and its use is preferably combined with microscopic techniques. With the appropriate care in the experiments and analyses, the results have been consistent with the values determined by direct methodologies. Details about Scherrer's equation in the investigation of nanoparticle size are provided in Refs. [50,53].

#### 5.4.2 Transmission Electron Microscopy

TEM is one of the most prevalent techniques for the nanoparticle size and shape analysis. Electrons are generally accelerated at 100 KeV or higher energy values, displaced on a thin

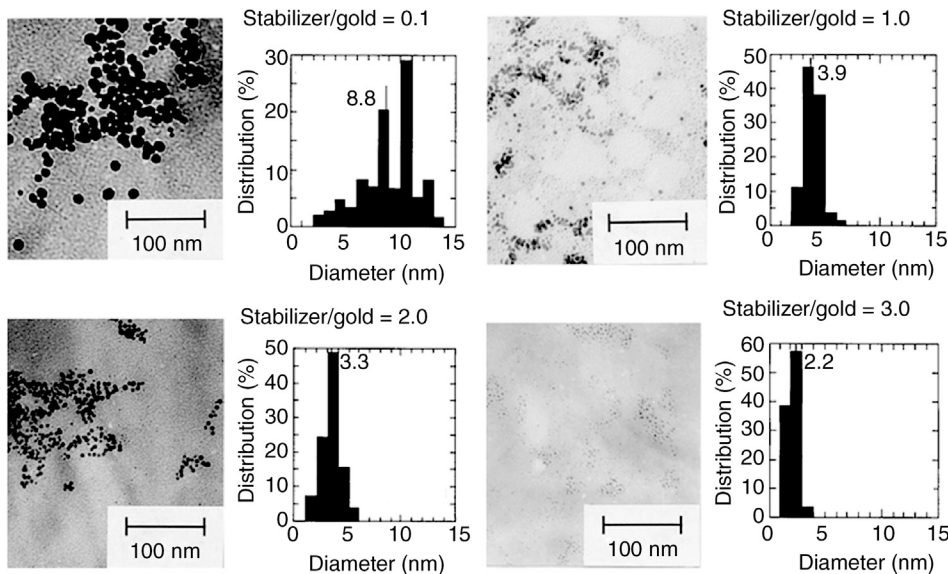


**FIGURE 5.6** Transmission electron microscopy (TEM) and size distribution of gold nanoparticles that were stabilized in 3-mercaptopropionate reduced via citrate, with different stabilizer/gold ratios. T. Yonezawa, T. Kunitake, Practical preparation of anionic mercapto ligand-stabilized gold nanoparticles and their immobilization, *Colloids Surf. A* 149 (1999) 193–199 [40].

layer of the sample, and elastically or inelastically scattered. The inelastic scattering occurs in heterogeneous regions, such as intergrain boundaries, defects, and density variations, and cause scattering effects that produce differences in the intensities of the transferred electrons [7]. The wavelength of the electron beam limits the image resolution, which may attain the Angstrom scale depending on the equipment.

Yonezawa and Kunitake, for example, produced gold nanoparticles that were stabilized in 3-mercaptopropionate reduced via citrate. The TEM investigation provided a detailed analysis of the form and size distribution (Fig. 5.6). Particles presented spherical shape and smaller dimensions when the stabilizer/gold ratio was higher [40]. From the analysis of the histograms, a narrow size distribution was observed in greater stabilizer/gold ratio, and a broad variation in size was observed when the ratio was 0.1.

### 5.4.3 Atomic Force Microscopy

AFM is an important tool for the investigation of the surface topography and roughness at the atomic level [54]. A flexible probe that is sensitive to an interaction force is displaced with a tracking pattern on the surface of a solid sample. The force that acts between the probe and the sample surface causes small deflections in the cantilever, which are detected by optical systems [54]. Surface scanning with a continuous pattern  $xy$ , which is performed with a cantilever with a tiny tip that moves up and down along the  $z$ -axis according to the topographic change of the surface can be translated by a computer into a topography image [54].

Three modes can be employed for AFM image acquisition: contact, noncontact and intermittent. The contact mode is not adequate for soft surfaces, such as biological samples and polymers, because the tip will be in constant contact with it. In some cases, the damage can be avoided by the intermittent mode, in which the tip is periodically in contact with the sample surface for a short period of time. In the noncontact mode, the tip fluctuates over the surface at a few nanometers of distance [54].

Sruanganurak et al. investigated the modification of the surface of natural latex rubber to minimize the friction effect, which is the main problem of latex application in gloves. Poly(methyl methacrylate) (PMMA) nanoparticles were deposited by the self-assembly technique (LbL) on the natural rubber substrates that were treated with polyacrylamide (natural rubber grafted with polyacrylamide, NR-g-PAAm). The AFM analysis that was employed in the intermittent mode (tapping mode) enabled the analysis of the surface morphology and roughness. In Fig. 5.7,  $C_s$  represents the surface coverage, which is expressed by  $C_s (\%) = (N/N_{\max}) * 100$ , where  $N$  is the number of adsorbed particles per unit area and  $N_{\max}$  is the maximum number of adsorbed particles in the same area, assuming hexagonal close packing [55].

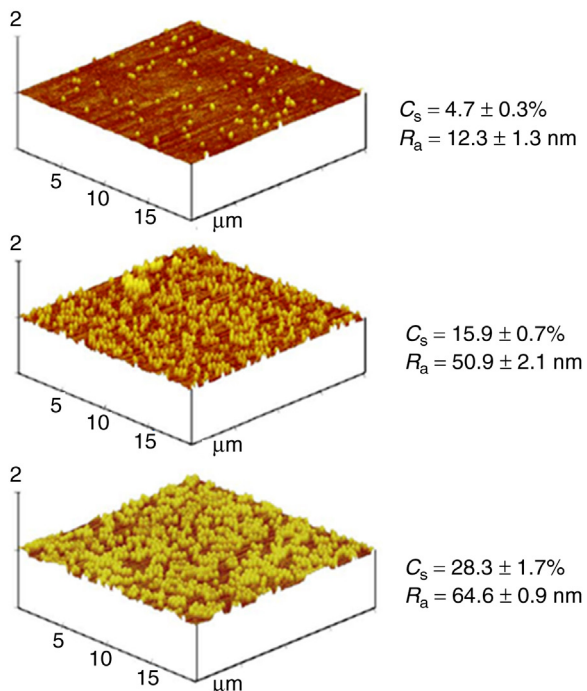


**FIGURE 5.7** Investigation of the average surface roughness ( $R_a$ ) of NR-g-PAAm covered with poly(methyl methacrylate) (PMMA) particles, with different  $C_s$  values. A. Sruanganurak, K. Sanguansap, P. Tangboriboonrat, Layer-by-layer assembled nanoparticles: a novel method for surface modification of natural rubber latex film, *Colloids Surf. A* 289 (2006) 110–117 [55].

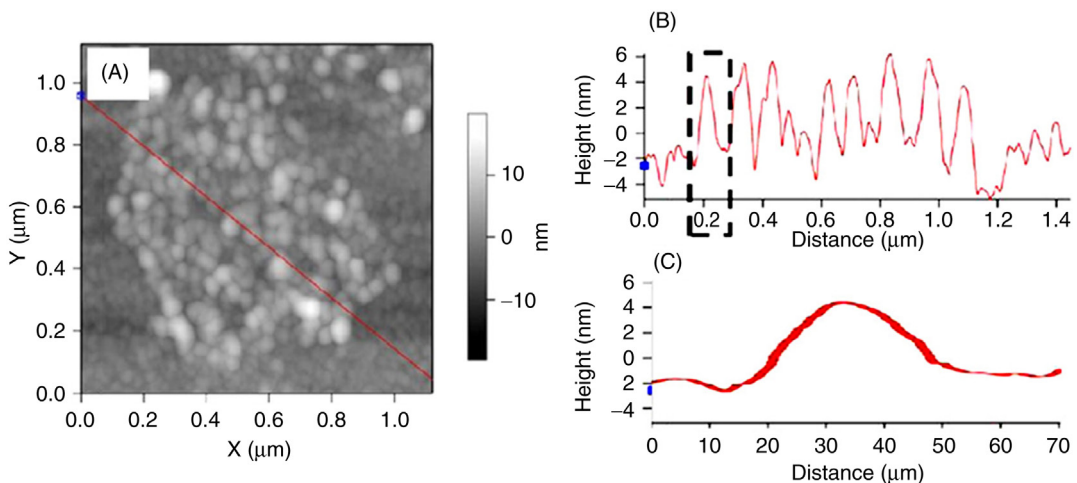


**FIGURE 5.8** Atomic force microscopy (AFM) image of (A) cast film of graphene–platinum colloidal suspension, (B) topology of the cross-section at the line showed in the image in (A), and (C) expanded image of the topology of the cross-section of a cluster [represented by the dashed rectangle in (B)]. Adapted from W. Chartarrayawadee, S.E. Moulton, D. Li, C.O. Too, G.G. Wallace, *Novel composite graphene/platinum electro-catalytic electrodes prepared by electrophoretic deposition from colloidal solutions*, *Electrochim. Acta* 60 (2012) 213–223 [56].

Chartarrayawadee et al. employed the AFM technique to confirm the anchorage of platinum nanoparticles on graphene sheets, as illustrated in Fig. 5.8. The composite was successfully applied for the catalysis in the reactions of solar cells, which are sensitized by dyes, and the generation of hydrogen from acid. According to the topological analysis of the cross-section, the heights of the clusters in the graphene-platinum composite varies from 3 to 6 nm, whereas the diameter varies from 40 to 100 nm. With the amplification of the topological image of a cluster [dashed rectangle in (B)], its dimension and shape can be observed [56].

## 5.5 Applications

### 5.5.1 Biosensors

Nanoparticles can exert many functions in applications such as biosensors, which favor the immobilization of biomolecules and the catalysis of electrochemical reactions, in addition to an increase in the charge transfer and biomolecule labeling [57]. The immobilization of biomolecules in the volume of a material can cause the denaturation or loss of bioactivity; however, the use of nanoparticles enables the immobilization and the preservation of the biocompatibility. The use of nanoparticles with catalytic properties produces high-sensitivity sensors, which attain limits of detection lower than 2 fM [57].

Molecular recognition is one of the most important points of biosensor selectivity because some biological entities can be recognized and linked to one another with high

selectivity and specificity [7]. These biological entities include antibodies, oligonucleotides, and enzymes. The antibodies—proteins of the immune system—recognize a virus as an intruder and bond to viruses to destroy them. For example, antibodies and oligonucleotides can easily bond to the surfaces of nanoparticles via thiol–Au bonds in the case of gold nanoparticles or covalent bonds at silanized surfaces via biotin–avidin bonds, in which avidin is bonded to the material surface [7].

Gold nanoparticles have been applied for the amplification of the analytical signal due to its ease of synthesis, narrow size distribution, efficient surface modification by thiols and other ligands and biocompatibility [58]. The metal nanoparticles can be guided to specific regions using the antigen–antibody recognition in the ligand–receptor interactions, for example, by bonding to cancer cells [19].

Biosensors that are based on molecular recognition, such as the antigen–antibody interaction, are referred to as immunosensors [59]. Li et al. developed a fast-detection immunosensor for *Escherichia coli*. The gold electrode was treated to receive  $-NH_2$  functional groups and after, alternated nanoparticle layers of gold and the chitosan–MWNT–thionine composite were produced via the LbL technique. Voltammetric readings guarantee the modification of electrodes, and the sensitivity and stability of the sensor are related to the amount of thionine mediator [60]. Subsequently, anti-*E. coli* O157:H7 was immobilized, followed by a period of incubation for 60 min in bovine serum albumin. The sensor proved to be efficient for the detection of *E. coli* in milk and water samples.

### 5.5.2 Catalysis

Since the surface atoms of nanoparticles are more reactive than the volumetric atoms of nanoparticles, they have sites with missing bonds, which increases the activity of nanoparticles and provides additional electronic states and a higher reactivity [6].

Fig. 5.9 illustrates the increase in surface area with the decrease in the volume size of the nanoparticles and the increase in surface area, which are proportional to its reactivity and catalytic activity.

The versatility of the nanoparticles enables their use as homogeneous and heterogeneous catalysts. In the first case, only the nanoparticle is employed; in the second case, it

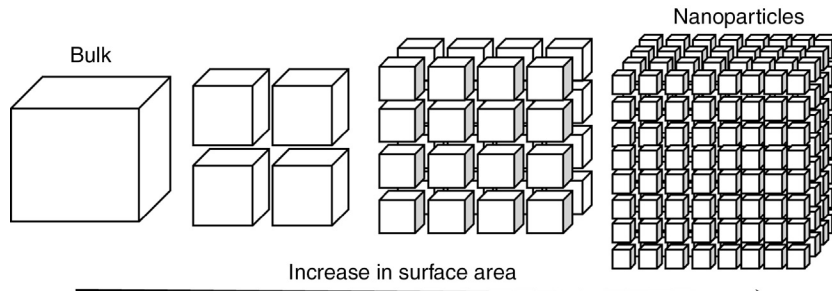


**FIGURE 5.9 Increase in surface area, which is proportional to its reactivity and catalytic activity.**

can be anchored or deposited on a substrate. Nanoparticles exhibit excellent performance as catalysts in many areas, including dehydrogenation, halogenation, oxidation, reduction, decomposition, and electron transfer reactions, and the catalytic efficiency is dependent on their shape, composition and size [6].

For example, the catalysis of oxidoreduction in fuel cells, in which a suitable catalyst is required for efficient redox reactions, can be cited. Metal colloidal particles, especially platinum, are very interesting due to their catalytic action in methanol oxidation reactions and oxygen reduction, which are responsible for the energy generation in direct methanol fuel cells (DMFC) [61]. Platinum nanoparticles have been applied with graphene as LbL films, and their catalytic activities were analyzed by cyclic voltammetry [62]. Graphene was modified with an ionic liquid to obtain a positively charged suspension, whereas the platinum nanoparticles were stabilized in citrate with negative charges. The LbL film that electrostatically formed presented high electrocatalytic activity in the reduction of oxygen [62]. The production of composite catalysts with more than one metal (generally Pt alloys) is interesting for applications in methanol oxidation in DMFCs. Yola et al. synthesized catalysts composed of Pt nanoparticles and bimetal particles (contain gold and silver with platinum) that were anchored in functionalized graphene oxide for the oxidation of methanol. The formed Au-Pt/GO was superior than other tested structures, which indicates a wide active surface, high electrocatalytic activity, and high tolerability to contamination by carbon monoxide (product of the methanol oxidation reaction) [63]. To reduce the mass of Pt that is required by the electrode and reduce the cost of energy generation, Zhao et al. synthesized core-shell-structured nanoparticles, an Au nucleus and a shell composed of Pt and Cu alloy to obtain a larger electrochemically active area that is superior to other structures (PtCu/C, AuPtCu/C and commercial Pt/C) due to the synergic effects between the nanostructured core and the shell with uniform dispersion [64].

The synthesis process by the Rampino and Nord method, for example, is extensively applied for the production of an aqueous suspension of platinum nanoparticles. This method involves  $K_2PtCl_4$  and polyacrylic acid solution that receives argon gas and is reduced by hydrogen gas [65]. Hao-Lin et al. proposed the modified synthesis of platinum nanoparticles with Nafion. The particles presented a size of approximately 4 nm, were adsorbed by the surfaces of the carbon nanotubes and employed as catalysts in proton exchange membrane fuel cells, which demonstrate a superior performance [66]. Other researchers applied in situ polymerization with platinum [67,68] for the modification of Nafion membranes to target the application in DMFCs. The in situ polymerization of pyrrole was performed on the Nafion membrane, followed by the reduction of platinum salt to form nanoparticles. The methanol permeability (one of the main problems in DMFCs) decreased with the time of pyrrole monomer impregnation [67].

### 5.5.3 Magnetic Nanoparticles in Biomedicine

The quantum effect and the large surface area of the magnetic nanoparticles produce a material with altered magnetic properties, which presents a superparamagnetic

phenomenon because each particle is considered to be a single magnetic domain [1]. Factors such as the biocompatibility and possible functionalization of the surfaces of magnetic nanoparticles elevate the potential for their use in biomedical applications.

The magnetic nanoparticles can be synthesized and encapsulated by polymers, which enables the functionalization of the surface according to the objective. Thus, different biological molecules, such as antibodies, proteins, and target ligands, can bond to the surfaces of these nanoparticles by amide or ester chemical bonds [1]. Among the most investigated applications are the controlled release of pharmaceuticals, applications in hyperthermia, imaging by nuclear magnetic resonance and the separation and selection of molecules [3,69].

The iron oxides are the most investigated materials, with an emphasis on maghemite ( $\gamma\text{-Fe}_2\text{O}_3$ ) and magnetite ( $\text{Fe}_3\text{O}_4$ ). The possibility of nanoparticles to be controlled by an external magnetic field enables their conduction through specific body parts and favors the release of medication in certain regions. The use of nanometric systems enables the direct delivery of the drug to the cells or specific tumor regions surrounded by a healthy tissue [70]. Peptides and proteins can bond to nanoparticles, permeate membranes and enable intracellular drug delivery [1]. When subjected to an external magnetic field of alternated frequency, the magnetic nanoparticles cause the heating of the location where they are located (magneto hyperthermia, as previously mentioned). Since tumor cells are more sensitive to a significant temperature increase than normal cells, they are destroyed at temperatures between 41 and 47°C [1,69].

Tissue regeneration is another well-explored area because stem cells have significant potential for substituting degenerated cells or repairing damaged tissue [1]. Superparamagnetic nanoparticles can be associated with stem cells to be transported to the location of interest. Many proteins and growth factors can be associated with these nanoparticles and, therefore, are distributed in the damaged tissue, where they can act to regenerate the affected area.

## 5.6 Final Considerations

The unique properties of nanoparticles have been extensively explored by the most diverse fields, which corroborates the prediction by Feynman regarding the potential of nanostructures. The changes in the physical and chemical properties of the nanoparticles are related to the increase in the number of surface atoms in relation to the volume. Similarly, the electronic properties are altered by the formation of discrete energy levels instead of the conventional band structure for volumetric materials. This chapter discussed typical synthesis processes for the production of metal and oxide nanoparticles according to the need of application. Additionally, the improvements in the processes of material characterization during the last decade significantly contributed to the investigation of nanoparticles. Although various studies have been performed, additional exploration is needed.

## List of Symbols

$C$	Solute concentration
$C_0$	Solubility
$C_s$	Surface coverage
$d$	Interplanar distance
$D$	Particle diameter
$\sigma$	Concentration of supersaturation
$\Delta G_v$	Gibbs free energy of volume
$\Delta \mu_v$	Surface energy
$\gamma$	Surface energy per unit area
$k$	Constant dependent on geometric factors
$K$	Boltzmann constant
$\lambda$	Wavelength
$N$	Number of particles adsorbed per unit area
$N_{\max}$	Maximum number of particles adsorbed per unit area
$\text{nm}$	Nanometers
$\Omega$	Atomic volume
$r$	Radius of spherical nucleus
$r^*$	Critical radius
$R_a$	Roughness average
$T$	Temperature
$\theta$	Incidence angle in relation to the considered plane
$w$	Full width at half maximum

## References

- [1] A.K. Gupta, M. Gupta, Synthesis and surface engineering of iron oxide nanoparticles for biomedical applications, *Biomaterials* 26 (2005) 3995–4021.
- [2] J. Lee, D.K. Chatterjee, M.H. Lee, S. Krishnan, Gold nanoparticles in breast cancer treatment: promise and potential pitfalls, *Cancer Lett.* 347 (2014) 46–53.
- [3] Q.A. Pankhurst, J. Connolly, S.K. Jones, J. Dobson, Applications of magnetic nanoparticles in biomedicine, *J. Phys. D: Appl. Phys.* 36 (2003) R167.
- [4] J.S. Bradley, G. Schmid, Noble Metal Nanoparticles, In: *Nanoparticles: From Theory to Application*, Wiley-VCH, Weinheim, 2004, pp. 186–198.
- [5] E. Katz, A.N. Shipway, I. Willner, Biomaterial-nanoparticle hybrid systems: synthesis, properties, and applications, In: *Nanoparticles: From Theory to Application*, Wiley-VCH, Germany, 2004, pp. 368–421.
- [6] Y.S. Lee, *Self-assembly and nanotechnology: a force balance approach*, John Wiley & Sons, New Jersey, (2008).
- [7] G. Cao, *Nanostructures & Nanomaterials: Synthesis, Properties & Applications*, Imperial College Press, London, (2004).
- [8] H.J. Fecht, Formation of nanostructures by mechanical attrition, In: *Nanomaterials: Synthesis, Properties and Applications*, Taylor & Francis, New York, 1996, pp. 89–110.
- [9] C.C. Koch, The synthesis and structure of nanocrystalline materials produced by mechanical attrition: a review, *Nanostruct. Mater.* 2 (1993) 109–129.

- [10] H.J. Fecht, Nanostructured materials and composites prepared by solid state processing, In: Nanostructured Materials: Processing, Properties and Applications, Noyes Publication, New York, 2002, pp. 73–114.
- [11] C. Lam, Y.F. Zhang, Y.H. Tang, C.S. Lee, I. Bello, S.T. Lee, Large-scale synthesis of ultra“ne Si nanoparticles by ball milling, *J. Cryst. Growth* 220 (2000) 466–470.
- [12] E.A. Dobisz, F.A. Buot, C.R.K. Marrian, Nanofabrication and Nanoelectronics, In: Nanomaterials: Synthesis, Properties and Applications, Taylor & Francis, London, 1996, pp. 495–540.
- [13] U. Hilleringmann, Lithography procedures, In: Nanotechnology and Nanoelectronics: Materials, Devices, Measurement Techniques, Springer-Verlag, Berlin, 2005, pp. 154–171.
- [14] H. Frey, H.R. Khan, *Handbook of Thin Film Technology*, Springer Science & Business Media, Berlin, (2015).
- [15] Muttaqin, T. Nakamura, S. Sato, Synthesis of gold nanoparticle colloids by highly intense laser irradiation of aqueous solution by flow system, *Appl. Phys. A* 120 (2015) 881–888.
- [16] M. Vinod, K.G. Gopchandran, Ag@Au core–shell nanoparticles synthesized by pulsed laser ablation in water: effect of plasmon coupling and their SERS performance, *Spectrochim. Acta A Mol. Biomol. Spectrosc.* 149 (2015) 913–919.
- [17] M. Hillenkamp, G. di Domenicantonio, C. Félix, Monodispersed metal clusters in solid matrices: a new experimental setup, *Rev. Sci. Instrum.* 77 (2006) 025104.
- [18] A.D.T. de Sá, V.T.A. Oiko, G. di Domenicantonio, V. Rodrigues, New experimental setup for metallic clusters production based on hollow cylindrical magnetron sputtering, *J. Vac. Sci. Technol. B* 32 (2014) 061804.
- [19] T.-H. Tran, T.-D. Nguyen, Controlled growth of uniform noble metal nanocrystals: aqueous-based synthesis and some applications in biomedicine, *Colloids Surf. B Biointerfaces* 88 (2011) 1–22.
- [20] V.K. LaMer, R.H. Dinegar, Theory, production and mechanism of formation of monodispersed hydro-sols, *J. Am. Chem. Soc.* 72 (1950) 4847–4854.
- [21] R. Viswanatha, D.D. Sarma, Growth of nanocrystals in solution, In: Nanomaterials Chemistry: Recent Developments and New Directions, Wiley-VCH, Weinheim, 2007, pp. 139–170.
- [22] G.M. Chow, Gonsalves, K.E., Particle synthesis by chemical routes, In: Nanomaterials: Synthesis, Properties and Applications, Taylor & Francis, New York, 1996, pp. 55–71.
- [23] H. Huang, X. Yang, Synthesis of chitosan-stabilized gold nanoparticles in the absence/presence of tripolyphosphate, *Biomacromolecules* 5 (2004) 2340–2346.
- [24] A. Murugadoss, H. Sakurai, Chitosan-stabilized gold, gold–palladium, and gold–platinum nano-clusters as efficient catalysts for aerobic oxidation of alcohols, *J. Mol. Catal. A: Chem.* 341 (2011) 1–6.
- [25] A. Abou-Okeil, A. Amr, F.A. Abdel-Mohdy, Investigation of silver nanoparticles synthesis using amine- $\beta$ -cyclodextrin, *Carbohydr. Polym.* 89 (2012) 1–6.
- [26] Y. Huang, D. Li, J. Li,  $\beta$ -Cyclodextrin controlled assembling nanostructures from gold nanoparticles to gold nanowires, *Chem. Phys. Lett.* 389 (2004) 14–18.
- [27] D. Chen, X. Qiao, X. Qiu, J. Chen, Synthesis and electrical properties of uniform silver nanoparticles for electronic applications, *J. Mater. Sci.* 44 (2009) 1076–1081.
- [28] L. Guo, S. Yang, C. Yang, P. Yu, J. Wang, W. Ge, et al. Synthesis and characterization of poly(vinylpyrrolidone)-modified zinc oxide nanoparticles, *Chem. Mater.* 12 (2000) 2268–2274.
- [29] M. Habib Ullah, T. Hossain, C.-S. Ha, Kinetic studies on water-soluble gold nanoparticles coordinated to poly(vinylpyrrolidone): isotropic to anisotropic transformation and morphology, *J. Mater. Sci.* 46 (2011) 6988–6997.
- [30] A. Gautam, G.P. Singh, S. Ram, A simple polyol synthesis of silver metal nanopowder of uniform particles, *Synth. Met.* 157 (2007) 5–10.

- [31] P.S. Roy, J. Bagchi, S.K. Bhattacharya, Size-controlled synthesis and characterization of polyvinyl alcohol coated palladium nanoparticles, *Transit. Metal Chem.* 34 (2009) 447–453.
- [32] L.C. Klein, Processing of nanostructured sol–gel materials, In: *Nanomaterials: Synthesis, Properties and Applications*, Taylor & Francis, New York, 1996, pp. 147–164.
- [33] M. Niederberger, M. Antonietti, Nonaqueous sol–gel routes to nanocrystalline metal oxides, In: *Nanomaterials Chemistry: Recent Developments and New Directions*, Wiley-VCH, Weinheim, 2007, pp. 119–138.
- [34] M. Niederberger, Nonaqueous Sol–Gel routes to metal oxide nanoparticles, *Acc. Chem. Res.* 40 (2007) 793–800.
- [35] H. Zeng, P.M. Rice, S.X. Wang, S. Sun, Shape-controlled synthesis and shape-induced texture of Mn–Fe<sub>2</sub>O<sub>4</sub> nanoparticles, *J. Am. Chem. Soc.* 126 (2004) 11458–11459.
- [36] J. Ba, J. Polleux, M. Antonietti, M. Niederberger, Non-aqueous synthesis of tin oxide nanocrystals and their assembly into ordered porous mesostructures, *Adv. Mater.* 17 (2005) 2509–2512.
- [37] C. de Mello Donegá, P. Liljeroth, D. Vanmaekelbergh, Physicochemical evaluation of the hot-injection method, a synthesis route for monodisperse nanocrystals, *Small* 1 (2005) 1152–1162.
- [38] N.A. Frey, S. Peng, K. Cheng, S. Sun, Magnetic nanoparticles: synthesis, functionalization, and applications in bioimaging and magnetic energy storage, *Chem. Soc. Rev.* 38 (2009) 2532.
- [39] J. Turkevich, P.C. Stevenson, J. Hillier, A study of the nucleation and growth processes in the synthesis of colloidal gold, *Discuss. Faraday Soc.* 11 (1951) 55–75.
- [40] T. Yonezawa, T. Kunitake, Practical preparation of anionic mercapto ligand-stabilized gold nanoparticles and their immobilization, *Colloids Surf. A* 149 (1999) 193–199.
- [41] T. Zhu, K. Vasilev, M. Kreiter, S. Mittler, W. Knoll, Surface modification of citrate-reduced colloidal gold nanoparticles with 2-mercaptosuccinic acid, *Langmuir* 19 (2003) 9518–9525.
- [42] F.G. Zhao, W.S. Li, Dendrimer/inorganic nanomaterial composites: tailoring preparation, properties, functions, and applications of inorganic nanomaterials with dendritic architectures, *Sci. China Chem.* 54 (2011) 286–301.
- [43] R.M. Crooks, M. Zhao, L. Sun, V. Chechik, L.K. Yeung, Dendrimer-encapsulated metal nanoparticles: synthesis, characterization, and applications to catalysis, *Acc. Chem. Res.* 34 (2001) 181–190.
- [44] E.N. Crespilho, M. Emilia Ghica, M. Florescu, F.C. Nart, O.N. Oliveira Jr., C.M.A. Brett, A strategy for enzyme immobilization on layer-by-layer dendrimer–gold nanoparticle electrocatalytic membrane incorporating redox mediator, *Electrochim. Commun.* 8 (2006) 1665–1670.
- [45] G.L. Hornyak, H.F. Tibbals, J. Dutta, J.J. Moore, *Introduction to Nanoscience and Nanotechnology*, CRC Press, Boca Raton, (2009).
- [46] C.J. Murphy, T.K. Sau, A.M. Gole, C.J. Orendorff, J. Gao, L. Gou, et al. Anisotropic metal nanoparticles: synthesis, assembly, and optical applications, *J. Phys. Chem. B* 109 (2005) 13857–13870.
- [47] C.P. Poole Jr., F.J. Owens, *Introduction to Nanotechnology*, Wiley-Interscience, New Jersey, (2003).
- [48] B.S. Mitchell, The structure of materials, in: B.S. Mitchell (Ed.), *An Introduction to Materials Engineering and Science: For Chemical and Materials Engineers*, John Wiley & Sons, New Jersey, 2004, pp. 1–135.
- [49] W.D. Callister, *Ciência e engenharia de materiais [Materials sciences and engineering]*, seventh ed., LTC, Rio de Janeiro, (2008).
- [50] H. Borchert, E.V. Shevchenko, A. Robert, I. Mekis, A. Kornowski, G. Grübel, et al. Determination of nanocrystal sizes: a comparison of TEM, SAXS, and XRD studies of highly monodisperse CoPt<sub>3</sub> particles, *Langmuir* 21 (2005) 1931–1936.
- [51] V.S. Zaitsev, D.S. Filimonov, I.A. Presnyakov, R.J. Gambino, B. Chu, Physical and chemical properties of magnetite and magnetite-polymer nanoparticles and their colloidal dispersions, *J. Colloid Interface Sci.* 212 (1999) 49–57.

- [52] U. Holzwarth, N. Gibson, The Scherrer equation versus the 'Debye-Scherrer equation', *Nat. Nanotechnol.* 6 (2011) 1534–1534.
- [53] A.L. Patterson, The Scherrer formula for X-ray particle size determination, *Phys. Rev.* 56 (1939) 978.
- [54] D.A. Skoog, F.J. Holler, S.R. Crouch, *Instrumental Analysis*, sixth ed., Cengage Learning, Belmont, CA, (2007).
- [55] A. Sruanganurak, K. Sanguansap, P. Tangboriboonrat, Layer-by-layer assembled nanoparticles: a novel method for surface modification of natural rubber latex film, *Colloids Surf. A* 289 (2006) 110–117.
- [56] W. Chartarrayawadee, S.E. Moulton, D. Li, C.O. Too, G.G. Wallace, Novel composite graphene/platinum electro-catalytic electrodes prepared by electrophoretic deposition from colloidal solutions, *Electrochim. Acta* 60 (2012) 213–223.
- [57] X. Luo, A. Morrin, A.J. Killard, M.R. Smyth, Application of nanoparticles in electrochemical sensors and biosensors, *Electroanalysis* 18 (2006) 319–326.
- [58] X. Cao, Y. Ye, S. Liu, Gold nanoparticle-based signal amplification for biosensing, *Anal. Biochem.* 417 (2011) 1–16.
- [59] M.C. Daniel, D. Astruc, Gold nanoparticles: assembly, supramolecular chemistry, quantum-size-related properties, and applications toward biology, catalysis, and nanotechnology, *Chem. Rev.* 104 (2004) 293–346.
- [60] Y. Li, P. Cheng, J. Gong, L. Fang, J. Deng, W. Liang, et al. Amperometric immunosensor for the detection of *Escherichia coli* O157:H7 in food specimens, *Anal. Biochem.* 421 (2012) 227–233.
- [61] G.S. Devi, V. Rao, Room temperature synthesis of colloidal platinum nanoparticles, *Bull. Mater. Sci.* 23 (2000) 467–470.
- [62] C. Zhu, S. Guo, Y. Zhai, S. Dong, Layer-by-layer self-assembly for constructing a graphene/platinum nanoparticle three-dimensional hybrid nanostructure using ionic liquid as a linker, *Langmuir* 26 (2010) 7614–7618.
- [63] M.L. Yola, T. Eren, N. Atar, H. Saral, İ. Ermiş, Direct-methanol fuel cell based on functionalized graphene oxide with mono-metallic and Bi-metallic nanoparticles: electrochemical performances of nanomaterials for methanol oxidation, *Electroanalysis* 28 (2015) 570–579.
- [64] Z.L. Zhao, L.Y. Zhang, S.J. Bao, C.M. Li, One-pot synthesis of small and uniform Au@PtCu core–alloy shell nanoparticles as an efficient electrocatalyst for direct methanol fuel cells, *Appl. Catal. B: Environ.* 174–175 (2015) 361–366.
- [65] L.D. Rampino, F. Nord, Preparation of palladium and platinum synthetic high polymer catalysts and the relationship between particle size and rate of hydrogenation, *J. Am. Chem. Soc.* 63 (1941) 2745–2749.
- [66] T. Hao-lin, P. Mu, M. Shi-chun, Y. Run-zhang, Synthesis of platinum nanoparticles modified with nafion and the application in PEM fuel cell, *J. Wuhan Univ. Technol.–Mater. Sci. Ed.* 19 (2004) 7–9.
- [67] L. Li, Y. Zhang, J.-F. Drillet, R. Dittmeyer, K.-M. Jüttner, Preparation and characterization of Pt direct deposition on polypyrrole modified Nafion composite membranes for direct methanol fuel cell applications, *Chem. Eng. J.* 133 (2007) 113–119.
- [68] M.A. Smit, A.L. Ocampo, M.A. Espinosa-Medina, P.J. Sebastián, A modified Nafion membrane with in situ polymerized polypyrrole for the direct methanol fuel cell, *J. Power Sources* 124 (2003) 59–64.
- [69] A. Singh, S.K. Sahoo, Magnetic nanoparticles: a novel platform for cancer theranostics, *Drug Discov. Today* 19 (2014) 474–481.
- [70] G.A. Hughes, Nanostructure-mediated drug delivery, *Nanomedicine: Nanotechnology, Biology and Medicine*. 1 (2005) 22–30.

# Magnetic Nanomaterials

M.A.G. Soler\*, L.G. Paterno\*\*

\*INSTITUTE OF PHYSICS, UNIVERSITY OF BRASÍLIA, UNIVERSITY CAMPUS  
DARCY RIBEIRO, BRASÍLIA, BRAZIL; \*\*INSTITUTE OF CHEMISTRY, UNIVERSITY  
OF BRASILIA, UNIVERSITY CAMPUS DARCY RIBEIRO, BRASILIA, BRAZIL

## CHAPTER OUTLINE

<b>6.1</b>	<b>Introduction .....</b>	<b>147</b>
<b>6.2</b>	<b>Basic Concepts of Magnetism.....</b>	<b>149</b>
6.2.1	Ferrimagnetism .....	154
6.2.2	Cubic Ferrites.....	155
6.2.3	Superparamagnetism.....	157
<b>6.3</b>	<b>SPIOs.....</b>	<b>160</b>
6.3.1	Synthesis of Iron Oxides via Coprecipitation .....	161
6.3.2	Synthesis of Iron Oxides via Thermal Decomposition .....	162
6.3.3	SPIO Particle Functionalization and the Preparation of Magnetic Colloids .....	163
<b>6.4</b>	<b>The Structure and Physico-Chemical Properties of the SPIO Systems.....</b>	<b>166</b>
6.4.1	Measurements of the Size and Agglomeration State.....	167
6.4.2	Composition and Structure.....	168
6.4.3	Surface Morphology and Properties .....	171
6.4.4	Magnetic Properties.....	174
<b>6.5</b>	<b>Biomedical Applications.....</b>	<b>177</b>
<b>6.6</b>	<b>Conclusions and Perspectives.....</b>	<b>180</b>
<b>List of Symbols .....</b>		<b>181</b>
<b>References .....</b>		<b>181</b>

## 6.1 Introduction

Magnetic materials of nanometric dimensions are found in nature, including the magnetite nanoparticles (NPs) present in many bacteria, insects, and larger animals. Many migratory animals also have magnetic NPs in their body and use them as biomagnetic compasses. For instance, salmon use the magnetite NPs present in their nasal fossa for orientation during their migratory travels [1]. Artificial magnetic nanomaterials have been developed since the 1980s, especially because of the availability of proper instrumentation to characterize

structures and properties at the nanoscale and to develop many synthesis routes and elaborate surface treatments. Magnetic nanostructures can be simply produced in the form of NPs of a specific magnetic material (metals, magnetic alloys, or oxides), molecular magnets or even as one-, two-, or three-dimensional arrangements such as nanothreads, mono- and multilayer films, NP agglomerates (clusters), dispersions in nonmagnetic lattices (nanocomposites), and others [2]. NPs can be prepared in different shapes such as spheres, rods, fibers, and polyhedrons in general, from cubes to multifaceted prisms [3,4].

Among the magnetic materials prepared at a nanometric dimension, special attention is drawn to those produced with the transition metals such as, Fe, Co, Ni, and their alloys; pure ferrites such as magnetite ( $\text{Fe}_3\text{O}_4$ ) and maghemite ( $\gamma\text{-Fe}_2\text{O}_3$ ); mixed ferrites such as, cobalt ( $\text{CoFe}_2\text{O}_4$ ), nickel ( $\text{NiFe}_2\text{O}_4$ ), manganese ( $\text{MnFe}_2\text{O}_4$ ), zinc ( $\text{ZnFe}_2\text{O}_4$ ), and copper ( $\text{CuFe}_2\text{O}_4$ ) ferrite;  $\text{BaFe}_{12}\text{O}_{19}$ ;  $\text{SmCo}_5$ ; manganese compounds; or core–shell structure [3]. Magnetic NPs in their colloidal state, with sizes on the order of 10 nm, have also been created, especially because of their relatively easy preparation and stability in aqueous or organic medium suspensions. In addition, the colloidal suspensions of magnetic nanomaterials known as ferrofluids, nanofluids (NFs), or magnetic fluids (MFs) respond to the action of a magnetic field gradient as though they were a single liquid and magnetic phase, making them interesting materials for different purposes [5].

Superparamagnetic cubic ferrites (e.g., maghemite, magnetite, and cobalt ferrite) present a spinel-like structure and form monodomains with diameters ranging from 5 to 20 nm. These NPs can be synthesized via wet chemical routes with a reasonable control of shape, size, composition, crystallinity, and physical properties [6–9]. Because of their superparamagnetic behavior [5,10], these nanomaterials are known as superparamagnetic iron oxides (SPIOs), and they consist essentially of an iron oxide core with a diameter of a few nanometers and a subnanometric surface layer composed of iron oxyhydroxide groups [11,12]. In the colloidal form, the surface must be functionalized to achieve stability in suspension. Functionalization can be obtained by a simple acid–base reaction that introduces surface charges to the particles or by coating with molecular species of small molecules (e.g., citric acid) as well as surfactants or polymers. This coating also promotes the anchorage of other chemical species that are able to perform diagnosis and therapy tasks *in vivo* [13]. Because of their biocompatibility, SPIO particles have great potential for biomedical applications (e.g., drug delivery systems, markers, magnetic hyperthermia, and improving magnetic resonance imaging contrast). In addition, these systems might have a large effect on new industrial technologies such as insulating oils for transformers, spintronics structures, bioelectrochemistry, catalysis, and chemical sensors [14–17]. Therefore, the design and control of the properties of low-dimensional structures are a challenge for the fields of fundamental and applied magnetism.

This chapter presents the principles of magnetism for low-dimensional systems in a general way, emphasizing the properties of the magnetic nanostructures formed by iron oxide-based colloids. The discussion also includes details about the most used chemical synthesis methods for the production of iron oxide NPs as well as for surface functionalization and the preparation of films. Lastly, their major physico-chemical properties and some of their biomedical applications are discussed.

## 6.2 Basic Concepts of Magnetism

When a solid material is subjected to the action of an external magnetic field  $H$ , a magnetic field  $B$  is induced inside the material. The relationship between  $B$  and  $H$  is a material property, in SI units [18]:

$$\bar{B} = \mu_0 (\bar{H} + \bar{M}) \quad (6.1)$$

where  $\bar{M}$  is the magnetization of the medium given by the magnetic moment per volume unit ( $\bar{M} = \frac{\vec{m}}{V}$ , where  $\vec{m}$  is the magnetic moment);  $\mu_0$  is the magnetic permeability of vacuum, equal to  $4\pi \times 10^{-7}$  Henry m<sup>-1</sup> (SI). The units of  $M$  and  $H$  are (A m<sup>-1</sup>), and those for  $\mu_0$  are weber (A m)<sup>-1</sup>, also known as Henry m<sup>-1</sup>; therefore, the units of  $B$  are weber m<sup>-2</sup>, or tesla (T), where 1 Gauss =  $10^{-4}$  T. The magnitude of  $M$  is proportional to the applied magnetic field  $H$ ,

$$M = \chi H \quad (6.2)$$

where  $\chi$  is the magnetic susceptibility of the material. In SI units,  $\chi$  is dimensionless.

The response of solid materials to the action of an external magnetic field depends on their atomic structure, electromagnetic excitation, pressure, and temperature. Even in the classical approximation, the electrons and nuclei of solids produce magnetic fields because they are moving charges that have intrinsic magnetic dipole moments. The factors that contribute to the atomic magnetic moment are the orbital angular momentum, the electron spin, and their interaction. Hence, magnetism is essentially a quantum mechanical phenomenon. The solution of Schrödinger's equation provides information about the energy shells or states occupied by the electrons and (with this solution) magnetic moments. The state of one electron is characterized by four quantum numbers [19,20]:

1. The principal quantum number ( $n$ ), with values of 1, 2, 3, ... corresponding to shells K, L, M, ....
2. The orbital angular momentum ( $l$ ), which describes the angular momentum of the orbital movement. For a given value of  $l$ , the angular momentum of an electron due to its orbital movement is equal to  $\hbar\sqrt{l(l+1)}$ . The number  $l$  can have integer numbers of 0, 1, 2, 3, ...  $n - 1$ . The electrons with  $l = 1, 2, 3, 4, \dots$  refer to the electrons s, p, d, f, ....
3. The magnetic quantum number ( $m_l$ ), which describes the component of the orbital angular momentum along a particular direction. For most cases, this direction is selected along an applied field. For a given value of  $l$ ,  $m_l = l, l-1, \dots, 0, \dots, -l+1, -l$ . For instance, the values allowed for the angular moment along a direction are  $2\hbar, \hbar, 0, -\hbar$ , and  $-2\hbar$  for a *d* electron.
4. The spin quantum number ( $m_s$ ), which describes the electron spin component along a particular direction, generally in the direction of the applied field. The electron spin is the intrinsic angular momentum that corresponds to the rotation of each electron around its internal axis. The possible values for  $m_s$  are  $\pm 1/2$ , and the corresponding spin angular momentum components are  $\pm \hbar/2$ .

According to the Pauli exclusion principle, it is not possible for two electrons to occupy the same state (i.e., each electron should have a unique set of quantum numbers  $n, l, m_l$ , and  $m_s$ ). The maximum number of electrons that occupy a given shell is given by [20]

$$2 \sum_{l=0}^{n-1} (2l+1) = 2n^2 \quad (6.3)$$

The movement of an electron can be considered as a stream flowing through a conducting wire. An electron with orbital angular momentum  $\hbar l$  has an associated magnetic moment  $\vec{\mu}_l$  given by

$$\vec{\mu}_l = -\frac{|e|}{2m} \hbar \vec{l} = -\mu_B \vec{l} \quad (6.4)$$

where  $\mu_B$  is the Bohr magneton. The absolute value of the magnetic moment is given by

$$|\vec{\mu}_l| = \mu_B \sqrt{l(l+1)} \quad (6.5)$$

and its projection along the direction of the applied field is

$$\mu_{lz} = -m_l \mu_B \quad (6.6)$$

In the case of the spin moment, the associated magnetic moment is expressed as

$$\vec{\mu}_s = -g_e \frac{|e|}{2m} \hbar \vec{s} = -g_e \mu_B \vec{s} \quad (6.7)$$

where  $g_e$  ( $=2.002290716$ ) is the spectroscopic splitting factor (or the  $g$ -factor for the free electron). The Bohr magneton expresses the magnetic dipole moment of the electron (i.e., the most fundamental magnetic moment), whose magnitude in SI is  $9.27 \times 10^{-24} \text{ JT}^{-1}$ . For each electron in an atom, the spin magnetic moment is  $\pm \mu_B$ .

The net magnetic moment of an atom is equal to the sum of the magnetic moments of each one of its electrons, including the contributions of the orbitals and their spin. For an atom with completely filled electron shells and subshells, there is a mutual of the moments (orbital and spin). Therefore, the materials formed by atoms with completely filled electron shells are unable to be permanently magnetized. These materials are known as diamagnetic materials. The eventual formation of a dipole moment in these materials only occurs when they are subjected to an external field that causes a temporary variation of the orbital movement. In terms of susceptibility, the diamagnetic materials have negative susceptibility; thus, the magnitude of the field induced internally by the action of an external field is lower than that in vacuum. In addition, the magnetic moment induced by the external field in these materials is extremely low and has a direction opposite to the applied field. In turn, the paramagnetic materials are formed by atoms with half-filled electron shells; therefore, they present a dipole moment. Nevertheless, dipoles are randomly oriented and are only aligned by the action of an external field, creating a small but

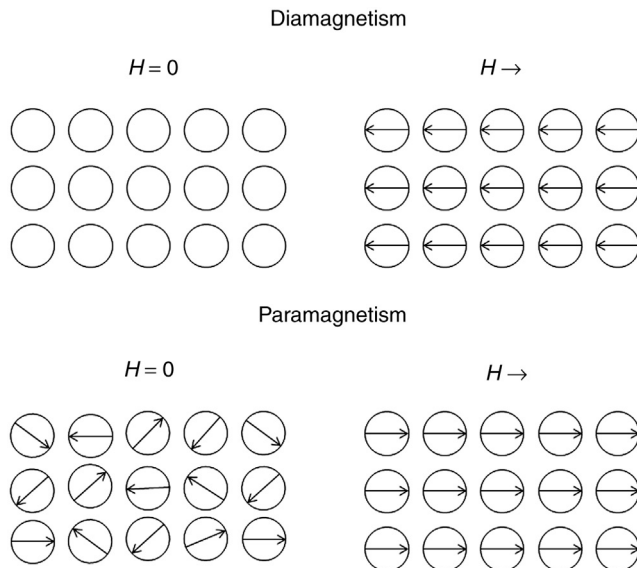


**FIGURE 6.1** An illustration of the magnetic dipole arrangement for diamagnetism and paramagnetism.

positive susceptibility. A scheme of these behaviors is presented in Fig. 6.1. Both diamagnetic and paramagnetic materials are considered as nonmagnetic because they only present magnetization in the presence of an external field [19].

The transition metals, for instance, iron, cobalt, nickel, and some rare-earth metals such as, gadolinium, are ferromagnetic, with positive susceptibility on the order of  $10^6$ . The antiferromagnetic materials present an antiparallel arrangement of spins that cancel each other and result in a net magnetic moment of zero. From a macroscopic point of view, ferrimagnetic materials are similar to ferromagnetic materials. The difference between them is in the origin of their net magnetic moments. Because these compounds are essentially ionic compounds such as, dual iron oxides (or ferrites), the magnetism of the ferrimagnetic materials is due to the spin moments of their unpaired metal ions in the crystalline lattice.

Magnetic materials have magnetic moments with a spontaneous long-range order. This order is due to a quantum electrostatic interaction known as exchange or interchange interaction. The interaction responsible for the magnetic order might be short-range (i.e., direct exchange interaction), long-range, or an indirect interaction [21]. Magnetic ordering (e.g., observed in the parallelism of atomic magnetic moments in ferromagnetic materials) is due to the exchange interaction. The presence of other interactions results in the formation of magnetic domains, regions of the sample where (to a first approximation) perfectly ordered moments can be considered. When an external magnetic field is applied, the borders of these domains (the domain walls) are displaced, causing changes in the ferromagnet magnetization [21]. Only materials with ferromagnetic or ferrimagnetic behaviors are considered as magnetic materials.

The formulation of the exchange interaction can be obtained from Schrödinger's equation for a two-electron system with spatial coordinates  $\vec{r}_1$  and  $\vec{r}_2$ , spin coordinates  $\sigma$ , and nondegenerate energy states. Conventionally,  $\sigma$  can be +1 or -1, corresponding to the z projection of the spins equal to +1/2 and -1/2, respectively. Assuming the existence of an interaction between the electrons, a Coulombic potential term is introduced into the Hamiltonian, which (in the CGS system) is given by [21]

$$V_{1,2}(\vec{r}_1, \vec{r}_2) = \frac{e^2}{r_{1,2}} \quad (6.8)$$

The obtained eigenvalues have a term that refers to the Coulombic energy and another term known as the exchange integral ( $J$ ) [21]. Hence, the introduction of the interaction term  $V_{1,2}$  between spins leads to a new energy term that depends on the relative orientation of these spins. In addition, it is necessary to include the atom pair interaction ( $i,j$ ), each one with an associated spin moment  $\vec{S}$  that considers the contribution of the spin moments of all of their electrons. The Heisenberg Hamiltonian equation describes the interactions for the neighbor atom pairs in the lattice, and it is given by [22]

$$\mathcal{H} = -2 \sum_{i,j} J_{ij} \vec{S}_i \cdot \vec{S}_j \quad (6.9)$$

where,  $i$  and  $j$  represent the positions of the atoms in the lattice, and  $J$  is the exchange constant. If  $J > 0$ , then the ferromagnetic interaction occurs, which couples the spins in a parallel manner ( $\uparrow\uparrow$ ). In turn, if  $J < 0$ , then the interaction is antiferromagnetic, and the spins are coupled in an antiparallel manner ( $\uparrow\downarrow$ ). The first type of interaction occurs in ferromagnets, whereas the second type occurs in antiferromagnetic and ferrimagnetic materials. Fig. 6.2 illustrates the arrangement of the dipole moments in the ferromagnetic, antiferromagnetic, and ferrimagnetic materials with their respective exchange constants.

As discussed at the beginning of this chapter, any description of magnetism (ferromagnetism and ferrimagnetism) should consider the total moments (orbital and spin) of the magnetic atom [20,21]. The total orbital angular momentum ( $\vec{L}$ ) of an atom is given by the sum of the orbital momenta of all of its electrons [20]:

$$\vec{L} = \sum_i \vec{l}_i \quad (6.10)$$

Naturally, the sum for a complete electron shell is zero. The same logic can be applied to the total spin moment ( $\vec{S}$ ), defined by [20]

$$\vec{S} = \sum_i \vec{s}_i \quad (6.11)$$

The result of the spin-orbit interaction, the total angular momentum ( $\vec{J}$ ), is given by [21]

$$\vec{J} = \vec{L} + \vec{S} \quad (6.12)$$

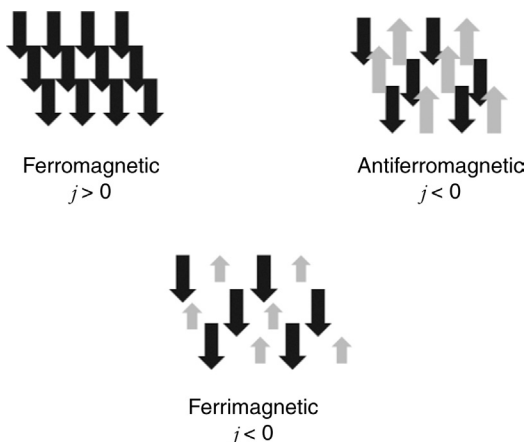


**FIGURE 6.2** An illustration of the dipole arrangements in ferromagnetic, antiferromagnetic, and ferrimagnetic systems, and the values of their exchange constant. Modified from D. Ortega, *Structure and Magnetism in magnetic nanoparticles*, in: N.T.K. Than (Ed.), *Magnetic Nanoparticles From Fabrication to Clinical Applications*, Taylor & Francis Group, Boca Raton, FL, 2012 [22].

The value of  $\bar{J}$ , also known as the spin-orbit or Russell-Saunders coupling, expresses the interaction between the spin and angular momenta of an electron orbit (note that  $\bar{J}$  differs from  $J$ ). Its magnitude and effect on the energy shells of the atom depend on the relative orientation of the magnetic moments of spin and orbit. The value of  $J$  can range from  $J = (L - S), (L - S + 1) \dots (L + S - 1), (L + S)$ . The spin-orbit interaction energy is given by  $\lambda \vec{L} \cdot \vec{S}$ , where  $\lambda$  is the coupling constant in  $\text{cm}^{-1}$ . When the coupling constant is positive (which occurs when the electron shell is less than half-filled), the minimum energy configuration (i.e., fundamental state) is obtained for antiparallel  $L$  and  $S$  (i.e.,  $J = L - S$ ). For a more than half-filled shell, the minimum energy configuration is given by  $J = L + S$ . For instance, consider the cobalt(II) ion: The 3d subshell of  $\text{Co}^{2+}$  contains 7 of the 10 electrons that it can accommodate; the subshell is more than half-filled, so the fundamental state is characterized by the quantum number  $J = L + S = 9/2$  [22]. The elements that have incomplete shells are known as “transition elements” and belong to groups 3d (iron group), 4d (palladium group), 5d (platinum group), 4f (lanthanides), and 5f (actinides). Unlike what occurs with closed shells where the sum of the projections of the angular momenta  $\vec{m}_l$  and  $\vec{m}_s$  is zero, the angular momenta of the incomplete shells are not zero; consequently, their magnetic moment is not zero. Thus, transition elements are the important elements for magnetism. However, a more external and incomplete shell (e.g., 4s) does not result in magnetic effects because the unpaired electron participates in the chemical bond.

Ferromagnetic materials consist of magnetic domains and present spontaneous magnetization at room temperature as well as the phenomena of saturation magnetization, and hysteresis. Spontaneous magnetization disappears above the critical temperature ( $T_c$ ) known as the Curie temperature, above which the material becomes paramagnetic. The graph of  $M$  versus  $H$  is known as the magnetization curve or  $M \times H$  curve. A magnetization

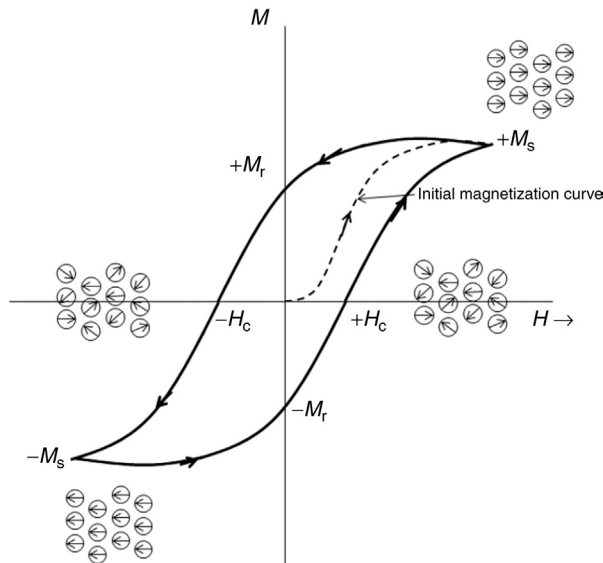


**FIGURE 6.3** A magnetic hysteresis curve of a ferromagnetic (or ferrimagnetic) material. The major magnetic magnitudes are indicated in the curve. The evolution of the magnetic ordering in a system as a function of the field is illustrated.

curve for the ferrimagnetic and ferromagnetic materials is presented in Fig. 6.3. The curve presents a saturation magnetization  $M_s$  above a determined value of the applied field. As the field decreases to zero after saturation, the magnetization is not reduced to zero, a phenomenon known as hysteresis, that is, important for technological applications. If the field is applied to a magnetic material at its demagnetized state, then the magnetization will have a value that ranges from zero to  $M_s$  when the field increases in the positive direction. When the field is reduced after saturation, the magnetization decreases to  $M_r$  (the remanent magnetization). The field applied in the opposite direction needed to reduce the magnetization to zero is known as the coercive field or coercivity,  $H_c$ . Magnetic materials are classified as hard or soft depending on their coercivity value. A hard magnet requires the application of a large field to reduce the remanence to zero or to saturate the magnetization. A soft magnet reaches saturation with small fields and is easily demagnetized. When the reverse field is increased further, magnetization saturation is reached with the opposite orientation. When the ferromagnet is demagnetized, the magnetization vectors in the different domains have random orientations and the total magnetization is equal to zero. The magnetization process causes the orientation of all domains to be the same.

### 6.2.1 Ferrimagnetism

The most important ferrimagnetic materials are the dual oxides composed of iron and another metal, generally known as ferrites. These ferrites can take a cubic or hexagonal shape. Cubic ferrites have a molecular formula of the type  $MFe_2O_4$  or  $MO \cdot Fe_2O_3$ , where  $M$

is a divalent transition metal such as Fe, Co, Ni, Mn, Cu, or Zn. Cobalt ferrite is considered as magnetically hard, whereas the other cubic ferrites are considered as soft. The most important hexagonal ferrites are barium hexaferrite ( $\text{BaO}\cdot\text{6Fe}_2\text{O}_3$ ) and strontium hexaferrite ( $\text{SrO}\cdot\text{6Fe}_2\text{O}_3$ ) [18].

Ferrites are ionic compounds, and their magnetic ions are responsible for their magnetic properties. The spins, whose action in ferrimagnetism and related phenomena result in spontaneous magnetic moments, occur in the ionic lattice. Only the contribution of the spins is considered because the orbital contribution can be negated in ferrites. Oxygen ions do not have a resultant moment. In the transition elements, the  $d$  shell can contain five spin-up electrons ( $+1/2$ ) and five spin-down electrons ( $-1/2$ ). The first electrons spin up to maximize the moment. According to the Pauli exclusion principle, the sixth electron must have a spin down. An ion with four electrons in  $3d$ , such as  $\text{Fe}^{2+}$ , should have a moment of  $4\mu_{\text{B}}$ , considering only the spin. In this case, the ionic compounds that are insulators are considered. In these materials, the electron energy levels do not superpose as they do in metals. Therefore, an integer number of electrons can be associated with each ion of the solid, such as, in the case of the free ion. The interaction between the atomic spins responsible for the magnetic order is the exchange interaction, an interaction of electronic origin. Therefore, the ferrimagnetic state is the result of the exchange interaction between the resultant spins of the different ions. Ferrimagnetism implies the existence of two non-identical sublattices, A and B, and usually at least three different exchange interactions,  $J_{AA}$ ,  $J_{AB}$ , and  $J_{BB}$  [23]. The ions of sublattice A are magnetized in one direction, whereas the ions of sublattice B are magnetized in the opposite direction. The opposite moments do not cancel each other out, resulting in spontaneous magnetization.

### 6.2.2 Cubic Ferrites

Cubic ferrites have a complex structure known as a spinel because it is similar to that of the spinel mineral ( $\text{MgO}\cdot\text{Al}_2\text{O}_3$ ). This structure has 56 ions per unit cell, which can be divided into eight subunits. The oxygen ions are larger (with an ionic radius on the order of 0.13 nm), and they are arranged in a face-centered cubic configuration with interstitials half-filled with much smaller metal ions (with an ionic radius ranging between 0.07 and 0.08 nm). The two types of metal ion coordination result in two magnetic sublattices in cubic ferrites: one tetrahedral (site A), in which the ions are located at the center of a tetrahedron and the vertices are occupied by oxygen ions, and another octahedral (site B), in which the metal ions are coordinated with six oxygen ions. The crystalline symmetry is cubic and corresponds to the  $O_h^7$  ( $Fd\bar{3}m$ ) spatial group. Fig. 6.4 shows the types of tetrahedral ( $T_d$ ) and octahedral ( $O_h$ ) coordination symmetries as well as the ion spatial geometries for a spinel-like cubic ferrite.

Direct spinel (or normal) and inverse structures might exist depending on the distribution of divalent and trivalent ions at sites A and B. In the direct spinel structure, all of the divalent metal ions occupy only the tetrahedral sites (A), whereas the trivalent metal ions occupy the octahedral sites (B). In the inverse spinel structure, all of the divalent ions

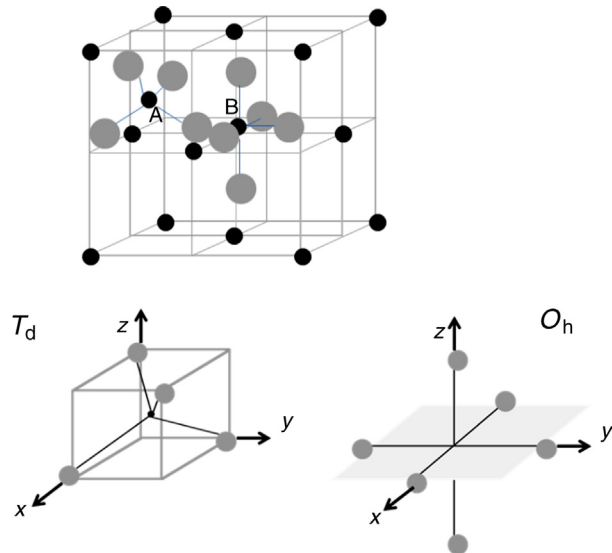


**FIGURE 6.4** A representation of the atomic arrangement as well as the tetrahedral ( $T_d$ ) and octahedral ( $O_h$ ) coordination geometries for a spinel-like cubic ferrite. The spheres in gray represent the  $O^{2-}$  ions, and the spheres in black represent the iron ions ( $Fe^{2+}$  or  $Fe^{3+}$ ). Adapted from B.D. Cullity, C.D. Graham, *Introduction to Magnetic Materials*, second ed., John Wiley & Sons, New Jersey, 2009 [18].

occupy the octahedral sites, whereas the trivalent ions are equally distributed between the two sites (i.e., half occupy the octahedral sites, and the other half occupy the tetrahedral sites). Fig. 6.5 shows the spin distribution in the inverse spinel structure of magnetite ( $Fe_3O_4$ ) [24]. As shown, the spin moment due to the  $Fe^{3+}$  ions is zero because their spin moments cancel each other out between sites A and B. In turn, the spin moments of the  $Fe^{2+}$  ions are aligned in parallel and in the same direction (sites B), which results in an effective magnetic moment responsible for the magnetization of the material. Moreover, in both the direct and inverse spinel structures, not all of the available sites are occupied by metal ions; only 1/8 of sites A and half of sites B are occupied. In practice, the synthesis conditions influence the arrangement of metal ions in ferrites of spinel-like structure, and it is not rare to obtain mixed ferrites. The mixed ferrites represent an intermediary arrangement between the direct and inverse structures. The degree of inversion is the parameter that describes this type of ferrite [23].

Magnetite is a typical inverse ferrite. In turn, maghemite is considered as a form of magnetite with an iron deficiency, and it has the chemical formula of  $\square_{1/3}Fe_{8/3}O_4$ , where  $\square$  represents a vacant site in the crystal. Given the crystallographic and magnetic representation of the magnetite structure in the two neighboring sites A and B, a given iron atom is antiferromagnetically coupled via superexchange to another iron atom of the same valence and ferromagnetically coupled via double exchange with an iron atom of a different valence. The two exchange interactions occur with regard to the oxygen ion.

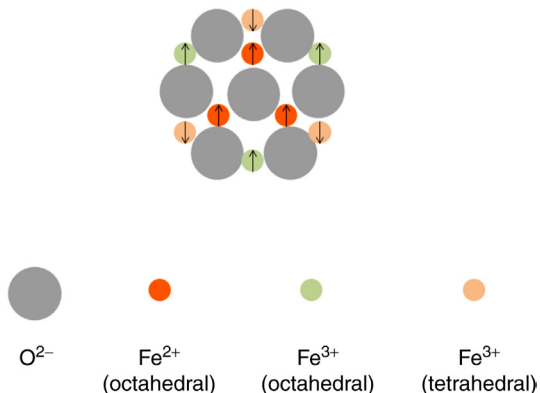


FIGURE 6.5 Scheme of the spin moment distribution for magnetite ( $\text{Fe}_3\text{O}_4$ ) with an inverse spinel structure. Adapted from W.D. Callister, *Materials Science and Engineering: an Introduction*, seventh ed., John Wiley & Sons New York 2007 [24].

### 6.2.3 Superparamagnetism

Superparamagnetic behavior is associated with the dependency of the structure of magnetic domains on the size of the material, and it occurs when its dimension reaches the nanometric scale. Any ferromagnetic or ferrimagnetic material below its Curie temperature contains small regions where mutual alignment of all magnetic dipole moments exists in the same direction. This region is known as the magnetic domain (Fig. 6.6). Within each domain, the magnetization has its own saturation value. The domain structure is organized to reduce magnetostatic energy. The size, shape, and orientation of the domains

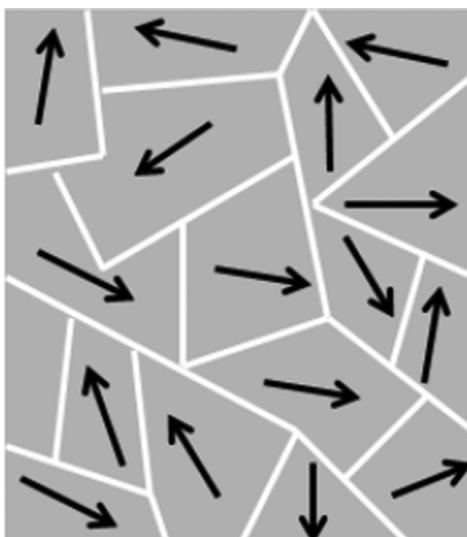


FIGURE 6.6 Magnetic domain structure. The arrows represent the direction of the effective magnetic moment in each domain. The white separating lines represent the domain walls.

depend on the interaction between the exchange, magnetostatic, and anisotropic energies of the system. In turn, the domains inside a material are separated by boundaries known as domain walls, through which the direction of the magnetization varies gradually. In a nonmagnetized material, the weighted sum of the magnetization vectors of all of the domains is zero, and the material does not have net magnetization.

When the volume of the magnetic material decreases to the nanometric scale, the typical domain size and the width of the wall-domain interfaces are reduced, thereby modifying its internal structure. The energy for the creation of a wall-domain interface in particles with volumes smaller than a given critical value is higher than the corresponding reduction in magnetostatic energy. In this boundary, no division into smaller domains occurs, and the magnetic structure of a single domain is maintained. For spherical particles, the critical diameter ( $D_c$ ), above which the material could be considered as a monodomain, was determined by Kittel, and it is on the order of 10–20 nm [25].

The magnetic behavior of a monodomain system is characterized by the mutual alignment of the atomic moments along the direction of the easy axis of magnetization, creating a large magnetic moment. In this type of magnetism, the magnetic moments of the particles behave similarly to a paramagnetic system, albeit with a total moment of a much larger magnitude ( $10^2$ – $10^4 \mu_B$ ) than those of the individual atoms ( $\mu_e \sim \mu_B$ ). This fact originated the name “superparamagnetism.”

In the superparamagnetic regimen, the orientation of the magnetic moments of particles floats around the easy axis of magnetization. The simplest model that describes the dynamics of the particle magnetic moments is the one-dimensional double-well potential [26], which is schematically illustrated in Fig. 6.7. The primary contribution to the double-well potential boundary is the magnetocrystalline anisotropy that aligns the magnetic moments in a given crystallographic direction (e.g., in the [111] direction for magnetite). The magnetization of a monodomain particle is oriented along the easy axis of magnetization as determined by the shape and magnetocrystalline anisotropy of the system. Depending on the domain size, the thermal energy  $kT$  can be sufficiently high, high enough ( $U = KV$ , the effective magnetocrystalline energy) to promote the reorientation of the magnetic moments against the magnetocrystalline energy barrier, thereby resulting in the fluctuation of the magnetic moments on a time scale of nanoseconds.

The typical relaxation time, which corresponds to the mean time taken by the magnetic moment to reorient itself in relation to the easy axis for a system of monodomain particles that do not interact among themselves, was calculated and is known as the Néel relaxation time ( $\tau_N$ ) (13) [27]

$$\tau_N = \tau_0 \exp^{(KV/k_B T)} \quad (6.13)$$

where the value of  $\tau_0$  typically ranges from  $10^{-11}$  to  $10^{-9}$  s,  $k$  is the Boltzmann constant ( $8.7 \times 10^{-5}$  eV K $^{-1}$ ),  $K$  is the effective anisotropy constant, and  $V$  is the particle volume.  $KV$  represents the effective magnetocrystalline energy barrier. Below a certain temperature, that is, the blocking temperature ( $T_B$ ), the changes in direction due to the thermal

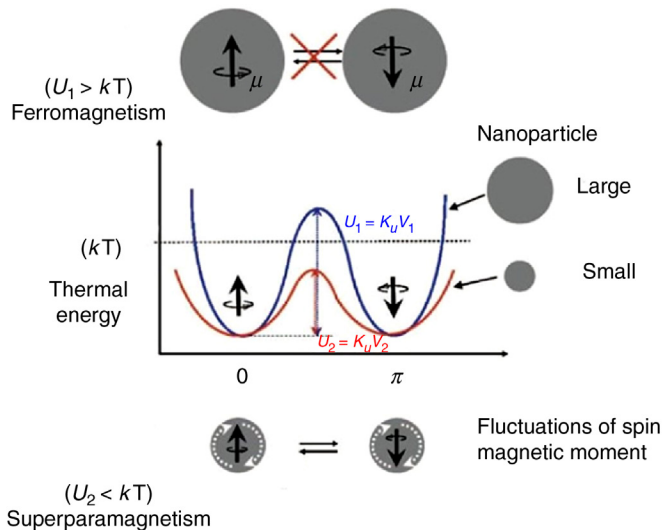


**FIGURE 6.7** The one-dimensional double-well potential representing the dynamics of magnetic moments in monodomain particles and the difference between the ferromagnetic and superparamagnetic behavior. Reproduced with authorization from Y.-W. Jun, et al., *Nanoscaling laws of magnetic nanoparticles and their applicabilities in biomedical sciences*, *Acc. Chem. Res.* 41 (2008) 179–189 [26].

activation occur at longer time scales than the observation time, causing the moments to appear as frozen. For a given observation time ( $\tau_{\text{obs}}$ ), typical for the experimental technique, the blocking temperature is defined as (6.14) [28]

$$T_B = \frac{KV}{k_B \ln(\tau_{\text{obs}}/\tau_0)} \quad (6.14)$$

At the blocking temperature, the reverse magnetization of a set of identical monodomain particles changes from blocked (with a hysteresis curve) to unblocked (without a hysteresis curve); the latter reveals the superparamagnetic behavior. Except for a scale factor that depends on the characteristic measurement time, the blocking temperature represents the point at which the thermal energy ( $k_B T_B$ ) is comparable to the effective magnetocrystalline energy barrier ( $KV$ ).

For the magnetization measurements with a typical measurement time on the order of 100 s, the blocking temperature of monodomain magnetic particles is  $T_B \cong KV/25k_B$ . The dependency of magnetization on the temperature  $M(T)$  at the zero-field-cooled (ZFC) condition has a maximum around the blocking temperature. On the time scale of the magnetization measurement (and above  $T_B$ ), the magnetic moment of the particle is free to align itself with the applied magnetic field. The magnetic behavior for a monodomain system as a function of temperature can be described using the first-order Langevin function (6.15) [29]

$$M(T) = M_s \left[ \coth\left(\frac{\mu H}{k_B T}\right) - \frac{k_B T}{\mu H} \right] \quad (6.15)$$

where  $M_S$  is the saturation magnetization and  $\mu$  is the magnetic moment of the monodomain particle.

Magnetic NPs dispersed in an FM can have two magnetic moment relaxation mechanisms: the previously discussed Néel mechanism and the Brownian mechanism. In the Brownian mechanism, the NPs change the orientation of their intrinsic magnetic moments via the rotation of the particle itself inside the carrier liquid due to thermal activation. Hence, in the absence of a magnetic field, the particles are randomly oriented in the FM sample, and the net magnetization is zero. The magnetization decay time of an FM sample due to its rotational diffusion is described as the Brownian relaxation time ( $\tau_B$ ) [30]

$$\tau_B = \frac{3\eta V_{hidr}}{k_B T_B} \quad (6.16)$$

where  $V_{hidr}$  is the hydrodynamic volume of the particle and  $\eta$  is the viscosity of the carrier fluid.

If both the Néel and Brownian relaxation mechanisms are present, then the mechanism with the briefer relaxation time will determine the behavior of the system, and the effective relaxation time ( $\tau_{eff}$ ) will be given by (6.17) [31]

$$\tau_{eff} = \frac{\tau_N \tau_B}{\tau_N + \tau_B} \quad (6.17)$$

### 6.3 SPIOs

SPIOs, as well as magnetite, maghemite, and cobalt ferrite NPs with diameters less than 20 nm, are currently receiving intense study because they have applications in biomedicine, electronics, data storage, catalysis, and other fields. Their easy production using chemical methods is clearly one of their major advantages.

Of the chemical methods used to synthesize iron oxide NPs, the most commonly cited are the coprecipitation of salts in aqueous medium and the thermal decomposition of organometallic precursors or coordination compounds [32]. Both methods essentially result in colloidal systems. Each presents advantages and disadvantages; however, they share the advantage of producing considerable amounts of nanomaterial at a lower cost than physical methods such as powder grinding or more sophisticated techniques such as epitaxy or plasma.

The production of stable colloidal particles requires the initial preparation of a core with high magnetization and the proper surface treatment. In addition, the majority of the aforementioned applications require a material with particles smaller than 20 nm on average, with a narrow size distribution and a homogeneous structure to guarantee uniform physical and chemical properties. Hence, the greatest challenge in the synthesis of SPIO particles is the precise control of the following parameters: size, size distribution, shape, core phase, and surface physico-chemical properties. The chemical methods regarding the synthesis and functionalization of SPIO systems are described in detail later.

### 6.3.1 Synthesis of Iron Oxides via Coprecipitation

The coprecipitation of  $\text{Fe}^{2+}$  and  $\text{Fe}^{3+}$  ions with a molar ratio of 1:2 in an alkaline aqueous medium ( $\text{pH} > 9$ ) at room temperature results in the immediate formation of a black precipitate of magnetite NPs according to the reaction [7]

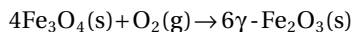


Eventually, the  $\text{Fe}(\text{II})$  ions can be replaced by the ions of other divalent metals, such as,  $\text{Co}(\text{II})$ ,  $\text{Ni}(\text{II})$ ,  $\text{Cu}(\text{II})$ , and  $\text{Zn}(\text{II})$ , when the objective is to obtain mixed ferrites of the type  $\text{MFe}_2\text{O}_4$ , where M represents the divalent metal [32–35]. The precipitation reaction of the mixed ferrites is generally conducted at temperatures between 95 and 99°C, followed by a surface passivation step (i.e., Fe enrichment) to prevent dissolution and oxidation [36].

In principle, any base can be used for precipitation; however,  $\text{NaOH}$  and  $\text{NH}_4\text{OH}$  are generally preferred because of their cost, availability, and high water solubility. The aqueous medium can also contain surfactants, neutral polymers, or polyelectrolytes that act as NP functionalization agents [37]. Regardless of these variants, the precipitate is already magnetic and immediately responds to the application of an external magnetic field. In fact, magnets are usually applied to help in the decantation and separation of the supernatant NPs.

The proposed mechanism [12,38] for this reaction considers that the hydrolysis in the alkaline aqueous medium is responsible for the initial formation of hydroxylated iron aquo complexes. These complexes undergo condensation reactions that form solid iron oxide lattices. The condensation reactions depend on the stoichiometric composition of the medium, the pH, and the ionic force. In particular, the pH and the ionic force of the medium have preponderant effects on the synthesis thermodynamics because they act in the protonation–deprotonation equilibrium of the hydroxylated groups at the surface of the new NPs. Its effect is the decrease of the particle/reaction medium interfacial tension and the increase of the surface area, which contributes to the coupling of aquo complexes in solution and the formation of the solid iron oxide lattice. The average particle size decreases with the increase of the pH [12,38].

Maghemite NPs are not directly obtained via coprecipitation; rather, they are obtained via a subsequent step with the oxidation of the magnetite particles according to the reaction [7]



The oxidation can be performed by bubbling oxygen or adding  $\text{Fe}(\text{NO}_3)_3$  in an aqueous magnetite NP suspension kept under agitation and heat [14], according to the scheme in Fig. 6.8. The magnetite→maghemite conversion can be observed with the naked eye; the initial black solid becomes brown as oxidation occurs.

NPs prepared via coprecipitation have an approximately spherical shape, with a diameter smaller than 10 nm. This method invariably produces polydisperse samples (i.e., the NPs produced by a single process have different diameters). In some cases, the polydispersion can be greater than 20%. Fig. 6.9A shows a transmission electron microscopy (TEM) image of a maghemite NP sample obtained via coprecipitation, followed by

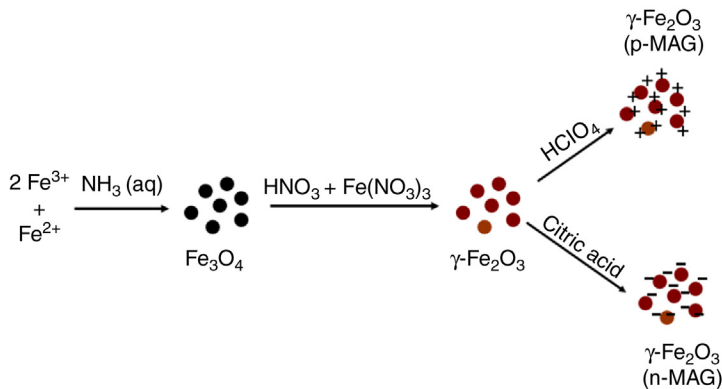


**FIGURE 6.8** An illustration of the synthesis process via the coprecipitation of magnetite ( $\text{Fe}_3\text{O}_4$ ), subsequent oxidation, and surface treatments to obtain maghemite NPs with a positively (p-MAG) or negatively (n-MAG) charged surface.

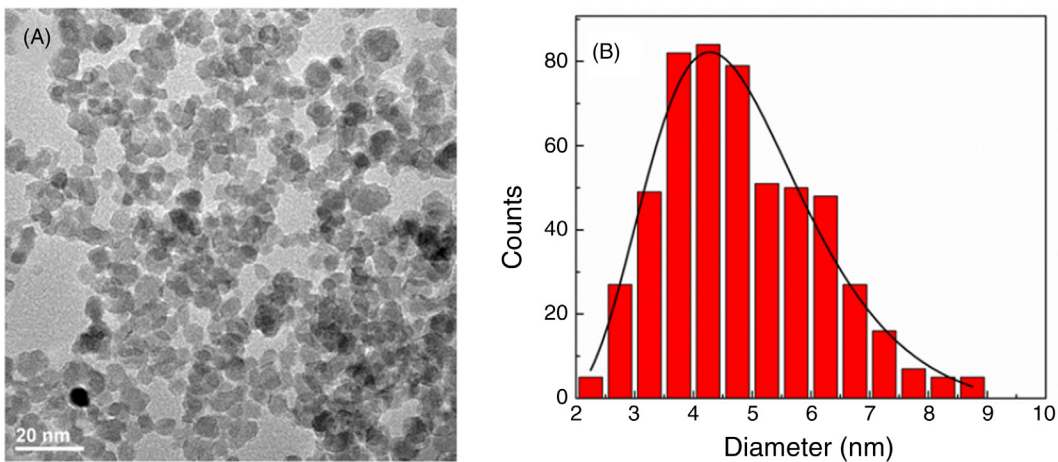


**FIGURE 6.9** TEM image obtained for maghemite NPs (A) and the corresponding particle size distribution (B).

functionalization with citric acid (obtained according to the scheme in Fig. 6.8). Fig. 6.9B shows the particle size histograms obtained from TEM images, and the solid line represents the data fit using a log-normal distribution. The images indicate that the particles have approximately a spherical shape with a mean diameter ( $D_m$ ) and standard deviation of  $4.6 \pm 0.1$  nm and  $0.28 \pm 0.04$ , which were obtained by fitting the data presented in Fig. 6.9B.

### 6.3.2 Synthesis of Iron Oxides via Thermal Decomposition

Another synthesis method used to produce SPIO particles is based on the thermal decomposition of metal precursors in the presence of high boiling point solvents [9,39–42]. The precursors can be organometallic compounds such as, iron pentacarbonyl ( $\text{Fe}[\text{CO}]_5$ )

[40] or complexes such as iron acetylacetone (Fe[acac]<sub>3</sub>) [41,42]. Alternately, the synthesis can be performed from iron oleate (Fe[olea]<sub>3</sub>), which is of low cost and lower toxicity [42]. Because the reactivity of the iron aquo complexes is high, it is difficult to control the condensation reactions that produce the solid; therefore, synthesis via coprecipitation is limited to the production of particles with a broader size distribution [12,38]. In turn, the decomposition method takes advantage of the strong interaction between an iron complex and a high boiling-point-coordinating solvent to control the nucleation and particle growth processes [39]. The elimination of the first ligand molecule is responsible for the nucleation of the particles, which occurs at a temperature approximately 50°C lower than that for the elimination of the other two. The particle growth at this temperature range is slow, guaranteed by the remaining ligand molecules that are only eliminated at higher temperatures. This dynamic allows the temporary separation of the nucleation and growth processes, resulting in samples with more uniform particles. Another important factor is the use of high boiling point solvents that enable the complete decomposition temperature of the precursor to be reached and that act as surfactants to promote the colloidal stability of the synthesized particles. Fig. 6.10 presents a TEM image of the monodisperse maghemite crystals obtained by Hyeon et al. [9].

Nevertheless, the decomposition method has two disadvantages. The first is the presence of an organic phase that, in the case of biomedical applications, requires one additional ligand exchange step for the particles to disperse in the aqueous medium. The second is the difficulty to produce equivalent amounts of NP materials in relation to the coprecipitation method because it is difficult to maintain a uniform temperature profile in a large reactor.

### 6.3.3 SPIO Particle Functionalization and the Preparation of Magnetic Colloids

The control over the surface chemistry of iron oxide NPs for colloidal systems has two fundamental purposes. The first is to prevent the agglomeration of particles, thereby

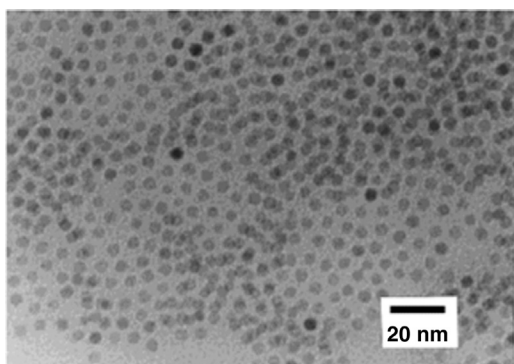


**FIGURE 6.10** A TEM image of maghemite nanocrystals with a mean diameter of 4 nm. Reproduced with the permission from T. Hyeon, et al., *Synthesis of highly crystalline and monodisperse maghemitenanocrystallites without a size-selection process*, *J. Am. Chem. Soc.* 123 (2001) 12798–12801 [9].

guaranteeing the stability of the colloidal state. The second is to manipulate the surface of the NPs so that it acts as a platform for the anchorage of the species of interest, especially pharmaceuticals, markers, therapeutic agents, biomolecules, and others. In addition, the surface modifications are fundamental for the compatibilization of the NPs when they are in contact with or injected into biologic systems [37,43,44].

The colloidal systems based on SPIO NPs can be classified as irreversible or lyophobic. The redispersion of the particles after they are dried is only reached when the surface has been previously treated so that a strong enough repulsion exists to prevent their aggregation. In the colloid dispersion, the Gibbs free energy increases when the disperse phase is distributed throughout the dispersing phase [45]. In fact, the minimum free energy is reached when the particles form one agglomerate. Therefore, the colloidal system is thermodynamically unstable, and the barrier for coagulation is only kinetic.

The constituent particles of a colloidal dispersion are in Brownian movement and therefore susceptible to frequent collisions [45]. Thus, the irreversible colloidal systems can remain as individual particles for a long period of time (even years) as long as a mechanism prevents their irreversible aggregation during particle collision. Two stabilization mechanisms can be applied to prevent colloidal aggregation [29,45]: (1) electrostatic stabilization, which describes when the surface of the dispersion particles is electrically charged (positively or negatively) to establish a mutual electrostatic repulsion in the aggregation of particles and (2) steric stabilization, which describes when the particle surface is coated with a polymer or surfactant layer or even small molecules that prevent aggregation by steric impediment. A combination of both mechanisms is known as electrosteric stabilization, which is generally obtained with polyelectrolytes.

The iron oxide NPs obtained via coprecipitation can be directly dispersed in an aqueous acid or alkaline medium, forming stable sols for an undetermined period of time. This condition is only possible because their diameter is smaller than 10 nm, and the presence of superficial oxyhydroxide groups are susceptible to acid–base reactions. The charges introduced by the displacement of the acid–base equilibrium at the surface of the iron oxide NPs cause a strong electrostatic interparticle repulsion that maintains their separation and disperses them in the carrier liquid [11]. Fig. 6.11 illustrates how the surface charge density ( $\Sigma$ ) of the iron oxide NP varies as a function of the pH of the magnetic colloid. Observe that when  $0 < \text{pH} < 6$ , the surface charge density of the NPs is at its maximum because the hydroxide groups are protonated. The respective fluid is stable (sol) with positively charged NPs. When  $6 < \text{pH} < 10$ , the protons are removed from the surface of the NPs, making them electrically neutral. The point of zero charge (PZC) for iron oxides is  $\text{pH} \approx 7.5$ . Under this condition, no repulsion forces exist to inhibit the aggregation and agglomeration of the particles, which end up flocculating. At  $\text{pH} > 10$ , the particles act as acids because they lose the hydroxyl proton and become negatively charged. The surface charge density reaches another maximum (of an inverse sign), and the respective fluid is also stable (sol).

Alternatively, the surface can be functionalized by ionic ligands such as tartarate [46], citric acid [47–49], dimercaptosuccinic acid (DMSA), and [50–53] polyphosphates [54–56].

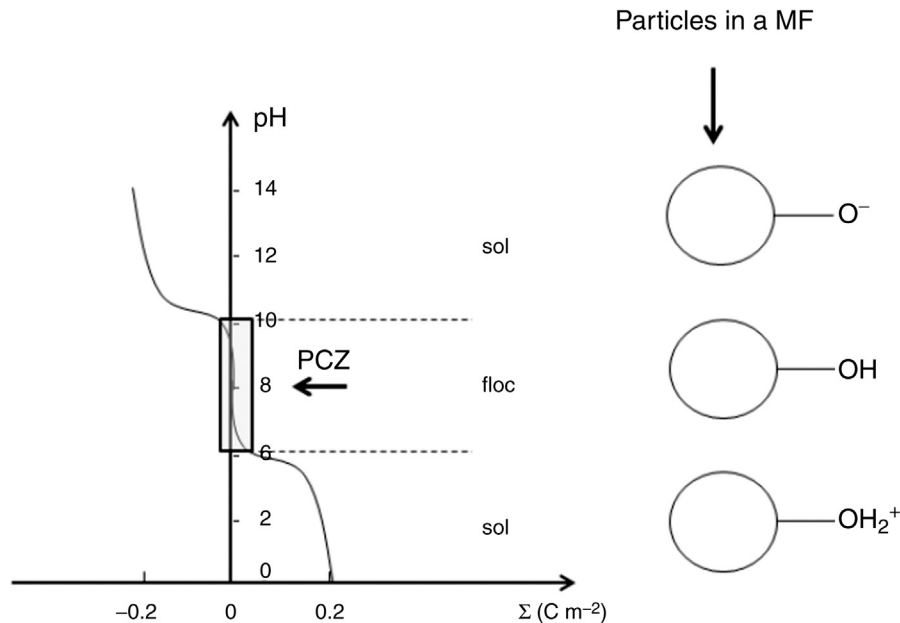


**FIGURE 6.11** A diagram showing the variation of the surface charge density ( $\Sigma$ , in  $C\ m^{-2}$ ) as a function of the pH for iron oxide NPs dispersed in an aqueous medium. The evolution of the NP surface chemistry in the fluid as a function of the pH is presented next to the diagram. Adapted from J.C. Bacri, et al., *Ionic ferrofluids: a crossing of chemistry and physics*, *J. Magn. Magn. Mater.* 85 (1990) 27–32 [11].

The functionalization of SPIO with citric acid or even sodium citrate enables the preparation of a stable FM biocompatible with a physiological medium ( $pH = 7$ – $7.2$ ). The DMSA molecule is particularly interesting because its two carboxylic groups are responsible for the interaction with the NP surface, whereas the two sulphydryl groups ( $—SH$ ) are used in conjugation via the disulfide bridge with biomolecules [50,52] and antibodies for tumor cell markers [50] or to intensify magnetic resonance image contrast [53]. Fig. 6.12 illustrates an iron oxide NP with DMSA molecules anchored at its surface via carboxylic groups. The free sulphydryl groups can establish disulfide bridges, including those between adjacent DMSA molecules [52]. DMSA has also been used for the phase transfer of particles synthesized in an organic medium to an aqueous medium [53]. The functionalization with phosphate groups has proven to be promising for guaranteeing magnetic phase stability against oxidation processes. Furthermore, it offers the proper functionality for coupling with proteins and cells [54–56].

The particles obtained via coprecipitation can also be functionalized via surfactants such as oleic acid and then dispersed in organic solvents such as hexane or toluene. Maghemite dispersions functionalized with oleic acid have been added to vegetal or mineral oil for application in transformers [14]. In this application, maghemite NPs promote heat conduction and improve the performance and useful life of the transformer parts. In addition, NPs functionalized via fatty acid can undergo a second functionalization step (e.g.,

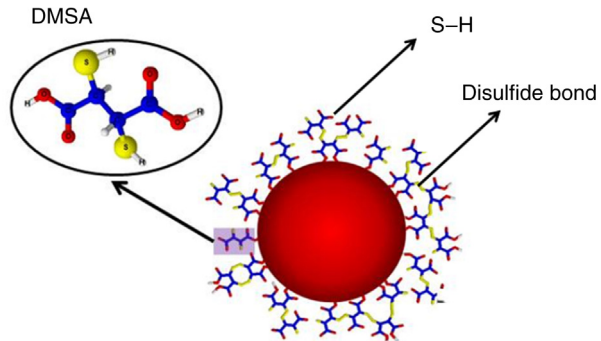


FIGURE 6.12 Schematic of an SPIO NP functionalized with DMSA.

by another fatty acid or an amine with a long carbon chain) to form a bilayer. The bilayer encapsulates the NP, allowing its dispersion in the aqueous medium, and simultaneously provides a microenvironment for the immobilization of hydrophobic species such as, pharmaceuticals and other therapeutic agents. For instance, curcumin was incorporated into dodecanoic acid bilayers and bonded to the surface of maghemite NPs to improve drug solubility and delivery efficiency [57].

The use of liposomes to encapsulate magnetic NPs and produce magnetoliposomes (MLs) has also been applied for functionalization for biomedical applications. MLs are biocompatible and physiologically stable structures that consist of a vesicle formed by phospholipids filled with magnetic NPs [58,59].

Many coatings can be used to simultaneously obtain an FM with steric or electrosteric stability, biocompatibility, and an anchorage platform for the species of interest, both for therapies and diagnosis (*in vivo* and *in vitro*). Generally, biocompatible polymers [e.g., polyethylene glycol (PEG), dextran, polyvinylpyrrolidone, polyvinyl alcohol, chitosan, gelatin, or even polypeptides] are employed [60,61].

The preparation of nanostructures with a core–shell structure is also a strategy to functionalize SPIO particles. Functionalization with a silica layer guarantees high stability for the NPs in silanol groups that act as a platform to immobilize species of biomedical interest. Using the Stöber method, silica is formed via the hydrolysis and condensation of tetraethoxysilane in an aqueous solution containing ethanol, ammonia, and the NPs [62,63].

## 6.4 The Structure and Physico-Chemical Properties of the SPIO Systems

The physico-chemical properties of SPIO systems are directly related to the spinel structure as well as morphological characteristics such as the size, shape, aggregation state, and chemistry of the surface of the NPs. Each characteristic is determined using different analysis techniques described in detail further.

### 6.4.1 Measurements of the Size and Agglomeration State

The size and shape of nanomaterials, including iron oxide NPs, are generally determined by the combined use of microscopy and X-ray diffraction techniques. The measurement of the magnetic properties can also be used for size estimates. Importantly, however, the mean diameter obtained by TEM ( $D_{\text{TEM}}$ ), which is a direct measurement, differs from that calculated indirectly using the magnetic measurements ( $D_M$ ); generally,  $D_{\text{TEM}} > D_M$ . The various experimental techniques provide different information about particle size, crystal size, and magnetic content [64]. Microscopy offers certain advantages, including the possibility of obtaining a large amount of digital images that can later be analyzed and provide a more realistic statistical distribution of particle size. Furthermore, with the advent of high-resolution TEMs (HRTEMs), the crystalline morphology and structure of the NPs can be determined with high accuracy (resolution  $\pm 0.1$  angstrom). In the case of colloidal systems, the preparation of the sample is relatively simple and consists of dripping the suspension into the sample holder and then waiting for the evaporation of the carrier (water or organic solvent). The parameters that describe NP size are determined using a histogram with the profile fitted to a log-normal distribution,  $P(D)$ , according to Eq. 6.18

$$P(D) = \frac{1}{D\sigma 4\pi^2} \exp\left[-\frac{(\ln D - \ln D_{\text{TEM}})^2}{2\sigma^2}\right] \quad (6.18)$$

where  $\sigma$  is the standard deviation of the diameter (dispersion) and  $D_{\text{TEM}}$  is the mean diameter [45].

The data obtained using the X-ray diffraction technique applied to nanocrystals provide information regarding their crystalline quality, with the possibility of estimating the value of the lattice constant and the mean diameter of the crystals. The mean diameter of the crystalline domain can be determined, for instance, using the full width at half maximum (FWHM) of the most intense reflection peak following Scherrer's equation [65], considering that the crystallinity of the samples is maintained:

$$D_c = \frac{0.9\lambda}{B \cos \theta_B} \quad (6.19)$$

where  $D_c$  represents the mean diameter of the crystalline domain, and  $\lambda$  is the wavelength of the incident X-ray.  $B$  is given by  $B = (B_{\text{med}}^2 - B_{\text{pad}}^2)^{1/2}$ , where  $B_{\text{med}}$  is the measured FWHM,  $B_{\text{pad}}$  is the FWHM of the standard sample used, and  $\theta_B$  is the angle of the most intense diffraction peak [65].

Magnetization measurements can also be used to determine the size of magnetic particles [66,67]. For instance, the derivative of the magnetization curve ZFC–field cooled (FC) in relation to temperature (i.e.,  $d[\text{ZFC}-\text{FC}]/dT$ ) results in a distribution whose maximum can be related to the critical volume of the particle. The equation for this calculation is [68]

$$V_c = \frac{25k_B T}{K} \quad (6.20)$$

where  $V_c$  is the critical volume,  $k$  is the Boltzmann constant, and  $T$  is the temperature (in Kelvin) that corresponds to the maximum of the distribution. For the maghemite NP samples immobilized in self-assembled films, a significant correlation was found between the size determined using X-ray diffraction and the size obtained by calculating the critical volume with the derivative of the ZFC-FC curve [69]. The first-order Langevin function, described by Eq. 6.15, can also be used to obtain the particle size distribution. However, this approximation does not consider the interparticle interaction, and it can only be used for systems containing SPIO particles that interact weakly. The difference between the values obtained using TEM and those using magnetization measurements support the existence of a magnetically dead layer at the surface of the NP.

#### 6.4.2 Composition and Structure

The chemical composition of an iron oxide is generally determined using traditional methods of analysis: atomic absorption spectrometry and X-ray fluorescence, both to determine the total iron content and that of other cations; colorimetric analysis (the *o*-phenanthroline method), to determine the Fe(II) content; and dichromatometry, to determine the Fe(III) content. Coordination can also be determined in parallel with microscopy techniques such as in energy dispersive spectroscopy (EDS) coupled to a scanning electron microscope. If the particle is functionalized with an organic ligand, then the coating composition can be determined using elemental analysis (e.g., CHN) [70] or by thermogravimetry [14].

The crystalline structure of NPs is determined using X-ray diffraction (the powder method). Iron oxides have a typical diffraction pattern of the spinel structure, whose maximum diffraction refers to the reflection of the (311) plane. This analysis can also be performed using electron diffraction coupled with TEM. An HRTEM can also provide images of the diffraction planes inside a single NP. However, it is difficult to distinguish magnetite from maghemite samples using only X-ray diffractograms because both materials generate similar diffractograms. To unequivocally identify each phase, it is necessary to use other techniques such as infrared spectroscopy (FT-IR), Raman scattering [71], or both. These techniques will be discussed in subsequent chapters.

The calculations predict five active Raman modes and four active bands in the infrared (IR) for the vibrational spectrum of the spinel structure. The predicted Raman modes are  $A_{1g}E_g$ , and the three modes  $T_{2g}(A_{1g} + E_g + 3T_{2g})$  [72]. The IR and Raman bands are sensitive to the oxidation states of the ions. The Raman or IR spectra depend on the preparation conditions of the iron oxides samples, especially those that are nanostructured. The IR absorption bands in the region between 200 and 900  $\text{cm}^{-1}$  refer to the vibration of the Fe-O bond, and they are different for maghemite and magnetite. The maghemite FT-IR spectrum in this range is composed of two wide bands that, depending on the particle size and preparation method, can be subdivided into more bands. The magnetite spectrum in the same region generally presents two well-defined peaks, enabling the distinction between the two iron oxide phases [73].

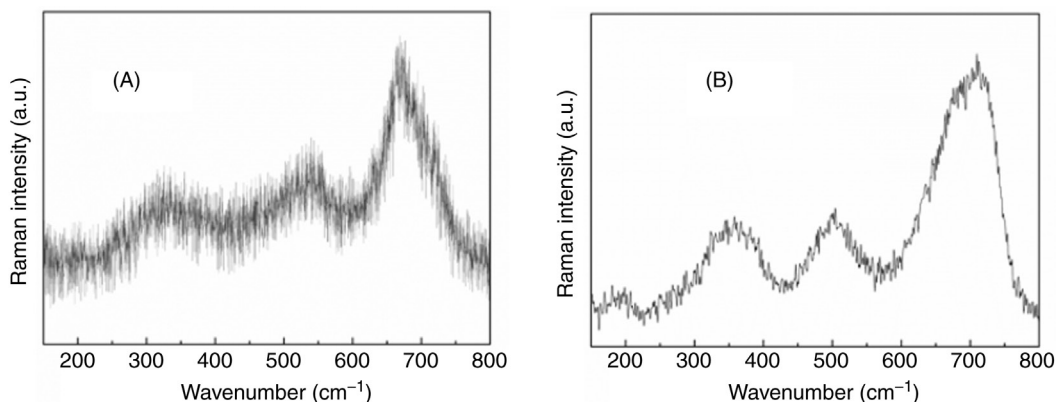


**FIGURE 6.13** Raman spectra obtained from magnetite (A) and maghemite (B) NP samples prepared by coprecipitation

Raman spectroscopy complements the other techniques previously mentioned, and it is the most appropriate to unequivocally identify the magnetite and maghemite phases [72]. For instance, as previously mentioned,  $\gamma\text{-Fe}_2\text{O}_3$  has an iron-deficient structure and wider Raman bands. Fig. 6.13A and B presents the Raman spectra obtained from powder samples of magnetite (A) and maghemite (B) NPs. The spectra were obtained using an argon laser ( $\lambda = 514 \text{ nm}$ ) at the lowest possible intensity to avoid degrading the sample [74]. The curve fitting (Lorentzian lines) process for the Raman spectrum of magnetite (A) shows the presence of three vibrational modes ( $E_g + T_{2g}$ , and  $A_{1g}$ ) out of the five predicted for the spinel structure [72], Fig. 6.13(B) shows the characteristic Raman spectrum of maghemite, which presents wider bands and a band at approximately  $720 \text{ cm}^{-1}$  associated with the oxidation of the iron ions at the octahedral site [72,75].

The effects of the sample preparation process, such as the oxidation of magnetite to maghemite, and the passivation of the surface of cobalt ferrite particles can be studied using Raman spectroscopy via the micro-Raman configuration [8,14,36]. The sensitivity of micro-Raman spectroscopy is high enough to detect the SPIO phase in multiple layers with fine polyelectrolytes (thickness = 60 nm) [76]. Fig. 6.14 shows the Raman spectrum obtained for a multilayer film formed by positively charged maghemite NPs (p-MAG) alternated with poly(sodium styrenesulfonate).

Important information regarding the short-range structure and magnetic properties of SPIO systems can be obtained using Mössbauer spectroscopy, which is discussed in the next volume [77]. The spectra can be obtained as a function of the temperature, with or without the application of an external magnetic field. This technique is also sensitive to the relaxation phenomena. The spectra at low temperatures can be fitted with two sextets that correspond to the two sites presented by the spinel structure. In the case of the spectra obtained at the temperature of liquid helium, the surface effects can be considered in nanomaterials, introducing a third sextet in the spectral fitting [35]. For instance, the effect of the synthesis route of the maghemite NPs on the magnetic disorder

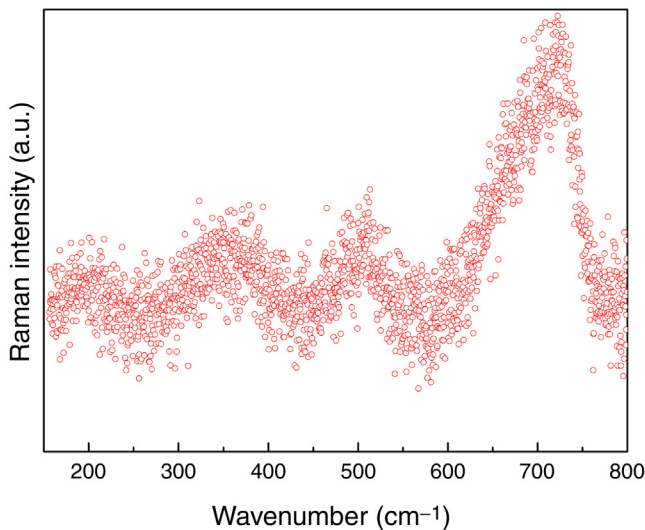


**FIGURE 6.14** The Raman spectrum of a multilayer film of positively charged maghemite NPs and PSS. The presented region is limited to the transitions regarding the iron oxide phase.

can be studied using the Mössbauer spectra obtained via the application of an external magnetic field [73].

Fig. 6.15 presents the Mössbauer spectra of cobalt ferrite NPs (diameter ~8 nm) obtained at different temperatures (4, 77, 165, and 300 K) without the application of an external magnetic field [35]. The Mössbauer spectrum obtained at the temperature of liquid helium has a slightly asymmetrical, hyperfine magnetic structure, similar to that observed for the cobalt ferrite NPs available in the literature. The spectral fitting was obtained using three well-defined sextets. The first (which had the highest value for the hyperfine field) was attributed to the Fe(III) ions located at the tetrahedral site of the spinel structure. The second sextet (which presented an intermediary value for the hyperfine field) was associated with the Fe(III) ions that occupy the octahedral site. The third sextet (which had the lowest hyperfine field) was attributed to the Fe(III) ions located next to the NP surface. According to Fig. 6.15, an asymmetrical widening of the sextet lines and the appearance of a doublet occur when the temperature increases; furthermore, the intensity of the doublet increases as the sextet intensity decreases. This behavior is characteristic of superparamagnetic relaxation, and the approach used for the fitting consists of the superposition of a hyperfine magnetic field with a quadrupole doublet. For the spectrum obtained at 77 K, the fitting using two sextets and one doublet indicates 512 and 458 kOe hyperfine fields attributed to Fe(III) at sites A and B, respectively. The central doublet is attributed to the superparamagnetic NPs present in the sample at that temperature, whereas the sextets refer to the blocked NPs (i.e., those at the magnetically ordered state). The relative area under the doublet related to the fraction of NPs in the superparamagnetic regimen increases from 6% at 77 K to 32% at room temperature.

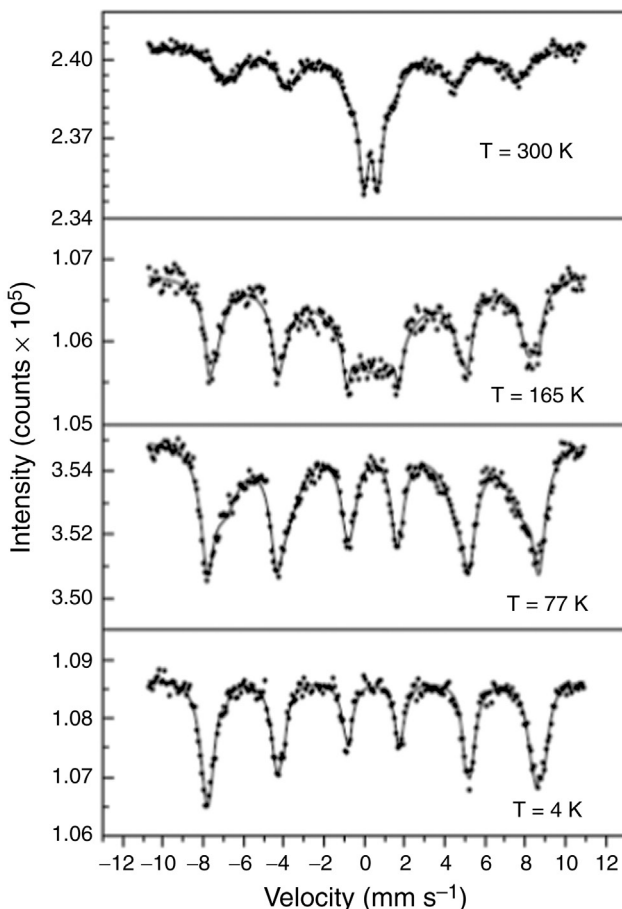


**FIGURE 6.15** The typical Mössbauer spectra of cobalt ferrite NPs at different temperatures. Reproduced with the permission from M.A.G. Soler, et al., *Surface passivation and characterization of cobalt–ferrite nanoparticles* *Surf. Sci.* 575 (2005) 12–16 [35].

#### 6.4.3 Surface Morphology and Properties

The properties that characterize the NP surface include the charge, surface area, and surface reactivity. Given that NPs interact with the cell membrane through its surface, these characteristics are considered as potential toxicity modulators [78].

The surface charge of the particles in an aqueous colloidal solution is determined by measuring the zeta potential [45,79]. The zeta potential ( $\zeta$ ) is expressed by Eq. 6.21 [45]

$$\zeta = \frac{3\mu\eta}{2\varepsilon_0 D}, \quad (6.21)$$

where  $\mu$  is the electrophoretic mobility of the particle,  $\eta$  is the viscosity,  $\varepsilon_0$  is the permittivity of vacuum, and  $D$  is the dielectric (static) constant of the medium. Generally, stable

solutions of charged colloids are prepared using NPs with zeta potential equal to or greater than (+/-) 30 mV. The measurement of the zeta potential is based on the knowledge that every charged particle in a liquid medium moves at a constant velocity ( $v$ ) under the action of an external electric field. Hence, the zeta potential value is determined by the electrophoretic mobility ( $\mu$ ) that, in turn, is calculated using the mean particle velocity ( $v$ ) under the action of the electric field  $E$  according to Eq. 6.22 [45]

$$\mu = \frac{v}{E} \quad (6.22)$$

The monitoring of the chemisorbed molecular layer at the surface of the SPIO particles is important for the design of magnetic colloids for different applications such as, specific cell tracking.

Raman spectroscopy has been used to characterize iron oxides for many years [80]. Only recently was this technique applied to study the microscopic details of the first NP surface coating layer (i.e., the NP surface-carrier liquid interface) [34,81,82]. Raman and photoacoustic spectroscopy can be applied together to study the formation of the disulfide bridges in DMSA-coated iron oxide NP systems [52]. Photoacoustic spectroscopy provides information about the presence of thiol groups (S—H), and the disulfide bridges (S—S) were monitored using Raman spectroscopy. This strategy enables the quantification of the [S—H]/[S—S] ratio over a wide range of the density values of DMSA molecules per NP area.

As previously discussed, the surface characteristics of NPs influence the long-term stability of the magnetic colloid, a mandatory characteristic for certain applications. For instance, if these particles are covered by organic acid, then the way they are bonded/anchored to the NP surface will influence colloidal stability. One study [14] was performed on the effect of the different oxidation conditions of NPs from magnetite to maghemite and the effect on the adsorption of oleic acid. Oleic acid-coated maghemite NPs were suspended in an insulating mineral oil and stored to study their stability as a function of time. The samples were characterized using thermogravimetry, Raman spectroscopy, and FT-IR; the results showed the significant influence of the oxidation protocol on the way that the oleic acid was anchored to the maghemite NP surface. The combined use of these techniques enabled the estimation of the relative content of the physisorbed and chemisorbed species. For instance, the suspensions prepared with NPs of smaller hydrodynamic radii and greater colloidal stability had only chemisorbed oleic acid at their surface.

The morphology of SPIOs can be investigated in detail by atomic force microscopy when they are immobilized on a solid substrate. The layer-by-layer self-assembly technique (electrostatic mode) described in detail in Chapter 4 (p. 134) is a simple and low-cost method that provides samples with different NP volumetric fractions with sufficient control [83]. The method consists of depositing a film on a solid substrate (glass, silica, mica sheets, etc.) via the successive immersion of the substrate, alternately, in cationic and anionic solutions/suspensions. The layers are adsorbed via electrostatic attraction in a spontaneous process, reaching equilibrium after a few minutes of deposition. The layer

thickness depends on different physico-chemical deposition parameters, especially those associated with the solution conditions (concentration, pH, ionic force, etc.), and it can vary from 1 nm to 20–30 nm (approximately). When dispersed in an aqueous acid medium, the SPIO particles act as cations and can therefore be adsorbed with different poly-anions. The film thickness varies linearly with the number of deposition cycles (bilayers); therefore, the deposition of films with different thicknesses can be applied. An example of the AFM topographical and phase images of a self-assembled film with cobalt ferrite ( $\text{CoFe}_2\text{O}_4$ ) and poly(styrene sulfonic acid)-doped poly(3,4-ethylenedioxythiophene) NPs, PEDOT:PSS, is shown in Fig. 6.16 [84]. The images at the top refer to a sample with a ( $\text{CoFe}_2\text{O}_4/\text{PEDOT:PSS}/\text{CoFe}_2\text{O}_4$ ) NP final layer, whereas the images at the bottom refer to a sample with a PEDOT:PSS final layer. The topographical images for both samples, Fig. 6.16A and C, are similar because they reflect the NP boundary, regardless of the polymer chain coating. In fact, the typical globular morphology of the NPs is predominant in both cases, with a similar mean quadratic roughness in both samples (3.3 nm for NPs at the top and 3.7 nm for the sample with the polyelectrolyte finish). However, the phase

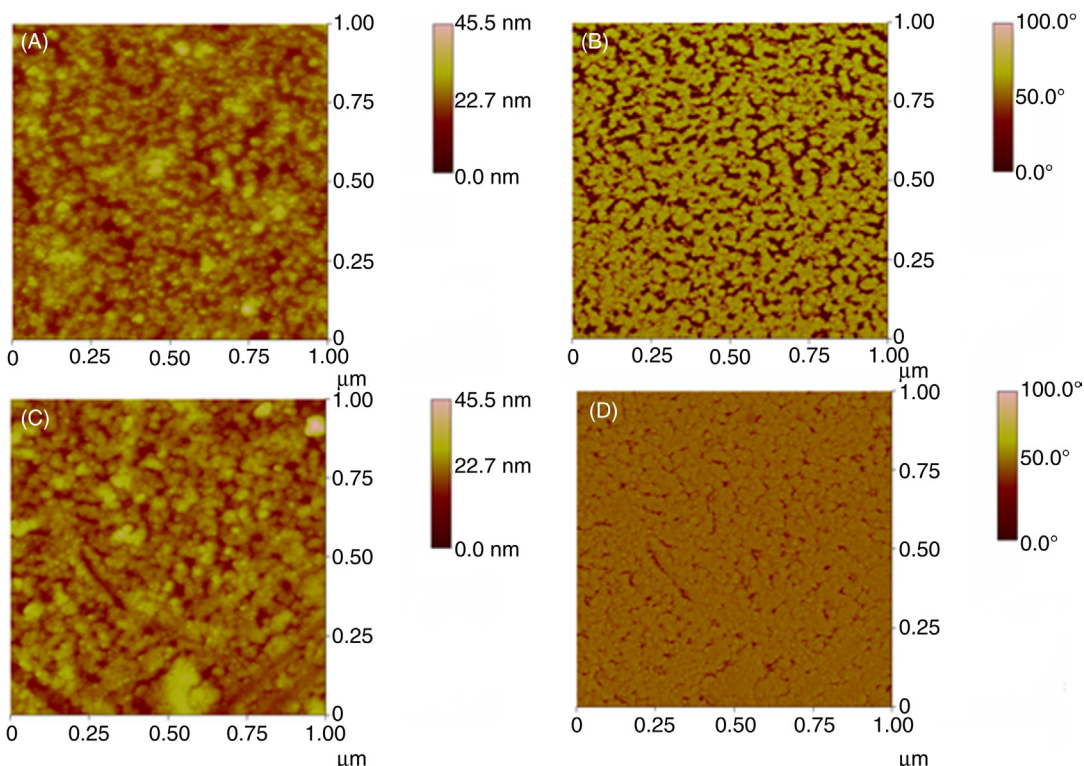


**FIGURE 6.16** AFM topographical (A and C) and phase (B and D) images of the  $(\text{CoFe}_2\text{O}_4/\text{PEDOT:PSS})_2$  films, varying the composition of the layer at the top of the structure: (A and B)  $\text{CoFe}_2\text{O}_4$  NP final layer and (C and D) PEDOT:PSS NP final layer. Reproduced with the permission from G.B. Alcantara, et al., Morphology of cobalt ferrite nanoparticle-polyelectrolyte multilayered nanocomposites, *J. Magn. Magn. Mater.* 323 (2011) 1372–1377 [84].

images have different appearances, Fig. 6.16B and D. When the last layer is formed using  $\text{CoFe}_2\text{O}_4$  NPs, the contrast between the NPs and the polymer is highlighted, and the boundaries and empty voids between the particles are more evident. When the last layer is formed by PEDOT:PSS, the phase image seems more planar than the topographical image. This result is because the NP surface and the voids between them are filled with the polyelectrolyte with different viscoelastic properties in relation to the NPs, and they are translated by the microscope as a single-phase image.

The NP distribution along the self-assembled film thickness can be investigated using high-resolution electron microscopy of the cross-section [85]. Fig. 6.17A shows the morphology of the cross-section of a  $(\text{PAni}/n\text{-MAG})_{10}$  nanofilm, where ten refers to the number of bilayers. The NPs are homogeneously distributed throughout the film, and no stratification exists in layers. The particles are individually encapsulated by a fine polyelectrolyte layer (clear boundary around the particles). This observation, as well as those performed using AFM, corroborate the NP packing model with polyelectrolyte. Fig. 6.17B shows the amplification of the NPs (n-MAG) in the film and indicates the crystalline planes associated with the  $\gamma\text{-Fe}_2\text{O}_3$  phase. The film thickness with 10 bilayers was estimated as 60 nm, confirming the value previously obtained using AFM [86]. TEM cross-sectional images obtained based on the number of bilayers indicated the systematic reduction of the particle-particle distance with the increase of bilayers [85,86]. This information is important, given that the dipolar interaction is influenced by the interparticle separation.

#### 6.4.4 Magnetic Properties

The magnetic characteristics of the nanoparticulate iron oxides can be evaluated using magnetization measurements as a function of the field ( $M \times H$  curve) and temperature. The measurements as a function of temperature are performed by cooling the sample, with or without field cooling (ZFC-FC) from room temperature ( $\sim 300$  K) to low temperatures (generally 2–4 K). The characteristic  $M \times H$  curves of the nanoparticulate iron oxides

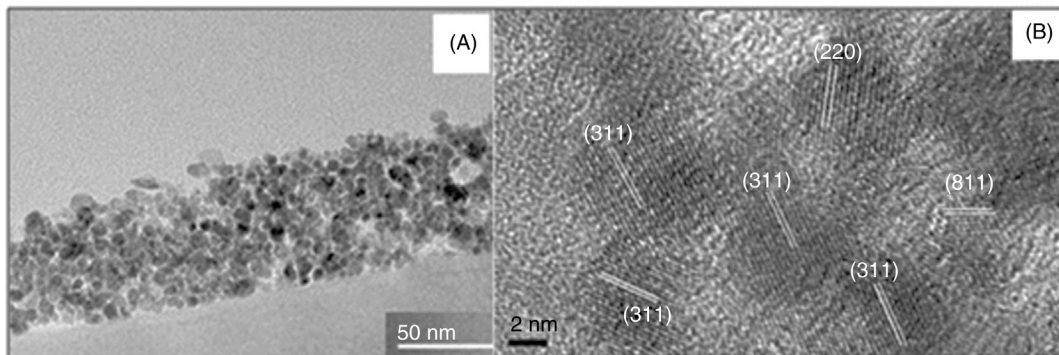


**FIGURE 6.17** High-resolution electron microscopy images of the cross-section of the  $(\text{PAni}/n\text{-MAG})_{10}$  nanofilm (A) and NPs inside the film, emphasizing the crystallographic planes (B). Adapted from M.A.G Soler et al., Assembly of  $\gamma\text{-Fe}_2\text{O}_3$ /polyaniline nanofilms with tuned dipolar interaction, *J. Nanopart. Res.* 14 (653) (2012) 1–10 [85]

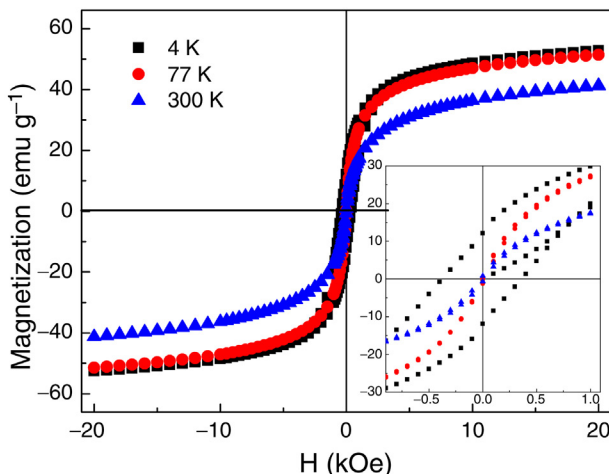


**FIGURE 6.18** Magnetization curves of the POX3OA sample obtained at different temperatures as indicated. The amplified curves for the low-field region are also shown. Reproduced with permission from W.R. Viali, et al., *Investigation of the molecular surface-coating on the stability of insulating magnetic oils*, *J. Phys. Chem. C* **144** (2010) 179–188 [14].

exhibit superparamagnetic behavior at temperatures higher than the blocking temperature and hysteresis for temperatures below it [14]. Fig. 6.18 shows the typical  $M \times H$  curves obtained at 4, 77, and 300 K in the range of  $\pm 20$  kOe for powder maghemite samples (diameter  $\sim 7$  nm). The curve included in Fig. 6.18 shows the details of the hysteresis curve in the range of  $\pm 1$  kOe for different temperatures. Remanence ( $M_R$ ) and coercivity ( $H_C$ ) were not observed at 300 K, as expected for a sample containing small particles (mean diameter = 7 nm) that do not interact. The saturation magnetization ( $M_S$ ) can be evaluated by plotting a graph of magnetization as a function of the reciprocal of the applied field [87]. The saturation magnetization values obtained using the  $M \times H$  curves are usually smaller than those determined using the corresponding bulk materials. In addition to depending on the structural quality of the particle, the saturation magnetization value also reflects surface effects. The reduction in the saturation magnetization value is likely because of the inclination of the spins close to the surface, disorders associated with the rupture of bonds, and the frustration of exchange interactions [88,89]. In nanoparticulate magnetic systems, the ZFC–FC curves are sensitive to the size, size distribution, morphology, and particle–particle interactions [90]. The ZFC–FC magnetization curves of the same maghemite sample with a DC field of 100 Oe, obtained in the range of 4–300 K, are presented in Fig. 6.19.

One study concerning the oxidation process of magnetite to maghemite showed that the values of  $M_S$  and  $T_B$  for samples oxidized at different degrees depend on particle size and the  $\text{Fe}^{3+}/\text{Fe}^{2+}$  ratio, regardless of the route used to oxidize the samples. After synthesis, the samples were coated with oleic acid, and the systematic reduction of  $T_B$  was observed because of the presence of the coating [14].

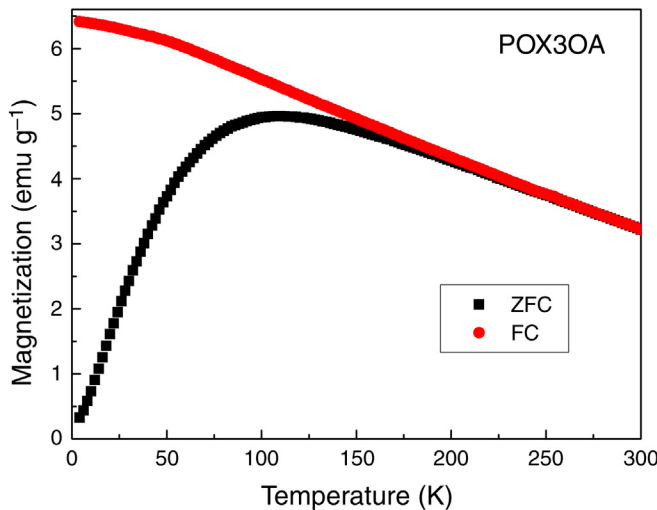


**FIGURE 6.19** The ZFC-FC curves of the POX3OA sample obtained using an applied field of 100 Oe. Reproduced with permission from W.R. Viali, et al., Investigation of the molecular surface-coating on the stability of insulating magnetic oils, *J. Phys. Chem. C.* 144 (2010) 179–188 [14].

The magnetic properties of the NP arrangements depend on the intrinsic characteristics of the individual particles as well as the chemical composition, stoichiometry, crystallinity, shape, magnetic anisotropy, and their interaction [91,92]. These interparticle interactions have an important effect; thus, the control of the distances between particles should be considered in the design of magnetic nanocomposites with specific properties. One way to control the interparticle distance is by varying the volumetric fraction (or mass fraction) of NPs in the nanocomposite via self-assembly (see item 6.4.3 for a discussion). This method has been explored in studies of particle–particle interactions, enabling the production of samples with a variable fraction of NPs [76,85,86,93].

The nanocomposites obtained using the self-assembly of magnetite and maghemite NPs exhibit superparamagnetic behavior at room temperature [76,85,86,93,94]. The polyaniline/maghemite bilayer system shows a superparamagnetic behavior from room temperature to 40 K and a similar saturation magnetization in relation to free particles in powder [86,94]. Moreover, the films start to present a coercive field of 149 Oe and a saturation magnetization of 50 emu g<sup>-1</sup> at 4 K; these values are comparable with those obtained using NPs in powder under the same measurement conditions (180 Oe and 55 emu g<sup>-1</sup>) [94]. However, the blocking temperature of the system increases as more bilayers are deposited, indicating an increase in interparticle interactions.

One way to evaluate the level of interparticle interaction is by performing ac susceptibility measurements. The ac magnetic susceptibility of a system composed of particles that do not interact can be described using the models proposed by Dormann and Gittlemann, which consider that the time ( $\tau$ ) required for the inversion of the magnetization orientation of each NP follows Arrhenius behavior [Eq. 6.13] [95,96]. The dependency of the imaginary component of ac susceptibility on frequency can be used to evaluate  $\tau_0$  and  $\Delta E$

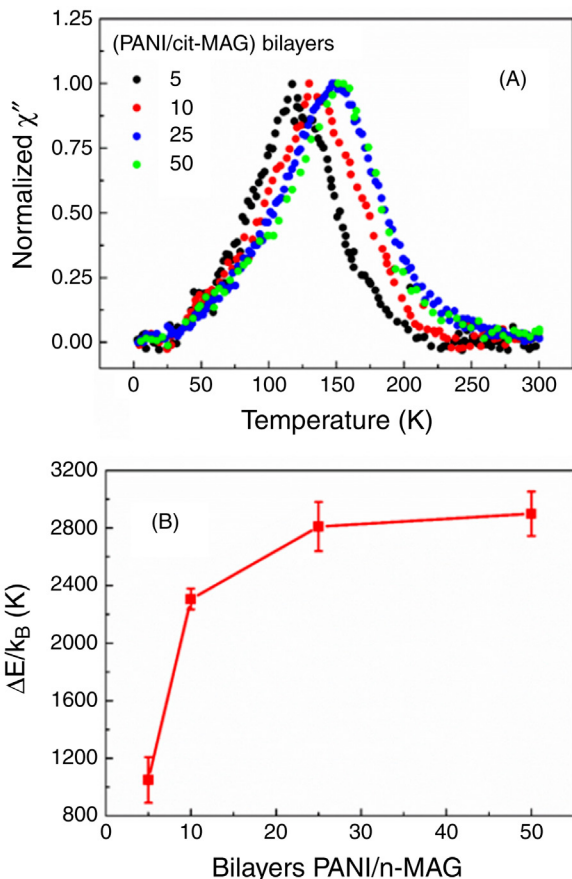


**FIGURE 6.20** The imaginary component ( $\chi''$ ) of magnetic susceptibility (A) and the effective energy barrier ( $\Delta E$ ) of the  $(\text{PANI}/n\text{-MAG})_N$  sample with a variable number of bilayers ( $N = 5, 10, 25$ , and  $50$  bilayers) (B). Reproduced with the permission from Assembly of  $\gamma\text{-Fe}_2\text{O}_3/\text{polyaniline}$  nanofilms with tuned dipolar interaction, *J. Nanopart. Res.* **14** (653) (2012) 1–10 [85].

using the Arrhenius curve [97]. Fig. 6.20 shows the results obtained using measurements of susceptibility for polyaniline/maghemit nanofilms. An asymptotic increase was observed in the effective energy wall  $\Delta E$  with the number of bilayers deposited, where saturation is reached with approximately 25 bilayers. The increase in  $\Delta E$  is attributed to the decrease of the interparticle distance that causes the densification of the film and increases the dipolar interaction between particles. In fact, the densification of the film can also be induced by increasing the NP concentration in the suspension, used for the film deposition.

## 6.5 Biomedical Applications

Biomedical applications of magnetic colloids can be carried out *in vivo* and *in vitro*. In the *in vivo* applications, the colloidal NPs are injected into the blood stream and are guided to the location of delivery with external manipulation by applying a magnetic field gradient,

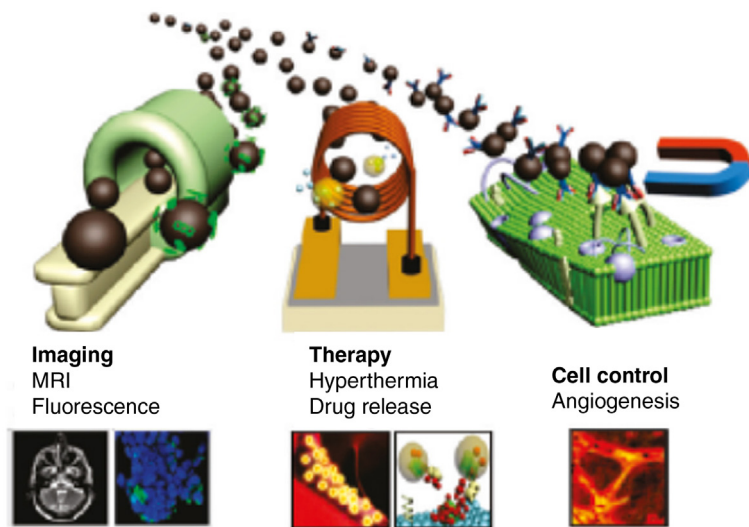


**FIGURE 6.21** An illustration of the potential applications of SPIO particles as a platform of theranostic agents. Reproduced with the permission from D. Yoo, *Theranostic magnetic nanoparticles*, Acc. Chem. Res. 44 (2011) 863–874 [13].

using molecular recognition to specifically bond to the target cells, or both. In some cases, the colloidal particles are alternatively injected directly into the area of interest. Once they are present in the target tissue, the complexes formed by the SPIO particles act as theranostic agents. A theranostic agent is defined as one that can perform diagnosis and therapy with a single platform [13,98,99]. The potential applications of theranostic agents using SPIO system-based platforms are shown in Fig. 6.21, including hyperthermia, controlled drug delivery, cell markers, and so on.

In particular, the iron oxide nanoparticulate systems exhibit, in addition to their biocompatibility, properties such as, superparamagnetism and a simultaneous capability to reach the target cell, obtain an image, and perform therapy; these characteristics make the platforms ideal for theranostic complexes. Although SPIO systems were initially used as T2 contrast agents to improve the sensitivity of magnetic resonance signals [100], they are currently recognized as efficient for other image modalities, as platform for therapeutic drugs, and/or ligands to reach the target [44,101–105].

The control of biodelivery is one of the major challenges in the design of SPIO-based complexes for control drug delivery (DDS) systems. Once they are injected, NPs can be quickly eliminated from the blood stream via the reticuloendothelial system (RES), which limits biomedical applications. The internalization and the subcell processing of the drugs are also critical issues in the design of drug delivery systems. To extend the permanence time in the bloodstream and reach target cells, it is necessary to break biologic barriers. These biologic barriers include the blood, liver, spleen, kidneys, blood-brain barrier, and tumor vasculature. This problem is addressed by designing the proper surface coating for

the SPIO particle to block the adsorption of blood components and improve the colloidal stability. PEG is one of the most commonly used materials to protect the SPIO complex. In addition, to avoid elimination via the filtering organs, the hydrodynamic size of the NP should be small because the RES absorbs materials larger than 100 nm [44].

Suspended SPIO particles that take the form of stable biocolloids were approved by the US Food and Drug Administration (FDA) in 1996 [106]. Since then, these particles have been used in clinical applications, for example, in diagnosis to improve the contrast of magnetic resonance imaging. SPIO-based colloids can be purchased from many companies such as Endorem (Guerbet, Sulzbach, Germany) and Resovist (Bayer HealthCare Pharmaceuticals, Berlin, Germany). Outside of Europe, Endorem is commercialized under the name Feridex [49]. In an attempt to detect diseases during the initial stage, NPs can be directed toward the lymph nodes and internalized by the macrophages, resulting in intracellular trapping and consequently improving the contrast of magnetic resonance imaging. This procedure was proposed to detect metastasis in patients with testicular [107] or gastric cancer [108].

Cancer treatment nanotherapy using SPIO complexes can be performed using magneto hyperthermia (MHT), chemotherapy, or gene therapy [44]. In addition to superparamagnetism, which allows the performance of MHT, SPIO particles can be used as an anchorage for target species, such as gene therapy agents, therapeutic proteins, and chemotherapeutics, to form the multifunction system illustrated in Fig. 6.22.

Hyperthermia in cancer therapy refers to the generation of heat at the tumor location [98]. The heating induced by the magnetic NPs present in the tumor is known as local

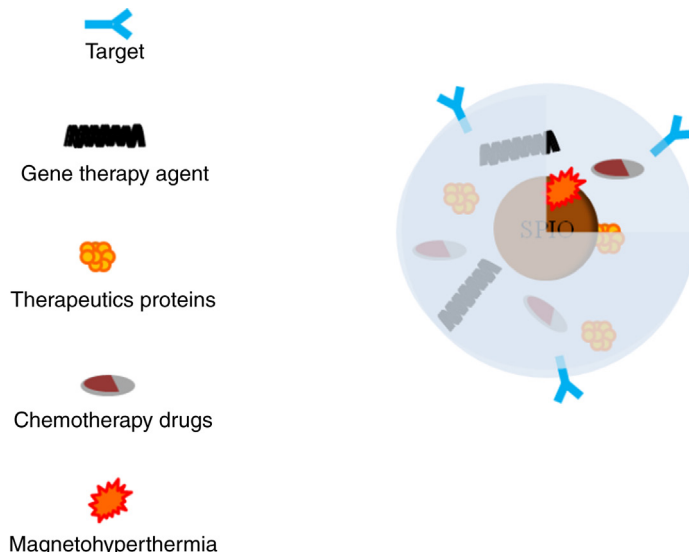


**FIGURE 6.22** The architecture of a theranostic nanotherapeutic system using an SPIO particle as a platform. Modified from F.M. Kievit, M. Zhang, Surface engineering of iron oxide nanoparticles for targeted cancer cells, *Acc. Chem. Res.* 44 (10) (2011) 853–862 [44].

MHT. The principle of MHT consists of the impregnation of magnetic NPs in the target tissue, followed by the generation of heat via the application of an alternating magnetic field. This thermal energy dissipates from the magnetic NPs by aligning the magnetic moments of the monodomains via the Néel and Brownian relaxation processes in response to the application of an alternating magnetic field. The local temperature can reach 40–42°C, which is enough to destroy the target cells [72,109,110]. Research has also verified that MHT therapy induces an antitumor immunity effect [111]. SPIO complex-assisted chemotherapy seeks to inhibit the growth of cancer cells, delivering agents that inhibit their cell function. The multifunctionality of magnetic NPs improves drug delivery, enables the local administration of higher doses, and minimizes induced side effects when the drug is administered in the conventional manner [112]. The transfection of cells using magnetic markers is assisted by noninvasive MRI and offers a way to improve the experimental control of cell therapies [113].

Another therapy that has been coupled to SPIO particles is photodynamic therapy (PDT), which has been used to treat a variety of cancerous and noncancerous diseases with minimal side effects. The use of the photosensitizers adsorbed in SPIO particles created a new class of complex materials that enable the combination of PDT and MHT [114,115]. This multifunctional magnetic complex can simultaneously increase the MRI contrast and allow the real-time visualization of tumor destruction, combining MRI contrast improvement with localized PDT [116].

Magnetic separation is one example of the in vitro application of SPIO particles. This technique consists of coupling the target material with an SPIO particle, and then, the medium is separated using magnetic field gradients [72]. This coupling depends on the functionalization of the NP. SPIO particles coated with antibodies can be used to isolate and separate immunogenic (or even functionalized) cells to recognize and isolate DNA.

## 6.6 Conclusions and Perspectives

The possibility of controlling the properties of NPs under the action of an external magnetic field is clearly the most important property of magnetic NPs. In particular, the biocompatibility associated with the surface control of SPIO particles makes them promising materials for biomedical applications. Biocompatible magnetic colloids used to improve MRI image contrast have been commercialized for some time. In addition, different strategies have been adopted to functionalize the SPIO surface and obtain platforms to couple a variety of biomedical devices to promote their localized and controlled delivery. Currently, efforts have focused on the development of SPIO platforms to couple bioagents, resulting in multifunction complexes adapted to simultaneously perform diagnosis and therapy (i.e., “theranostics”). Theranostics are designed to perform diagnosis and therapy more efficiently than conventional methods, improving the cost, side effects, and benefit relationships. Different agents can be included in the system composition, generally at the surface or on the shell (in the case of nanoparticulate core–shell systems) of SPIOs.

The magnetic behavior of SPIO systems can also be used in dozens of applications other than biomedicine, especially in microelectronics, energy, catalysis, and sensors. How to control the interparticle interaction effects in a system of magnetic NPs and use them to execute desired tasks for a device remain major questions. The breakthroughs in experiments, theory, and simulation have partially answered these questions; hence, this field of study is leading the way to other applications of magnetic nanomaterials. SPIO systems require relatively simple preparations and are of low cost via synthesis routes that enable the total control of the intrinsic properties of NPs. The literature provides much information about the chemistry of iron, the major actor in this scenario. Moreover, the support of the chemistry of colloids has been fundamental for the development of these systems.

SPIO systems will certainly be part of the composition of most intelligent biomedical devices, which should become increasingly present in our daily lives. In addition, new electronic devices and other applications will also benefit from the properties of SPIO systems that, by themselves, open new opportunities for basic research and the development of new products.

## List of Symbols

$L$	Orbital angular momentum
$J$	Exchange integral
$\bar{J}$	Total angular momentum
$\tau_N$	Néel relaxation time
$\tau_B$	Brownian relaxation time
$\tau_{\text{eff}}$	Effective relaxation time
$\zeta$	Zeta potential
$n$	Principal quantum number
$T_c$	Curie temperature
$M_s$	Saturation magnetization
$M_r$	Remanent magnetization
$T_d$	Tetrahedral coordination
$O_h$	Octahedral coordination
$D_{\text{TEM}}$	Mean diameter obtained by transmission electron microscopy
$D_M$	Mean diameter calculated indirectly with the magnetic measurements
$T_B$	Blocking temperature

## References

- [1] M.M. Walker, et al. Structure and function of the vertebrate magnetic sense, *Nature* 390 (1997) 371–376.
- [2] D. Sellmeyer, R. Skomski, *Advanced Magnetic Nanostructures*, Springer, New York, NY, (2006).
- [3] D. Ling, et al. Chemical synthesis and assembly of uniformly sized iron oxide nanoparticles for medical applications, *Acc. Chem. Res.* 48 (5) (2015) 1276–1285.
- [4] T.T. Thuy, et al. Next generation magnetic nanoparticles for biomedical applications, in: N.T.K. Thanh (Ed.), *Magnetic Nanoparticles From Fabrication to Clinical Applications*, Taylor & Francis Group, Boca Raton, FL, 2012.

- [5] M.A.G. Soler, et al. Superparamagnetic iron oxides, Encyclopedia of Nanoscience and Nanotechnology, 23, American Scientific Publishers, Valencia, California, 2011, pp. 513–532.
- [6] M.A. Willard, et al. Chemically prepared magnetic nanoparticles, *Inter. Mater. Rev.* 49 (2004) 125–170.
- [7] Y.S. Kang, et al. Synthesis and characterization of nanometer-size  $\text{Fe}_3\text{O}_4$  and  $\gamma\text{-Fe}_2\text{O}_3$  particles, *Chem. Mater.* 8 (1996) 2209–2211.
- [8] M.A.G. Soler, et al. Aging investigation of cobalt ferrite nanoparticles in low pH magnetic fluid, *Langmuir* 23 (2007) 9611–9617.
- [9] T. Hyeon, et al. Synthesis of highly crystalline and monodisperse maghemite nanocrystallites without a size-selection process, *J. Am. Chem. Soc.* 123 (2001) 12798–12801.
- [10] S. Bedanta, W.J. Kleemann, Superparamagnetism, *J. Phys. D* 42 (2009) 013001.
- [11] J.C. Bacri, et al. Ionic ferrofluids: a crossing of chemistry and physics, *J. Magn. Magn. Mater.* 85 (1990) 27–32.
- [12] J.P. Jolivet, et al. Iron oxide chemistry. From molecular clusters to extended solid networks, *Chem. Commun.* (2004) 481–487.
- [13] D. Yoo, et al. Theranostic magnetic nanoparticles, *Acc. Chem. Res.* 44 (2011) 863–874.
- [14] W.R. Viali, et al. Investigation of the molecular surface-coating on the stability of insulating magnetic oils, *J. Phys. Chem. C* 144 (2010) 179–188.
- [15] G. Li, et al. Spin valve biosensors: signal dependence on nanoparticle position, *J. Appl. Phys.* 99 (2006) 08P107.
- [16] X. Teng, et al. Platinum-maghemit core–shell nanoparticles using a sequential synthesis, *Nano Lett.* 3 (2003) 261–264.
- [17] C.J. Belle, et al. Size dependent gas sensing properties of spinel iron oxide nanoparticles, *Sens. Actuat. B* 160 (2011) 942–950.
- [18] B.D. Cullity, C.D. Graham, *Introduction to Magnetic Materials*, second ed, John Wiley & Sons, New Jersey, (2009).
- [19] N. Spaldin, *Magnetic Materials*, Cambridge University Press, Cambridge, UK, (2006).
- [20] K.H. Buschow, F.R. Boer, *Physics of Magnetism and Magnetic Materials*, Kluwer Academic/Plenum Publishers, New York, (2003).
- [21] A.P. Guimarães, *Magnetism and Magnetic Resonance in Solids*, John Wiley & Sons, New York, (1998).
- [22] D. Ortega, Structure and magnetism in magnetic nanoparticles, in: N.T.K. Thanh (Ed.), *Magnetic Nanoparticles From Fabrication to Clinical Applications*, Taylor & Francis Group, Boca Raton, FL, 2012.
- [23] S. Krupicka, P. Novák, , in: E.P. Wohlfarth (Ed.), *Oxide Spinels, Ferromagnetic Materials*, vol. 3, North-Holland Publishing Company, Amsterdam, 1982.
- [24] W.D. Callister, *Materials Science and Engineering: an Introduction*, seventh ed., John Wiley & Sons, New York, (2007).
- [25] A.P. Guimarães, *Principles of Nanomagnetism*, Springer, Berlin, (2009).
- [26] Y.-W. Jun, et al. Nanoscaling laws of magnetic nanoparticles and their applicabilities in biomedical sciences, *Acc. Chem. Res.* 41 (2008) 179–189.
- [27] M.L. Néel, Théorie du traînage magnétique des ferromagnétiques en grains fins avec applications aux terres cuites, *Ann. Geophys.* 5 (1949) 99–136.
- [28] W.C. Nunes, et al. Temperature dependence of the coercive field in single-domain particle systems, *Phys. Rev. B* 70 (2004) 014419.

- [29] R.E. Rosensweig, *Ferrohydrodynamics*, Cambridge University Press, Cambridge, (1985).
- [30] W.F. Brown, Thermal fluctuations of a single-domain particle, *J. Appl. Phys.* 34 (1963) 1319–1320.
- [31] M.I. Shliomis, Y.L. Raikher, Experimental investigations of magnetic fluids, *IEEE Trans. Magn.* 16 (1980) 237–250.
- [32] D.A.J. Herman, et al. How to choose a precursor for decomposition solution-phase synthesis: the case of iron nanoparticles, *Nanoscale* 7 (2015) 5951–5954.
- [33] J.A. Gomes, et al. Synthesis of core-shell ferrite nanoparticles for ferrofluids: chemical and magnetic analysis, *J. Phys. Chem. C* 112 (2008) 6220–6227.
- [34] P.C. Morais, et al. Raman study of ionic water-based copper and zinc ferrite magnetic fluids, *J. Magn. Magn. Mater.* 201 (1999) 105–109.
- [35] M.A.G. Soler, et al. Surface passivation and characterization of cobalt–ferrite nanoparticles, *Surf. Sci.* 575 (2005) 12–16.
- [36] T.E.O. Melo, et al. Investigation of surface passivation process on magnetic nanoparticles by Raman spectroscopy, *Surf. Sci.* 600 (2006) 3642–3645.
- [37] A.H. Lu, et al. Magnetic nanoparticles: synthesis, protection, functionalization, and application, *Angew. Chem. Int. Ed. Engl.* 46 (2007) 1222–1244.
- [38] J.P. Jolivet, et al. Design of metal oxide nanoparticles: control of size, shape, crystalline structure and functionalization by aqueous chemistry, *C.R. Chimie* 13 (2010) 40–51.
- [39] S.G. Kwon, T. Hyeon, Colloidal chemical synthesis and formation kinetics of uniformly sized nanocrystals of metals, oxides, and chalcogenides, *Acc. Chem. Res.* 41 (2008) 1696–1709.
- [40] S. Sun, H. Zeng, Size-controlled synthesis of magnetite nanoparticles, *J. Am. Chem. Soc.* 124 (2002) 8204–8205.
- [41] R.H. Gonçalves, et al. Magnetite colloidal nanocrystals: a facile pathway to prepare mesoporous hematite thin films for photoelectrochemical water splitting, *J. Am. Chem. Soc.* 133 (2011) 6012–6019.
- [42] J. Park, et al. Ultra-large-scale syntheses of monodisperse nanocrystals, *Nat. Mater.* 3 (2004) 891–895.
- [43] M.K. Yu, et al. Targeting strategies for multifunctional nanoparticles in cancer imaging and therapy, *Theranostics* 2 (2012) 3–44.
- [44] F.M. Kievit, M. Zhang, Surface engineering of iron oxide nanoparticles for targeted cancer cells, *Acc. Chem. Res.* 44 (10) (2011) 853–862.
- [45] R.J. Hunter, *Foundations of Colloid Science*, Clarendon Press, Oxford, (1986).
- [46] S. Neveu, Size-selective chemical synthesis of tartrate stabilized cobalt ferrite ionic magnetic fluid, *J. Coll. Int. Sci.* 255 (2002) 293–298.
- [47] P.C. Morais, et al. Preparation and characterization of ultra-stable biocompatible magnetic fluids using citrate-coated cobalt ferrite nanoparticles, *Thin Solid Films* 515 (2006) 266–270.
- [48] S. Kückelhaus, et al. Optical emission spectroscopy as a tool for the biodistribution investigation of cobalt–ferrite nanoparticles in mice, *J. App. Phys.* 97 (2005) 10Q910.
- [49] K. Andreas, et al. Highly efficient magnetic stem cell labeling with citrate-coated superparamagnetic iron oxide nanoparticles for MRI tracking, *Biomaterials* 33 (2012) 4515–4525.
- [50] N. Fauconnier, et al. Thiolation of maghemite nanoparticles by dimercaptosuccinic acid, *J. Coll. Int. Sci.* 194 (1997) 427–433.
- [51] C.R.A. Valois, et al. The effect of DMSA-functionalized magnetic nanoparticles on transendothelial migration of monocytes in the murine lung via a  $\beta 2$  integrin-dependent pathway, *Biomaterials* 31 (2010) 366–374.
- [52] M.A.G. Soler, et al. Spectroscopic study of maghemite nanoparticles surface-grafted with DMSA, *J. Phys. Chem. A* 115 (2011) 1003–1008.

- [53] Y.M. Huh, et al. In vivo magnetic resonance detection of cancer by using multifunctional magnetic nanocrystals, *J. Am. Chem. Soc.* 127 (2005) 12387–12391.
- [54] T.J. Daou, et al. Phosphate adsorption properties of magnetite-based nanoparticles, *Chem. Mater.* 19 (2007) 4494–4505.
- [55] C. Yee, et al. Self-assembled monolayers of alkanesulfonic and-phosphonic acids on amorphous iron oxide nanoparticles, *Langmuir* 15 (1999) 7111–7115.
- [56] R. Frantz, et al. Phosphonate derivatives of pyridine grafted onto oxide nanoparticles, *Tetrahedron Lett.* 43 (2002) 9115–9117.
- [57] FF Souza, et al. Curcumin associated magnetite nanoparticles inhibit in vitro melanoma cell growth, *J. Nanosci. Nanotechnol.* 11 (2011) 7603–7610.
- [58] M. De Cuyper, M. Joniau, *Magnetoliposomes*, *Eur. Biophys. J.* 15 (1988) 311–319.
- [59] M.A.G. Soler, et al. Raman spectroscopy of magnetoliposomes, *J. Magn. Magn. Mater.* 252C (2002) 415–417.
- [60] A.K. Gupta, M. Gupta, Synthesis and surface engineering of iron oxide nanoparticles for biomedical applications, *Biomaterials* 26 (2005) 3995–4021.
- [61] A.F. Thünemann, et al. Maghemite nanoparticles protectively coated with poly(ethyleneimine) and poly(ethylene oxide)-block-poly(glutamic acid), *Langmuir* 22 (2006) 2351–2357.
- [62] M.P.S. Almeida, et al. Preparation and size-modulation of silica-coated maghemite nanoparticles, *J. Alloy. Comp.* 500 (2010) 149–152.
- [63] R. Pedroza, et al. Raman study of nanoparticle-template interaction in a  $\text{CoFe}_2\text{O}_4/\text{SiO}_2$ -based nano-composite prepared by Sol-gel method, *J. Magn. Magn. Mater.* 289 (2005) 139–141.
- [64] J. Popplewell, L. Sakhnini, The dependence of the physical and magnetic properties of magnetic fluids on particle size, *J. Magn. Magn. Mater.* 149 (1995) 72–78.
- [65] B.D. Cullity, *Elements of X-Ray Diffraction*, Addison Wesley Pub. Co, New York, (1978).
- [66] R.W. Chantrell, et al. Measurements of particle size distribution parameters in ferrofluids, *IEEE Trans. Magn.* 14 (1978) 975–977.
- [67] K. ÓGrady, A. Bradbury, Particle size analysis in ferrofluids, *J. Magn. Magn. Mater.* 39 (1983) 91–94.
- [68] H. Mamiya, et al. Extraction of blocking temperature distribution from zero-field-cooled and field-cooled magnetization curves, *IEEE Trans. Magn.* 41 (2005) 3394–3396.
- [69] L.G. Paterno, et al. Fabrication and characterization of nanostructured conducting polymer films containing magnetic nanoparticles, *Thin Solid Films* 517 (2009) 1753–1758.
- [70] M.A.G. Soler, et al. Study of molecular surface coating on the stability of maghemite nanoparticles, *Surf. Sci.* 601 (2007) 3921–3925.
- [71] N.B. Colthup, L.H. Daly, S.E. Wiberley, *Introduction to Infrared and Raman Spectroscopy*, third ed., Academic Press, San Diego, CA, (1990).
- [72] M.A.G. Soler, Q. Fanyao, Raman spectroscopy of iron oxide nanoparticles, *Raman Spectroscopy for Nanomaterials Characterization*, Springer, Berlin, 2012, pp. 379–416.
- [73] P. Tartaj, The preparation of magnetic nanoparticles for applications in biomedicine, *J. Phys. D* 36 (2003) R182–R197.
- [74] S.W. Da Silva, et al. Stability of citrate-coated magnetite and cobalt–ferrite nanoparticles under laser irradiation: a Raman spectroscopy investigation, *IEEE Trans. Magn.* 39 (2003) 2645–2647.
- [75] G.V.M. Jacintho, et al. Structural investigation of  $\text{MFe}_2\text{O}_4$  ( $\text{M} = \text{Fe}, \text{Co}$ ) magnetic fluids, *J. Phys. Chem. C* 113 (2009) 7684–7691.
- [76] L.G. Paterno, et al. Tuning of magnetic dipolar interactions of maghemite nanoparticles embedded in polyelectrolyte layer-by-layer films, *J. Nanosci. Nanotechnol.* 8 (2012) 6672–6678.

- [77] D.P.E. Dickson, F.J. Berry, Principles of Mössbauer Spectroscopy, in: D.P.E. Dickson, F.J. Berry (Eds.), *Mössbauer Spectroscopy*, Cambridge University Press, Cambridge, 1986.
- [78] A. Sharma, et al. Toxicological considerations when creating nanoparticle-based drugs and drug delivery systems, *Expert Opin. Drug Metab. Toxicol.* 8 (2012) 47–69.
- [79] R.M. Pashley, M.E. Karaman, *Applied Colloid and Surface Chemistry*, John Wiley & Sons Ltd, Chichester, (2004).
- [80] W.B. White, B.A. De Angelis, Interpretation of the vibrational spectra of spinels, *Spectrochim. Acta Part A* 23A (1967) 985–995.
- [81] P.C. Morais, et al. Raman investigation of uncoated and coated magnetic fluids, *J. Phys. Chem. A* 104 (2000) 2894–2896.
- [82] P.C. Morais, et al. Raman spectroscopy in magnetic fluids, *Biomol. Eng.* 17 (2001) 41–49.
- [83] M.A.G. Soler, L.G. Paterno, Layer-by-layer assembly of magnetic nanostructures, *J. Nanofluids* 1 (2012) 101–119.
- [84] G.B. Alcantara, et al. Morphology of cobalt ferrite nanoparticle–polyelectrolyte multilayered nanocomposites, *J. Magn. Magn. Mater.* 323 (2011) 1372–1377.
- [85] M.A.G. Soler, et al. Assembly of  $\gamma\text{-Fe}_2\text{O}_3$ /polyaniline nanofilms with tuned dipolar interaction, *J. Nanopart. Res.* 14 (653) (2012) 1–10.
- [86] L.G. Paterno, et al. Layer-by-layer assembly of bifunctional nanofilms: surface-functionalized maghemite hosted in polyaniline, *J. Phys. Chem. C* 113 (2009) 5087–5095.
- [87] A.D. Franklin, A.E. Berkowitz, The approach to saturation on dilute ferromagnetics, *Phys. Rev.* 89 (1953) 1171.
- [88] K.V. Shafi, et al. Sonochemical preparation and size-dependent properties of nanostructured  $\text{Co}\text{-Fe}_2\text{O}_4$  particles, *Chem. Mater.* 10 (1998) 3445–3450.
- [89] L.D. Tung, et al. Magnetic properties of ultrafine cobalt ferrite particles, *J. Appl. Phys.* 93 (2003) 7486–7488.
- [90] L. Machala, et al. Amorphous iron(III) oxides: a review, *J. Phys. Chem. B* 111 (2007) 4003–4018.
- [91] G.C. Papaefthymiou, Nanoparticle magnetism, *Nano Today* 4 (2009) 438–447.
- [92] A.F. Rebolledo, et al. Signatures of clustering in superparamagnetic colloidal nanocomposites of an inorganic and hybrid nature, *Small* 4 (2008) 254–261.
- [93] B.P. Pichon, et al. Magnetotunable hybrid films of stratified iron oxide nanoparticles assembled by the layer-by-layer technique, *Chem. Mater.* 23 (2011) 3668–3675.
- [94] L.G. Paterno, et al. Magnetic nanocomposites fabricated via the layer-by-layer approach, *J. Nanosci. Nanotech.* 10 (2010) 2679–2685.
- [95] J.L. Dormann, et al. Magnetic relaxation in fine-particle systems, *Adv. Chem. Phys.* 98 (1996) 283.
- [96] J.I. Gittleman, et al. Superparamagnetism and relaxation effects in granular  $\text{Ni-SiO}_2$  and  $\text{Ni-Al}_2\text{O}_3$  films, *Phys. Rev. B* 9 (1974) 3891–3897.
- [97] M.A. Novak, et al. Relaxation in magnetic nanostructures, *J. Magn. Magn. Mat.* 294 (2005) 133–140.
- [98] C.S.S.R. Kumar, F. Mohammad, Magnetic nanomaterials for hyperthermia-based therapy and controlled drug Delivery, *Adv. Drug Deliv. Rev.* 63 (2011) 789–808.
- [99] S. PARVEEN, et al. Nanoparticles: a boon to drug delivery, therapeutics, diagnostics and imaging, *Nanomedicine: Nanotechnol. Biol. Med.* 8 (2012) 147–166.
- [100] K. Hola, et al. Tailored functionalization of iron oxide nanoparticles for MRI, drug delivery, magnetic separation and immobilization of biosubstances, *Biotechnol. Adv.* 33 (2015) 1162–1176.
- [101] M.W. Freeman, et al. Magnetism in medicine, *J. Appl. Phys.* 31 (1960) 404S–405S.

- [102] J. Dobson, Gene therapy progress and prospects: magnetic nanoparticle-based gene delivery, *Gene Therapy* 13 (2006) 283–287.
- [103] S. Moritake, et al. Functionalized nano-magnetic particles for an in vivo delivery system, *J. Nanosci. Nanotechnol.* 7 (2007) 937–944.
- [104] C. Alexiou, et al. In vitro and in vivo investigations of targeted chemotherapy with magnetic nanoparticles, *J. Magn. Magn. Mater.* 293 (2005) 389–393.
- [105] O.A. Garden, et al. A rapid method for labelling CD4+ T cells with ultrasmall paramagnetic iron oxide nanoparticles for magnetic resonance imaging that preserves proliferative, regulatory and migratory behaviour in vitro, *J. Immunol. Methods* 314 (2006) 123–133.
- [106] J. Oh, et al. Detection of magnetic nanoparticles in tissue using magneto-motive ultrasound, *Nanotechnology* 17 (2006) 4183–4190.
- [107] M.G. Harisinghani, et al. Pilot study of lymphotrophic nanoparticle-enhanced magnetic resonance imaging technique in early stage testicular cancer: a new method for noninvasive lymph node evaluation, *Urology* 66 (2005) 1066–1071.
- [108] Y. Tatsumi, et al. Preoperative diagnosis of lymph node metastases in gastric cancer by magnetic resonance imaging with ferumoxtran-10, *Gastric Cancer* 9 (2006) 120–128.
- [109] I. Hilger, et al. Towards breast cancer treatment by magnetic heating, *J. Magn. Magn. Mater.* 293 (2005) 314–319.
- [110] E. Pollert, K. Záveta, Manocrystalline oxides in magnetic fluid hyperthermia, in: N.T.K. Than (Ed.), *Magnetic Nanoparticles From Fabrication to Clinical Applications*, Taylor & Francis Group, Boca Raton, FL, 2012.
- [111] M. Yanase, et al. Antitumor immunity induction by intracellular hyperthermia using magnetite cationic liposomes, *Jpn. J. Cancer Res.* 89 (1998) 775–782.
- [112] M.L.B. Carneiro, et al. Free rhodium (II) citrate and rhodium (II) citrate magnetic carriers as potential strategies for breast cancer therapy, *J. Nanobiotechnol.* 9 (11) (2011) 3–17.
- [113] A. Del Campo, et al. Multifunctional magnetite and silica–magnetite nanoparticles: synthesis, surface activation and applications in life sciences, *J. Magn. Magn. Mater.* 293 (2005) 33–40.
- [114] P.P. Macaroff, et al. Evaluation of new complexes of biocompatible magnetic fluid and third generation of photosensitizer useful to cancer treatment, *IEEE Trans. Magn.* 41 (2005) 4105–4107.
- [115] R. Di Corato, Combining magnetic hyperthermia and photodynamic therapy for tumor ablation with photoresponsive magnetic liposomes, *ACS Nano* 9 (2015) 2904–2916.
- [116] R. Kolpeman, et al. Multifunctional nanoparticle platforms for in vivo MRI enhancement and photodynamic therapy of a rat brain cancer, *J. Magn. Magn. Mater.* 293 (2005) 404–410.

# Nanocomposites of Polymer Matrices and Lamellar Clays

F.R. Passador\*, A. Ruvolo-Filho\*\*, L.A. Pessan\*\*

\*INSTITUTE OF SCIENCE AND TECHNOLOGY, FEDERAL UNIVERSITY OF SÃO PAULO,  
SÃO PAULO, SÃO PAULO, BRAZIL; \*\*DEPARTMENT OF MATERIALS ENGINEERING,  
FEDERAL UNIVERSITY OF SÃO CARLOS, SÃO CARLOS, SÃO PAULO, BRAZIL

## CHAPTER OUTLINE

7.1	Polymer Nanocomposites .....	187
7.2	Structures of Lamellar Clays.....	188
7.3	Structure of Polymer Nanocomposites .....	189
7.4	Methods for Obtaining Polymer Nanocomposites .....	191
7.5	Compatibilization in Nanocomposites with Nonpolar Matrices.....	192
7.6	Nanocomposites with Polar Matrices .....	193
7.6.1	Structure and Properties.....	193
7.7	Nanocomposites with Nonpolar Matrices .....	196
7.7.1	Structure and Properties.....	197
7.8	Final Considerations.....	203
	References .....	204

## 7.1 Polymer Nanocomposites

The constant search for new materials that provide the properties demanded for applications motivates research in industries, universities, and technological institutions around the world. The development of polymer nanocomposites stands out among the currently most promising technologies for improving the thermal, mechanical, gas, and organic vapor barrier properties of materials.

A polymer nanocomposite is a composite material comprising a polymer matrix and an inorganic dispersive phase that has least one dimension that is nanometric in scale. Due to the large aspect ratio of the inorganic layers, large polymer–clay surface interactions can occur, which enables the improvement in the properties.

In traditional polymer composites, the addition of large micrometric inorganic loads (between 10 and 40% weight concentration) can significantly increase the mechanical properties of the polymers. These properties can also be increased by using loads with high aspect ratios (such as glass and carbon fiber). The higher the aspect ratio of the

inorganic load is, the greater the contact area with the polymer matrix is, which may increase the reinforcement by transferring a higher voltage from the matrix to the inorganic load. Therefore, the addition of a nanometric material with a high aspect ratio and a high stiffness to a polymer matrix may improve the performance of the polymer even more. Studies of this type of composite have been reported in the literature since 1950. However, since 1990, more attention has been given to nanocomposites because researchers at Toyota presented a study of the use of polyamide 6 (PA6) with organophilic clay in the construction of timing belts for motorized vehicles. The addition of clay at 5% by weight improved the characteristics of this material significantly when compared to unmodified PA6 resin [1].

Since then, different polymer matrices and inorganic loads have been combined to obtain new materials with different properties. Among the more frequently used inorganic loads, one can highlight laminar silicates [1–6], metal nanoparticles [7], carbon nanotubes [8,9], silica [10], calcium carbonate [11], and zinc oxide [12]. This chapter discusses the production, morphology, and properties of nanocomposites of polymer matrices with lamellar clays.

## 7.2 Structures of Lamellar Clays

Among the inorganic loads with potential for use in the production of nanocomposites, one can highlight lamellar or layered clays, which are composed of hydrated aluminum silicate and formed by layers with nanometric thicknesses; montmorillonite is the most widely used in the production of nanocomposites. Fig. 7.1 presents the basic crystalline structure of a silicate with a 2:1 structure. It is composed of three main layers: a central octahedral layer of alumina or magnesia and two outer tetrahedral layers of silica. The

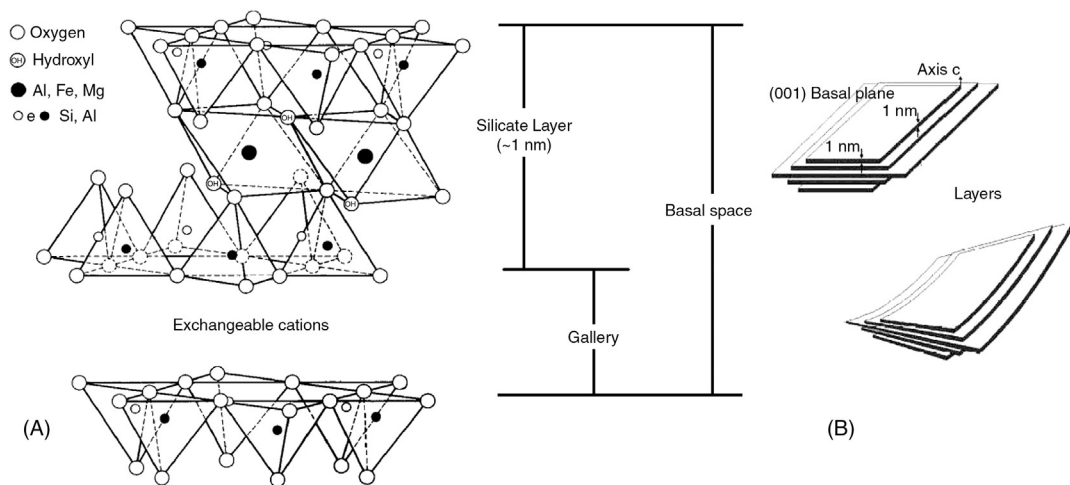


FIGURE 7.1 (A) Structure of a 2:1 phyllosilicate and (B) illustration of the flexibility of the lamellae [1].

layers are joined at the ends so that the oxygen ions of the octahedral layer also belong to the tetrahedral layer. The thickness of the layer is approximately 1 nm, and its lateral dimensions can vary from 30 nm to several micrometers.

Naturally, clay minerals are hydrophilic and can be dispersed in water to form thixotropic gels. To make these clay minerals compatible with hydrophobic polymers such as polyolefins, modifications of the clay surface are performed by exchanging hydrated cations with organic cations, decreasing the surface energy of the clay and increasing the distance between the layers [13]. The vast majority of organophilic clays are obtained from smectite clays; montmorillonite is the most common due to intrinsic characteristics of this clay mineral, which include the small size of its crystals and its high cation exchange capacity (CEC), which is used to characterize the degree of isomorphous substitution [1,14]. The CEC of smectites varies from 80 to 150 meq/100 g, which is much higher than those of other clay minerals (which are smaller than 40 meq/100 g).

In addition to the salt used as the organic treatment agent in clay minerals, the form in which this substitution is performed affects the formation of nanocomposites. One of the methods most frequently used to introduce alkylammonium ions between the layers is the ion exchange reaction [14]. This reaction consists of forming, in solution, the desired ion by dissolving the amine with a strong acid or with a salt that has a long alkyl chain containing atoms bonded to counterions, such as chloride and bromide, in hot water at approximately 80°C. These solutions are poured into a montmorillonite dispersion in hot water. A mixer is used to precipitate the particles, which are collected, washed, and then dried. During the drying process, the particles pile up again [14].

The surface treatment is important because it not only makes the clay organophilic and improves the characteristics of its interactions with nonpolar polymers but also increases the distance between the layers. In fact, surface treatment is used even when the polymers are polar and polarity modification of the clay is not fundamental to the production of nanocomposites.

By chemically modifying the surface of the clay, the organic salts allow a favorable penetration of the polymer precursors into the interlamellar regions. The role of the organic salt in the process of clay delamination depends on its chemical nature as well as the length and polarity of its chains [16].

### 7.3 Structure of Polymer Nanocomposites

To obtain nanocomposites with optimized properties, the clay lamellae should be dispersed and distributed appropriately in the polymer matrix. In addition, in several cases, a significant improvement of the diverse properties of the nanocomposites is reached when the polymer molecules between the clay lamellae are intercalated to a certain level or the lamellae are separated until they are completely dispersed and form an exfoliated structure. The nanocomposites are formed by distancing the clay lamellae because the forces that keep the lamellae together are relatively weak with subsequent penetration of the polymer chains in the interlamellar regions.

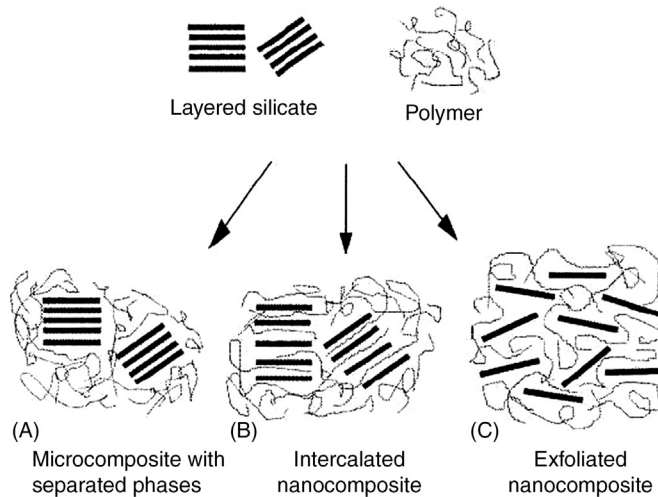


**FIGURE 7.2** Schematic representation of the different types of composites that can be formed by mixing lamellar silicates and polymers. (A) Microcomposites (with separation of both phases), (B) intercalated nanocomposites, and (C) exfoliated nanocomposites [1].

After the separation of the clay lamellae, it is expected that polymer chains bond physically or chemically to their surfaces to form interfaces that are strong enough to maintain their bonds under high strains and flexible enough to allow the transfer of these strains from the polymer matrix to the clay lamellae.

Depending on the nature of the components used (clay, an organic modifier of the clay, a polymer matrix, and a compatibilizing agent) and on the preparation method, it is possible to obtain composites with the three main types of structure shown in Fig. 7.2.

When the polymer is not able to intercalate between the silicate layers, the structure formed is similar to that of a conventional composite, shown in Fig. 7.2A, which provides little or no improvement of the properties. The second structure, which occurs in intercalated nanocomposites, is formed when one or more extended polymer chains are intercalated between the clay lamellae, which increases the distance between them while preserving the lamellar organization, as shown in Fig. 7.2B. In a third case, that of exfoliated nanocomposites, the clay lamellae are completely separated and dispersed, and the system does not present any order, as shown in Fig. 7.2C [1].

Structural characterization of polymer nanocomposites with lamellar clay is usually performed using two main complementary techniques: high-angle X-ray diffraction (XRD) and transmission electron microscopy (TEM). The intercalation and/or exfoliation process can be verified through XRD by observing the shift of the  $(0\ 0\ 1)$  diffraction peak of clay for values smaller than  $2\theta$  (for intercalation) or the absence of this peak (for exfoliation), which implies a loss of the structural regularity of the clay layers. The dispersion state and the distribution of the inorganic load in the polymer matrix are observed using TEM.

## 7.4 Methods for Obtaining Polymer Nanocomposites

In general, three main strategies can be used to obtain polymer–clay nanocomposites: intercalation of the polymer in solution, *in situ* polymerization, and intercalation in the melted state (melted intercalation).

When a polymer is intercalated in solution, the organically modified clay and the polymer are dispersed in an organic polar solvent. The silicates in layers can be easily dispersed in an appropriate solvent. The polymer dissolves in the solvent and then adsorbs to the layers of expanded silicates. When the solvent evaporates, the layers regroup and form an intercalated structure [17,18]. The selection of an appropriate solvent is a primary criterion for obtaining the desired level of exfoliation of an organophilic clay.

*In situ* polymerization involves the insertion of an appropriate monomer into the clay galleries before the polymerization process. The silicate layers are “swollen” by the liquid monomer (or a solution of the monomer) to ensure that the polymer forms between the intercalated layers. Polymerization can be initiated by heat, radiation, or the diffusion of an appropriate initiator, such as an organic initiator or a fixed catalyst, through cation exchange [1,15].

When nanocomposites are obtained by melted intercalation, the clay is directly dispersed in the melted polymer. During mixing in the melted state, the strain that the polymer exerts on the clay depends on its molecular weight. High levels of shear stress help reduce the size of the clay particles, which aids the intercalation and/or exfoliation process. The mechanism proposed for the action of the shear flow during the exfoliation of organically modified clay in melted intercalation is shown in Fig. 7.3. Initially, particles break down and form piles (tactoids) that disperse through the matrix, as shown in Fig. 7.3A. The transfer of strain from the polymer to these tactoids leads to stronger shearing, which

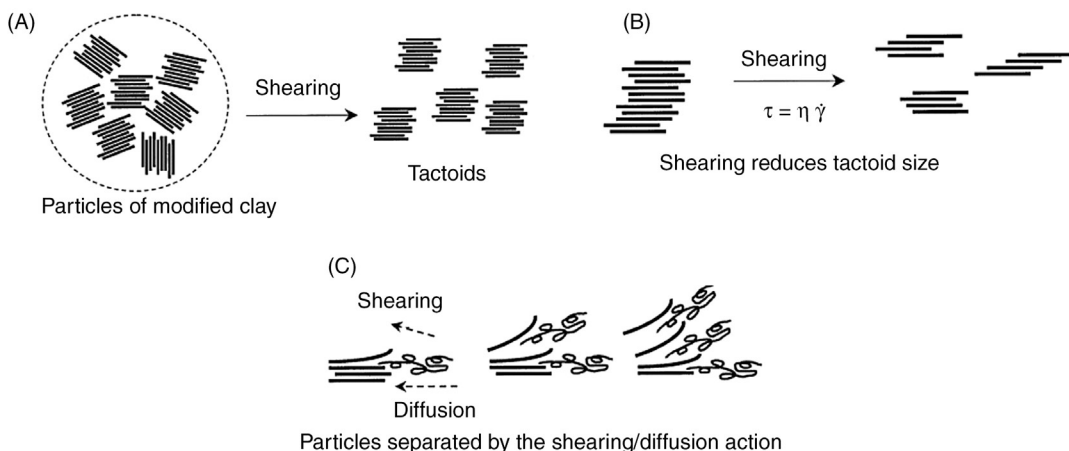


FIGURE 7.3 Effect of shearing on the intercalation and/or exfoliation of organically modified clay during melted intercalation [19].

breaks these tactoids into smaller piles (Fig. 7.3B). Finally, the individual layers are separated through a combination of shearing and diffusion of the polymer chains in the galleries; this step depends fundamentally on time and on the chemical affinity between the polymer and the clay (Fig. 7.3C) [19].

Thermodynamic models [20–22] have been used to explain the formation of nanocomposites by melted intercalation. Vaia and Giannelis [22] showed that this process occurs as a result of the concurrent action of entropic and enthalpic changes. The main factors contributing to changes in the free energy during the formation of the nanocomposite are the confinement of polymer chains between the clay layers, changes in the conformation of the surfactant molecules, and the appearance of new molecular interactions between the polymer, the surfactant, and the surface of the clay lamellae. The global decrease in the entropy of the system due to the confinement of polymer chains in silicate galleries can be compensated for by increasing the conformational freedom of the surfactant molecules and by separating the clay lamellae with a less confining medium. Therefore, these two opposing effects make the total entropic variation of the system small and negative, that is, the formation of a nanocomposite is entropically unfavorable. Therefore, the intercalation of the polymer must be managed, mostly by enthalpic variations.

The enthalpy of the mixture can be assumed to be favorable because the magnitude and number of interactions between the polymer chains and the surfactant molecules fixed on the surfaces of the clay lamellae are maximized when both contain polar groups. Therefore, intercalated nanocomposites can be obtained in systems that feature weak interactions between polymers and clays, and exfoliated nanocomposites can be produced by systems that feature strong interactions between polymers and clays, which exfoliates the layers. For nonpolar polymers, direct intercalation with clay lamellae is difficult and requires the use of compatibilizers.

## 7.5 Compatibilization in Nanocomposites with Nonpolar Matrices

Recent studies have shown that organically modified clays can be efficiently exfoliated in matrices of polar polymers, such as polyamides, using appropriate processing conditions and techniques. However, obtaining exfoliated nanocomposites based on the polyolefins that are more frequently used, such as polypropylene (PP) and polyethylene (PE), has proven more difficult because these materials are hydrophobic and appropriate interactions with the polar surface of the aluminosilicates in the clay do not occur [16,23,24]. The compatibility of the inorganic load with the polymer matrix is a significant challenge in the preparation of nanocomposites and can be improved by chemically modifying the surfaces of the particles in the components and by adding compatibilizers between the surfactant and the polymer matrix. Strength is promoted by the clay that sediments due to the efficiency of the compatibilization and by the restricted mobility of the polymer chains that are in contact with the clay lamellae.

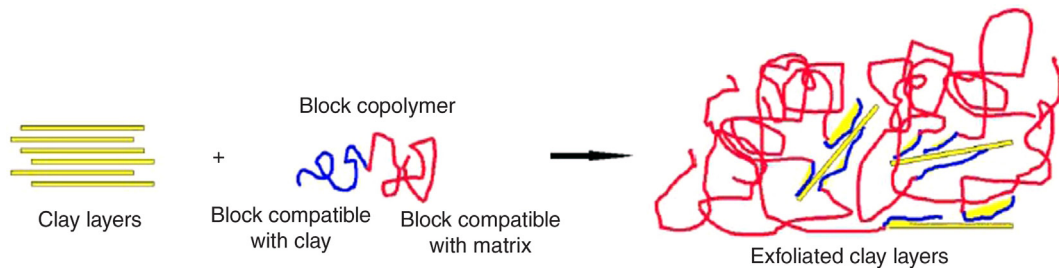


**FIGURE 7.4** Schematic representation of the action of a block copolymer during exfoliation of the clay lamellae in a polymer matrix [20].

Two main and joint strategies are currently used to enable chemical and physical interactions between the components of nanocomposites with nonpolar matrices. The first consists of making the surfaces of the inorganic particles organophilic, and the second consists of incorporating a comonomer with hydrophilic characteristics into the polymer chains.

Hydrophilic units can be directly inserted into the polymer chain in the matrix using copolymerization techniques in the presence of monomers and using reactive extrusion in the presence of polymers grafted with maleic anhydride, acrylic acid, or another functional group. An ideal compatibilizing agent between two noncompatible components must have parts that combine thermodynamically with both components. Surfactants provide these functions only partially because their ionic parts interact favorably with the surfaces of the clay particles. The long branches of alkyl groups, however, exhibit only limited compatibility with polymer chains. More efficient compatibilization can be obtained by using macrosurfactants, such as block or grafted copolymers, as shown in Fig. 7.4, to combine blocks that can react with the surface of a solid particle and with the polymer matrix and then improve the interaction between the surface of the clay and the polymer chains [20].

## 7.6 Nanocomposites with Polar Matrices

Among the various polar polymer matrices used in the preparation of nanocomposites, polyamide is the one that stands out the most; a broad range of studies of nanocomposites of polyamide and lamellar clay can be found in the literature [1,19,25–31]. Other polar polymer matrices that stand out are poly(ethylene terephthalate) [4,32–37], poly(vinyl chloride) [38–42], and polycarbonate [43–46].

### 7.6.1 Structure and Properties

In general, the properties of polymer nanocomposites are highly dependent on their microstructures. A nanocomposite with an exfoliated and well-dispersed structure features important modifications to the mechanical, physical, and chemical properties of its matrix, which are due to the stronger polymer-clay interactions that occur in these

systems. The thermal stability of these polymer nanocomposites is higher than those of pure polymers because of the presence of anisotropic layers of clay in the polymer matrix, which slow or stop the diffusion of volatile products through the nanocomposite.

Nanocomposites with concentrations of clay on the order of 2–10% may show significant improvements in their properties over those of pure polymers. Among the main improvements are in mechanical properties, such as increases in the elastic modulus, the maximum tensile strength, and the flexural modulus, in barrier properties, such as a reduced permeability to gases, optical properties, and ionic conductivity.

The advantage of adding a smaller amount of clay during the formulation and preparation of a nanocomposite in the melted state causes the final density of the material to decrease, which contributes to the production of lighter components and reduces wear and tear to the equipment used to process these materials.

In addition to these properties, the preparation of polymer/lamellar clay nanocomposites includes improvements to their thermal stability and the ability to promote flame retardancy.

A good example of a nanocomposite with a polar matrix that has excellent properties is PA6 with organically modified montmorillonite clay (OMMT). Fig. 7.5 presents a TEM micrograph of a nanocomposite of PA6 with the addition of 5% OMMT by weight, which was obtained by melted intercalation in a twin-screw extruder.

The morphology of this nanocomposite comprises individual lamellae that are completely exfoliated, well dispersed and distributed, which strengthens the polymer matrix significantly.

The excellent dispersion of the clay lamellae promotes a significant increase in the elastic modulus from 2.7 GPa for pure PA6 to 4.7 GPa with the added nanoload. Oliveira et al.

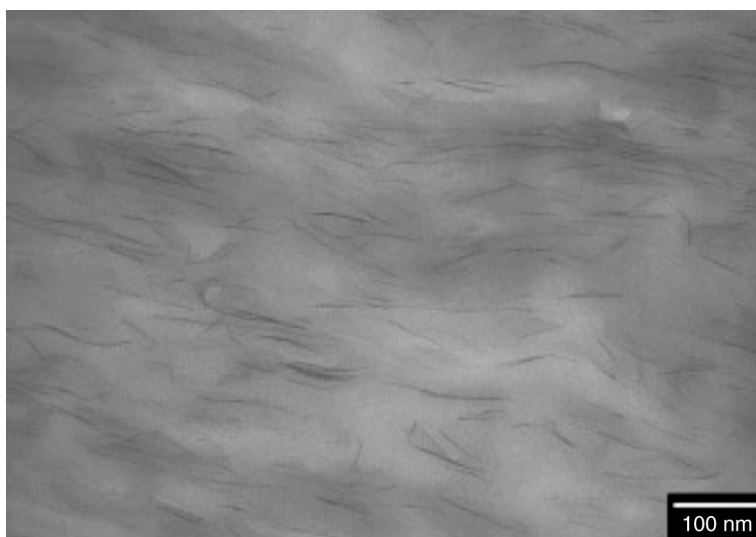


FIGURE 7.5 TEM micrograph of a PA6/OMMT (95%/5%) nanocomposite.

[5] reported an increase of more than 50°C in the heat deflection temperature (HDT) of this nanocomposite ( $HDT_{PA6} = 55^\circ\text{C}$  and  $HDT_{\text{nanocomposite}} = 108^\circ\text{C}$ ).

The improvement in these mechanical properties has been connected to the dispersion, the degree of exfoliation, the aspect ratio of the clay, and the polymer–clay interfacial interactions. Luo and Daniel [46] studied epoxy/clay nanocomposites and observed that a high degree of dispersion increases the elastic modulus. The efficiency of the strengthening of the nanocomposite was attributed to the fraction of exfoliated material because the effective aspect ratio of the incorporated additive becomes extremely elevated in exfoliated nanocomposites. However, this effect can restrict the delamination of other layers of clay that could be exfoliated but remain aggregates. Therefore, partial intercalation may contribute positively to the increase in the elastic modulus because a higher concentration of clay may be intercalated and, therefore, may be in the structure of a material with a high aspect ratio. Therefore, the high aspect ratios of exfoliated particles and intercalated aggregates is desirable for strengthening the nanocomposites.

In addition to preparing nanocomposites using matrices that consist of only one polymer, several research groups have been developing nanocomposites with polymer matrices that consist of mixtures of two or more polymers; these are nanocomposites of polymer blends. Polymer blends are excellent alternatives for adding value to materials because the physical and chemical properties of these polymer matrices are modified to allow a vast range of applications [47]. Polymer blends are polymeric systems that originate in the physical mixture of two or more polymers and/or copolymers that do not undergo significant chemical reactions [47,48].

A balance between properties is a typical result of using a polymer blend as a nanocomposite matrix. The addition of lamellar clay significantly increases the elastic modulus of the nanocomposite, that is, the stiffness of the material increases. However, the impact resistance (IR) of the nanocomposite decreases, that is, it becomes more fragile. An alternative for improving both properties could be the addition of a second phase that has excellent resistance to impact but does not mix with the polymer matrix to balance the mechanical properties (tenacity vs. stiffness). An example of such a system is the nanocomposite of PA6 with OMMT with the addition of a second phase composed of an acrylonitrile–butadiene–styrene (ABS) blend as an impact modifier for engineered polymers.

Fig. 7.6 shows the morphology of a nanocomposite of the PA6/ABS blend with OMMT developed by Oliveira et al. [5].

The morphology features elongated ABS domains. Inside these domains, it is possible to observe polybutadiene particles with a wide range of sizes in addition to exfoliated lamellae, which are only in the matrix of PA6. In this case, the clay lamellae prevent the coalescence of the dispersed polybutadiene domains, which reduces the size of this elastomeric phase. Regarding mechanical properties, one can observe that the addition of clay does not alter the Izod IR of the system from that of the PA6/ABS blend. However, adding clay to the blend increases the elastic modulus significantly ( $E_{PA6/ABS} = 2.8 \text{ GPa}$  and  $E_{PA6/ABS/OMMT} = 4.2 \text{ GPa}$ ) [5].

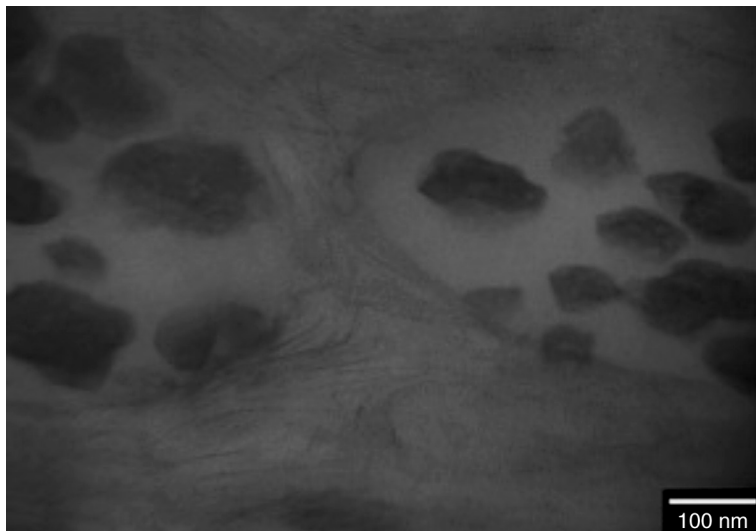


**FIGURE 7.6** TEM micrograph of a PA6/ABS/OMMT (57.5/37.5/5%) nanocomposite.

Several other examples can be found in the literature on nanocomposites with polar matrices, including studies of different treatments of lamellar clays, compatibilization of the polymer matrix, and different sequences for mixing the components to identify the best relationship between structure and properties.

## 7.7 Nanocomposites with Nonpolar Matrices

Polyolefins are widely used for applications in the packaging, automotive, and electric industries, where thermal and mechanical resistance and gas and vapor transport properties are very important. The main representatives of this class of polymer are PE [6,17,23,24,49–56] and PP [3,21,57–60], which are the most frequently used in preparing nanocomposites with nonpolar matrices.

However, obtaining exfoliated nanocomposites from polyolefins and clay is still a significant challenge because polyolefins are hydrophobic and do not interact appropriately with the polar surface of the clay. The surfaces of clays are treated with quaternary ammonium salts to make them hydrophobic. For PE and PP, organophilization of the clay is not enough to guarantee the formation of exfoliated nanocomposites, and therefore, it is necessary to use compatibilizing agents, which are more commonly added during in situ polymerization and melted intercalation.

Different routes of compatibilization and/or types of compatibilizing agents used in the formation of nanocomposites with intercalated/exfoliated structures have been reported in the literature. Among the compatibilizing agents that are most common and most appropriate for nanocomposites are polyolefins grafted with maleic anhydride. They increase the chemical and structural affinity of the clay for the polymer matrix and

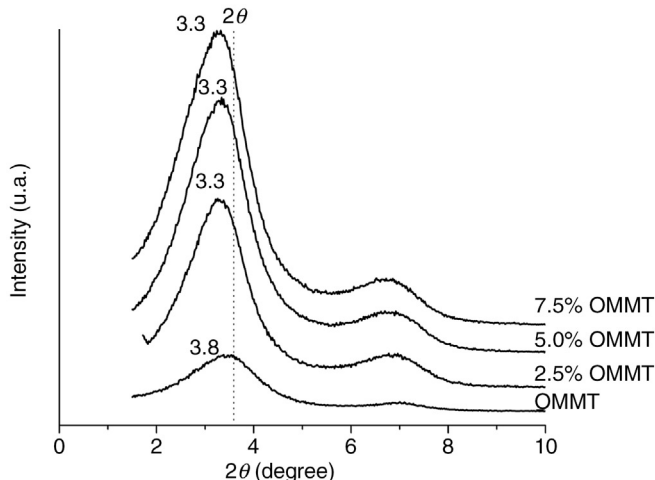


**FIGURE 7.7** XRD patterns of lamellar clay (OMMT) and HDPE/LLDPE nanocomposite blends with different concentrations of lamellar clay (2.5, 5.0, and 7.5% by weight).

promote significant improvement of mechanical and barrier properties in addition to being able to mix with polymer matrices, as shown in the following sections.

### 7.7.1 Structure and Properties

Among polyolefins, high-density polyethylene (HDPE) has a great deal of potential for applications in the packaging and electric sectors. However, it is difficult to obtain nanocomposites of HDPE and lamellar clay because, in addition to weak interactions between the nonpolar matrix and the clay, there are difficulties in processing such materials due to their high viscosities when melted. To ease the process and obtain nanocomposites of polyolefins and lamellar clays that have good properties, Passador et al. developed [6] HDPE/linear low-density polyethylene (LLDPE) nanocomposite blends. Adding LLDPE, which has a chemical structure that is similar to that of HDPE and a lower viscosity, aids processing by modifying the morphology and the properties of the polymer blend. Fig. 7.7 shows XRD patterns of OMMT and the HDPE/LLDPE nanocomposite blends with different concentrations of clay. Fig. 7.8 shows TEM micrographs of these nanocomposites.

Analysis of the XRD patterns in Fig. 7.7 shows a small shift of the diffraction peak for smaller angles referring to the crystallographic plane (0 0 1) in relation to the OMMT, which indicates a small increase in the basal spacing ( $2\theta = 3.8$  degree corresponds to a basal spacing of 2.32 nm, while  $2\theta = 3.3$  degree corresponds to one of 2.68 nm). This suggests that a significant fraction of the tactoids in the system remain unchanged, that is, the distance between the clay lamellae does not change. Therefore, the shear that results from mixing in the melted state is not enough to efficiently delaminate the clay mineral. There is also a secondary reflection at  $2\theta = 7.4$  degree, which corresponds to crystallographic plane (0 0 2) of the nanocomposite but is shifted to a smaller angle.

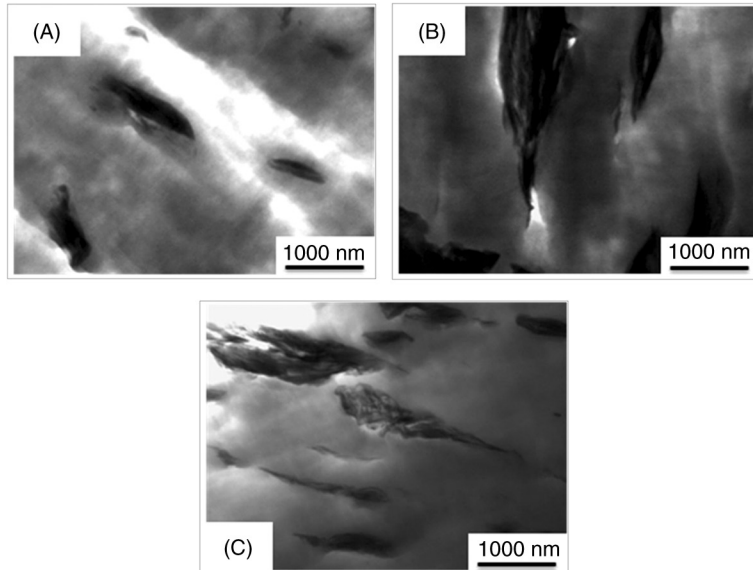


**FIGURE 7.8** TEM micrographs of HDPE/LLDPE/OMMT nanocomposites (A) with 2.5% OMMT by weight, (B) with 5.0% OMMT by weight, and (C) with 7.5% OMMT by weight.

Unlike the PA6/ABS system, in which the polymer blend is immiscible, that is, phase separation occurs, the HDPE/LLDPE system presents full miscibility in the melted state, where it forms a single phase, as shown by the micrographs in Fig. 7.8. The addition of lamellar clay allows the formation of a microcomposite with a structure that is mostly composed of agglomerates or tactoids of lamellar clay. The small amount of interaction between the components (the matrix and the load) does not allow these tactoids to break down during processing, and increasing the amount of lamellar clay results in larger agglomerates in the polymer matrix.

In this system, it is necessary to add compatibilizing agents to increase the interaction between the polymer matrix and the lamellar clay. Compatibilizing agents grafted with maleic anhydride that have melt flow indices that are similar to those of materials used as polymer matrices have been studied. With these, the compatibilizing agents and polymers are expected to be miscible, and the compatibilized HDPE/LLDPE blend is expected to have a better affinity for the organic modifier of the lamellar clay.

Fig. 7.9 shows the XRD patterns and Fig. 7.10 shows the TEM micrographs of the HDPE/LLDPE/OMMT nanocomposite blend compatibilized with high-density polyethylene grafted with maleic anhydride (HDPE-g-MA).

With the addition of a compatibilizing agent (HDPE-g-MA), the diffraction peak referring to the crystallographic plane (0 0 1) undergoes a more significant shift for smaller values of  $2\theta$ , which corresponds to an increase in the interlamellar spacing in the clay mineral. This suggests that the polymer chains may have been intercalated between the lamellar silicate layers. As the lamellar clay content of the polymer matrix increases, an increase

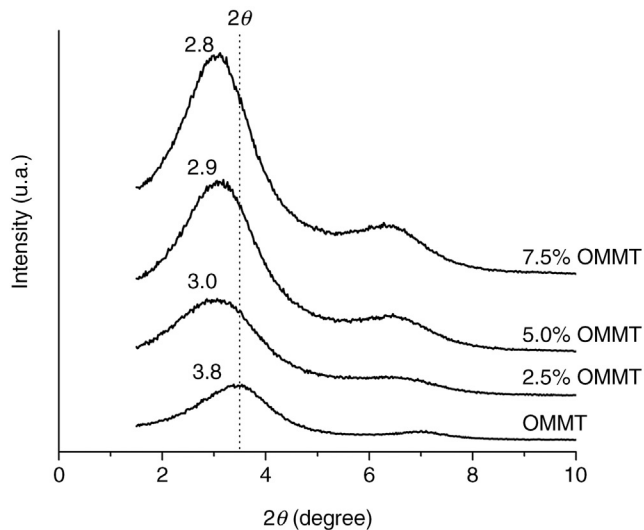


FIGURE 7.9 XRD patterns of OMMT and HDPE/LLDPE nanocomposite blends with different concentrations of lamellar clay (2.5, 5.0, and 7.5% by weight) and with the compatibilizing agent HDPE-g-MA.

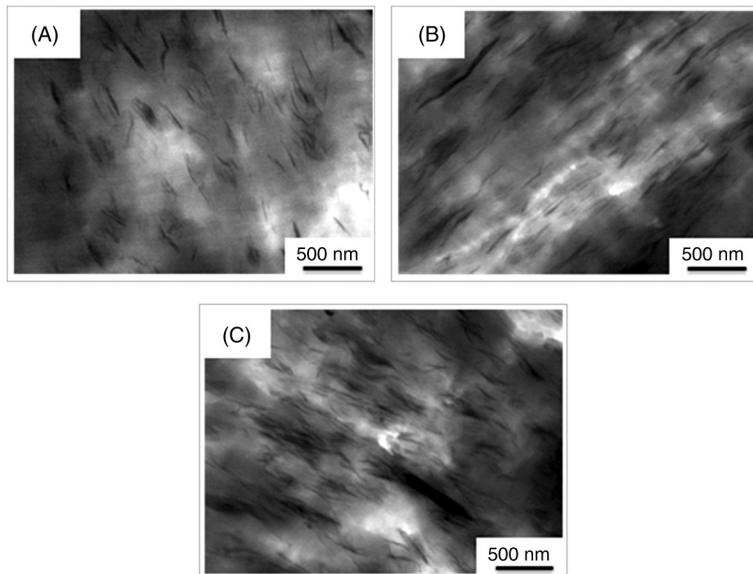


FIGURE 7.10 TEM micrographs of HDPE/LLDPE/OMMT nanocomposites with the compatibilizing agent HDPE-g-MA (A) with 2.5% OMMT by weight, (B) with 5.0% OMMT by weight, and (C) with 7.5% OMMT by weight.

of the basal spacing is observed: 2.96 nm for 2.5% OMMT, 3.04 nm for 5.0% OMMT, and 3.17 nm for 7.5% OMMT.

The compatibilizing agent completely modifies the morphology of the HDPE/LLDPE nanocomposites. The addition of HDPE-g-MA, which has a high viscosity, combines with the imposed shear during the extrusion process to ease the process of breaking down and reducing the size of the tactoids in the organophilic clay and, consequently, helps polymer chains intercalate between the silicate layers and the lamellar clay that is dispersed throughout the polymer matrix. The compatibilizing agent can reduce the size of the load particles due to thermodynamic factors (compatibilization due to the surfactant in organophilic lamellar clays) and kinetics (an increase in the viscosity due to the presence of clay nanoparticles). The morphology of these systems is created by intercalated lamellae; however, the presence of some exfoliated lamellae of organophilic clay and tactoids that have been significantly reduced in size compared to the morphologies of the nanocomposites shown in Fig. 7.8 are also noted.

In addition to the effects on the morphology, modifications to the mechanical and gas permeability properties are also observed. The effect that adding clay has on the elastic and flexural moduli are shown in Fig. 7.11.

The elastic modulus or Young's modulus is the ratio of stress to strain within the elastic limit, where the strain is completely reversible, proportional to the stress, and directly related to the stiffness of the material. This is a much-sought after property in studies involving polymer nanocomposites.

In general, nanocomposites have mechanical properties that are superior to those of HDPE/LLDPE blends. Comparing nanocomposites with lamellar clay contents of up to 5.0% by weight shows that nanocomposites without added compatibilizing agents present mechanical properties that are very close to those of nanocomposites compatibilized with HDPE-g-MA. This behavior, which was also observed by Spencer et al. [56] when they studied HDPE-g-MA/HDPE blends, is due to the lower crystallinity of the former with respect to the latter. However, when 7.5% lamellar clay by weight is added, the improved dispersion that results from the addition of the compatibilizing agent surpasses the properties of nanocomposites with large numbers of tactoids.

The three-point bending test measures the maximum flexural strength of a material. At the loading point, the top surface of the specimen is compressed, while the bottom surface is under tension. Because the specimen is subjected to compressive and tensile stresses when it is bent, the magnitude of its flexural strength is greater than its tensile fracture strength. Good performance of a nanocomposite in the three-point bending test is related to good dispersion and distribution of the lamellar clay in the polymer matrix. The values of the flexural modulus obtained are smaller than those of the elastic modulus; however, a significant increase in the flexural modulus is observed when organophilic lamellar clay is added; this is the result of the good interface created. In addition, the good distribution of stress observed in the nanocomposites developed, leads to an increase of 100% in the flexural modulus of the nanocomposite compatibilized with HDPE-g-MA containing 7.5% lamellar clay by weight.

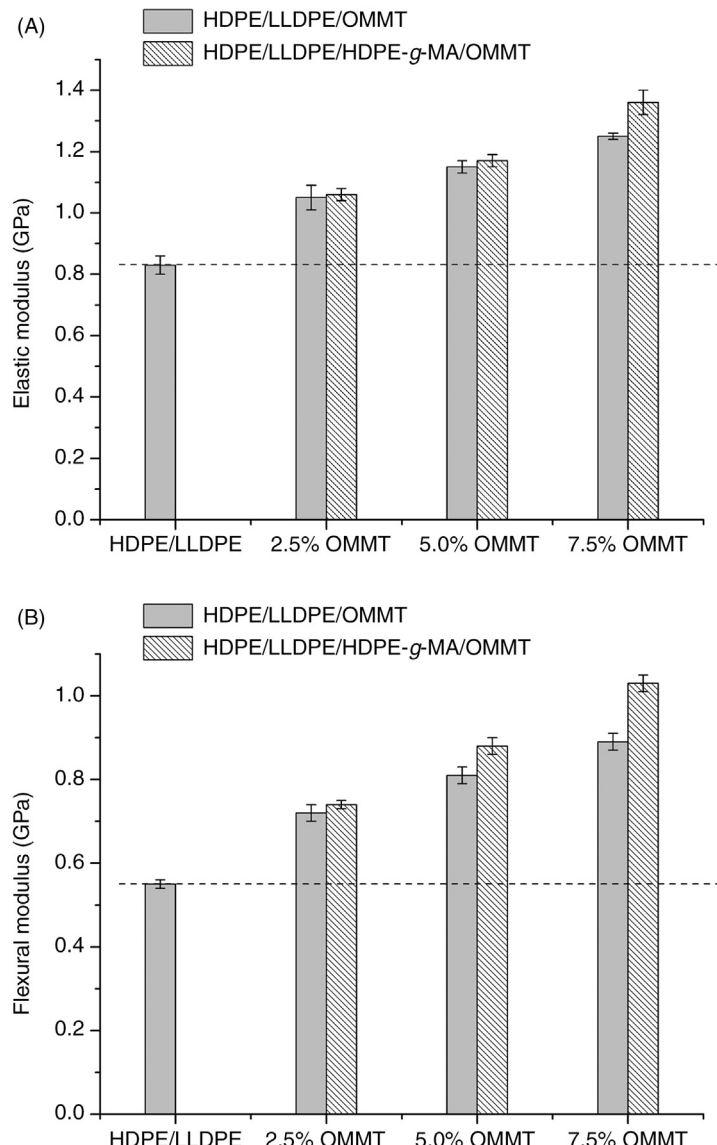


**FIGURE 7.11** Mechanical properties of HDPE/LLDPE nanocomposite blends with and without compatibilizing agents. (A) The elastic modulus obtained from the uniaxial tensile test and (B) the flexural modulus obtained from the three-point bending test.

In addition to decreasing the mechanical properties, adding lamellar clay can decrease the gas permeability of the polymer matrix.

The ability of a polymer film or membrane to transport gas and vapor molecules depends strongly on the molecular structure of the polymer matrix and is very sensitive to changes in it [61]. The addition of clay to a polymer system leads to changes in its transport

properties in the vast majority of cases. The permeability to small molecules of a nanocomposite that contains clay can be significantly less than that of a pure polymer because of the large aspect ratio and the impermeability of clay lamellae, which are responsible for the effects of tortuosity when they are dispersed in a polymer matrix [62–64]. Several theoretical models have been proposed in the literature to express the tortuosity factor as a function of the form, orientation, disperse state, and volume fraction of impermeable particles.

Nielsen [65] developed a permeability model for composites that includes the effect of tortuosity; for measurements in nanocomposites the following expression is used:

$$\frac{P}{P_0} = \frac{1 - \phi_{NC}}{\tau} = \frac{(1 - \phi_{NC})}{\left(1 + \frac{L}{2W}\phi_{NC}\right)}, \quad (7.1)$$

where  $P$  and  $P_0$  are the permeabilities of the nanocomposite and the pure polymer, respectively. The tortuosity factor  $\tau = (d'/d) = 1 + (L/2W)\phi_{NC}$  is defined as the ratio of the distance or real path ( $d'$ ) that the penetrator must cross to the shorter distance ( $d$ ) that it would cross if there were no silicate in the layer. It is expressed in terms of the length ( $L$ ) and thickness ( $W$ ) of the clay layer and the volumetric fraction of the load ( $\phi_{NC}$ ). Loads with high-form factors ( $L/W$ ) lead to high tortuosities and, consequently, the permeability of such a nanocomposite is less than that of a pure polymer. Fig. 7.12 illustrates a model of the path of a penetrator diffusing through a nanocomposite.

The model proposed by Nielsen is limited because clay layers are assumed to be oriented perfectly transverse to the direction of permeation and of the same size, the diffusivity of the matrix is not changed by the presence of the clay, and preferential transport does not occur at polymer/clay interfaces.

Examples of the effects of the addition of lamellar clay on the permeability of HDPE/LLDPE nanocomposite blends to oxygen are presented in Table 7.1.

It is anticipated that the addition of an inorganic load will increase the mean free path for diffusion and decrease the permeability coefficient. In HDPE/LLDPE nanocomposite blends without compatibilizers, the agglomeration of lamellar clay and the poor dispersion of the inorganic load in the matrix help increase the number of microvoids in the polymer matrix and, therefore, aid diffusion. The oxygen permeability coefficient increases, in

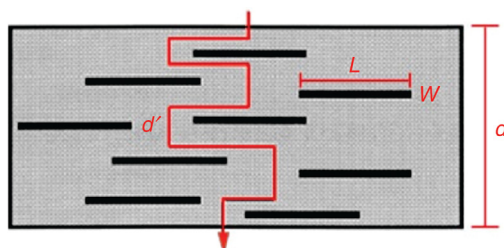


FIGURE 7.12 Model of the path of a penetrator diffusing through a nanocomposite.

**Table 7.1** Oxygen Permeability of the Films Obtained Using An OX-TRAN 2/21 T Oxygen Transmission Rate System and the Degree of Crystallinity (%) Obtained from the Cooling Curve of Differential Scanning Calorimetry (DSC) Tests

Sample	$P_{O_2}$ (Barrier)	Crystallinity (%)
HDPE/LLDPE	1.44 ± 0.22	65
HDPE/LLDPE/OMMT (2.5%)	2.28 ± 0.05	62
HDPE/LLDPE/OMMT (5.0%)	1.83 ± 0.41	63
HDPE/LLDPE/OMMT (7.5%)	0.98 ± 0.05	66
HDPE/LLDPE/OMMT/HDPE-g-MA (2.5%)	1.18 ± 0.17	66
HDPE/LLDPE/OMMT/HDPE-g-MA (5.0%)	1.16 ± 0.36	61
HDPE/LLDPE/OMMT/HDPE-g-MA (7.5%)	0.98 ± 0.05	57

comparison with polymer blends, for concentrations of up to 5% OMMT by weight. However, with 7.5% lamellar clay, the permeability coefficient decreases because the degree of crystallinity increases when the system's OMMT concentration increases. Therefore, in addition to the tortuosity created by the clay tactoids, there is a larger fraction of crystalline phase that contributes to the increase in the diffusion path, which decreases the effective coefficient of permeability to oxygen.

The addition of a high concentration of a compatibilizing agent to a nanocomposite can have some effects, such as a decrease in the density of the crystalline domain of the blend and an increase in the amorphous character and fluctuations of the free volume. However, it aids the process of breaking down tactoids and dispersing the clay lamellae in the polymer matrix, which increases the gas diffusion path, as observed for HDPE/LLDPE nanocomposite blends compatibilized with HDPE-g-MA. In addition, the oxygen permeability coefficient decreases when the OMMT concentration increases. The morphological changes due to the addition of the compatibilizing agent allow the tortuosity to increase in response to the intercalated and well-dispersed state of the clay lamellae in the polymer matrix despite lower barrier properties intrinsically presented by HDPE-g-MA. This decrease in the coefficient of permeability is connected to good inorganic load dispersion, high wettability by the matrix, and strong interactions at the interface that decrease the number of microvoids, which could help the diffusion process.

## 7.8 Final Considerations

The development of new materials that provide the properties demanded by applications, especially those in the automotive, electrical power, and packaging industries, has attracted the interest of large industries and research groups. Among the different techniques used to obtain these properties, one can highlight the preparation of nanocomposites with polymer matrices by adding lamellar clays with at least one nanoscale dimension.

Two large groups of polymer matrices can be used to prepare these nanocomposites, polar matrices, and nonpolar matrices, and it is possible to combine materials from the

two groups. The nanocomposite of PA6 and organophilic lamellar clay is an excellent example of how the polarity of the polymer matrix affects the interactions between the polymer and the clay, in addition to modifying the morphology, and the thermal and mechanical properties of the nanocomposite, which can be compared to those of pure PA6. For non-polar matrices, such as polyolefins, obtaining exfoliated nanocomposites is more difficult because polyolefins are hydrophobic and there is a lack of appropriate interactions with the polar surface of aluminosilicate clay. The compatibility of inorganic loads with polymer matrices is a big challenge in the preparation of nanocomposites that can be improved by chemically modifying the surfaces of the particles of the components and by adding compatibilizing agents between the surfactant and the polymer matrix. The strengthening promoted by the clay is determined by the efficiency of the compatibilization and the restricted mobility of the polymer chains that are in contact with the clay lamellae.

## References

- [1] M. Alexandre, P. Dubois, Polymer-layered silicate nanocomposites: preparation, properties and uses of a new class of materials, *Mater. Sci. Eng.* 28 (1–2) (2000) 1–63.
- [2] F. Hussain, M. Hojjat, M. Okamoto, R.E. Gorga, Review article: polymer-matrix nanocomposites, processing, manufacturing, and application: an overview, *J. Compos. Mater.* 40 (17) (2006) 1511–1575.
- [3] C.G. Martins, N.M. Larocca, D.R. Paul, L.A. Pessan, Nanocomposites formed from polypropylene/EVA blends, *Polymer* 50 (7) (2009) 1743–1754.
- [4] S.E. Vidotti, A.C. Chinellato, G.H. Huo, L.A. Pessan, Preparation of poly(ethylene terephthalate)/organoclay nanocomposites using a polyester ionomer as a compatibilizer, *J. Polym. Sci. Part B* 45 (22) (2007) 3084–3091.
- [5] A.D. Oliveira, N.M. Larocca, D.R. Paul, L.A. Pessan, Effects of mixing protocol on the performance of nanocomposites based on polyamide 6/acrylonitrile-butadiene-styrene blends, *Polym. Eng. Sci.* 52 (9) (2012) 3084–3091.
- [6] F.R. Passador, A.C. Ruvolo-Filho, L.A. Pessan, Effect of blending protocol on the rheological properties and morphology of HDPE/LLDPE blend-based nanocomposites, *Int. Polym. Proc.* 27 (3) (2012) 378–385.
- [7] M.U. Jurczyk, A. Kumar, S. Srinivasan, E. Stefanakos, Polyaniline-based nanocomposite materials for hydrogen storage, *Int. J. Hydrogen Energy* 32 (8) (2007) 1010–1015.
- [8] G. Terife, K.A. Narh, Properties of carbon nanotube reinforced linear low density polyethylene nanocomposites fabricated by cryogenic ball-milling, *Polym. Comp.* 32 (12) (2011) 2101–2109.
- [9] C.M. Chang, K.Y. Hsu, Y.L. Liu, Matrix-polymer-functionalized multiwalled carbon nanotubes as a highly efficient toughening agent for matrix polymers, *J. Polym. Sci. B* 50 (16) (2012) 1151–1155.
- [10] M. Rahimi, I. Iriarte-Carretero, A. Ghanbari, M.C. Bohm, F. Muller-Plathe, Mechanical behavior and interphase structure in a silica-polystyrene nanocomposite under uniaxial deformation, *Nanotechnology* 23 (30) (2012) 305702.
- [11] D. Eiras, L.A. Pessan, Mechanical properties of polypropylene/calcium carbonate nanocomposites, *Mater. Res. Ibero Am. J. Mater.* 12 (4) (2009) 517–522.
- [12] A. Olad, R. Nosrati, Preparation, characterization, and photocatalytic activity of polyaniline/ZnO nanocomposite, *Res. Chem. Intermediat.* 38 (2) (2012) 323–336.
- [13] C.E. Powell, G.W. Beall, Physical properties of polymer/clay nanocomposites, *Curr. Opin. Solid St. M.* 10 (2006) 73–80.

- [14] S.C. Tjong, Structural and mechanical properties of polymer nanocomposites, *Mater. Sci. Eng.* 53 (3–4) (2006) 73–197.
- [15] T.J. Pinnavaia, G.W. Beall, *Polymer – Clay Nanocomposites*, John Wiley & Sons, Inc., New York, (2000).
- [16] R.A. Vaia, R.K. Teukolsky, E.P. Giannelis, Interlayer structure and molecular environment of alkylammonium layered silicates, *Chem. Mater.* 6 (7) (1994) 1017–1022.
- [17] M. Alexandre, P. Dubois, T. Sun, J.M. Garces, R. Jérôme, Polyethylene-layered silicate nanocomposites prepared by the polymerization-filling technique: synthesis and mechanical properties, *Polymer* 43 (8) (2002) 2123–2132.
- [18] S.S. Ray, M. Okamoto, Polymer/layered silicate nanocomposites: a review from preparation to processing, *Prog. Polym. Sci.* 28 (11) (2003) 1539–1641.
- [19] T.D. Fornes, P.J. Yoon, H. Keskkula, D.R. Paul, Nylon 6 nanocomposites: the effect of matrix molecular weight, *Polymer* 42 (25) (2001) 9929–9940.
- [20] H. Fischer, Polymer nanocomposites: from fundamental research to specific applications, *Mater. Sci. Eng. C* 23 (6–8) (2003) 763–772.
- [21] Y. Wang, F.B. Chen, K.C. Wu, Effect of the molecular weight of maleated polypropylenes on the melt compounding of polypropylene/organoclay nanocomposites, *J. Appl. Polym. Sci.* 97 (4) (2005) 1667–1680.
- [22] R.A. Vaia, E.P. Giannelis, Lattice model of polymer melt intercalation in organically-modified layered silicates, *Macromolecules* 30 (25) (1997) 7990–7999.
- [23] S. Hotta, D.R. Paul, Nanocomposites formed from linear low density polyethylene and organoclays, *Polymer* 45 (2) (2004) 7639–7654.
- [24] J. Heinemann, P. Reichert, R. Thomann, R. Mulhaupt, Polyolefin nanocomposites formed by melt compounding and transition metal catalyzed ethene homo- and copolymerization in the presence of layered silicates, *Macromol. Rapid Comm.* 20 (8) (1999) 423–430.
- [25] Y. Kojima, A. Usuki, M. Kawasumi, A. Okada, T. Kurauchi, O. Kamigaito, K. Kaji, Fine structure of nylon 6-clay hybrid, *J. Polym. Sci. Part B* 32 (4) (1994) 625–630.
- [26] T.D. Fornes, D.R. Paul, Modeling properties of nylon 6/clay nanocomposites using composite theories, *Polymer* 44 (17) (2003) 4993–5013.
- [27] E. Picard, A. Vermogen, J.F. Gérard, E. Espuche, Barrier properties of nylon 6-montmorillonite nanocomposite membranes prepared by melt blending: influence of the clay content and dispersion state. Consequences on modeling, *J. Membrane Sci.* 292 (2007) 133–144.
- [28] T.D. Fornes, D.L. Hunter, D.R. Paul, Effect of sodium montmorillonite source on nylon 6/clay nanocomposites, *Polymer* 45 (7) (2004) 2321–2331.
- [29] F. Chavarria, R.K. Shah, D.L. Hunter, D.R. Paul, Effect of melt processing conditions on the morphology and properties of nylon 6 nanocomposites, *Polym. Eng. Sci.* 47 (11) (2007) 1847–1864.
- [30] M.A. Souza, N.M. Larocca, E.M. Araújo, L.A. Pessan, Preparation and characterization of nanocomposites of polyamide 6/Brazilian clay with different organic modifiers, *Mater. Sci. Forum* 570 (2008) 18–23.
- [31] R.A. Paz, A.M.D. Leite, E.M. Araújo, T.J.A. Mélo, R. Barbosa, E.N. Ito, Nanocomposites de Poliamida 6/Argila Organofílica: Efeito do Peso Molecular da Matriz na Estrutura e Propriedades Mecânicas e Termomecânicas, *Polímeros: Ciência e Tecnologia* 18 (4) (2008) 341–347.
- [32] S.E. Vidotti, A.C. Chinellato, L.F. Boesel, L.A. Pessan, Poly (ethylene terephthalate)-organoclay nanocomposites: morphological, thermal and barrier properties, *J. Metastable Nanocryst. Mater.* 22 (2004) 47–54.
- [33] L.F. Boesel, L.A. Pessan, Poly(ethylene terephthalate)-organoclay nanocomposites: morphological characterization, *J. Metastable Nanocryst. Mater.* 14 (2002) 89–94.

- [34] Z. Ke, Y.P. Bai, Improve the gas barrier property of PET film with montmorillonite by in situ interlayer polymerization, *Mater. Lett.* 59 (27) (2005) 3348–3351.
- [35] Y.M. Wang, J.P. Gao, Y.Q. Ma, U.S. Agarwal, Study on mechanical properties, thermal stability and crystallization behavior of PET/MMT nanocomposites, *Compos. Part B Eng.* 37 (6) (2006) 399–407.
- [36] M.C. Costache, M.J. Heidecker, E. Manias, C.A. Wilkie, Preparation and characterization of poly(ethylene terephthalate)/clay nanocomposites by melt blending using thermally stable surfactants, *Polymer Adv. Tech.* 17 (9–10) (2006) 764–771.
- [37] B. Wen, X.F. Xu, X.W. Gao, Y.F. Ding, F. Wang, S.M. Zhang, M.S. Yang, Highly exfoliated poly(ethylene terephthalate)/clay nanocomposites via melt compounding: effects of silane grafting, *Polym. Plast. Technol. Eng.* 50 (4) (2011) 362–371.
- [38] T. Peprniecek, J. Duchet, L. Kovarova, J. Malac, J.F. Gerard, J. Simonik, Poly(vinyl chloride)/clay nanocomposites: X-ray diffraction, thermal and rheological behavior, *Polym. Degrad. Stabil.* 91 (8) (2006) 1855–1860.
- [39] M.A. Souza, A. Rodolfo Jr., L.A. Pessan, Nanocomposites de poli (cloreto de vinila) (PVC)/argila organofílica, *Polímeros: Ciência e Tecnologia* 16 (4) (2006) 257–262.
- [40] W.H. Awad, G. Beyer, D. Benderly, W.L. Lido, P. Songtipya, M.D. Jimines-Gasco, E. Manias, Materials properties of nanoclay PVC composites, *Polymer* 50 (8) (2009) 1857–1867.
- [41] J. Pagacz, K. Pielichowski, Preparation and characterization of PVC/montmorillonite nanocomposites: a review, *J. Vinyl Addit. Techn.* 15 (2) (2009) 61–76.
- [42] M. Mondragon, S. Sanches-Valdes, M.E. Sanches-Espindola, J.E. Rivera-Lopez, Morphology, mechanical properties, and thermal stability of rigid PVC/clay nanocomposites, *Polym. Eng. Sci.* 51 (4) (2011) 641–646.
- [43] A.J. Hsieh, P. Moy, F.L. Beter, P. Madison, E. Napadensky, J.X. Ren, R. Krishnamoorti, Mechanical response and rheological properties of polycarbonate layered-silicate nanocomposites, *Polym. Eng. Sci.* 44 (5) (2004) 825–837.
- [44] F.J. Carrion, A. Arribas, M.D. Bermudez, A. Guillamon, Physical and tribological properties of a new polycarbonate-organoclay nanocomposite, *Eur. Polym. J.* 44 (4) (2008) 968–977.
- [45] J. Feng, J.W. Hao, J.X. Du, R.J. Yang, Effects of organoclay modifiers o the flammability, thermal and mechanical properties of polycarbonate nanocomposites filled with a phosphate and organoclays, *Polym. Degrad. Stab.* 97 (1) (2012) 108–117.
- [46] J.J. Luo, I.M. Daniel, Characterization and modeling of mechanical behavior of polymer/clay nanocomposites, *Compos. Sci. Technol.* 63 (2003) 1607–1616.
- [47] F.R. Passador, A. Rodolfo Jr., L.A. Pessan, Estado de mistura e dispersão da fase borrachosa em blendas PVC/NBR, *Polímeros: Ciência e Tecnologia* 16 (3) (2006) 174–181.
- [48] L.A. Utracki, *Polymer Alloys and Blends: Thermodynamics and Rheology*, Hanser Publishers, New York, (1989).
- [49] K. Chrissopoulou, I. Altintzi, S.H. Anastasiadis, E.P. Giannelis, M. Pitsikalis, N. Hadjichristidis, N. Theophilou, Controlling the miscibility of polyethylene/layered silicate nanocomposites by altering the polymer/surface interactions, *Polymer* 46 (26) (2005) 12440–12451.
- [50] E. Jacquemet, E. Espuche, J.-F. Gérard, J. Duchet, P. Mazabraud, Morphology and gas barrier properties of polyethylene-based nanocomposites, *J. Polym. Sci. B* 44 (2) (2006) 431–440.
- [51] A. Durmus, M. Woo, A. Kaşgöz, C.W. Macosko, M. Tsapatsis, Intercalated linear low density polyethylene (LLDPE)/clay nanocomposites prepared with oxidized polyethylene as a new type compatibilizer: structural mechanical and barrier properties, *Eur. Polym. J.* 43 (9) (2007) 3737–3749.
- [52] M. Zanetti, L. Costa, Preparation and combustion of polymer/layered silicate nanocomposites based upon PE and EVA, *Polymer* 45 (13) (2004) 4367–4373.

- [53] T.G. Gopakumar, J.A. Lee, M. Kontopoulou, J.S. Parent, Influence of clay exfoliation on the physical properties of montmorillonite/polyethylene composites, *Polymer* 43 (20) (2002) 5483–5491.
- [54] J. Morawiec, A. Pawlak, M. Slouf, A. Galeski, E. Piorkowska, N. Krasnikowa, Preparation and properties of compatibilized LDPE/organo-modified montmorillonite nanocomposites, *Eur. Polym. J.* 41 (5) (2005) 1115–1122.
- [55] S.H. Ryu, Y.W. Chang, Factors affecting the dispersion of montmorillonite in LLDPE nanocomposite, *Polym. Bull.* 55 (5) (2005) 385–392.
- [56] M.W. Spencer, L. Cui, Y. Yoo, D.R. Paul, Morphology and properties of nanocomposites based on HDPE/HDPE-g-MA blends, *Polymer* 51 (5) (2010) 1056–1070.
- [57] H.A. Patel, G.V. Joshi, R.R. Pawar, H.C. Bajaj, R.V. Jasra, Mechanical and thermal properties of polypropylene nanocomposite using organically modified Indian bentonite, *Polym. Comp.* 31 (2010) 399–404.
- [58] M. Okamoto, P.H. Nam, P. Manti, T. Kotaka, N. Hasegawa, A. Usukli, A house of cards structure in polypropylene/clay nanocomposites under elongational flow, *Nano Lett.* 1 (2001) 295–298.
- [59] F. Bellucci, A. Terenzi, A. Leuteritz, D. Pospielch, A. Franche, G. Traverso, G. Camino, Intercalation degree in PP/organoclay nanocomposites: role of surfactant structure, *Polymer Adv. Tech.* 19 (6) (2008) 547–555.
- [60] Y. Dong, D. Bhattacharyya, Effects of clay type, clay/compatibiliser content and matrix viscosity on the mechanical properties of polypropylene/organoclay nanocomposites, *Compos. Part A Appl. Sci. Manuf.* 39 (7) (2008) 1177–1191.
- [61] J. Comyn, *Polymer Permeability*, Elsevier Applied Science Publishers, London, (1998).
- [62] J.H. Lee, D. Jung, C.E. Hong, K.Y. Rhee, S.G. Advani, Properties of polyethylene-layered silicate nanocomposites prepared by melt intercalation with PP-g-MA compatibilizer, *Compos. Sci. Technol.* 65 (13) (2005) 1996–2002.
- [63] M. Kato, N. Okamoto, A. Hasegawa, A. Tsukigase, A. Usuki, Preparation and properties of polyethylene-clay hybrids, *Polym. Eng. Sci.* 43 (6) (2003) 1312–1316.
- [64] A.R. Morales, C.V.M. Cruz, L. Peres, E.N. Ito, Nanocomposites de PEAD/PEBDL—Avaliação da esfoliação da argila organofílica pela aplicação do modelo de Nielsen e das propriedades mecânicas, ópticas e permeabilidade, *Polímeros: Ciência e Tecnologia* 20 (1) (2010) 39–45.
- [65] L.E. Nielsen, Models for the permeability of filled polymers systems, *J. Macromol. Sci. Chem.* 1 (5) (1967) 929–942.

# Mathematical Fundamentals of Nanotechnology

R. Marchiori

*INTERDISCIPLINARY DEPARTMENT OF SCIENCE AND TECHNOLOGY, FEDERAL UNIVERSITY  
OF RONDÔNIA, ARIQUEMES, RONDÔNIA, BRAZIL*

## CHAPTER OUTLINE

<b>8.1</b>	<b>Introduction .....</b>	<b>209</b>
<b>8.2</b>	<b>Classical Mechanics .....</b>	<b>211</b>
8.2.1	The Classical Formalism at the Nanometric Scale.....	211
<b>8.3</b>	<b>Quantum Mechanics .....</b>	<b>212</b>
8.3.1	The Energy of Quantum Systems—Stationary Conditions .....	212
8.3.2	Periodic Structure of a Crystal Lattice—The Bloch Theorem.....	213
8.3.3	Crystal Lattice and Reciprocal Lattice .....	215
8.3.4	Electronic Structure.....	216
8.3.5	Graphene.....	219
8.3.6	Carbon Nanotubes .....	221
	<b>List of Symbols .....</b>	<b>230</b>
	<b>References .....</b>	<b>231</b>

## 8.1 Introduction

Classical mechanics, with its deterministic description of the behavior of matter, does not provide the correct mathematical structure to describe the physics and molecular interactions of matter at the atomic level. This representation is an average of a sufficiently large number of molecular interactions that is valid at the macroscopic scale. At the microscopic level, the laws of physics that describe the interactions between atoms, molecules, or nanoparticles can no longer be described by the deterministic laws of classical mechanics because they require a more appropriate description, which is offered by the mathematical formalism of quantum mechanics. This formalism modifies the deterministic perspective from the classical description to a probabilistic perspective of the behavior of matter. In the mathematical construction of quantum mechanics, time and space are interconnected, which is different from classical mechanics, in which they are independent.

In the space-time universe of quantum mechanics, this interdependence between the spatial and temporal dimensions has drastic consequences in the interpretation of reality at the atomic level [1,2]. The laws of quantum physics deviate from those that we are accustomed to observing, which thereby conflicts with intuitive comprehension and provides an extremely unconventional description of reality [3].

Several theories consider that quantum mechanics is also valid at a macroscopic scale, but the direct interaction of the observer with the object, which occurs at this scale, causes the “collapse” of the possible energetic configurations of the object into a specifically determined configuration, which represents the highest probability configuration. Thus, any object, such as the Moon, is visible and exists where we see it because we are looking at it. If that was not the case, the speculations of some quantum physicists would lead to the determination that it is not there and that it occupies all possible energetic configurations with some probability; that is, any position within space-time in the universe!

The essential characteristic in the advent of nanotechnology around 1985 was the development of knowledge and technology that allowed us to manipulate and analyze physical phenomena and material properties at the atomic scale, which made it possible to access knowledge about material properties based on interactions between particles at the nanometric scale. At this scale, which is the order of magnitude of interatomic distances, the energy levels that are accessible to a physical system are no longer continuous as in classical mechanics, in which energy can assume any value in a continuous manner. At the nanometric scale, wave-particle duality is manifest, which causes the discretization of energy. In other words, energy can acquire only specific, discrete values to respect the boundary conditions that emerge from the wave nature of matter; these conditions exclude certain configurations of the system and, consequently, certain relative energy values because the system is defined by atomic or molecular interactions. Thus, the mathematical formalism of quantum mechanics is needed to calculate the energy of the system at this scale.

At the nanometric scale, the classical formalism becomes an approximation that loses validity. To handle nanomaterials such as carbon nanotubes or graphene, which are currently the nanostructured materials with the greatest potential for use, quantum mechanics provides the mathematical background that describes the energy levels that are accessible to these materials.

When a material has properties due to its nanometric-scale structure and morphology, quantum theory is the only theory that can appropriately describe these properties, which indicates that the wave behavior of elementary particles becomes important at this scale. This behavior is described directly by the de Broglie equation,  $\lambda = h/p$ , which shows the dual wave-particle character of matter by relating the momentum  $p$ , which is a classical property that is directly proportional to the mass and velocity of the particle, to the wave property of matter, which is given by the corresponding wavelength  $\lambda$ , and Planck's constant  $h$  is the proportionality factor. The wavelength  $\lambda$  only assumes detectable values for extremely small masses, such as in the case of elementary particles and nanostructured materials.

Boundary conditions can be used to maintain a physical system in equilibrium at the nanometric scale; these conditions are related to the characteristics of the material and determine its electrical, optical, and other properties.

Therefore, quantum mechanics must be used in nanotechnology and can be summarized in the following essential points:

- The nanometric scale, which is on the order of the size of an atom, involves the wave behavior of matter and requires the use of a wave function in the Schrödinger equation to describe the movement of a particle at this scale.
- The interaction of particles with matter at the nanoscale, such as the movement of an electron in electrical conduction by a nanostructured material, is limited by the boundary conditions. These conditions limit particle movement in the crystal lattice of the material, which forces the electrons into trajectories that are defined by the periodic interaction potential of the Bravais lattice of the material. This determines the discretization of the energy, whose possible levels are calculated by the mathematical formalism of quantum mechanics.

## 8.2 Classical Mechanics

### 8.2.1 The Classical Formalism at the Nanometric Scale

Particle dynamics can be represented from the classical formalism that describes the dynamics of a physical system. However, the particles of microscopic systems follow wave movement laws; that is, at the nanometric scale, elementary particles behave like waves, and their description requires the introduction of a wave function  $\psi(r,t)$  to describe their movement.

In general, the function  $\psi(q)$  is a complex function, with  $q = (q_1, q_2, \dots, q_n)$  being the generalized coordinates that represent the “state” of a dynamic system with  $n$  degrees of freedom. Due to the objectives of this chapter, a more extensive formalism of a quantum system will not be addressed. This chapter will only cover the aspects that are necessary to understand the relationship between quantum mechanics and nanotechnology.

In general, the evolution of a system, such as the simplest case of a particle, must be consistent with the mechanics equation [4,5]:

$$E = p^2/2m + V \quad (8.1)$$

which represents the energy  $E$  of a particle of mass  $m$  and momentum  $p$  as a function of the kinetic energy  $p^2/2m$  and the potential energy  $V$ . The quantum mechanics equation that corresponds to Eq. 8.1 and involves the wave function will also have to satisfy the postulates of Einstein (1905), de Broglie (1921), and de Jammer (1966), (1974) [4,6–8]:

$$E = \hbar\nu = \hbar\omega \quad \text{and} \quad p = \hbar k \quad (8.2)$$

and be valid for wave movement, which can be written in the form:

$$\hbar\omega = \hbar^2 k^2 / 2m + V(x,t) \quad (8.3)$$

where  $\hbar = h/2\pi$ .

A general mathematical procedure is available to handle the behavior of any microscopic system of particles: the Schrödinger theory of quantum mechanics [9–14].

## 8.3 Quantum Mechanics

The Schrödinger theory is based, among others phenomenological processes, on the laws of wave movement to express the space-time position of elementary particles in terms of probability, which the particles of any microscopic system obey; when this description is required, the system is called a quantum system.

A wave function  $\Psi(r,t)$  for the general three-dimensional case of propagation with time  $t$  in the direction  $r$  can be represented using a sine wave [10]:

$$\Psi(r,t) = \sin 2\pi \left( \frac{r}{\lambda} - v \cdot t \right) \quad (8.4)$$

where  $\Psi(r,t)$  is the wave function,  $\lambda$  is the wavelength, and  $v$  is the oscillation frequency. To write the wave function more easily, the following variables are introduced:  $k = 2\pi/\lambda$  and  $\omega = 2\pi v$ , where  $k$  is the angular wave number, and  $\omega$  is the angular oscillation frequency. The wave function then becomes:

$$\Psi(r,t) = \sin(kr - \omega t) \quad (8.5)$$

The Schrödinger equation must also satisfy the linearity in  $\Psi(r,t)$ , which guarantees that wave functions can produce the constructive and destructive interferences that are characteristic of wave behavior. Remember that because the Schrödinger equation [9] is consistent with Eq. 8.1, it is not valid when it is applied to particles with relativistic velocities. In the case of a free particle, a potential function must satisfy the condition:

$$V(r,t) = V_0 = \text{const.} \quad (8.6)$$

This guarantees that no force is applied to the particle because the force  $F$  is equal to:

$$F = -\frac{\partial V(r,t)}{\partial x} = 0. \quad (8.7)$$

These conditions and concepts form the basis of the description of particles in matter and, in particular, the behavior of elementary particles, such as electrons in the crystal lattice of a material.

### 8.3.1 The Energy of Quantum Systems—Stationary Conditions

To describe the properties of nanostructured materials, it is necessary to obtain the eigenvalues of the energy of the system [9–14]. The Hamiltonian formulation of the time-independent Schrödinger equation is used to find the eigenvalues for the energy of a quantum system, as is shown in the example with carbon nanotubes at the end of this chapter. The

majority of atomic and molecular systems show time-independent conditions; this means that the potential energy does not depend explicitly on time, or  $V(r,t) \equiv V(r)$ . Under these conditions, the wave function in Eq. 8.4 can be written by separating the variables:

$$\Psi(r,t) = \psi(r) \cdot \varphi(t) \quad (8.8)$$

Thus, the Hamiltonian formulation of the time-independent Schrödinger equation is [10]:

$$\hat{H}\psi(r) \equiv H(\hat{q}^0, \hat{p}^0)\psi(r) = E\psi(r) \quad (8.9)$$

where  $\hat{H}$  is the Hamiltonian operator that is used in the quantum formalism, and  $\hat{q}^0$  and  $\hat{p}^0$  are the sets of operators that express the position and velocity of the particle, respectively. Acceptable solutions for this equation exist only for specific energy values  $E$ , which are called the eigenvalues of the potential energy  $V(r)$  that is generated by the crystal lattice of the system. An eigenfunction  $\psi(r)$  for the energy corresponds to each eigenvalue; using the Bohr interpretation, these eigenfunctions are wave functions whose energy is the energy of the stationary states of the system. The quantization of energy [10,11,13] emerges naturally in the Schrödinger theory due to the wave nature of matter. Only certain discrete energy values, which are obtained from the time-independent Schrödinger equation, permit solutions for the wave function. Considering the discrete set of eigenvalues  $E_i$  of the system, the Schrödinger equation can be written as [10]:

$$\hat{H}\psi_i(r) = E_i\psi_i(r) \quad (8.10)$$

This equation allows one to obtain the eigenvalues for the energy of the system and is used for stable molecular aggregates at the nanometric scale. The analysis of the solutions to this equation provides information about the mechanical, thermal, and electrical properties of these nanomolecules, as is shown in the following paragraphs.

### 8.3.2 Periodic Structure of a Crystal Lattice—The Bloch Theorem

The main nanomolecules that are studied and used in nanotechnology applications have periodic structures due to their crystal lattice; therefore, the interaction potential of the electrons in the molecule is of the type [15,16]:

$$V(\vec{r}) = V(\vec{r} + \vec{R}) \quad (8.11)$$

where  $\vec{R}$  is the vector that represents the interatomic distance in the molecule. The vector notation that is used here is necessary to describe the crystal lattice of these nanomolecules. The electrons of these molecules occupy discrete energy states that are defined through quantum mechanics by the presence of a periodic potential that is related to the crystal structure of the nanomolecule. To find the eigenvalues of the energy of the wave functions of the electrons, appropriate approximations are used to simplify the problem without significantly altering the description of the system. This allows these molecular systems to be studied using various mathematical modeling techniques, such as the “tight

binding" (TB) approximation. When this approximation is applied to the method known as the "linear combination of atomic orbitals" (LCAO), the monoelectronic states in a crystal approximately maintain their atomic behavior because the interactions between the electronic states of the neighboring atoms are relatively small and thus only represent system perturbations. In this approximation, the Hamiltonian operator  $H$  is equal to [17]:

$$H = H_{\text{atom}} + H_{\text{crystal}} \approx H_{\text{atom}} \quad (8.12)$$

This operator results from the interaction of the atom with the electron ( $H_{\text{atom}}$ ) and the effect due to the interaction with the crystal ( $H_{\text{crystal}}$ ), which is considered to be a perturbation; thus, the eigenfunction  $\psi(\vec{r})$  of the electron becomes the eigenfunction of  $H_{\text{atom}}$  with the eigenvalue  $E_0$ . The reason for this is that these valence electrons are found in deep potential wells that are generated by the crystal lattice of the molecule and do not have the properties of free electrons. In other words, the potential energy that acts on the electrons due to the interaction with other electrons is much smaller than the atomic energy potential in the crystal lattice (Bravais lattice). Therefore, the Hamiltonian operator assumes the following form [18]:

$$\hat{H} \approx \sum_i \hat{T}_i + \sum_R \hat{V}(\vec{r} - \vec{R}) \quad (8.13)$$

where  $\hat{T}_i$  is the kinetic energy operator for all of the electrons  $e_i$ , and  $\hat{V}(\vec{r} - \vec{R})$  is the complete potential of the crystal lattice at the atomic site  $\vec{R}$ . The wave function  $\psi(r)$  of the electron in the crystal lattice for a defined value of the wave vector  $\vec{k}$  is:

$$\psi_k(r) = \sum_R C_{kR} \varphi(\vec{r} - \vec{R}) \quad (8.14)$$

in which the positions  $\vec{R}$  of the sites that are occupied by the atoms determine the periodicity of the Bravais lattice. The wave vector  $\vec{k}$  has the direction and orientation of the wave propagation and the magnitude  $|k| = 1/\lambda$ . The wave function  $\varphi(\vec{r} - \vec{R})$  describes the electron that is close to the atomic site in  $\vec{R}$ . The sum is extended to all of the sites of the crystal lattice, so this is a LCAO. The coefficient  $C_{kR}$  is obtained from the Bloch theorem, which allows the expression of the eigenfunction of the electron in the periodic potential of the crystal lattice. The probability density of the wave function  $\varphi(\vec{r})$  of the electron in the periodic potential is also periodic and is equal to:

$$|\varphi(\vec{r} + \vec{R})|^2 = |\varphi(\vec{r})|^2 \quad (8.15)$$

Using the normalization of the electronic distribution in the unit cell, it is equal to:

$$\int |\varphi(\vec{r} + \vec{R})|^2 dV = \int |\varphi(\vec{r})|^2 dV = 1 \quad (8.16)$$

Rewriting Eq. 8.16 yields the Bloch theorem [17]:

$$\varphi_k(\vec{r} + \vec{R}) = e^{ikR} \varphi_k(\vec{r}) \quad (8.17)$$

This equation represents the boundary conditions for solutions to the Schrödinger equation for a periodic potential. In this case, the eigenfunction of the electron in the Hamiltonian can be written in the form of a plane wave  $e^{ikR}$  with the periodicity of the Bravais lattice multiplied by the wave function  $\varphi_k(\vec{r})$ . In Eq. 8.14 for the wave function of the electron in the crystal lattice, the coefficients  $C_{kR}$  can be written as:

$$C_{kR} = N^{-1/2} e^{ikR} \quad (8.18)$$

where  $N$  is the number of atoms in the crystal. This term is used because the crystal is finite, which determines the finite number of translation vectors of the Bravais lattice, which consists of  $N = N_x N_y N_z$  unit cells.

The normalization condition of the wave function in the expression of the density in the occupied space determines the application of the square root of the number of atoms  $N$  in the crystal (Eq. 8.18). Thus, Eq. 8.18 becomes:

$$\Psi_k(\vec{r}) = N^{-1/2} \sum R e^{ikR} \varphi(\vec{r} - \vec{R}) \quad (8.19)$$

### 8.3.3 Crystal Lattice and Reciprocal Lattice

The crystalline structure of a material can be accurately represented by considering only the electrons around it, which allows the formation of an indirect microscopic image of the material. Because electrons behave as waves, they can suffer reflections due to the periodicity of the crystal lattice of the material; these reflections are called Bragg reflections. The discussion of Bragg reflections leads to the notions of a “reciprocal lattice” or “reciprocal space” and “Brillouin zones.” The study of X-ray diffractions that are generated by the crystal lattices of materials permits the acquisition of crystal lattice parameters from the diffraction angles  $\theta$ , which form a spectrum of lines that correspond to the constructive interference of the incident rays. The reflection of the incident X-rays that is defined by Bragg's law is shown in Fig. 8.1 [19,20]:

$$2d \sin \theta = n\lambda \quad (8.20)$$

where  $d$  is the distance between two parallel atomic planes,  $n$  is a positive whole number, and  $\lambda$  is the wavelength of the incident electromagnetic wave. Bragg's law provides the conditions for the occurrence of constructive interference of the waves that are scattered by point charges at points in the lattice, which permits the calculation of the lattice

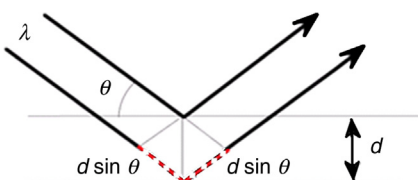


FIGURE 8.1 Reflection of X-ray radiation that is incident on the atomic planes of a material that are separated by a distance  $d$ .

parameters, or the spacing  $d$  between the crystal planes as a function of the diffraction angles  $\theta$ . If the path difference  $2d \sin\theta$  between two parallel rays is a multiple of the wavelength of the incident rays, the interference will be constructive.

To determine the intensity of each scattering that is produced by a spatial distribution of electrons within each cell of the crystal lattice, it is necessary to consider the numerical density of the electrons  $n(r)$  because the intensity of the incident light that is scattered by a volume element is proportional to this density. The electronic density is naturally periodic for the translation operation that is defined by the vector  $\vec{T}$  in the crystal lattice of the material. A diffraction figure of a crystal can be considered to be a representation of the reciprocal lattice of the crystal in contrast to the direct image of the real crystal lattice. Each crystal structure has two lattices: the crystal lattice and the reciprocal lattice. The concept of a reciprocal lattice is essential to describe nanomolecules, such as, carbon nanotubes or graphene. The definition of the vectors of the reciprocal lattice contributes to the calculation of the spectrum of eigenvalues of the energy of these nanostructures.

Using the concepts that will be discussed in the following paragraphs to define the “Brillouin zone,” it is possible to define the structure of the valence and conduction energy bands in nanostructures, the number of electrons that belong to the Brillouin zone and, thus, the occupation of these bands by electrons. These factors characterize the material as a conductor, semiconductor or insulator and describe the behavior of the material in the presence of external fields.

#### 8.3.3.1 Reciprocal Lattice

If  $\vec{a}_1$ ,  $\vec{a}_2$  and  $\vec{a}_3$  are primitive vectors of the crystal lattice, the translation vectors of the reciprocal lattice  $b_1$ ,  $b_2$ , and  $b_3$  must satisfy the condition [17]:

$$\vec{a}_i \cdot \vec{b}_j = 2\pi\delta_{ij} \quad (8.21)$$

where  $\delta_{ij}$  is the Kronecker delta ( $\delta = 1$  for  $i = j$ ,  $\delta = 0$  for  $i \neq j$ ). The unit cell of the reciprocal lattice, with all of its symmetry properties, is called the first Brillouin zone, and its points are the wave vectors  $\vec{k}$ .

#### 8.3.3.2 First Brillouin Zone

The Brillouin formulation is the most important diffraction condition for solid-state physics and is the only one that is used to describe the energy bands of electrons in addition to expressing the elementary excitations in crystals. The first Brillouin zone is the unit cell of the reciprocal lattice; this provides a geometric interpretation of the diffraction condition that is generated by the crystal lattice of the material [17]. The boundaries of the Brillouin zone of the linear lattice in one dimension are at  $k = \pm \pi/a$ , where  $a$  is the parameter of the crystal lattice of the material.

### 8.3.4 Electronic Structure

As was already emphasized, a material’s electronic structure can be analyzed to study its properties and structure. This analysis of materials, primarily nanostructured materials,

is an area of theoretical investigation in which quantum mechanics is applied to describe the spatial distribution and energy levels of electrons that make up the studied system. Through the analysis of the density of states (DOS) of the electrons, the electronic structure determines the electrical conduction properties of the material, which define whether it is an electrical insulator, semiconductor, or conductor.

#### 8.3.4.1 Density of States—Discretization of Energy in Quantum Systems

The DOS is a property that is used extensively in quantum systems in condensed matter physics; it refers to the energy level of the electrons, photons, or phonons in a solid crystal. The electronic DOS quantifies how “packed” the electrons in a quantum mechanical system are in energy levels. The DOS can vary from zero for an energy level that is inaccessible to the electrons, with no space occupied by them, to a defined occupation value at a specific energy level that is accessible to the electrons of the material. There is a direct correlation between the concept of quantized energy levels that is described by quantum mechanics and the DOS. The DOS is an energetic configuration due to the wave property of matter. In some systems, the interatomic spacing, the crystal structure, and the atomic charge of the material only allow electrons of certain wavelengths to propagate in the system, which also limits the possible directions of wave propagations. Each wave occupies a different mode or state that can have the same wavelength or the same quantized energy levels. This determines the degeneracy of states with the same energy and the absence of states in other energies that are incompatible with the system in which no space is occupied by the system. In the case of electronic states, the DOS permits the calculation of the number of electrons for each energy level, and the diagram of these states defines the electrical conduction properties of a material. DOS is usually denoted with one of the symbols  $g$ ,  $\rho$ ,  $n$ , or  $N$ . If the DOS is the function  $g(E)$ , one can write the expression  $\Delta N = g(E) \cdot \Delta E$ , which represents the number of states  $\Delta N$  with energies between  $E$  and  $E + \Delta E$ . If the fundamental state is completely occupied by electrons (full valence band) and the first excited state overlaps the valence band (an electron-hole pair in the conduction band), the material will be a conductor. However, if the bands are separated by an excitation energy  $E_g$ , which is called a bandgap, the material will be an insulator or a semiconductor as shown in Fig. 8.2 for graphene. Thus, whether a material is an insulator or semiconductor depends

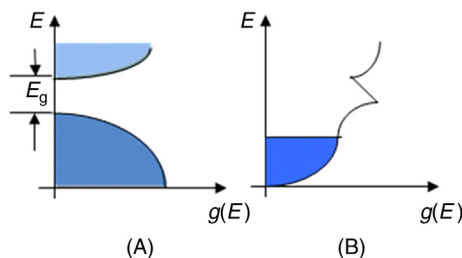


**FIGURE 8.2** Occupation density  $g(E)$  of the valence and conduction bands. (A) Semiconductor characteristics. (B) Metallic characteristics.

on the value of the energy gap  $E_g$  between the valence and conduction bands. In general, the bandgap  $E_g$  is on the order of eV ( $E_g \sim$  eV) for insulating materials and  $E_g \sim 10^{-1}$  eV for semiconductors. Several semiconducting materials, such as silicon, have a bandgap in another range of values ( $E_g \sim 1.1$  eV), and materials such as ZnO, GaN, and AlN have bandgaps of a few eV in the energy band that corresponds to ultraviolet radiation.

The Fermi energy is defined as the maximum energy value in the valence band that corresponds to the energy level of the last state that was occupied by the electrons in the material. The Fermi surface is the surface in the  $k$ -space that comprises the occupied electronic states. However, in the case of materials that are “doped” with other elements, other energy levels are accessible to the system, which modifies the conductive properties of the material. In the presence of defects and impurities in the material due to doping, there is a readjustment of the effective Fermi energy to a new energetic configuration that favors electronic conduction.

#### *8.3.4.2 Quantum Confinement of Electrons in the Volume of the Material*

In a quantum system under stationary conditions, the confinement of electrons limits its energy to certain specific “discrete” levels due to the confinement in the volume of the material, which excludes specific energy values. For example, this condition determines the electrical behavior of nanomaterials, such as graphene or carbon nanotubes, as will be explained in the following paragraphs.

Consider a material with the dimensions  $L_x$ ,  $L_y$ , and  $L_z$  and volume  $V = L_x L_y L_z$ . The stationary conditions of the system (Bloch theorem) require that the wave functions of the electrons belong to the crystal lattice of the material to respect the boundary conditions, which means that the electronic wave functions can only have certain wavelengths  $\lambda_n$  that correspond to the wave numbers  $k_n = 2\pi/\lambda_n$ . The potential of the electrons within the material does not depend on the location of the particle; that is, it is constant and can be considered null for ease of calculation.

Under these conditions, the energy levels of the electrons become “quantized” at discrete values depending on the values that are allowed by the wave vector  $\vec{k}$ :

$$E_n = \frac{p^2}{2m} = \frac{\hbar^2 k_n^2}{2m} \quad (8.22)$$

which is the solution for the eigenstates of the energy of the Schrödinger equation of the system. In the formalism of the quantum theory that uses the wave vector  $\vec{k}$  in the energy expression, the energy of the electrons is  $E = (\hbar k)^2/2m$ , and the energy of the photons is  $E = \hbar c k$ . The periodic wave function  $\psi(x)$  of the electrons, which is expressed by a sin function of the type  $\psi(x) = A \sin(2\pi x/\lambda)$ , will have to respect the boundary conditions of the system, which is the condition  $\psi(x) = \psi(0) = \psi(L) = 0$  due to the confinement of electrons in the material. The stationary oscillations of the system are represented in Fig. 8.3, where  $n$  is the order of oscillation of the wave function of the electron and  $L$  is the distance between the walls. For  $n = 1$ , the wavelength is double the size of the material, and it changes phase at the edges to respect the stationary condition;  $n = 2$  represents  $\lambda = L$ .

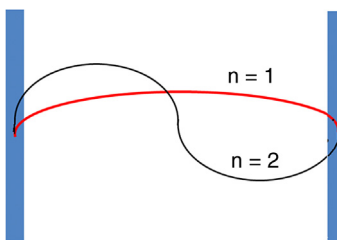


**FIGURE 8.3** Quantum confinement condition of electrons with the resulting definition of the discrete energy values  $E_n$ .

Only certain oscillations of the specific wavelengths  $\lambda_n$  can respect the boundary conditions with the resulting discretization of the energy at defined values.

For  $\psi(L) = A \cdot \sin(2\pi L/\lambda) = 0$  and  $2\pi L/\lambda = n\pi$ , the resulting values of  $\lambda_n$  are therefore  $\lambda_n = 2L/n$  and  $k_n = 2\pi/\lambda_n = n\pi/L$ . Eq. (8.22) therefore becomes:

$$E_n = \frac{p^2}{2m} = \frac{\hbar^2(k_n)^2}{2m} = \frac{\hbar^2(n\pi)^2}{2m(L)^2} \quad (8.23)$$

The quantum confinement of electrons in atoms and molecules is due to the stable and stationary condition of electrons in the atomic and molecular orbitals. The theory that describes the electronic density around nuclei in a material finds an important simplification in the description of molecular orbitals in the LCAO.

The DOS leads to the concept of a “fundamental state,” which is the lowest energy state of a system that contains  $N$  electrons without any type of interaction. This state is filled by the electrons of the system from the lowest energy until it is occupied by the last electron for the molecular orbital with the lowest possible energy. These orbitals represent the states that are accessible to the quantum system due to the crystal lattice, charges, and other factors. The structure of the molecular orbitals and the corresponding energies will be discussed in the following chapters. The set of orbitals that correspond to each energy level of the system determines the formation of bands of energy, the valence band and the conduction band.

### 8.3.5 Graphene

As an application of the concepts that were introduced in the previous paragraphs, the molecular structure of graphene is shown in real space and in reciprocal space (Fig. 8.4B) to determine the band structure that defines the electronic behavior of graphene. The Brillouin zone for graphene can be defined as the rhombus that is formed by the lattice vectors of the reciprocal space  $\vec{b}_1$  and  $\vec{b}_2$ .

#### 8.3.5.1 Electronic Structure of Graphene

The electronic structure of a graphene molecule that is defined by the LCAO theory is composed of a valence band and a conduction band. Fig. 8.5 shows the structure of the valence and conduction bands that are occupied by the electrons as calculated using the TB

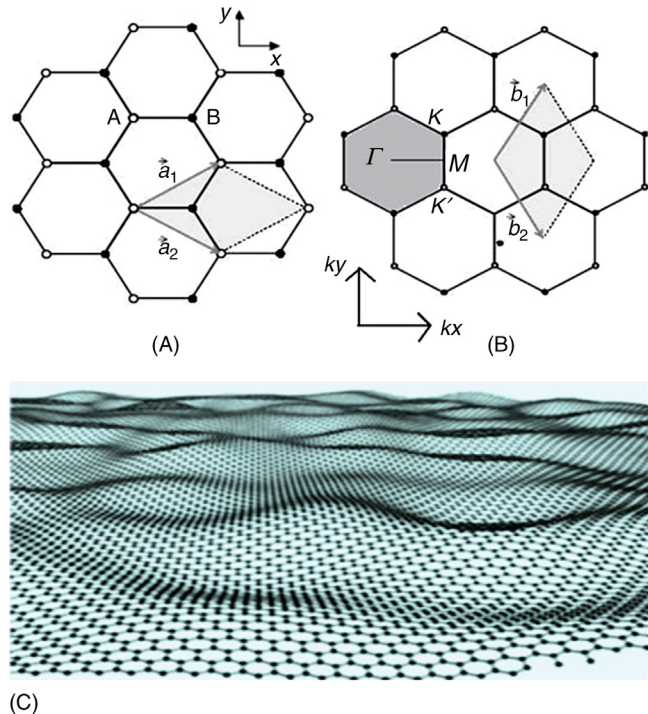


**FIGURE 8.4** (A) Graphene's structure in real space. The rhombus represents the unit cell of graphene and is delimited by the network vectors  $\vec{a}_1$  and  $\vec{a}_2$ . This area involves two atoms, which are indicated as A and B. (B) Graphene structure in reciprocal space showing the unit vectors  $\vec{b}_1$  and  $\vec{b}_2$  and the Brillouin zone that is delimited by them. The shaded hexagon shows the Brillouin zone that is considered because it represents all of the symmetry operations of the unit cell of graphene [21]. (C) Representation of a graphene sheet.

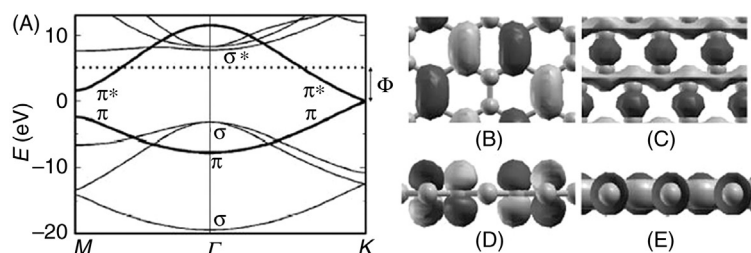


**FIGURE 8.5** Electronic properties of graphene. (A) Structure of the electronic bands: band  $\pi$  (last occupied band) and band  $\pi^*$  (conduction band, first unoccupied) touch each other at the  $K$  points of the first Brillouin zone. The Fermi energy is set to zero. (B) and (D) Electronic configuration of  $\pi$  states at the  $K$  points in bonding orbitals. (C) and (E)  $\sigma$  states at  $\Gamma$  points far from the Fermi energy that are occupied by the electrons of the graphitic  $sp_2$  bonds plan [23].

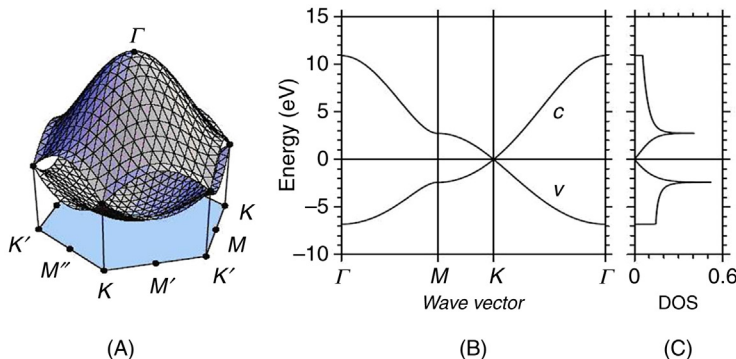


**FIGURE 8.6** (A) Diagram showing the conduction and valence bands in the first Brillouin zone of hexagonal graphene [21]. The points of high symmetry  $\Gamma$ ,  $K$ ,  $K'$ ,  $M$ ,  $M'$ , and  $M''$  are shown in the hexagonal projection. (B) Valence and conduction bands in the high-symmetry directions  $\Gamma K$ ,  $K M$ , and  $M \Gamma$  of the Brillouin zone of graphene. (C) Density of states (DOS) of graphene [23].

approximation and the corresponding electron cloud in the  $\pi$  valence orbitals (bonding) and  $\pi^*$  conduction orbitals (antibonding). These bands determine the electrical conduction properties of graphene as shown in the DOS diagram for graphene (Fig. 8.5C). The  $\pi$  and  $\pi^*$  bands that are shown in Fig. 8.5A are also shown in three dimensions in Fig. 8.6A. These bands are close to the Fermi energy level at points of high symmetry in the Brillouin zone of graphene (points  $K$ ,  $K'$ ,  $\Gamma$  and  $M$  in Figs. 8.4A–B and 8.5). These points are due to the symmetry of the hexagonal structure of graphene and represent special conditions in the description of the electrical properties of graphene [22].

The valence and conduction bands degenerate at the points  $K$  and  $K'$  of the reciprocal space, which are found at the Fermi level (Fig. 8.6C), which determines the electrical conduction properties of graphene. The energy gap between the valence and conduction bands is zero, which characterizes graphene as a zero-gap semimetallic material.

### 8.3.6 Carbon Nanotubes

#### 8.3.6.1 Structure of Carbon Nanotubes

Carbon nanotubes [24] can be considered as one or several sheets of graphene that are rolled into a perfect cylinder [25,26]. The size of these materials is on the order of magnitude of an atom [diameters from 0.7–2 nm for single-walled carbon nanotubes (SWNTs) to 10 nm for multiwalled carbon nanotubes (MWNTs)]. Quantum mechanics is used to describe these nanomolecules because the movement of electrons is “confined” in the direction of the circumference of the nanotubes in a very limited number of configurations to respect the stationary conditions of the wave functions as was explained in the preceding paragraphs. A continuous number of electronic states is permitted in the direction of the tube’s length because the length of the tube is much greater than the wavelength of the electronic wave functions. Placing the permitted values for the wave vector  $\vec{k}$  in the first Brillouin zone of graphene generates a series of parallel lines called “cutting lines.” The length, number, and orientation of these lines depend on the chiral indices ( $n, m$ ) of the nanotubes,

which are called “chiral vectors.” For many properties, the carbon nanotube can be considered as a unidimensional crystal with a translation vector  $\vec{T}$  along its main axis and a small number of carbon atoms on its circumference. The structure of a carbon nanotube can be determined unambiguously by the chiral vector  $\vec{C}_h$  (Fig. 8.7A), which, when rolling the graphene sheet, coincides with the circumference of the nanotube. The chiral vector can be written as a function of the lattice vectors  $\vec{a}_1$  and  $\vec{a}_2$  of graphene as follow:

$$\vec{C}_h = n\vec{a}_1 + m\vec{a}_2 \quad (8.24)$$

### 8.3.6.2 Lattice Vectors in Real Space

To specify the symmetry properties of carbon nanotubes as a 1D system, it is necessary to express the lattice vector, which is the translation vector  $\vec{T}$  (Fig. 8.7) that has the direction of the primary axis of the nanotube. The translation vector  $\vec{T}$  of a nanotube can be written as a function of  $n$  and  $m$  as  $\vec{T} = t_1\vec{a}_1 + t_2\vec{a}_2$ , where  $t_1 = (2m+n)/d_R$ , and  $t_2 = (2n+m)/d_R$ . The length of the translation vector is  $\vec{T} = \sqrt{3}\vec{C}_h/d_R$ , where  $d_R$  is the maximum common divisor of  $(2n+m, 2m+n)$ . By defining  $d$  as the greatest common divisor of  $(n, m)$ , the values of  $d$  and  $d_R$  are related by [28]:

$$d_R = \begin{cases} d & \text{if } (n-m) \text{ is not a multiple of } 3d \\ 3d & \text{if } (n-m) \text{ is a multiple of } 3d \end{cases} \quad (8.25)$$

For the nanotube (6, 2) that is shown in Fig. 8.7,  $d_R = d = 2$ , and  $(t_1, t_2) = (5, 7)$ . For achiral zigzag and armchair nanotubes,  $T = \sqrt{3}a$  and  $T = a$ , respectively. The area of the unit cell of the nanotube can be found by calculating the vector product of the two vectors  $\vec{T}$  and  $\vec{C}_h$ ,  $|\vec{C}_h \times \vec{T}| = \sqrt{3}a^2(n^2 + nm + m^2)/d_R$ . Dividing this value by the area of the unit cell of graphene  $|\vec{a}_1 \times \vec{a}_2| = \sqrt{3}a^2/2$  results in the number of hexagons in the unit cell of the nanotube:

$$N = \frac{2(n^2 + nm + m^2)}{d_R} \quad (8.26)$$

In the case of nanotube (6, 2),  $N$  is equal to 26, so the unit cell of this nanotube has 52 carbon atoms because there are two carbon atoms in the unit cell of graphene. For achiral nanotubes,  $N = 2n$ .

### 8.3.6.3 Application of Quantum Theory to Carbon Nanotubes

The description of carbon nanotubes is based on the analysis of graphene, whose electrons make strong covalent  $\sigma$ -type bonds along the graphitic plane that do not significantly affect the electronic properties of the nanotubes because they are far from the Fermi energy. The electrons that occupy the  $p_z$  atomic orbitals, which are perpendicular to the planes, interact with the  $p_z$  orbitals of neighboring atoms and generate weak interactions with the creation of  $\pi$  bonding molecular orbitals and antibonding  $\pi^*$  molecular orbitals. The bond energy of these orbitals is close to the Fermi energy in the first Brillouin zone and

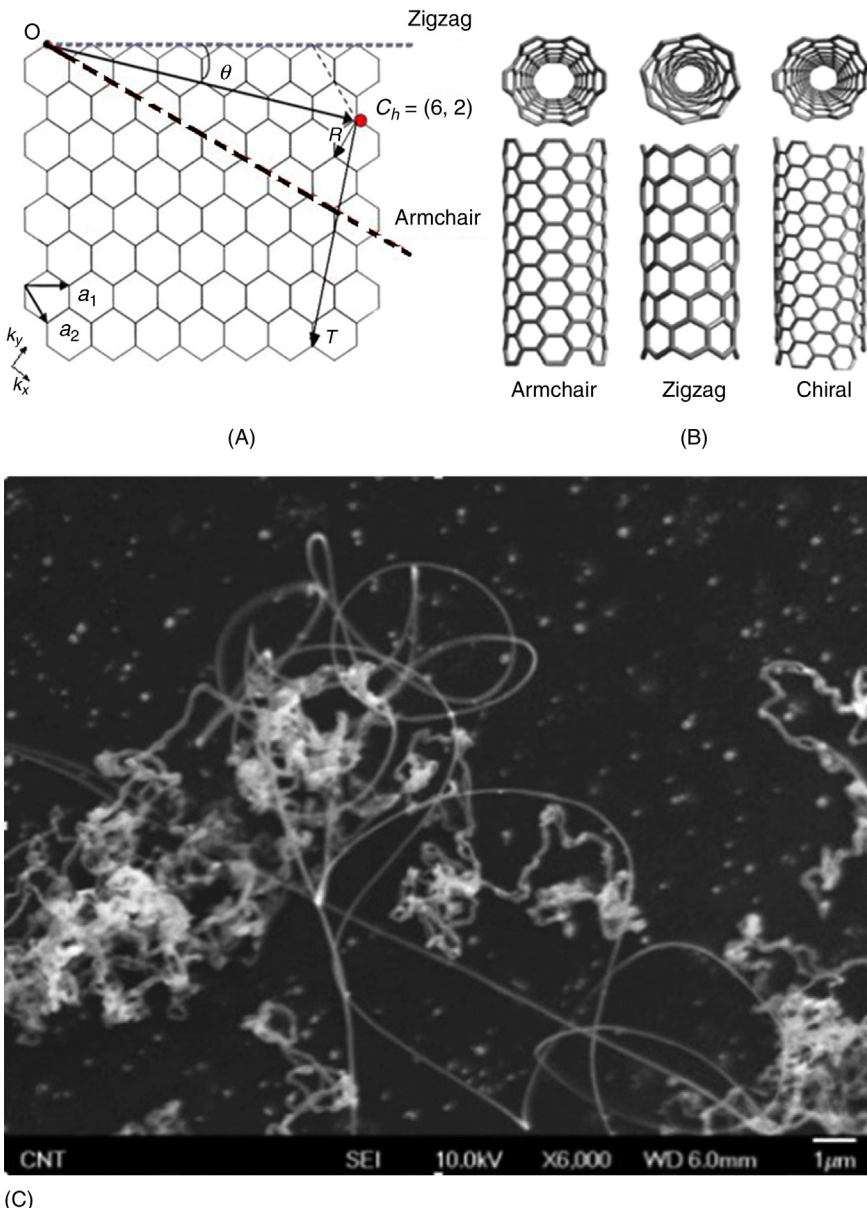


**FIGURE 8.7** (A) Projection of an open nanotube on a graphene layer. When the graphene sheet is closed to form a nanotube, the chiral vector  $\vec{C}_h$  becomes the circumference of the cylinder (nanotube), and the translation vector  $\vec{T}$  is aligned parallel to the nanotube's axis. The vector  $\vec{R}$  is the vector of symmetry,  $\theta$  indicates the chiral angle, and  $\vec{a}_1$  and  $\vec{a}_2$  are the unit vectors of graphene. The unit cell of the nanotube is defined by the rectangle that is defined by the two vectors  $\vec{C}_h$  and  $\vec{T}$ . (B) Helical arrangement in achiral and chiral nanotubes. (C) FEG microscopy image of carbon nanotubes [27].

is responsible for the weak interaction between the SWNTs in bundles in the same manner that it acts in graphite to generate weak bonds between the planes. The relatively simple Hamiltonian formalism is normally used to describe the  $\pi$  and  $\pi^*$  electronic bands, which is known as the TB approximation.

#### 8.3.6.4 Application of the TB Model

By applying the TB formalism to carbon nanotubes [18], it is possible to write the Bloch states for the  $p_z$  orbital of the electron in each carbon atom in the Brillouin zone of graphene. Rewriting Eq. 8.10 yields:

$$\psi_k^A(r) = \frac{1}{(N)^{1/2}} \sum_{R_A} \exp(i\mathbf{k} \cdot \mathbf{R}_A) \chi(r - \mathbf{R}_A) \quad (8.27)$$

and

$$\psi_k^B(r) = \frac{1}{(N)^{1/2}} \sum_{R_B} \exp(i\mathbf{k} \cdot \mathbf{R}_B) \chi(r - \mathbf{R}_B) \quad (8.28)$$

The A and B indices refer to the two carbon atoms that occupy the primitive cell. The sums are extended to all of the sites of the crystal lattice in relation to the position of the electron in A, where the wave function is a linear combination of the wave functions relative to the atomic sites, which also applies to the electron of atom B.  $\chi(r)$  represents the wave function of the  $p_z$  atomic orbital normalized to an isolated atom, while the wave function of the electron in the main cell is the linear combination of the wave functions for each atom:

$$\Psi = \psi_k^A(r) + \lambda \psi_k^B(r) \quad (8.29)$$

Considering the general expression for the Hamiltonian operator [10]:

$$H_{\mu\nu}(k) = \int \Psi^\mu(k, r) \hat{H} \Psi^\nu(k, r) d^3r \quad (8.30)$$

substituting Eq. 8.29 into  $H\Psi = E\Psi$  (Eq. 8.9) [10], the following components are obtained:

$$H_{AA} + \lambda H_{AB} = E \quad (8.31)$$

$$H_{BA} + \lambda H_{BB} = \lambda E \quad (8.32)$$

The coefficient  $\lambda$  is eliminated using the variational principle [29], which obtains the most appropriate eigenvalues for the energy. The  $H_{ii}$  terms are:

$$H_{AA} = H_{BB} = \alpha \quad (8.33)$$

With the parameter  $\alpha$  that is defined from the expression for the Hamiltonian that is valid in the TB approximation:

$$\alpha(r) = \int |\chi_\mu(r)|^2 \left[ \sum_{R \neq 0} V(r - R) \right] d^3r \quad (8.34)$$

where  $\alpha$  represents the effect of the distant potentials, or the crystal field, on the electron of the atom under consideration. The terms  $H_{AB} = H_{BA}^* = \int \psi_A^*(r) \hat{H} \psi_B(r) d^3r$  are obtained from Eqs. 8.27 and 8.28, which represent the wave functions for the  $p_z$  atomic orbitals of the electrons of the primitive cell:

$$H_{AB} = \beta \left[ \exp\left(ik_x \frac{1}{\sqrt{3}}\right) + 2 \exp\left(-ik_x \frac{a}{2\sqrt{3}}\right) \cos\left(\frac{k_y a}{2}\right) \right] \quad (8.35)$$

The parameter  $\beta$  is defined as the Hopping term and represents the quantity that is related to the overlap between the  $p_z$  atomic orbitals via the potential:

$$\beta(R) = \int \chi_\mu^*(r) \left[ \sum_R V(r-R) \right] \chi_\mu(r-R) d^3r \quad (8.36)$$

This term defines the width of the energy bands. The components  $k_x$  and  $k_y$  of the wave vector  $\vec{k}$  are shown in Fig. 8.7A. A  $2 \times 2$  matrix is thus obtained, and setting the determinant equal to zero leads to the secular Schrödinger equation:

$$\text{Det} \begin{pmatrix} H_{AA} - \epsilon & H_{AB} \\ H_{BA} & H_{BB} - \epsilon \end{pmatrix} = 0 \quad (8.37)$$

The spectrum of eigenvalues of the graphene sheet is obtained by calculating the determinant of the matrix as a function of the components  $k_x$  and  $k_y$  of the wave vector  $\vec{k}$ :

$$\epsilon(k_x, k_y) = \alpha \pm \beta \left[ 1 + 4 \cos\left(\frac{\sqrt{3}k_x a}{2}\right) \cos\left(\frac{k_y a}{2}\right) + 4 \cos^2\left(\frac{k_y a}{2}\right) \right]^{1/2} \quad (8.38)$$

where  $a$  is the length of the vectors  $\vec{a}_1$  and  $\vec{a}_2$  of the primary lattice. Eq. 8.38, which was obtained for graphene, determines the electronic structure of the carbon nanotube and defines the energy dispersion to the energy bands that is related to the  $\pi$  orbitals of graphene as shown in Fig. 8.5A.

By considering the structure of the carbon nanotube, two new vectors of the reciprocal lattice, the vector  $K_\perp$  in the direction of the circumference and the vector  $K_\parallel$  along the axis of the nanotube (Fig. 8.8), can be defined from the relationship:

$$R_i \cdot K_j = 2\pi \delta_{ij} \quad (8.39)$$

which is translated as:

$$C_h \cdot K_\perp = 2\pi, \quad T \cdot K_\perp = 0; \quad (8.40)$$

$$C_h \cdot K_\parallel = 0, \quad T \cdot K_\parallel = 2\pi, \quad (8.41)$$

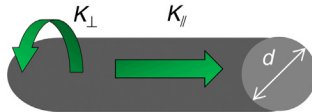


**FIGURE 8.8** Representation of the wave vectors in the directions of the translational vector  $\vec{T}$  ( $K_{\parallel}$ ) and of the chiral vector  $\vec{C}_h$  along the circumference ( $K_{\perp}$ ).

Using the expressions for the vectors  $t_1$  and  $t_2$  (Section 8.3.6.2), obtained due to the condition  $C_h \cdot T = 0$ ; the following is valid:

$$K_{\parallel} = 1/N(-t_2 b_1 + t_1 b_2) \quad (8.42)$$

$$K_{\perp} = 1/N(mb_1 - nb_2) \quad (8.43)$$

where  $b_1$  and  $b_2$  are the vectors of the reciprocal lattice of graphene, and  $N$  is the number of hexagons per unit cell.

The wave vector  $K_{\perp}$ , which is associated with the chiral vector  $\vec{C}_h$ , is now quantized with a finite number of states  $k$ , while the wave vector  $K_{\parallel}$ , which is associated with the translation vector  $\vec{T}$  along the axis of the tube, is continuous if the difference  $\Delta k$  between the two contiguous values of  $K_{\parallel}$  is infinitesimal ( $\Delta k = 2\pi/T \rightarrow 0$ ), which is respected for a nanotube of length  $T \rightarrow \infty$ . The energy eigenvalues can therefore be written in the form:

$$\varepsilon_p^{\text{nанотрубка}}(k) = \varepsilon^{\text{графен}}[kK_{\parallel} + pK_{\perp}] \quad (8.44)$$

The indices  $k$  and  $p$  can assume the values:

$$-\pi/T < k < \pi/T; \quad p = 0, 1, \dots, N-1 \quad (8.45)$$

For example, consider a nanotube  $(n, m)$ , where  $C_h = na_1 + ma_2$ . The wave functions must satisfy the periodicity condition of the tube:

$$C_h \cdot k = 2\pi q \quad (8.46)$$

where  $q$  is a whole number, and  $\vec{k}$  is a wave vector of graphene in the first Brillouin zone. Considering the case of an armchair-type nanotube, the indices that define the chiral vector are equal:  $n = m$ . The length  $C$  of the circumference of the nanotube is:

$$C = |C_h| = \sqrt{C_h \cdot C_h} = a\sqrt{n^2 + nm + m^2} \quad (8.47)$$

$$C = a\sqrt{3}n \quad (8.48)$$

Considering the quantization that is defined in Eq. 8.46, the following is valid:

$$C \cdot k = a\sqrt{3}n k_x = 2\pi q \quad (8.49)$$

where  $k_x$  is the component of the wave vector  $\vec{k}$  in the direction of the chiral vector  $C_h$ , and  $q = 1, 2, \dots, 2n$ .

Substituting this result into Eq. 8.38 results in:

$$\varepsilon_q^{(n,n)}(k) = \alpha \pm \beta \left[ 1 + 4 \cos\left(\frac{q\pi}{n}\right) \cos\left(\frac{ka}{2}\right) + 4 \cos^2\left(\frac{ka}{2}\right) \right]^{1/2} \quad (8.50)$$

where  $-\pi/a < k < \pi/a$ .

Consider a nanotube with the indices  $n = 5, m = 5$  as an example.  $C_h = 5a_1 + 5a_2$ , and the spectrum to the eigenvalues of this type of carbon nanotube is:

$$\varepsilon_q^{(5,5)}(k) = \alpha \pm \beta \left[ 1 + 4 \cos\left(\frac{q\pi}{5}\right) \cos\left(\frac{ka}{2}\right) + 4 \cos^2\left(\frac{ka}{2}\right) \right]^{1/2} \quad (8.51)$$

The spectrum of the energy eigenvalues can be visualized as a function of the wave vector  $\vec{k}$  as shown in Fig. 8.9. The number of hexagons  $N$  per unit cell is:

$$N = 2 \cdot (n^2 + m^2 + nm) / d_R = 10 \quad (8.52)$$

Since there are 2 atoms/cell, 20 electrons occupy 10 orbitals.

The increasing energetic behavior of the orbitals in the case of the conduction band  $\pi^*$  from the edge ( $k = -\pi/a$ ) to the center of the Brillouin zone indicates a greater anti-bonding state of the electrons in the molecule. The width of each band is related to the energy dispersion in the band, which is proportional to the overlap between the orbitals of neighboring atoms. Fig. 8.9 shows that some of the orbitals are degenerate; that is, they are characterized by the same binding energy. The last orbital that is occupied in the  $\pi$  band and the first unoccupied orbital in the  $\pi^*$  conduction band cross the Fermi energy, which

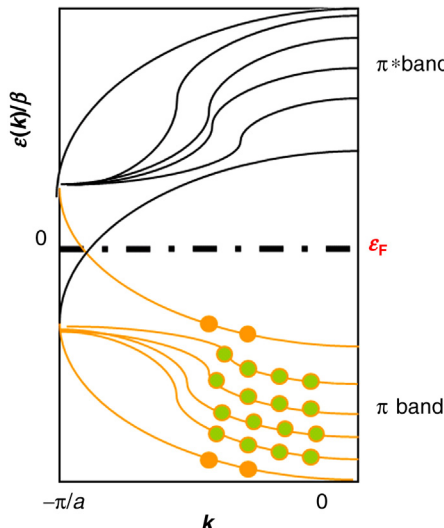


FIGURE 8.9 Occupation of the valence band  $\pi$  for carbon nanotube (5, 5). The circles represent the occupation of orbitals by the electrons for each allowed K-point [18].

means that there is an overlap between the orbitals in the two bands, which confers metallic conduction characteristics to the nanotube.

#### 8.3.6.5 Electronic Structure of a Carbon Nanotube

As a first approximation, the electronic structure of a carbon nanotube can be obtained from the 2D structure of graphene. In the case of a SWNT, however, the quantum confinement of the 1D electronic states along the circumference of the nanotube must be considered. Placing the permitted values for the wave vector in the first Brillouin zone of graphene generates a series of parallel lines that indicate the wave vector values  $\vec{k}$  for the considered nanotube; the length, number and orientation of these “cutting lines” depend on the chiral indices  $(n, m)$  of the nanotube. In the case of armchair-type nanotubes, such as the  $(5, 5)$  nanotube that was considered in the preceding section, the boundary conditions that are defined by the Bloch functions that are related to the chiral vector  $C_h$  are valid:

$$\psi_k(r + C_h) = e^{ikr} C_h \psi_k(r) \quad (8.53)$$

The value of  $k_x$  is calculated as in the previous section. Rewriting Eq. 8.49 for the wave vector  $k_x$  results in [25]:

$$k_x^v = \frac{v}{N_x} \frac{2\pi}{\sqrt{3}a} \quad (8.54)$$

where  $v = 1, \dots, N_x$  with the number of hexagons  $N_x = 5$ . This shows the presence of 5 modes that are permitted for the wave vector  $k_x$ . These possible energetic configurations are normally represented using a hexagon that reproduces the first Brillouin zone (BZ) for graphene as shown in Fig. 8.10A; inserting these lines into the diagram in Fig. 8.5A, which shows the valence and conduction bands in the first hexagonal Brillouin zone of graphene, results in the configuration that is shown in Fig. 8.10B. Fig. 8.10A–B show the wave vectors  $k$  for SWNTs in the first hexagonal BZ of graphene using the cutting lines; the discrete values of the wave vector  $\vec{k}$  are indicated in the direction of the vector  $K_1$  due to the

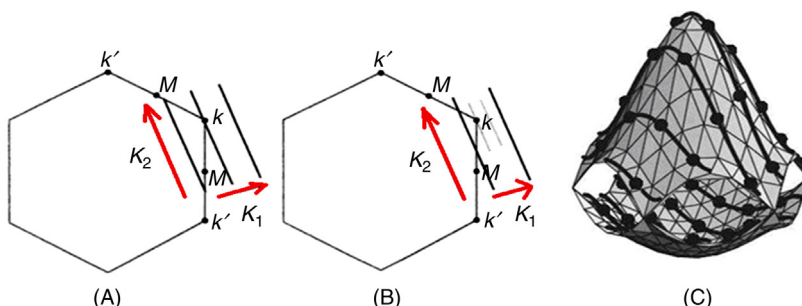


**FIGURE 8.10** Illustrations of the allowed  $k$  values in the first Brillouin zone for (A) a metallic nanotube and (B) a semiconductor nanotube; (C) cutting lines in the case of a  $(4, 2)$  nanotube for illustrative purposes [21].

periodic condition of the electronic wave function in the direction along the diameter of the nanotube, while in the longitudinal direction of the nanotube for the  $K_2$  vector, the wave vector assumes continuous values because it lacks boundary conditions that limit the discrete quantum states for the wave vectors  $k$  in this direction. In Fig. 8.10C, the lines of the values of the wave vector  $\vec{k}$  cut the valence and conduction bands of a carbon nanotube with indices (4, 2). Fig. 8.10A represents a metallic nanotube because the cutting line intersects a point  $K$  on the edge of the hexagon at the Fermi energy of graphite. Fig. 8.10B refers to the case of a semiconductor nanotube because the cutting line does not pass through the point  $K$ .

The zone-folding approximation is used to represent the energy bands of carbon nanotubes in a diagram; the basic idea is that the electronic structure of a specific nanotube is determined by the overlap of the electronic bands of graphene. The cutting lines that correspond to the permitted wave vectors  $k$  that are related to the nanotube under consideration result in the diagram that is illustrated in Fig. 8.11.

The energy dispersion is obtained by substituting the values of  $k_x$  into Eq. 8.38. Fig. 8.11 shows the energy bands with degenerate and nondegenerate orbitals for 10 orbitals in the valence band and 10 in the conduction band. The DOS is shown on the right side of the figure. For zig-zag type tubes with chirality  $(n, 0)$ , the permitted wave vectors are:

$$k_y^v = \frac{v}{N_y} \frac{2\pi}{a} \quad (8.55)$$

where  $v = 1, \dots, N_y$ . For example, the tube (9, 0) has nine lines of permitted wave vectors (Fig. 8.12).

The relationship of the dispersion of the energy bands and the calculation of the electronic DOS indicate that this is a metallic nanotube because the valence and conduction

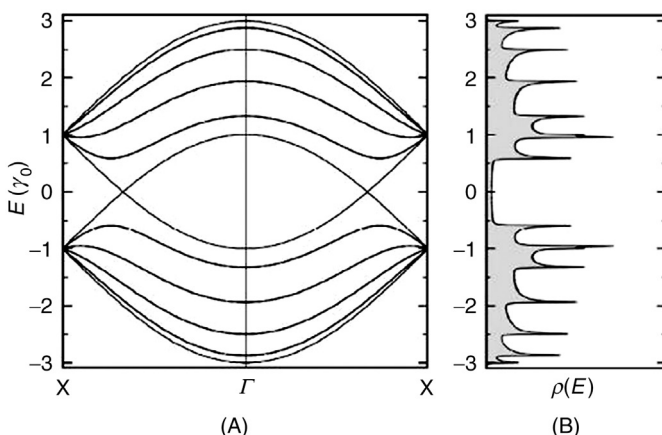


**FIGURE 8.11** (A) Diagram of the molecular orbitals in the energy bands for the electronic states of the nanotube (5, 5), which was obtained using the zone-folding approximation; (B) the corresponding DOS of electrons; the Fermi energy is placed on the zero energy level [23].

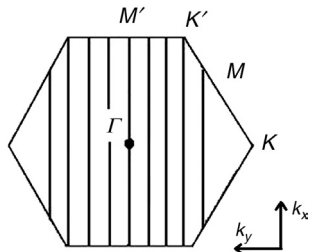


FIGURE 8.12 Illustration of the allowed values of  $k$  (cutting lines) for an armchair nanotube (9, 0) in the first Brillouin zone.

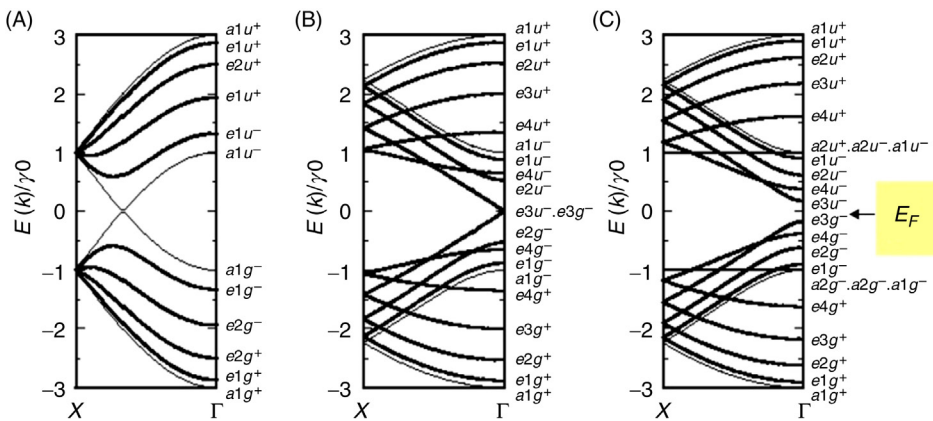


FIGURE 8.13 (A–B) Energy dispersion ratios for the considered metallic nanotubes. (C) Semiconductor nanotube with a bandgap  $\neq 0$  [30].

bands touch at the Fermi energy ( $k = 0$ ) as shown in Fig. 8.13B. When a bandgap is present between the bands (Fig. 8.13C), the nanotube behaves like a semiconductor. The DOS diagrams show how the DOS between the  $\pi$  and  $\pi^*$  bands is greater than 0 for the metallic case and is equal to 0 in the semiconductor case.

Once the basic physical concepts that govern the behavior of matter at the atomic to nanometric scales have been introduced, it is possible to address the incredible properties of nanostructured materials.

Several possible applications for nanomaterials that are already being studied and used based on the exotic material properties at the nanometric scale will be described in the following chapters.

## List of Symbols

$E$	Energy
$\Lambda$	Wavelength
$H$	Planck's constant
$H \hbar$	Reduced Planck's constant

$p$	Momentum
$\sigma$	Bonding atomic orbital
$\pi$	Band of valence molecular orbitals
$\pi^*$	Band of conduction molecular orbitals
$\psi(r, t)$	Wave function
$r$	Position
$t$	Time
$m$	Mass
$V$	Potential energy
$v$	Frequency
$\omega$	Angular frequency
$k$	Wave number
$F$	Force
$\hat{H}$	Hamiltonian operator
$\delta_{ij}$	Kronecker delta
$a$	Lattice parameter
$g(E)$	Density of electronic states
$E_g$	Gap energy
$a_i$	Vectors of the crystal lattice
$b_i$	Reciprocal space lattice vectors
$C_h$	Chiral vector
$p_i$	Atomic orbitals p ( $n = 2$ )
$\beta$	Hopping term
$\epsilon$	Energy eigenvalue
SWNT	Single Wall Nanotube
MWNT	Multi Wall Nanotube

## References

- [1] E.G. Segré, *Dos raios X aos quarks–Físicos modernos e suas descobertas [Modern Physicists and Their Discoveries]*, Editora Universidade de Brasília, Brasília, (1987).
- [2] A. Einstein, Über einen die Erzeugung und Verwandlung des Lichtes betreffenden heuristischen Gesichtspunkt, *Annalen der Physik*[série 4] 17 (1905), 132–148.
- [3] H. Everett III, *The theory of the universal wave function*, in: S. Bryce, DeWitt, Neill Graham (Eds.), *The Many-Worlds Interpretation of Quantum Mechanics*, Princeton University Press, Princeton, 1973.
- [4] P.A.M. Dirac, *The Principles of Quantum Mechanics*, fourth ed., Oxford University Press, Ely House, London, (1958).
- [5] D. Griffiths, *Introduction to Quantum Mechanics*, second ed., Pearson, Prentice-Hall, London, 2005.
- [6] L. De Broglie, Sur La Degradation du quantum dans les transformation successives des radiations de haute fréquence, *Compte rendus de l'Academie des Sciences de Paris* 173 (1921), 1162–1165.
- [7] M. Jammer, *The Conceptual Development of Quantum Mechanics*, McGraw-Hill, New York, 1966.
- [8] M. Jammer, *The Philosophy of Quantum Mechanics*, Wiley, New York, 1974.
- [9] E.R.J.A. Schrodinger, Quantisierung als Eigenwertproblem, *Annalen der Physik* 384 (4) (1926) 361–376.
- [10] R. Eisberg, R. Resnick, *Quantum Physics of Atoms, Molecules, Solids, Nuclei and Particles*, second ed., J. Whiley and Sons, New Jersey, USA, 1985.

- [11] T.S. Kuhn, *Black-body Theory and the Quantum Discontinuity (1894–1912)*, Oxford University Press, Oxford, 1978.
- [12] R.P. Feynman, *The Strange Theory of Light and Matter*, expanded edition, Princeton University Press, Princeton, 2006.
- [13] M. Planck, *Über eine Verbesserung der Wienschen Spektralgleichung*, Verhandlungen der Deutschen physikalische Gesellschaft 2 (1900) 202–204.
- [14] L. Van Dommelen, *Fundamental Quantum Mechanics for Engineers*, 2004, Copyright © 2004, 2007, 2008, 2010, 2011, and on, Leon van Dommelen.
- [15] E. Wigner, F. Seitz, *On the constitution of metallic sodium*, Phys. Rev. 43 (1933) 804.
- [16] J.C. Slater, *Electronic energy bands in metals*, Phys. Rev. 45 (1934) 794.
- [17] C. Kittel, *Introduction to Solid State Physics*, eighth ed., John Wiley and Sons, United States of America, 2005.
- [18] J.D.M. Vianna, A. Fazzio, S. Canuto, *Teoria Quântica de Moléculas e Sólidos: Simulação computacional [Solids and Molecules Quantum Theory: Computational Simulation]*, Livraria da Física-Brasil, São Paulo, 2004.
- [19] W.H. Bragg, *The nature of Röntgen rays*, Transactions and proceedings and report of the Royal Society of South Australia 31 (1907) 94–98.
- [20] J. Mehra, H. Rechenberg, Springer, New York, 1982–1987.
- [21] M.S. Dresselhaus, et al., *Raman Spectroscopy of carbon nanotubes*. Phys. Rep. 409, 2005, 47–99.
- [22] R. Daniel et al., *Experimental review of graphene*, PACS numbers: 81.05.ue, 72.80.Vp, 63.22.Rc, 01.30.Rr, 2011.
- [23] J.C. Charlier, *Electronic and transport properties of nanotubes*, Rev. Mod. Phys. (2007) 79.
- [24] S. Iijima, *Helical microtubes of graphitic carbon*, Nature 354 (1991) 56.
- [25] P.J.F. Harris, *Carbon Nanotubes and Related Structures: New Materials for the 21st Century*, Cambridge University Press, Cambridge, 2003.
- [26] B. Bhushan, *Springer Handbook of Nanotechnology*, Springer-Verlag Berlin Heidelberg, Berlin, Heidelberg, New York, Hong Kong, London, Milan, Paris, Tokyo, 2004.
- [27] R. Marchiori, *Produção Por Ablação A Laser e Caracterização de Nanotubos de Carbono [Carbon Nanotubes Production by Laser Ablation and their Characterization]*, Doctorate Thesis, Florianópolis, 227f. Departamento de Engenharia de Materiais, Universidade Federal de Santa Catarina, Florianópolis-SC, Brazil, 2007.
- [28] R. Saito, G. Dresselhaus, M.S. Dresselhaus, *Physical Properties of Carbon Nanotubes*, Imperial College Press, London, 1998.
- [29] R.P. Feynmann, *Space-Time Approach to Non-Relativistic Quantum Mechanics*, Rev. Mod. Phys. 20 (1948) 367.
- [30] R. Saito, et al. *Electronic structure of graphene tubules based on C<sub>60</sub>*, Phys. Rev. B46 (1992) 1804.

# Carbon-Based Nanomaterials

J.R. Siqueira, Jr.\*, Osvaldo N. Oliveira, Jr.\*\*

\*INSTITUTE OF EXACT SCIENCES, NATURAL AND EDUCATION, FEDERAL UNIVERSITY OF TRIÂNGULO MINEIRO (UFTM), UBERABA, MINAS GERAIS, BRAZIL; \*\*SÃO CARLOS INSTITUTE OF PHYSICS, UNIVERSITY OF SÃO PAULO (USP), SÃO CARLOS, SÃO PAULO, BRAZIL

## **CHAPTER OUTLINE**

<b>9.1</b>	<b>Introduction .....</b>	<b>233</b>
<b>9.2</b>	<b>Fullerenes.....</b>	<b>234</b>
9.2.1	Fullerene Properties.....	235
9.2.2	Applications of Fullerenes .....	235
<b>9.3</b>	<b>Carbon Nanotubes .....</b>	<b>237</b>
9.3.1	Properties of Carbon Nanotubes.....	237
9.3.2	Synthesis of Carbon Nanotubes .....	240
9.3.3	Applications of Carbon Nanotubes.....	240
<b>9.4</b>	<b>Graphene .....</b>	<b>243</b>
9.4.1	Properties and Synthesis of Graphene.....	243
9.4.2	Graphene Applications .....	244
<b>9.5</b>	<b>Conclusions and Perspectives.....</b>	<b>246</b>
<b>Acknowledgments.....</b>		<b>247</b>
<b>References .....</b>		<b>247</b>

## 9.1 Introduction

Carbon is one of the most plentiful and versatile elements in the universe. Due to its allotropic characteristics, carbon forms compounds that have completely different properties depending on the arrangement of the adjacent carbon atoms. Diamond and graphite are two typical examples. Diamond is a material known to have the highest hardness, whereas graphite is fragile and brittle [1,2]. Carbon nanostructures are among the most promising in nanotechnology because they can be used in different fields. In electronics, the combination of a molecular-sized diameter (on the order of 1 nm) with a microscopic-scale length and optical and electrical properties enable carbon nanostructures to be used for the production of innovative devices [2–5]. Composites derived from these nanostructures may exhibit mechanical properties, the electrical and thermal conductivities are useful for applications, and there are desirable features for protection from corrosion in new engineering products

[2–4]. Carbon nanomaterials may also provide new functionalities in biomedical applications, such as sensing and the controlled delivery of pharmaceuticals and drugs [5,6].

For these applications to be commercially viable, there are still major challenges to overcome. Methods for large-scale synthesis, methods for incorporating and dispersing these nanomaterials, such as matrix composites, and methods for the precise control to manipulate and make electrical connections in nanocircuits [1,2] are warranted.

Among the many carbon structures, we highlight fullerenes, carbon nanotubes (CNTs), and graphene. In the following sections, we discuss each of these materials and how they have been used in nanotechnology. We hope that this chapter provides the readers a brief compendium of the properties, applications, and trends in the use of these carbon nano-materials.

## 9.2 Fullerenes

Fullerene is considered to be the third allotropic form of carbon, after graphite and diamond [7,8]. Discovered in 1985 by Harold W. Kroto (University of Sussex, Brighton, England), Robert F. Curl and Richard E. Smalley (Rice University, Houston, Texas, USA) [9], fullerene has an icosahedral symmetrically closed-cage structure, which is formed by 20 hexagons and 12 pentagons in which each carbon atom is bonded to 3 other carbon atoms with  $sp^2$  hybridization [7–9], as shown in Fig. 9.1. Because of its similarity to a building by the American architect Richard Buckminster Fuller, fullerene is called *buckminsterfullerene* [9]. It is a molecule with 60 carbon atoms ( $C_{60}$ ) that are arranged in the shape of a soccer ball with a 7 Å diameter. Due to its shape, fullerene is also known as *buckyball*. Unlike graphite or diamond crystals, which have atom arrangements, fullerene forms molecular crystals and can be considered as a zero-dimensional carbon structure [7,8]. Its discovery

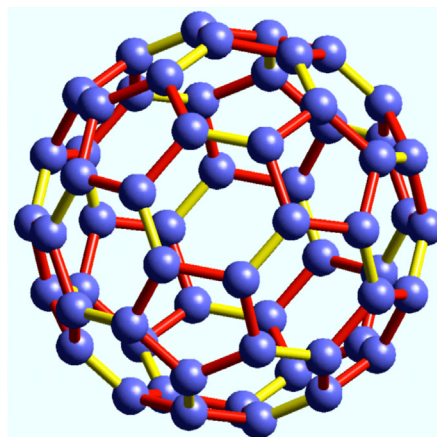


FIGURE 9.1 Schematic representation of the  $C_{60}$  fullerene structure, which is also called *buckminsterfullerene* or *buckyball*.

revolutionized research on new allotropes of carbon and nanostructured materials, and its discoverers received recognition with the Nobel Prize in Chemistry in 1996 [7,8].

### 9.2.1 Fullerene Properties

In the icosahedral symmetrically closed-cage structure, there are two bond lengths in the fullerenes with “double bonds” in the 6:6 ring, which are shorter than the 6:5 bonds. The C<sub>60</sub> is not “superaromatic” because it does not contain double bonds in the pentagonal rings, resulting in low electron delocalization. Thus, C<sub>60</sub> behaves as an electron-deficient alkene and is therefore reactive with electron-donor species. Its molecular stability is due to its geodesic-shaped structure and its electronic bonds. In principle, there may be an infinite number of fullerenes as long as its structure forms an icosahedron with hexagonal and pentagonal rings.

In addition to the C<sub>60</sub> molecule, fullerene may have larger structures, such as C<sub>70</sub>, C<sub>76</sub>, and C<sub>78</sub>, and smaller structures, such as C<sub>28</sub> and C<sub>36</sub>. In the 1990s, C<sub>60</sub> and other fullerenes began to be produced in large quantities via the condensation of soot that is generated in graphite vaporization [10]. Fullerenes may also occur naturally in materials affected by high-energy events, such as lightning and meteors, and in geological samples [7,8].

One of the most widely used processes of synthesis is based on the *Krätschmer-Huffman* method in which an electric arc is generated on graphite electrodes in a helium atmosphere at a pressure of approximately 200 torr. To separate out the fullerene, carbon soot from evaporated graphite is dissolved in a nonpolar solvent. Subsequently, the solvent is dried, and the C<sub>60</sub> and C<sub>70</sub> fullerenes are separated from the residue. Under an optimum current and pressure of helium flow, yields of up to 70% of C<sub>60</sub> and 15% of C<sub>70</sub> are achieved. The laser vaporization method is also used to produce fullerene. In a typical system, a Nd:YAG pulsed laser operating at 532 nm and 250 mJ is used as the source, and the graphite target is maintained in an oven at 1200°C. Although the yields are low, fullerenes have also been produced via deposition of soot from flames involving, for example, the combustion of benzene and acetylene [8,11].

Fullerenes have excellent mechanical properties, resisting high pressures and returning to their original shape even after subjected to more than 3000 atm. Theoretical calculations indicate that a single C<sub>60</sub> molecule has a bulk modulus of 668 GPa when compressed to 75% of its size. This property makes fullerenes harder than steel and diamond, whose *bulk* modules are 160 and 442 GPa, respectively. Fullerenes can withstand collisions of up to 15,000 mph against stainless steel and maintain its shape, demonstrating their high stability. The optical properties of the fullerenes are also renowned for the delocalized  $\pi$  electrons, which generate nonlinear optical responses and intensity-dependent refractive indices [11,12].

### 9.2.2 Applications of Fullerenes

Fullerenes can be applied in several fields and, currently, are most notable in organic solar cells [13]. The high electron affinity and the ability to carry a charge make fullerene the

best electric charge acceptor for this type of device. Fullerenes have a *lowest unoccupied molecular orbital* (LUMO) with a low energy compared with the organic charge donors that have high electron affinities [13,14]. With this LUMO energy, C<sub>60</sub> can be reversibly reduced with up to six electrons, denoting its ability to stabilize a negative charge. Polymer blends that are combined with fullerenes exhibit ultrafast photo-induced charged transfer (at approximately 45 fs). Thus far, the greatest efficiency for a polymer solar cell is due to the polymer/fullerene heterojunction. The fullerene (most commonly C<sub>60</sub>) acts as an n-type semiconductor (electron acceptor) and is combined with a p-type polymer (electron donor), typically a polythiophene. The polymer/fullerene blend is deposited as a film to act as an active layer to create what is known as a *bulk* heterojunction [13,14], as shown in Fig. 9.2.

Solar cell efficiency steadily increases. Although the energy conversion efficiency of a polymer/fullerene heterojunction solar cell is still low (approximately 10%), compared to conventional silicon cells (20% efficiency), the production cost of this type of solar cell may be significantly lower. Furthermore, organic solar cells can be flexible, rolled up, and scattered over any surface [13–15]. Plastic photovoltaic devices can be used to cover internal and external walls of buildings. Additionally, cells of any color and texture can be manufactured. For example, a cell phone can be painted with this material, and its battery can be charged while a person walks with it on a sunny day. Organic solar cells are also expected to be used in advertising, such as on light banners, liquid crystal displays, and food packaging [13–15].

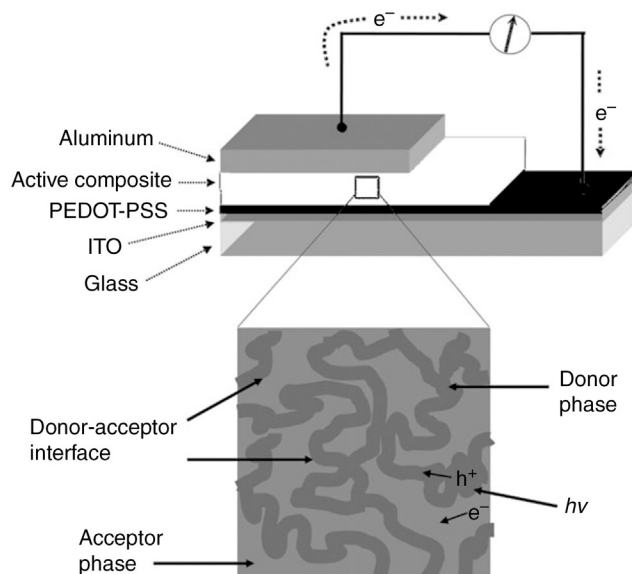


**FIGURE 9.2** Schematic illustration of a heterojunction solar cell that is composed of an active polymer/fullerene layer. Modified from B.C. Thompson, J.M. Fréchet, *Polymer-fullerene composite solar cells*, *Angewante Chemie* 47 (2008) 58–77 [13]. Copyright 2008 John Wiley & Sons, Inc.

Fullerenes can be used in other organic electronic devices. In organic field effect transistors, they serve as an n-type semiconductor to increase charge mobility and stability [8,13]. Interdigitated capacitors with fullerenes were used in sensors that explore the electron acceptor properties of fullerene films [16]. In optical limiters, fullerenes induce a decrease in transmittance with an increase of incident light. This allows all of the light below an activation threshold to pass through, for example, maintaining the light transmission at a constant level below the damage threshold for the eye or an optical sensor [16]. Fullerene hydride shows promise for storing hydrogen gas in electrical vehicles that use a fuel cell. This is encouraging because the available hydrogen storage technologies, such as compressed gas or storage as metallic hydrides, are dangerous and/or have low hydrogen storage densities [16].

In the medical and pharmaceutical fields, fullerene derivatives can be used in photodynamic therapy for cancer, such as in antibacterial agents and in neuroprotective drugs [1,8]. Due to its ability to include atoms, fullerenes are suitable as drug carriers. Additionally, noble gases can be encapsulated in fullerenes for use in nuclear magnetic resonance. Fullerenes are also antioxidants and react with free radicals, thus preventing cell damage or death. For example, fullerene has an antioxidant performance that is 100 times more effective than vitamin E. In engineering, fullerenes are employed to strengthen metal alloys [1,8,12].

## 9.3 Carbon Nanotubes

CNTs are among the most studied nanostructures in recent decades [4]. They are a few nanometers in diameter and form one-dimensional structures because the length is orders of magnitude larger than the diameter. They have different properties from other allotropes of carbon, such as graphite and diamond, with unique mechanical and electrical characteristics. The discovery of CNTs has not been fully elucidated, but they have been known in the scientific community since 1991 because of the publication by Sumio Iijima [17]. That article presented a method to obtain cylindrical and concentric carbon structures, which were later called multiwalled carbon nanotubes (MWNTs) [17]. In 1993, Iijima and Donald Bethune (an IBM researcher) published separate studies that included methods to obtain single-walled carbon nanotubes (SWNTs). After these independent findings, nanotubes became an object of study in various fields of science [18].

The importance of CNTs for nanotechnology is reflected in their numerous application possibilities. In engineering, CNTs have been studied to create new composites for the aeronautics industry [19]. They have also been used in nanodevices and electronic nano-circuits to manufacture new chips for computers [20].

### 9.3.1 Properties of Carbon Nanotubes

The great interest in CNTs is due to their outstanding properties, such as high mechanical strength and elasticity, chemical, thermal and structural stability, and high conductivity

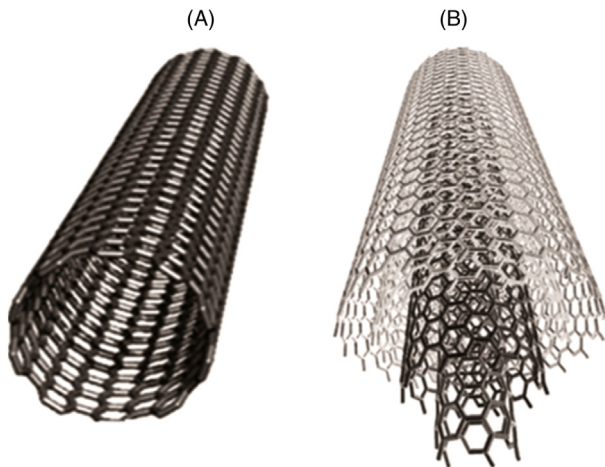


**FIGURE 9.3** (A) A representation of the single-walled carbon nanotube (SWNT) structure and (B) a multiwalled carbon nanotube (MWNT). Modified from J.J. Gooding, Nanostructuring electrodes with carbon nanotubes: a review on electrochemistry and applications for sensing, *Electrochim. Acta* 5 (2005) 3049–3060 [23]. Copyright 2005 Elsevier.

[1,5,19,20]. CNTs are formed only by carbon and have a cylindrical shape. The structure can be compared to a graphene sheet rolled into a tube shape in which the ratio between the length and diameter makes it almost a one-dimensional structure [17,18]. The two most important structures are SWNTs and MWNTs, as shown in Fig. 9.3. SWNTs have a simple cylinder structure, and MWNTs consist of several concentric SWNTs. The length and diameter of the MWNT structures are very different from SWNTs, which implies differences in their properties [21,22]. Their properties depend on the atomic arrangement of how the “graphene sheet is rolled up” and on the tube diameter, length, and morphology [21–23].

The properties of SWNTs are determined by the structure formed by the bonds between the carbon atoms of the graphene sheet [21,22]. SWNT structures depend on the chirality of the tube, which is defined by the chiral vector ( $\vec{C}_h$ ) and the chiral angle ( $\theta$ ), as shown in Fig. 9.4. The vector  $\vec{C}_h$  is the linear combination of the base vectors  $a_1$  and  $a_2$  of a simple hexagon via the relationship  $\vec{C}_h = n\vec{a}_1 + m\vec{a}_2$ , where  $n$  and  $m$  are integers and  $\vec{a}_1$  and  $\vec{a}_2$  are the single cell vectors of a two-dimensional matrix that is formed by the graphene sheet in which the direction of the nanotube axis is perpendicular to the chiral vector, as shown in Fig. 9.4A.

The chiral vector pair ( $n,m$ ) indicates the direction in which the graphene sheet is rolled. The values of this pair allow three types of arrangements for SWNTs: zigzag, armchair, and chiral, as shown in Fig. 9.4B. The pair ( $n,m$ ) determines the nanotube chirality and therefore its optical, mechanical and, in particular, electrical properties [21,22]. If ( $n,m$ ) is a multiple of 3, the nanotubes are of the armchair type with metallic behavior, that is, they have a Fermi level in a partially filled band (Fig. 9.5A). When ( $n,m$ ) is not a multiple of 3, the nanotubes are the zigzag type and have semiconductor behavior (Fig. 9.5B).

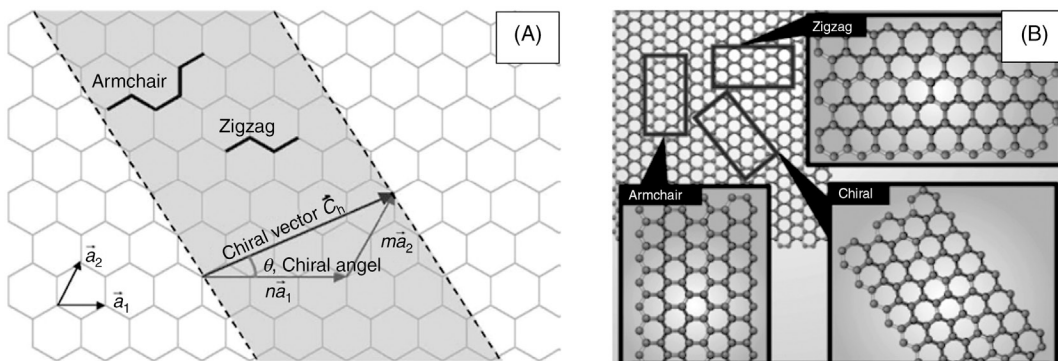


**FIGURE 9.4** (A) Schematic diagram of how a graphene sheet is rolled up to form a carbon nanotube and (B) representation of the three types of SWNT structures obtained with the  $(n,m)$  pair from the chiral vector. Modified from E.T. Thostenson, Z.F. Ren, T.W. Chou, *Advances in the science and technology of carbon nanotubes and their composites: a review*, *Comp. Sci. Technol.* 61 (2001) 1899–1912 [21]. Copyright 2001 Elsevier.

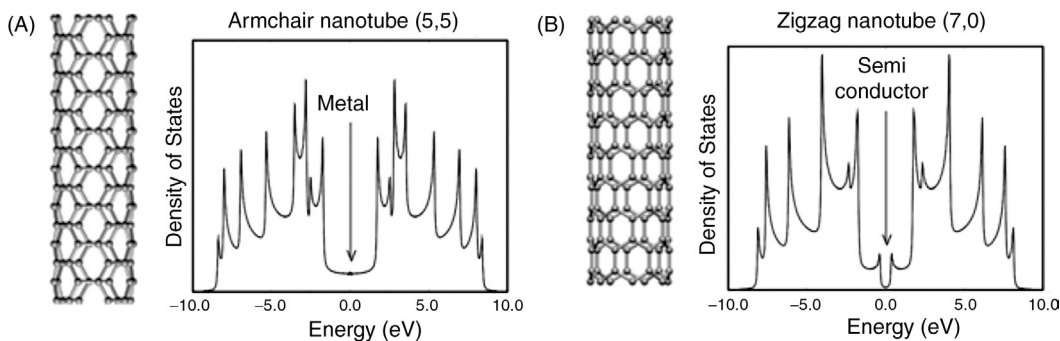


**FIGURE 9.5** Electronic structure of nanotubes. (A) armchair (metallic) and (B) zigzag (semiconductor). Reprinted with permission from J.C. Charlier, *Defects in carbon nanotubes*, *Acc. Chem. Res.* 35 (2002) 1063–1069 [22]. Copyright 2002 American Chemical Society.

The  $(n,m)$  relationships that are formed with the nanotube structure, the chiral angle, and the type of nanotube are listed in detail in Table 9.1.

MWNTs are described by models developed from electron microscopy images. They generally have a coaxial cylindrical shape, are formed as a coaxial polygon, or are rolled-up graphene sheets. MWNTs are formed by several graphene sheets that are rolled around each other concentrically with a distance between the sheets of 3.4–3.6 Å [21,22]. The length

**Table 9.1** Relationship of the  $(n,m)$  Pair with the Type of SWNT and Its Chiral Angle

$(n,m)$	Structure	Chiral Angle (Degree)
$n = m$	Armchair	$\Theta = 0$
$m = 0$	Zigzag	$\Theta = 30$
$m \neq n$	Chiral	$0 \leq \Theta \leq 30$

and diameter of MWNTs are different from the length and diameter of SWNTs, which implies different properties. Another factor that defines the type of nanotube formed (SWNT or MWNT) is related to synthesis.

### 9.3.2 Synthesis of Carbon Nanotubes

There are many methods for synthesizing CNTs that produce different types with different properties. The three main methods are electric arc, pulsed laser, and chemical vapor deposition (CVD) [2,11,19].

- *Electric arc:* An electric arc discharge is generated between two cylindrical graphite electrodes in a steel chamber with an inert gas. The cathode and anode are kept at a distance that is less than 1 nm, allowing the current to flow so that plasma is generated between the electrodes. The temperature in the plasma region is approximately 4000 K. In this environment, the anode graphite undergoes sublimation and is deposited on the cathode or the inner walls of the chamber (soot) where the CNTs are found. To obtain MWNTs via this method, it is necessary to use catalysts to form beams of these types of nanotubes. The amount and quality of the CNTs depend on the product concentration in the chamber. This was the first method used to synthesize nanotubes and is still one of the most widely used [2].
- *Pulsed laser:* This is similar to the electric arc discharge method. The carbon is vaporized by irradiation via a laser in the presence of an inert gas. The graphite is placed inside a quartz tube and placed in a controlled-temperature tubular oven. The tube is emptied, and the temperature is increased to 1200°C, and then, the tube is filled with an inert gas (He or Ar). The laser sweeps across the graphite surface, vaporizing it and forming CNTs. During this process, it is possible to form both SWNTs and MWNTs without a catalyst [2].
- *CVD:* This involves the decomposition of a vapor or gas that contains carbon atoms, which are usually hydrocarbons in the presence of a metal catalyst, via heat treatment. The nanotubes are nucleated and formed via the decomposition of the volatile precursors and deposited on a substrate. The important parameters in this process are the type of catalyst, the substrate temperature (between 500 and 700°C) and the type of substrate, which defines the growth region of the CNTs. This technique allows CNTs to grow in an orderly manner with nanostructures designed specifically for some applications [2].

### 9.3.3 Applications of Carbon Nanotubes

The characteristics that result in CNTs that have different physicochemical properties allow their application in several fields. Sensors and biosensors are worth mentioning because there are hundreds of articles published from a multidisciplinary approach that involve physics, chemistry, biology, biochemistry, electronics, and materials science. The manufacturing of electronic nanodevices is the aim of this type of study, in addition to

the integration of CNTs with biomolecules in nanosensors and nanoactuators. The latter applications can aid in diagnosing diseases, provide drug delivery control, and process biomaterials, for example. The sensing can be performed via conventional techniques: electrical, optical, or electrochemical [5,6,23–30].

The integration of CNTs with biological compounds (proteins, enzymes, antibodies, DNA) in electrical devices, such as biosensors, is due to the size compatibility because electronic circuit components have dimensions that are comparable to biomolecules. Electrostatic interactions and charge transfer, which are typical in biological processes, can be detected via electronic nanocircuits, which is helpful in detecting biological species [23–30]. For example, the diameter of a SWNT is comparable to the size of molecules, such as DNA (1 nm), whereas its length is greater, which provides a convenient interface for micrometric scale circuits. Additionally, the high-reactivity and effective area of CNTs provide synergy with organic molecules [23–27].

In biosensors that contain CNTs, there are typically electrodes that are modified via the immobilization of a biomolecule, such as an enzyme, as the recognition element [28,29]. CNTs are suitable for facilitating charge transfer in reactions with electroactive species in solution, in addition to increasing the electroactive surface area of the electrodes. In many cases, there is also synergy in the use of CNTs with other nanomaterials or biomolecules, for example, a more efficient catalysis of redox reactions of analytes, surface functionalization, and the compatibility of interactions with other types of nanomaterials (e.g., metal nanoparticles and quantum dots). Concerning biosensors, CNTs form suitable matrices for immobilizing biomolecules without the loss of biological activity. These biosensors that contain CNTs have been used to diagnose diseases, such as some cancers and tropical diseases (e.g., Chagas and leishmaniosis), and in traditional clinical tests, such as the measurement of glucose, urea, cholesterol, and uric acid [5,23–30]. Fig. 9.6 shows a representation of different types of sensors and biosensors that include CNTs.

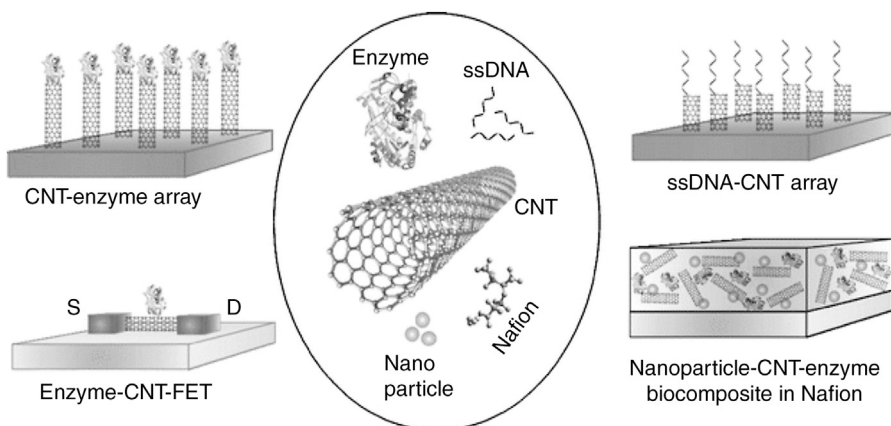


FIGURE 9.6 Representation of different types of sensors that contain CNTs. Modified from A. Merkoçi, *Nanobiomaterials in electroanalysis*, *Electroanalysis* 19 (2007), 739–741 [30]. Copyright 2007 John Wiley & Sons, Inc.

SWNT semiconductors have been used in field-effect transistors (FET) to detect biological species under ambient temperatures and conditions. Nanotube field-effect transistors (NTFET) are obtained with the replacement of the solid-state gate with a layer of adsorbed molecules that modulates nanotube conductance. There are two classical NTFET device designs. The first design uses a single CNT as an electron channel between the source and drain electrodes. In the second type, a set of CNTs serves as a collective channel between the source and drain. The nanotube-analyte interaction may have one of two effects. The first effect is the charge transfer from the analyte molecules to the CNTs. In the second mechanism, the adsorbed analyte in the CNT walls decreases conductance [25–27]. The difference between these two types of mechanisms is obtained via measurements in a transistor. If a charge transfer occurs, the voltage threshold becomes much more positive (removing electrons) or more negative (donating electrons).

In energy storage, CNTs have been used as supercapacitors because of their high electrical conductivity, large surface area, mechanical strength, and low weight. Additionally, the possibility of modifying CNTs in chemical synthesis and their combination with other nanomaterials to improve the performance of the supercapacitors are important [31–33]. Other advantages are flexibility and optical transparency, allowing the development of flexible electronic devices, such as more pliable cell phones and computers. For this type of application, supercapacitors that contain only CNTs exhibit excellent electrical conductivity and a large surface area but do not reach the expected performance because of the contact resistance between the electrode and the current collector. Therefore, metal oxides (including those in nanoparticles) are incorporated into nanotubes to reduce the contact resistance and increase the storage density of supercapacitors [31–33].

In addition to the interest in devices, CNTs are useful as engineering materials because of their mechanical properties. CNTs have an elasticity of 1000 GPa, which is 5 times that of steel, a rupture tension of 63 GPa, and tensile strengths 50 (SWNTs) and 200 (MWNTs) times higher than that of steel. Adding to these characteristics is the lower density of CNTs compared with metals. With these properties, CNTs can be useful for aerospace engineering, such as in aircraft fuselages [19]. CNTs can form ultraresistant foams that work as high-compression springs. Threads made with CNTs are being studied to make fabrics in clothing that may be stronger than Kevlar, a material used currently in bullet-proof vests [34].

Regarding products that are closer to industrialization, CNTs can be used as reinforcement in composites in which one of the phases has a nanometric size. One possibility is to apply CNTs in a polymer matrix to improve electronic properties and increase mechanical strength, for example, in plastic containers that require electrostatic shielding, such as in cell phones [35]. CNTs can also modify the mechanical properties of biodegradable polymeric nanocomposites that are used for tissue engineering and to manufacture artificial bones, cartilage, muscles, and nervous tissue. Another advantage of CNTs is the assistance they provide to bone cell proliferation and bone formation from functionalized surfaces [36–38].

## 9.4 Graphene

Graphene is a nanomaterial arranged in a two-dimensional layer of carbon atoms with  $sp^2$  hybridization that are connected in a hexagonal lattice structure. Graphene was discovered in 2004 by Andre Geim and Konstantin Novoselov from the University of Manchester, England [39]. This material has driven research in nanoscience and nanotechnology because of graphene's exceptional electrical, mechanical, and chemical properties. Graphene can be used in sensors, batteries, supercapacitors, solar and fuel cells, and in biotechnology. The recognition of the importance of graphene resulted in its discoverers being awarded the Nobel Prize in Physics in 2010 [40–44].

Graphene has a remarkable band structure due to its crystalline structure. The carbon atoms form a hexagonal lattice in a two-dimensional plane in which each carbon atom is approximately 1.42 Å from its three neighboring atoms via a  $\sigma$  bond with each other. The fourth bond is a  $\pi$  bond that is oriented out of the plane. The  $\pi$  orbital is a pair of symmetrical lobes oriented along the  $z$  axis and centered on the core. From these  $\pi$  bonds, the so-called  $\pi$  and  $\pi^*$  bands form, which are responsible for most of the electronic properties of graphene [40–44].

### 9.4.1 Properties and Synthesis of Graphene

Graphene has many properties that are superior to any other material. For example, it has a high electron mobility of  $2.5 \times 10^5 \text{ cm}^2 \text{ Vs}^{-1}$  at ambient temperature, a Young's modulus of 1.0 TPa, and a thermal conductivity above 3000 W/mK. Additionally, it absorbs a significant fraction of white light ( $\sim 2.3\%$ ), has complete impermeability to any gas, and can sustain extremely high electrical current densities (one million times higher than copper). Furthermore, graphene is easily chemically functionalized [40–45].

The great advance in research on graphene has occurred because, among other reasons, it is cheap to obtain in a high quality. The synthesis methods can be divided into two groups, the *bottom-up* approach and the *top-down* approach [44]. The *bottom-up* approach consists of the growth of graphene sheets by combining the basic structural units. In this approach, organic synthesis methods are used, enabling graphene growth directly via molecular organic precursors. These precursors usually consist of benzene ring molecules with highly reactive functional groups, enabling controlled two-dimensional growth of the graphene sheet. Another method to grow two-dimensional graphene sheets is based on the growth *in situ* on catalyst substrates (e.g., Cu, Ni, Fe), such as via CVD, arc discharge, or SiC epitaxial growth. The major limitation of these techniques is that they still do not produce graphene in large amounts and uniformly, and they are expensive [44].

The *top-down* approach involves the breaking of the interplanar Van der Waals bonds of graphite. In this approach, chemical and mechanical exfoliation methods are used on graphite. These approaches have limitations in obtaining the two-dimensional graphene crystal. The mechanical or chemical graphite exfoliations do not allow complete control of the number of carbon layers in the graphene and the two-dimensional crystal lattice

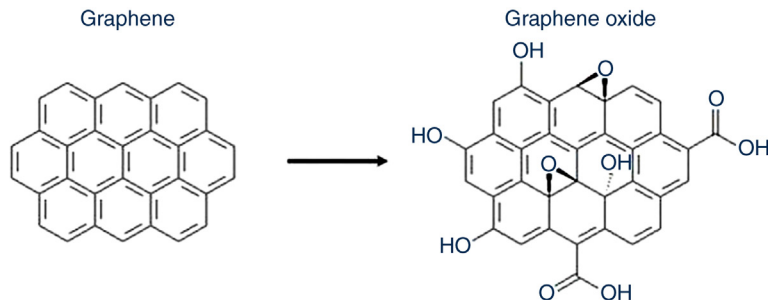


**FIGURE 9.7** Simplified schematic representation of the graphene and graphene oxide structures. Modified from Ref. [46]. Copyright 2013 Elsevier.

quality, limiting performance. In particular, exfoliating graphite in solution requires surface modifications to break the Van der Waals bonds and the formation of structural defects on the graphene carbon lattice. An intermediate species in this type of processing is known as graphene oxide (GO) due to its high density of oxygen functional groups. With GO, it is possible to obtain colloidal solutions that are stable for long periods of time. This characteristic is important for the formation of nanocomposites by combining graphene with other types of materials, such as polymers, biomolecules, and nanoparticles. Surface charge measurements (zeta potential) of GO have indicated that GO is negatively charged when dispersed in water [44]. Fig. 9.7 shows a simplified representation of the graphene and GO structures.

GO can be converted into graphene via reduction processes, producing products with properties similar to those of graphene. However, reduced GO has significant structural differences compared to graphene [41–44]. The main purpose of the chemical reduction of GO is to obtain graphene with mechanical and conductive properties that are similar to graphene produced via the scotch tape method. GO reduction allows regeneration of the graphitic structure with deoxygenation and dehydration, restoring the conductivity of the material and restructuring the sp<sub>2</sub> bonds in the carbon matrix [41–44].

The reduction of GO can be performed using several methods, including chemical methods with reducing agents, such as hydrazine, hydrogen plasma, dimethylhydrazine, hydroquinone, sodium borohydride, ascorbic acid, alcohols, and strong alkaline solutions, electrochemical methods, thermal methods, and ultraviolet radiation methods. Importantly, the conductivity of the reduced GO depends on both the methodology used to oxidize the graphite and the reduction methodology. The structural defects that appear during the oxidation of graphene also lead to the removal of carbon atoms from the aromatic structure of the carbon planes, creating nanometric zones of discontinuity that are impossible to recover via reduction [41–44].

#### 9.4.2 Graphene Applications

Similar to fullerenes and CNTs, graphene also excels in applications in different fields. Graphene is employed in renewable energy sources and as transparent electrodes in

dye-sensitized solar cells. Because doping can change the position of the Fermi level, graphene can act both as an electron acceptor and donor [41–44]. With the lower cost to produce graphene via liquid phase or thermal exfoliation, the increasing use of graphene can be expected in dye solar cells, especially in applications where the mechanical flexibility is crucial [41–44].

Graphene has been studied for next-generation lithium-ion batteries and in cathodes with high electrical conductivity [4,42]. With its morphology similar to a sheet, graphene can act as a conductive membrane and form a *core-shell* or nanocomposite with a sandwich-type structure. The increase in electrical conductivity of these morphologies that contain graphene can help overcome a major limitation of lithium-ion batteries, which is low power density. Additionally, the high thermal conductivity of graphene may be helpful for high current charges that generate a significant amount of heat in a battery. As anodes, the nanosheets of graphene can be used to intercalate lithium crystals in the layers [4,42].

Supercapacitors, also called electrochemical capacitors or ultracapacitors, are hosts of energy whose mechanism is associated with the electrical double layer at the interface between the electrode and the electrolyte [31,32]. Graphene is suitable for supercapacitors because of its flexibility, transparency, high electrical conductivity, large surface area, mechanical resistance, and low weight, which can allow the development of flexible electronic devices that can be incorporated in clothing and cell phones and allow the development more pliable computers. Additionally, graphene can be combined with other nanomaterials in search of synergy, as shown in Fig. 9.8 [47–52].

One challenge to produce graphene electrodes on a large scale is to avoid agglomeration of the plates because the agglomerations decrease the effective surface area, causing negative effects on the properties. To control this agglomeration, the plates are separated with nanoparticles, which also favors the electrochemical properties [47–52]. For example, metal oxides (in *bulk* or nanoparticles) are incorporated into graphene to decrease the contact resistance and increase the specific capacitance and energy density of supercapacitors. The combination of graphene and oxide in nanocomposites can generate supercapacitors with high performances, but the oxide must have a low cost and toxicity [47–52]. In this aspect, magnesium oxides may be preferable to ruthenium oxide because of their lower cost [50,51].

The unique electronic properties of graphene provide a glimpse of high-performance logic circuits of future decades, for example, in logic transistors, high-frequency transistors, flexible electronic devices, such as touch screens and electronic paper (*e-paper*), and organic light emitting diodes [42]. Graphene can also be used in photonics, photodetectors, optical modulators, optical polarization controllers, *mode-locked* solid state lasers, and insulators [42].

Like CNTs, graphene has been widely used in several types of sensors and biosensors (e.g., optical, chemical, and piezoelectric). For biosensors, in particular, graphene can be even more useful than CNTs, mainly because its two-dimensional structure facilitates functionalization for the incorporation of biomolecules and nanoparticles [53–55].

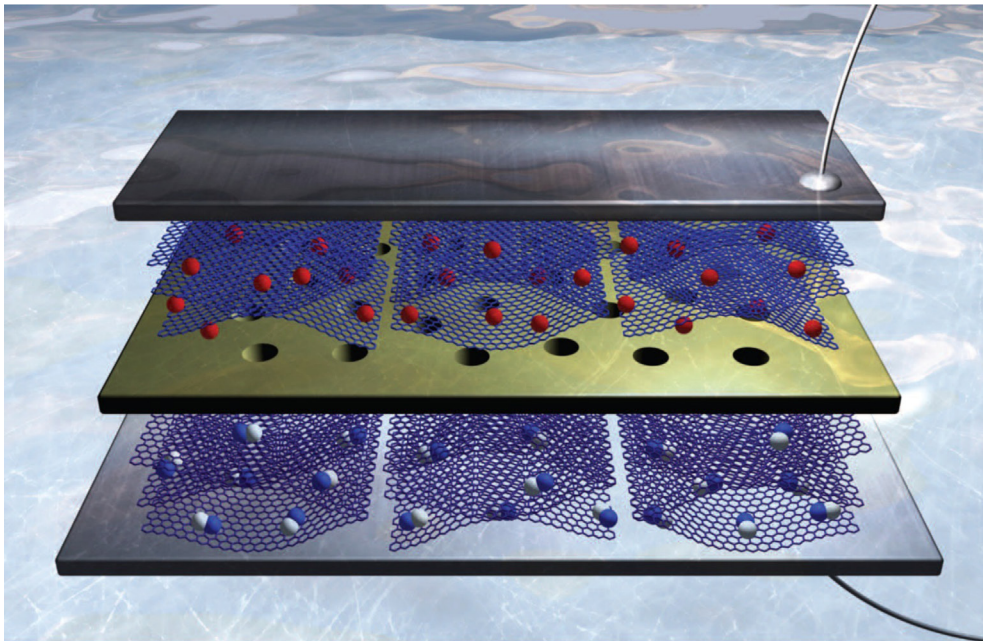


**FIGURE 9.8 Schematic representation of a supercapacitor with two electrodes modified with graphene separated by a membrane.** Modified from K.S. Novoselov, V.I. Faíko, L. Colombo, P.R. Gellert, M.G. Schwab, K. Kim, *A roadmap for graphene*, *Nature* 490 (2012) 192–200 [42]. Copyright 2012 *Nature*.

Graphene also has a higher biocompatibility and larger surface area, which can produce higher performance than CNTs or other carbon materials in biosensors [53–55].

For biomedical applications, graphene is promising due to its large surface area, chemical purity, and possibility of functionalization for drug delivery systems [42]. Its mechanical properties suggest applications in tissue engineering and regenerative medicine. Due to its single atomic layer thickness, conductivity, and mechanical resistance, graphene is suitable as a support for biomolecules to perform transmission electron microscopy [42]. Additionally, functionalized graphene can generate ultra-sensitive devices that are quick and capable of detecting biological molecules, such as glucose, cholesterol, hemoglobin, and DNA [53–55]. Graphene compounds are biocompatible with different cell types (such as mammalian and bacterial cells) both in vitro and in vivo and produce antibacterial effects [46].

## 9.5 Conclusions and Perspectives

Fullerenes, nanotubes, and graphene are the main nanomaterials derived from carbon, and they have unique properties that make them attractive for forming materials for use in a wide range of technologies. Although they have many common fields of application, in this chapter, we highlighted the importance of the use of fullerenes in photovoltaic solar

cells, CNTs in sensors and biosensors, and graphene in supercapacitors for energy storage. Despite the significant number of studies in these areas, there is still much to investigate to fully understand the possibilities. Therefore, we described the main characteristics, properties, and applications of these carbon nanostructures, which are responsible for boosting nanotechnology.

## Acknowledgments

The authors thank the National Council for Scientific and Technological Development (Conselho Nacional de Desenvolvimento Científico e Tecnológico—CNPq) (477668/2013-5), the Minas Gerais State Research Foundation (Fundação de Amparo à Pesquisa do estado de Minas Gerais—FAPEMIG) (APQ-01763-13 and APQ-01358-13), and the São Paulo Research Foundation (Fundação de Amparo à Pesquisa de São Paulo—FAPESP) (2013/14262-7) for their financial support.

## References

- [1] O.A. Shenderova, V.V. Zhirnov, D.W. Brenner, Carbon nanostructures critical, *Rev. Solid State Mater. Sci.* 27 (2002) 227–356.
- [2] K. Koziol, B.O. Boskovic, N. Yahya, Synthesis of carbon nanostructures by CVD method, in: N. Yahya (Ed.), *Carbon and Oxide Nanostructures, Advanced Structured Materials*, 5, Springer-Verlag, Berlin, Heidelberg, 2010.
- [3] A.J. Page, F. Ding, S. Irle, K. Morokuma, Insights into carbon nanotube and graphene formation mechanisms from molecular simulations: a review, *Rep. Prog. Phys.* 78 (2015) 38.
- [4] Y. Li, J. Wu, N. Chopra, Nano-carbon-based hybrids and heterostructures: progress in growth and application for lithium-ion batteries, *J. Mater. Sci.* 50 (2015) 7843–7865.
- [5] E. Katz, I. Willner, Biomolecule-functionalized carbon nanotubes: applications in nanobioelectronics, *ChemPhysChem* 5 (2004) 1085–1104.
- [6] I. Willner, B. Willner, Biomolecule-based nanomaterials and nanostructures, *Nano Lett.* 10 (2010) 3805–3815.
- [7] Rocha, R.C. Filho, Os Fulerenos e sua espantosa geometria molecular [Fullerenes and their amazing molecular geometry], *Química Nova na Escola* 4 (1996) 7–11.
- [8] B.C. Yadav, KumarF R., Structure, properties and applications of fullerenes, *Int. J. Nanotechnol. Appl.* 2 (2008) 15–24.
- [9] H.W. Kroto, J.R. Heath, S.C. O'Brien, R.F. Curl, R.E. Smalley, C60 Buckminsterfullerene, *Nature* 318 (14) (1985) 162–163.
- [10] C.W.K. Isaacson, J.A. Field, Quantitative analysis of fullerene nanomaterials in environmental systems: a critical review, *Environ. Sci. Technol.* 43 (2009) 6463–6474.
- [11] M.S. Dresselhaus, G. Dresselhaus, P.C. Eklund, *Science of Fullerenes and Carbon Nanotubes*, Academic Press, Boston, MA, (1996).
- [12] R. S. Rouff, The bulk modulus of C60 molecules and crystals: a molecular mechanics approach, *Appl. Phys. Lett.* 59 (1991) 1553–1557.
- [13] B.C. Thompson, J.M. Fréchet, Polymer-fullerene composite solar cells, *Angew. Chem.* 47 (2008) 58–77.
- [14] S. Günes, H. Neugebauer, N.S. Sariciftci, Conjugated polymer-based organic solar cells, *Chem. Rev.* 107 (2007) 1324–1338.

- [15] B.M. Alice, M. Milton, Y. Sun, Infrared spectroscopy of all-carbon poly[60] fullerene dimer model, *Chem. Phys. Lett.* 288 (1998) 854–860.
- [16] J.C. Withers, R.O. Loutfy, T.P. Lowe, Fullerene commercial vision, *Fullerene Sci. Techn.* 5 (1997) 1–31.
- [17] S. Iijima, Helical microtubules of graphitic carbon, *Nature* 354 (1991) 56.
- [18] S. Iijima, T. Ichihashi, Single-shell carbon nanotubes of 1-nm diameter, *Nature* 363 (1993) 603.
- [19] O. Gohardani, M.C. Elola, C. Elizetxea, Potential and prospective implementation of carbon nanotubes on next generation aircraft and space vehicles: a review of current and expected applications in aerospace sciences, *Prog. Aerosp. Sci.* 70 (2014) 42–68.
- [20] U.N. Maiti, W.J. Lee, J.M. Lee, Y. Oh, J.Y. Kim, J.E. Kim, J. Shim, T.H. Han, S.O. Kim, 25th anniversary article: chemically modified/doped carbon nanotubes & graphene for optimized nanostructures & nanodevices, *Adv. Mater.* 26 (2014) 40–67.
- [21] E.T. Thostenson, Z.F. Ren, T.W. Chou, Advances in the science and technology of carbon nanotubes and their composites: a review, *Compos. Sci. Technol.* 61 (2001) 1899–1912.
- [22] J.C. Charlier, Defects in carbon nanotubes, *Acc. Chem. Res.* 35 (2002) 1063–1069.
- [23] J.J. Gooding, Nanostructuring electrodes with carbon nanotubes: a review on electrochemistry and applications for sensing, *Electrochim. Acta* 5 (2005) 3049–3060.
- [24] J. Wang, Carbon-nanotube based electrochemical biosensors: a review, *Electroanalysis* 17 (2005).
- [25] B.L. Allen, P.D. Kichambare, A. Star, Carbon nanotube field-effect-transistor-based biosensors, *Adv. Mater.* 19 (2007) 1439–1451.
- [26] S.N. Kim, J.F. Rusling, F. Papadimitrakopoulos, Carbon nanotubes for electronic and electrochemical detection of biomolecules, *Adv. Mater.* 19 (2007) 3214–3228.
- [27] K. Balasubramanian, M. Burghard, Biosensors based on carbon nanotubes, *Anal. Bional. Chem.* 385 (2006) 452–468.
- [28] O.N. Oliveira Jr., R.M. Iost, J.R. Siqueira Jr., F.N. Crespiho, L. Caseli, Nanomaterials for diagnosis: challenges and applications in smart devices based on molecular recognition, *ACS Appl. Mater. Interfaces* 6 (2014) 14745–14766.
- [29] J.R. Siqueira Jr., L. Caseli, F.N. Crespiho, V. Zucolotto, O.N. Oliveira Jr., Immobilization of biomolecules on nanostructured films for biosensing, *Biosens. Bioelectron.* 25 (2010) 1254–1263.
- [30] A. Merkoçi, Nanobiomaterials in electroanalysis, *Electroanalysis* 19 (2007) 739–741.
- [31] X. Li, B. Wei, Supercapacitors based on nanostructured carbon, *Nano Energy* 2 (2013) 159–173.
- [32] G. Yu, X. Xie, L. Pan, Z. Bao, Y. Cui, Hybrid nanostructured materials for high-performance electrochemical capacitors, *Nano Energy* 2 (2013) 213–234.
- [33] S.W. Lee, J. Kim, S. Chen, P.T. Hammond, Y. Shao-Horn, Carbon nanotube/manganese oxide ultrathin film electrodes for electrochemical capacitors, *ACS Nano* 4 (2010) 3889–3896.
- [34] V. Obradović, D.B. Stojanović, I. Živković, P.S. Radojević, R. Uskoković, R. Aleksić, Dynamic mechanical and impact properties of composites reinforced with carbon nanotubes, *Fiber. Polym.* 16 (2015) 138–145.
- [35] S. Pande, A. Chaudhary, D. Patel, B.P. Singh, R.B. Mathur, Mechanical and electrical properties of multiwall carbon nanotube/polycarbonate composites for electrostatic discharge and electromagnetic interference shielding applications, *RSC Adv.* 4 (2014) 13839–13849.
- [36] A.B. Duran, E.M. Carpenter, T.I. Malinin, J.C. Rodriguez-Manzaneque, L.P. Zanello, Carboxyl-modified single-wall carbon nanotubes improve bone tissue formation in vitro and repair in an in vivo rat model, *Int. J. Nanomed.* 9 (2014) 4277–4291.
- [37] A. Gupta, B.J. Main, B.L. Taylor, M. Gupta, C.A. Whitworth, C. Cady, J.W. Freeman, S.F. El-Amin III, In vitro evaluation of three-dimensional single-walled carbon nanotube composites for bone tissue engineering, *J. Biomed. Mater. Res. A* 102 (2014) 4118–4126.

- [38] H. Wang, C. Chu, R. Cai, S. Jiang, L. Zhai, J. Lu, X. Li, S. Jiang, Synthesis and bioactivity of gelatin/multiwalled carbon nanotubes/hydroxyapatite nanofibrous scaffolds towards bone tissue engineering, *RSC Adv.* 5 (2015) 53550–53558.
- [39] K.S. Novoselov, A.K. Geim, S.V. Morozov, Electric field in atomically thin carbon films, *Science* 306 (2004) 666–669.
- [40] K. Geim, Graphene: status and prospects, *Science* 324 (2009) 1530–1534.
- [41] M.J. Allen, V.C. Tung, R.B. Kaner, Honeycomb carbon: a review of graphene, *Chem. Rev.* 110 (2010) 132–145.
- [42] K.S. Novoselov, V.I. Faíko, L. Colombo, P.R. Gellert, M.G. Schwab, K. Kim, A roadmap for graphene, *Nature* 490 (2012) 192–200.
- [43] K. Sambasivudu, M. Yashwant, Challenges and opportunities for the mass production of high quality graphene: an analysis of worldwide patents, *Nanotech Insights*, 2012.
- [44] V. Dhand, K.Y. Rhee, H.J. Kim, D.H. Jung, A comprehensive review of graphene nanocomposites: research status and trends, *J. Nanomater.* 2013 (2013) 14.
- [45] R.R. Nair, P. Blake, A.N. Grigorenko, K.S. Novoselov, T.J. Booth, T. Stauber, N.M. Peres, A.K. Geim, Fine structure constant defines visual transparency of graphene, *Science* 320 (2008) 1308.
- [46] A.M. Pinto, I.C. Gonçalves, F.D. Magalhães, Graphene-based materials biocompatibility: a review, *Colloid. Surf. B* 111 (2013) 188–202.
- [47] X. Dong, L. Wang, D. Wang, C. Li, J. Jin, Layer-by-layer engineered Co-Al hydroxide nanosheets/graphene multilayer films as flexible electrode for supercapacitor, *Langmuir* 28 (2013) 293–298.
- [48] Z. Niu, J. Du, X. Cao, Y. Sun, W. Zhou, H.H. Hng, J. Ma, X. Chen, S. Xie, Electrophoretic build-up of alternately multilayered films and micropatterns based on graphene sheets and nanoparticles and their applications in flexible supercapacitors, *Small* 8 (2012) 3201–3208.
- [49] W. Liu, X. Yan, J. Lang, J. Chen, Q. Xue, Influences of the thickness of self-assembled graphene multilayer films on the supercapacitive performance, *Electrochim. Acta* 60 (2012) 41–49.
- [50] G.D. Moon, J.B. Joo, Y. Yin, Stacked multilayers of alternating reduced graphene oxide and carbon nanotubes for planar supercapacitors, *Nanoscale* 5 (2013) 11577.
- [51] M. Zhi, C. Xiang, J. Li, M. Li, N. Wu, Nanostructured carbon–metal oxide composite electrodes for supercapacitors: a review, *Nanoscale* 5 (2013) 72.
- [52] W. Liu, X. Yan, Q. Xue, Multilayer hybrid films consisting of alternating graphene and titanium dioxide for high-performance supercapacitors, *J. Mater. Chem. C* 1 (2013) 1413.
- [53] T. Kuila, S. Bose, P. Khanra, A.K. Mishra, N.H. Kim, J.H. Lee, Recent advances in graphene-based biosensors, *Biosens. Bioelectron.* 26 (2011) 4637–4648.
- [54] W. Shao, J. Wang, W.J. Liu, I.A. Aksay, Y. Lin, Graphene based electrochemical sensors and biosensors: a review, *Electroanalysis* 22 (2010) 1027–1036.
- [55] Y. Huang, X. Dong, Y. Shi, C.M. Li, L.J. Li, P. Chen, Nanoelectronic biosensors based on CVD grown graphene, *Nanoscale* 2 (2010) 1485–1488.



# Index

## A

Acrylonitrile-butadiene-styrene (ABS) blend, 195  
Alkaline electrolytes, 74  
Alloys production, mechanical friction, use of, 127  
Aluminum anodization, 76, 77, 79  
Ammonium borate, 76  
Ammonium tartrate, 76  
Amphiphilic molecules, 35  
Anodic oxide films, 68  
Anodization, 67  
    oxide formation of valve metals, 67  
    oxide properties modification, by anodic doping, 90  
    self-organization in anodic oxides, 76  
    under strong electric fields, 70  
    TiO<sub>2</sub> nanotubes, electrochemical synthesis, 85  
Anodization potential, 78, 83, 87  
Anodization reactions, 58, 90  
Antiferromagnetic materials, 151  
    dipole arrangements, 153  
    exchange constant value, 153  
*Aspergillus niger*, 23  
Atomic force microscopy (AFM), 109  
    image acquisition  
    three modes, 138  
    roughness investigation, 137  
    surface topography investigation, 137  
Atomic-scale microscopy, 7  
    nanoscience/nanotechnology, 7  
Average surface roughness, investigation, 138

## B

Binders, 49  
Biocompatible polymers, 166  
Biomagnetic compasses, 147  
Biomedical devices, 24  
Biomimicry, 8, 24

Bloch theorem, 213–215  
Blocking temperature, 158, 159  
Bohr magneton, 150  
Boltzmann constant, 129, 158  
Boric acid, 76  
Bragg reflections, 215  
Bragg's law, 135  
Bravais lattice, 215  
Brazilian Agricultural Research Corporation (EMBRAPA), 7  
Brewster angle microscopy, 109  
Brillouin zones, 215  
Brownian mechanism, 160  
Brownian relaxation time, 160  
Buckminsterfullerene, 234  
Buckyball, 234  
Bulk heterojunction, 235

**C**

Carbon nanotubes (CNTs), 23, 221, 237  
    applications, 240  
    biosensors, 241  
    diagnosis of diseases, 241  
    engineering materials, 242  
    integration of, with biological compounds, 241  
    as reinforcement in composites, 242  
    as supercapacitors, 242  
    electrical characteristics, 237  
    electronic structure, 228–230, 239  
    energy dispersion, 229  
        ratios, 230  
    mechanical characteristics, 237  
    molecular orbitals in energy bands, 229  
    occupation of valence band, 227  
    properties of, 237  
    schematic diagram of, rolling of graphene sheet, 239  
    structure, 221  
        application of quantum theory to, 222

- Carbon nanotubes (CNTs) (*cont.*)  
 lattice vectors in real space, 222  
 TB model, 224  
 synthesis, 240  
   CVD, 240  
   electric arc, 240  
   pulsed laser, 240  
 types of sensors containing CNTs, 241  
 wave vectors, representation of, 226  
 zone-folding approximation, 229
- Cell membranes  
 chemical composition, 45  
 physicochemical properties, 45
- C-60 fullerene, 1
- Chemical erosion, 82
- Chiral vectors, 221
- Cholesteryl benzoate, 20  
 double melting point of, 19  
 structure, 20
- Chronoamperometry, 63
- Chronopotentiometry, 63
- Classical mechanics, 211  
 classical formalism at, nanometric scale, 211  
 degrees of freedom, 211  
 quantum mechanics equation, 211
- CMC. *See* Critical micelle concentration (CMC)
- CMOSs. *See* Complementary metal-oxide semiconductors (CMOSs)
- Cobalt ferrite films, atomic force microscopy topographical image, 173
- Cobalt ferrite nanoparticles, Mössbauer spectra, 171
- Coercive field, 153
- Complementary metal-oxide semiconductors (CMOSs), 17
- Control drug delivery (CDD) systems, 178
- Coordination number, 49
- Coupling constant, 153
- Critical micelle concentration (CMC), 37
- Crystal lattice  
 electronic structure, 216  
 density of states, discretization of energy, 217–218
- quantum confinement of electrons, volume of material, 218–219
- mathematical modeling techniques, 213  
 periodic structure of, 213  
 reciprocal lattice and, 215  
 wave function, 214  
 wave vector, 214
- Crystalline anatase phase, 88
- Crystallization processes, 62
- Curie temperature, 153
- Cyclic voltammetry, 63, 141
- Cyclic voltammogram, 65
- Cyclodextrin, chemical structure, 50
- D**
- Data-storage chips, 17
- de Broglie equation, 210
- de Broglie wavelength, 133
- Degree of inversion, 155
- Demchak and Fort (DF) model, 110  
 capacitor model of, 111  
 Langmuir films, characterizing, 110
- Dendrimers, 132  
 advantages, 132  
 metal nanoparticles, synthesis of, 133  
 tree-like morphology, macromolecules of, 132
- Detergents, 35  
 adsorption, 36  
 and surfactants, 35
- Diamagnetic materials, 150
- Diamagnetism  
 illustration of magnetic dipole arrangement, 151  
 magnetic dipole arrangement, 151
- Digital screens, 17
- Dimercaptosuccinic acid (DMSA), 164
- Dipalmitoylphosphatidylcholine (DPPC), 44
- Dipalmitoylphosphatidylglycerol (DPPG), 44
- Direct methanol fuel cell (DMFC)-type fuel cells, 141
- DMSA-coated iron oxide nanoparticles disulfide bridge formation, 172

DPPC. *See* Dipalmitoylphosphatidylcholine (DPPC)

DPPG. *See* Dipalmitoylphosphatidylglycerol (DPPG)

**E**

Effective relaxation time, 160

EIL. *See* Electron-injection layer (EIL)

EL. *See* Emitting layer (EL)

Electrochemical cells, 56

- definition, 56
- three-electrode, experimental configuration, 58
- types, 56

Electrochemical circuit, 57

Electrochemical reaction, 60

- charge-transfer, 60
- chemical reaction, 60
- crystallization, 60
- diffusion, 60

Electrochemistry, 54

- electrochemical cells, 56
- definition, 56
- types, 56
- faradaic processes, 54
- non-faradaic processes, 54

Electrodeposition, 60

Electrolysis, 56

Electrolytic breakdown, 69

Electrolytic cell, 56

Electron-hole pair recombination, 93

Electron-injection layer (EIL), 20

Electron microscopes, high-resolution, 17, 174

Electron state

- magnetic quantum number, 149
- orbital angular momentum, 149
- principal quantum number, 149
- spin quantum number, 149

EMBRAPA. *See* Brazilian Agricultural Research Corporation (EMBRAPA)

Emitting layer (EL), 20

Endorem, 179

Enzymatic biosensor, glucose detection, 133

Etching techniques, 17

Exchange integral, 152

Exfoliated nanocomposites, 190

Extrusion, 43

**F**

Faradaic processes, 54

Fermi energy, 218

Ferrimagnetic materials, 152

- dipole arrangements, 153
- exchange constant value, 153

Ferrites, 154–155

Ferrofluids, 148

Ferromagnetic materials, 151, 153

- dipole arrangements, 153
- exchange constant value, 153
- magnetic hysteresis curve, 154
- rare-earth metals, 151
- transition metals, 151

First Brillouin zone, hexagonal graphene

- conduction and valence bands in, 221
- illustrations of allowed wave vector, 228, 230

First-order Langevin function, 159

Fullerene, 234

- applications, 235
- as drug carriers, 237
- medical and pharmaceutical fields, 237
- organic electronic devices, 237
- organic solar cells, 235
- solar cell efficiency, 236

icosahedral symmetrically closed-cage structure, 234

processes of synthesis, 235

properties, 235

- electron-deficient alkene, 235
- mechanical properties, 235
- molecular stability, 235
- optical properties, 235

schematic representation of, C60 fullerene, 234

zero-dimensional carbon structure, 234

Fundamental state, 219

**G**

Galvanostatic, 68

Galvanostatic anodization curve, 72

Galvanostatic method, 75

Giant magnetoresistance (GMR), 18  
 Gibbs free energy, 164  
     per unit volume, 129  
 Gibbs theory, 35  
 Global positioning system (GPS), 19  
 GMR. *See* Giant magnetoresistance (GMR)  
 Gold nanoparticles, 3  
     preparation, 126  
     via sodium citrate, 131  
     size distribution, 137  
     transmission electron microscopy (TEM), 137  
 Gold nanorod, different aspect ratios  
     optical spectra, 135  
     photographs, 135  
     transmission electron micrographs, 135  
 Gouy-Chapman model, 60  
 GPS. *See* Global positioning system (GPS)  
 Graphene, 219, 243  
     applications, 244  
         biomedical applications, 246  
         high-performance logic circuits, 245  
         for next-generation lithium-ion batteries, 245  
         in sensors and biosensors, 245  
         supercapacitors, 245  
     band structure, 243  
     Brillouin zone of, 219  
     electronic properties, 220  
     electronic structure, 219–221  
     properties, 243  
         electron mobility, 243  
         thermal conductivity, 243  
     schematic representation, 244  
     structure in real space, 220  
     synthesis, 243  
         bottom-up approach, 243  
         top-down approach, 243  
 Graphene oxide (GO), 243  
     chemical reduction, purpose, 244  
     schematic representation, 244  
     structural defects, 244  
 Graphene-platinum colloidal suspension,  
     atomic force microscopy (AFM) image, 139

**H**  
 Hafnium oxides ( $\text{HfO}_2$ ), 18  
 Hamiltonian operator, 213  
 Hard anodization cell, 83  
 Hard anodization method, 83  
 HDPE. *See* High-density polyethylene  
 Heisenberg Hamiltonian equation, 152  
 Helmholtz model, 59  
 Helmholtz plane, 60  
 Heterojunction solar cell  
     polymer/fullerene, 236  
     schematic illustration of, 236  
 $\text{HfO}_2$ . *See* Hafnium oxides ( $\text{HfO}_2$ )  
 High-density polyethylene (HDPE), 197  
     mechanical properties of, 201  
     morphology of, 200  
     oxygen permeability of films, 203  
     in packaging and electric sectors, 197  
     TEM micrographs of, 198  
     XRD patterns of OMMT and, 197, 199  
 High-energy grinding process, 127  
 High-time-resolution signal acquisition, 71  
 Hole-transporting layer (HTL), 20  
 Hopping term, 225  
 Host-guest complex, 34  
 HTL. *See* Hole-transporting layer (HTL)  
 Hydrogen atoms, 4  
 Hysteresis, 153

**I**  
 Indium tin oxide (ITO), 19  
 Intercalated nanocomposites, 190  
 International Organization for Standardization-Technical Committee (ISO-TC), 3  
 ISO-TC. *See* International Organization for Standardization-Technical Committee (ISO-TC)  
 ITO. *See* Indium tin oxide (ITO)

**K**  
 Krätschmer-Huffman method, 235  
 Kronecker delta, 216

**L**

Lamellar clays  
 cation exchange capacity (CEC), 189  
 composition, 188  
 flexibility of, 188  
 structures, 188  
 surface treatment, 189  
 used, in production of nanocomposites, 188  
 XRD patterns of HDPE/LLDPE  
   nanocomposite blends and, 197

Langmuir-Blodgett technique, 106  
 applications, 113–114  
 biotechnological applications, 118  
 characterization methods, 118  
 different Langmuir monolayer  
   deposition, 112  
 different LB film types, 113  
 disadvantage, 109, 110  
 history, 106  
 Langmuir-Schaefer (LS) method, 107  
 monolayer deposition method, 107  
 nonpolar tail group (hydrophobic), 108  
 novel LbL deposition strategies, 117  
 overview, 108–109  
 polar head group (hydrophilic), 108  
 pressure and surface potential, 109  
   liquid surface tension, 109  
 prototype of Langmuir, 107  
 schematic illustration of, fabrication of  
   spherical shells, 119  
 schematic representation of Langmuir, 107  
 spray- and spin-LbL methods, 117  
 surface potential, 110  
 wave-damping phenomenon, 106  
 Langmuir-Schaefer (LS) method, 107  
 Laser vaporization method, 235  
 Layer-by-layer technique, 114  
   applications, 118  
   characterization methods, 118  
   historical prospectus, 114  
   mechanisms of, LbL film formation, 115–117  
   overview, 114–115  
   schematic representation of, traditional LbL  
     deposition process, 115  
   spray- and spin-LbL methods, 117

LCDs. *See* Liquid crystal displays (LCDs)  
 Lift-off metallization process, 128  
 Linear combination of atomic orbitals  
   (LCAO), 213  
 Linear low-density polyethylene (LLDPE)  
   nanocomposite blends, 197  
 mechanical properties of, 201  
 morphology of, 200  
 oxygen permeability of films, 203  
 TEM micrographs of, 198  
 XRD patterns of OMMT and, 197, 199  
 Lipid aggregates, 37  
 Lipid bilayers, 39  
   structure, 40  
 Liposomes, 43  
   biomedical applications, 43  
   preparation method, 41  
 Liquid condensate phase (stage C), 108  
 Liquid crystal displays (LCDs), 19  
 Lithographic methods, 79  
 Lithography, 17  
   electronic and optical devices  
     production, 128  
     steps, 128  
 LLDPE. *See* Linear low-density  
   polyethylene  
 Lowest unoccupied molecular orbital  
   (LUMO), 235  
 Lycurgus cup, 126

**M**

Macrocycles, 34  
 Maghemite, 156  
 nanoparticles, positively charged, Raman  
   spectrum, 170  
 particle size distribution, 162  
 synthesis process  
   via coprecipitation of magnetite, 162  
   transmission electron microscopy (TEM)  
     image, 162, 163  
 Magnetic colloids, biomedical  
   applications, 177–180  
 in vitro application, 177  
   magnetic separation, 180  
 in vivo application, 177

- Magnetic domain, 157  
 structure, 157
- Magnetic moment, 150
- Magnetic nanoparticles  
 biomedical applications, 141  
 controlled release of pharmaceuticals, 142  
 encapsulation, 142  
 surface functionalization, 142  
 synthesis, 142
- Magnetic sensor, 18
- Magnetic susceptibility, 149
- Magnetic tunnel junction (MTJ), 18
- Magnetism  
 basic concepts, 149–160  
 cubic ferrites, 155–156  
 ferrimagnetism, 154–155  
 superparamagnetism, 157–160  
 quantum mechanical phenomenon, 149
- Magnetite, 156  
 inverse spinel structure  
 spin moment distribution, 157  
 and maghemite nanoparticles  
 self-assembly, 176
- Magnetization decay time, 160
- Magnetization process, 153
- Magnetocrystalline anisotropy, 158
- Magnetocrystalline energy boundary, 158
- Magnetoliposomes (MLs), 166
- Mass variation, 63
- MEMS. *See* Micro Electro Mechanical Systems (MEMS)
- Metal nanoparticles synthesis  
 via reduction by borohydride, inside  
 dendrimer, 133
- Metal reduction, 132–133  
 metal precursors, 132  
 acetates, 132  
 acetyl ketones, 132  
 chlorides, 132  
 nitrates, 132  
 oxides, 132
- reducing agents, 132  
 ascorbic acid, 132  
 citrates, 132  
 dehydrogenating gases, 132
- glycol ethylene, 132  
 hydrazine, 132  
 hydrides, 132
- Micelles, 37  
 critical micelle concentration, 37  
 formation, 37  
 dependence on surfactant concentration, 38
- Microarrays, 12
- Microcomposites, 190
- Micro Electro Mechanical Systems (MEMS), 12
- Microfluidics, 83
- Microprocessors, 17
- Micro-Raman configuration, 169
- MLs. *See* Magnetoliposomes (MLs)
- MLVs. *See* Multilamellar vesicles (MLVs)
- Molecular magnets, 147
- Molecular recognition, 34  
 biosensor selectivity, 139  
 host-guest complex, 34  
 principles of, 12
- Montmorillonite clay (OMMT)  
 TEM micrograph, 194, 196, 198, 199  
 XRD patterns of HDPE/LLDPE  
 nanocomposite blends and, 199
- Mössbauer spectroscopy, 169, 170
- MTJ. *See* Magnetic tunnel junction (MTJ)
- Multicyclic supramolecular systems, 49
- Multilamellar vesicles (MLVs), 41
- Multilayer formation process, 115  
 initial adsorption of material, 115  
 relaxation of adsorbed layer (slower process), 115
- Multiwalled carbon nanotubes (MWNTs), 237  
 length and diameter, 237  
 structures, 238
- N**
- Nanoarrays, 12
- Nanobots, 26
- Nano Electro Mechanical Systems (NEMS), 12
- Nanofluids (NFs), 148

- Nanoindentation, 79  
 Nanomaterials, 53  
     to create new products, 71  
     defined, 53  
     electrical behavior, 218  
     electrochemical synthesis, 54  
     magnetic materials of, 147  
     size and shape of, 167  
 Nanomedicine, 24  
 Nanometric array, 87  
 Nanoparticle formation, physicochemical aspects  
     Gibbs free energy, 129  
     growth phenomena, 129, 130  
     nucleation, 129, 130  
     solute concentration, 129  
     supersaturation, 130  
     surface energy, 130  
 Nanoparticles  
     applications, 139–142  
         biosensors, 139–140  
             immunosensors, 140  
             molecular recognition based, 139, 140  
         cancer treatment, 125  
         catalysis, 140–141  
             oxidoreduction in fuel cells, 141  
         diagnosis, 125  
         high-sensitivity sensors, 139  
         magnetic nanoparticles in biomedicine, 141–142  
     characterization methods, 135–139  
         atomic force microscopy (AFM), 137–139  
         transmission electron microscopy (TEM), 136–137  
         X-ray diffraction (XRD), 135–136  
     colloidal aggregation prevention, 164  
     definition, 126  
     electrophoretic mobility, 171  
     preparation  
         decomposition method, 162–163  
             disadvantage, 163  
         via coprecipitation, 161  
     properties, 133–134  
         magnetic properties, 134  
         shape and size, dependence on, 126  
     spin orientations, 134  
     tunneling effect, 134  
 stabilization, 131  
     agglomeration process, 131  
     stabilizers, use of, 131  
     surfactants, use of, 131  
 stabilization mechanisms, 164  
 surface charge density variation, 165  
 surface charge determination  
     zeta potential, 171  
 surface energy minimization, 131  
 surface functionalization, 164  
 surface manipulation, 163  
 synthesis methods, 126–133  
     bottom-up methods, 129–133  
         chemical vapor deposition, 129  
         laser ablation, 129  
         metal reduction, 132–133  
         molecular beam epitaxy, 129  
         nanoparticle stabilization, 131  
         physicochemical aspects of  
             nanoparticle formation, 129–130  
         pulse laser deposition, 129  
         sol-gel synthesis, 131–132  
         sputtering deposition, 129  
     liquid phase  
         growth phenomena, 129  
         nucleation, 129  
     top-down methods, 127–128  
         lithography, 128  
         mechanical friction, 127  
     zero-dimensional nanostructures, 126  
 Nanoporous alumina, 80  
     illustration for fabrication, 80  
 Nanoreactors, 132  
     control of synthesis processes, 132  
     polyamidoamine (PAMAM), 133  
 Nanoscale, 1  
 Nanoscale materials, 26  
 Nanoscience, 3  
     concepts, 3  
     defined, 3  
     history, 3  
     principles, 3  
 Nanoscopic luminescent devices, 84

- Nanostructured films, 59  
 electrodeposition process, 62  
 single-constituent metallic films, 64  
 synthesis by electrodeposition, 59
- N**  
**Nanostructures**, 1
- Nanotechnology**, 1  
 actions, 14  
 commercial products involving, 17  
 definition, 3  
 investments, 14  
 research, 14  
 strategies, 14
- Nanotube fabrication**, 83
- National Institute of Science and Technology Policy (NISTEP)**, 15
- National Nanotechnology Initiative of the US (NNI)**, 3
- National Science Foundation (NSF)**, 14
- Natural latex rubber, surface modification**, 138
- Néel relaxation time**, 158
- NEMS. See Nano Electro Mechanical Systems (NEMS)**
- Neutral electrolytes**, 74
- Ni-Co alloy**, 64
- NISTEP. See National Institute of Science and Technology Policy (NISTEP)**
- NNI. See National Nanotechnology Initiative of the US (NNI)**
- Non-faradaic processes**, 54
- Nonpolar matrices**, 196  
 compatibilization in nanocomposites, 192  
 nanocomposites, 196  
 structure and properties, 197
- NSF. See National Science Foundation (NSF)**
- Nucleation processes**, 62
- O**
- OLED. See Organic light-emitting diode (OLED)**
- Oleic acid-coated maghemite nanoparticles, characterization**  
 Raman spectroscopy, 172  
 thermogravimetry, 172
- OMMT. See Organically modified montmorillonite clay**
- One-dimensional double-well potential particle magnetic moments dynamics**, 159  
**superparamagnetic regimen**, 158
- Optical emission spectroscopy equipment**, 71
- Organically modified montmorillonite clay (OMMT)**, 194  
 TEM micrographs of, 199  
 XRD patterns, 199
- Organic light-emitting diode (OLED)**, 13
- Organometallic compounds**, 162
- Organometallic nanowires**, 7
- Organophilic clay**  
 effect of shearing on, intercalation and/or exfoliation, 191  
 exfoliation of, 191
- Ostwald ripening**, 130
- Oxide film**, 58
- P**
- PAA. See Polyacrylic acid (PAA); Porous anodic alumina (PAA)**
- PAMAM. See Polyamidoamine (PAMAM); Polyamidoamine dendrimer (PAMAM)**
- (PAni/n-MAG)10 nanofilm**  
 high-resolution electron microscopy images, 174
- Parallel electrochemical reactions**, 68
- Parallel-plate capacitor**, 59
- Paramagnetic materials**, 150
- Paramagnetism, magnetic dipole arrangement**, 151
- Pauli exclusion principle**, 150, 155
- PDT. See Photodynamic therapy (PDT)**
- Perchloric acid**, 76
- Phosphate aqueous solution**, 76
- Phospholipids, properties**, 42
- Phospholipid vesicles**, 43
- Phosphoric acid**, 74
- Photoacoustic spectroscopy**, 172
- Photocurrent**, 93
- Photodynamic therapy (PDT)**, 180
- Photonic crystals**, 83
- Phthalocyanine, chemical structure**, 49

- Platinum nanoparticles  
modified synthesis, 141  
with Nafion, 141  
production, 141
- Polarization, 68
- Polar matrices, 193  
degree of exfoliation, 195  
mechanical properties, 195  
structure and properties, 193
- Polyacid acrylic (PAA), 116
- Polyacrylic acid (PAA), 44
- Polyamidoamine (PAMAM), 133
- Polyamidoamine dendrimer (PAMAM), 44
- Polyaniline/maghemit nanofilms,  
susceptibility measurements, 177
- Polymeric nanomaterials, 23
- Polymer nanocomposites, 187  
compatibilization, with nonpolar  
matrices, 192  
copolymerization techniques, 193  
methods for obtaining, 191  
morphology, 194  
nonpolar matrices and, 196  
permeability of, 202  
polar matrices and, 193  
schematic representation, action of block  
copolymer, 193  
schematic representation of, different types  
of composites, 190  
structural characterization, 190  
structure, 189–190  
thermal stability, 193
- Polyolefins, 196  
compatibilizing agents, 196  
exfoliated nanocomposites, 196
- Polyvinyl pyridine (PVP) multilayers, 116
- Porous anodic alumina (PAA), 69  
hexagonal configuration schematic, 76  
potentiostatic formation process, 78
- Porphyrin, chemical structure, 49
- Potentiostatic, 68
- Potentiostatic regime, 68
- POX3OA sample  
magnetization curves, 175  
ZFC-FC curves, 176
- Prostheses, 24
- Protonation-deprotonation equilibrium, 161
- Pulsed anodization, 75
- Q**
- QCEM. *See* Quartz-crystal electrochemical  
microbalance (QCEM)
- Quantum confinement of electrons, volume of  
material, 218–219  
discrete levels, 218  
quantum confinement condition of  
electrons, 219  
wave vector, 218
- Quantum electrostatic interaction, 151
- Quantum mechanics, 212  
oscillation frequency, 212  
quantum system, 212  
wave function, 212
- Quantum system, 212  
eigenvalues for, 212  
energy, stationary conditions, 212  
Hamiltonian formulation, 213
- Quantum trapping, 133
- Quartz-crystal electrochemical microbalance  
(QCEM), 63
- R**
- Raman modes, 168
- Raman spectroscopy, 169, 172
- Rapid thermal annealing, 79
- Reciprocal lattice, 216
- Responsible Research Innovation (RRI)  
program, 15
- Robots, 26
- RRI program. *See* Responsible Research  
Innovation (RRI) program
- Russell-Saunders coupling, 153
- S**
- Saturation magnetization, 153
- SAXS. *See* Small-angle X-ray scattering (SAXS)
- Scanning tunneling microscope (STM), 6, 63
- Scherrer's equation, 136, 167
- Schrödinger's equation, 149, 152
- Schrödinger theory, 212, 213

- Science of Science and Innovation Policy (SciSIP), 15
- SciSIP. *See* Science of Science and Innovation Policy (SciSIP)
- Self-aggregated disperse systems, 34
- Self-organized systems, 35
- cell membranes, 45
    - chemical composition, 45
    - physicochemical properties, 45
  - detergents, 35
  - lipid bilayers, 39
  - liposomes, 43
    - biomedical applications, 43
  - liposomes and multilayer systems, preparation method of, 41
  - micelles, 37
  - vesicular systems, 39
- Silicate, 2:1 phyllosilicate structure, 188
- Silicon, 18
- Silver nanoparticles, light-sensitive, 126
- Single-walled carbon nanotubes (SWNTs), 237
- chiral vector pair, 238
  - in field-effect transistors (FET), 242
  - properties of, 238
  - relationship of  $(n,m)$  pair with, 239
  - schematic diagram of, rolling of graphene sheet, 239
  - structures, 238
- Small-angle X-ray scattering (SAXS), 136
- Sol-gel synthesis
- colloidal dispersions of oxides production, 131
  - core-shell nanostructures production, 131
  - nonaqueous synthesis, 132
    - solvent control, 132
    - surfactant control, 132
  - precursor, 131
- Sonication, 42
- Spin-assisted LbL method, 117
- Spinel, 155
- Spinel-like cubic ferrite, atomic arrangement, 156
- Spin-orbit interaction energy, 153
- Spontaneous magnetization, 155
- Spray- and spin-LbL methods, 117
- Stabilizer/gold ratio, 137
- Staphylococcus aureus*, 23
- Stearic acid monolayer
- Demchak and Fort (DF) model, 110
  - surface potential isotherm, 112
  - typical surface pressure isotherm for, 108
- Stern model, 60
- STM. *See* Scanning tunneling microscope (STM)
- Stöber method, 166
- Supercapacitors, 245
- schematic representation, 246
- Superparamagnetic cubic ferrites, 148
- Superparamagnetic iron oxides (SPIOs) systems, 160–166
- agglomeration state measurement, 167–168
  - cancer treatment nanotherapy, 179
    - chemotherapy, 179
    - gene therapy, 179
    - magneto hyperthermia (MHT), 179
  - chemical composition determination
    - atomic absorption spectrometry, 168
    - colorimetric analysis, 168
    - energy dispersive spectroscopy (EDS), 168
    - X-ray fluorescence, 168
  - composition and structure, 168–170
  - crystalline morphology, 167
  - crystalline quality, X-ray diffraction technique, 167
  - high-resolution TEMs (HRTEMs), 167
  - magnetic colloids preparation, 163–166
  - magnetic properties, 174–176
  - microscopy, 167
  - morphology investigation, atomic force microscopy, 172
  - nanoparticles, functionalization by DMSA, 166
  - particle functionalization, 163–166
  - physico-chemical properties, 166–176
  - size measurement, 167–168
  - structure, 166–176
  - surface morphology and properties, 171–174

- synthesis
  - via coprecipitation, 161
  - via thermal decomposition, 162–163
- theranostic agents, applications, 178
- Superparamagnetic relaxation, 170
- Superparamagnetism, 158
- Supramolecular chemistry, 50
- Supramolecular system, 33
  - classification, 33
  - macrocycle compounds, 33
  - systems with molecular self-aggregation, 33
- scientific applications, 33
  - biomimetic systems, 33
  - in catalysis, 33
  - molecular recognition, 33
  - transport of substances, 33
  - technological applications, 33
- Surface conduction electrons, 134
- Surface plasmon absorption, 134
- Surface potential
  - definition, 110
  - measurement, 110
- Surfactants, 35
  - amphiphilic substances, 35
  - examples, 36
  
- T**
- TEM. *See* Transmission electron microscopy (TEM)
- Template-driven synthesis, 34
- Tetraborate, 76
- Tetrahydrofuran (THF), 132
- Theranostic agent, definition, 177
  
- Theranostic nanotherapeutic system
  - architecture of, 179
- Thermal cracking, 70
- Thermionic valves, 67
- THF. *See* Tetrahydrofuran (THF)
- TiO<sub>2</sub> nanotubes, 85
- Tissue regeneration, 142
- Titanium oxidation technique, 85
- Tortuosity factor, 202
- Total angular momentum, 152
- Transistors, 17
- Transition elements, 153
- Transmission electron microscopy (TEM), 64
  
- U**
- US Food and Drug Administration, 179
  
- V**
- Valve metals, 67
- Vesicular systems, 39
  
- W**
- Wave-damping phenomenon, 106
- Web of Science (WOS), 15
- WOS. *See* Web of Science (WOS)
  
- X**
- X-ray diffraction (XRD) technique,
  - investigation of
  - atomic arrangement, 136
  - crystallinity degree, 135
  - crystallites size, 135
- X-ray radiation, reflection of, 215